FULL SKY IMAGING POLARIMETRY FOR INITIAL POLARIZED MODTRAN VALIDATION

by

Nathaniel Joel Pust

A dissertation submitted in partial fulfillment
of the requirements for the degree

of

Doctor of Philosophy

in

Engineering

MONTANA STATE UNIVERSITY
Bozeman, Montana

April 2007

APPROVAL

of a dissertation submitted by

Nathaniel Joel Pust

This dissertation has been read by each member of the dissertation committee and has been found to be satisfactory regarding content, English usage, format, citations, bibliographic style, and consistency, and is ready for submission to the Division of Graduate Education.

Dr. Joseph A Shaw
Committee Chair

Approved for the Department of Electrical and Computer Engineering

Dr. James N. Peterson
Department Head

Approved for the Division of Graduate Education

Dr. Carl A. Fox
Vice Provost

STATEMENT OF PERMISSION TO USE

In presenting this dissertation in partial fulfillment of the requirements for a doctoral degree at Montana State University, I agree that the Library shall make it available to borrowers under rules of the Library. I further agree that copying of this dissertation is allowable only for scholarly purposes, consistent with "fair use" as prescribed in the U.S. Copyright Law. Requests for extensive copying or reproduction of this dissertation should be referred to ProQuest Information and Learning, 300 North Zeeb Road, Ann Arbor, Michigan 48106, to whom I have granted "the exclusive right to reproduce and distribute my dissertation in and from microform along with the non-exclusive right to reproduce and distribute my abstract in any format in whole or in part."

Nathaniel Pust

April 2007

ACKNOWLEDGEMENT

I would like to thank Dr. Joseph Shaw for his guidance and commitment to this research, Paul Nugent and Nick Jurich for lending a sounding sampling algorithm, Kevin Repasky for valuable discussion on LIDAR inversion, and my family for their steady support. Also, thanks to the Office of Air Force Scientific Research for funding this ongoing research.

TABLE OF CONTENTS

TABLE OF CONTENTS – CONTINUED

TABLE OF CONTENTS – CONTINUED

TABLE OF CONTENTS – CONTINUED

LIST OF TABLES

Tables Page

LIST OF FIGURES

Figures Page

LIST OF FIGURES – CONTINUED

Figures Page

LIST OF FIGURES – CONTINUED

Figures Page

LIST OF FIGURES – CONTINUED

Figures Page

LIST OF FIGURES – CONTINUED

Figures Page

LIST OF FIGURES – CONTINUED

Figures Page

LIST OF FIGURES – CONTINUED

Figures Page

LIST OF FIGURES – CONTINUED

Figures Page

LIST OF FIGURES – CONTINUED

Figures Page

LIST OF FIGURES – CONTINUED

Figures Page

LIST OF FIGURES – CONTINUED

Figures Page

ABSTRACT

Although military studies of the last ten years have shown that visible polarimetry supplies supplemental surveillance information, the polarimetric signatures of ground-based objects greatly depend on the illuminating skylight polarization. The polarization of a pure molecular atmosphere is easily modeled, but aerosols and clouds modify clear-sky polarization substantially. The Air Force has developed a polarimetric atmospheric radiative transfer model (MODTRAN-P) to simulate atmospheric effects. To assist MODTRAN-P code validation, a full-sky visible polarimeter has been developed using liquid crystal variable retarders (LCVRs). Unique calibration issues of LCVR instruments are addressed. A fisheye lens can be exchanged for a telephoto lens to provide system flexibility. This allows comparison between changing sky and changing target signatures. Calibration accuracy is within ±3% Degree of Linear Polarization (DoLP). Comparison of measured data with MODTRAN-P calculations shows that single-scatter models over-predict the sky polarization, while the improperly implemented multiple-scatter models under-predict it. Furthermore, a model comprising only one scattering path looking directly at a cloud insufficiently predicts polarization. The polarization is dependent upon whether or not there are clouds in surrounding areas. Similarly, clouds affect adjacent clear sky polarization, but further instrumentation is needed to understand whether this is caused by sub-visual cloud layers in these clear-sky areas or by illumination from neighboring clouds. Halo and cloud polarizations are also treated briefly.

INTRODUCTION

Over the last decade, a desire for new techniques in military surveillance has led the United States Air Force to consider polarization of light as a potential source of supplemental surveillance information. Polarization signatures accompanied by traditional surveillance methods have the potential to give better target identification. Initial polarization research has found several problems. One problem is the dependence of the target polarization signature upon the illuminating background light. Scattering in the atmosphere causes background light to be highly polarized in clear skies, but day-to-day changes in aerosols and clouds modify the polarization of the skylight. After light is reflected from an object, the polarization signature depends both upon the reflection characteristics of the object and the polarization of the illuminating light. Therefore, varying states of background light will cause varying polarimetric target signatures. Initial focus on polarization by the military has shifted from the visible bands to the long wave infrared to evade these problems since the light seen in the long wave infrared is dominated by emission, not reflection (Tyo et al, 2006). Therefore, the long-wave polarization signature is less dependent upon both the background and the source—scene—sensor geometry. Furthermore, the infrared signature is fairly consistent both day and night. Still, visible polarization may contribute useful surveillance information if the problem of the background polarization is addressed thoroughly. Until this problem is addressed, the capability to compare data from separate days with differing atmospheres is restricted. Also, although these problems have been observed, research needs to be done to correlate the target changes with sky measurements.

Clarifying the intricacies of the problem requires both modeling target characteristics—such as roughness and index of refraction—and modeling the various background sky polarizations. Light in the atmosphere exists with many different polarization states. In a sky free of clouds and dense aerosols, polarization is high in directions approximately 90° from the sun, but falls off as the angle moves away from 90°. This creates a stripe of high polarization across the sky surrounded by areas of lower polarization. This polarization stripe rotates throughout the day with the sun's position in the sky. The maximum degree of polarization also changes through the day. Models based upon the Rayleigh equation easily model this polarized sky dome for pure molecular scattering with considerable accuracy (Coulson, 1988, pg. 199). However, when clouds and aerosols are added to the sky, both the complexity of the Mie scattering equations and the increased effects of multiple scattering require a more complex model. Developing a thorough atmospheric radiative transfer model with polarization capability has become necessary. The Air Force has determined that this is best accomplished by modifying the longstanding Moderate Resolution Transmission Code (MODTRAN) to account for polarization.

MODTRAN is a proven model for calculating atmospheric radiation transfer that has been meticulously developed over the last 20 years (Berk et al., 2006). The standard version of MODTRAN does not account for polarization, but models unpolarized atmospheric radiance and transmittance at different wavelengths and zenith angles under various atmospheric conditions. Atmospheric scientists use MODTRAN and similar codes to predict quantities such as spectral sky radiance (Berk et al., 2005), effects of

water vapor upon thermal emission (Thurairajah, 2004), and Earth-to-space optical transmission (Manor, 2003). Polarized MODTRAN, dubbed MODTRAN-P, is a new version of MODTRAN that is being developed by the Air Force to add the polarization capability (Fetrow et al., 2002). Among other capabilities, this model will enable quick prediction of the background light polarization. These models can then be used to predict target signature variation for various sky conditions in surveillance studies. As with any model, MODTRAN-P needs to be validated before it can become valuable. Although the infrared and mid-infrared bands also need validation, the focus of the work reported here is on visible and near-infrared polarization.

To accomplish the goals of this study, two objectives prompted the design and development of an accurate full-sky imaging polarimeter. First, an accurate full-sky polarimeter was needed that could contribute to visible-band validation of MODTRAN-P. This instrument would measure polarization of the skylight and provide a better understanding of cloud and aerosol effects upon clear-sky polarization signatures. Also, measurements could be compared directly against model predictions. Second, a polarimeter that would directly measure both the sky and a ground-based target was necessary. This instrument would firmly quantify changes seen in target signatures with changes observed in the atmosphere. There are also many other scientific purposes for a full-sky imaging polarimeter. For example, very little has been written on polarimetric cloud identification (Horvath et al, 2002). Since clouds are primarily unpolarized, measured sky could be compared with a predicted clear-sky model to find areas of reduced polarization. These areas could be interpreted as clouds of different thicknesses

when accompanied by spectral data. Furthermore, there is a wealth of information contained within a full-sky polarization image that may contribute to improved retrieval of aerosol optical and microphysical properties (Vermeulen et al., 2000).

Throughout the last two years I have built and calibrated a polarimetric imaging system (Figure 1.1). This system is capable of measuring polarimetric signatures for targets, using a narrow field of view (FOV), and full-sky measurements using a large FOV. This system has been accurately calibrated and has been used to begin validation of the visible bands of the MODTRAN-P atmospheric model. Also, clear-sky polarization, cloudy sky polarization, and the effects of different atmosphere signatures on targets have been assessed.

In Chapter 2, a basic explanation of light polarization is given along with methods of quantifying and measuring polarization of light. Sources of measurable terrestrial polarization are discussed briefly. Finally, both the strengths and weaknesses of the designs of previous investigators are discussed. Chapter 3 lays out the design of the polarimeter built for this research. The decision to base the instrument on a liquid crystal variable retarder (LCVR) is defended, along with the selection of other polarimeter components. The validity of using devices that have variable polarization effects across the aperture is also discussed. Finally, the optical performance of the modeled optical train is assessed. Chapter 4 describes calibration of each component of the polarimeter. The unique calibration issues that burden LCVR-based designs are also addressed. In Chapter 5, the effects of differing sky backgrounds on the polarization signature of a set of metal plates are discussed. Also, effects of shadows and dew are treated briefly.

Chapter 6 addresses the effects of clouds, aerosols, and solar zenith angle upon sky polarization. The effects of surrounding sky upon one point in the sky—whether cloud or clear-sky—is also discussed. The polarization of Mie scattering from clouds and halo-forming ice crystals is briefly discussed. Chapter 7 is dedicated to the validation of MODTRAN-P. The methods used to obtain model input parameters are discussed. The primary topic of this chapter is comparison of the measured and modeled maximum degree of linear polarization. Finally, recommendations are given for future MODTRAN-P development and validation.

Figure 1.1. The visible-wavelength imaging polarimeter designed in this project, shown operating in full-sky mode.

BACKGROUND

Basic Principles of Light Polarization

Polarization is a fundamental property of light. The spatial orientation of the electric field in a Transverse Electromagnetic (TEM) wave defines the polarization angle of each propagating light wave. Like color and brightness, polarization is a separate property of light but is one that we cannot see directly. Each light wave can itself have a range of polarization angles from 0 to 180°.

General Description of Polarization

The most general description of the polarization of a single light wave is in terms of an ellipse. The total field is represented as the sum of two orthogonal electric fields: E_x is the component in the $\hat{\mathbf{x}}$ direction, while E_y is the component in the $\hat{\mathbf{y}}$ direction. Each of these components has a magnitude and phase. Since absolute phase of light cannot be measured readily, the phases can be reduced to a relative phase (ϕ) between the two components. The total electric field is then described as

$$E = \hat{\mathbf{x}}E_{x_0}\cos(\omega t - kz) + \hat{\mathbf{y}}E_{y_0}\cos(\omega t - kz + \phi) \qquad (2.1)$$

ω is the frequency of light, ϕ is the relative phase, t is time, E_{xo} and E_{yo} are the maximum electric field amplitudes, and k is the wavenumber.

Although Equation 2.1 can be used to describe all possible polarization states of a single light wave, several special-case polarization states exist. These polarization states are most easily understood for those unfamiliar with polarization.

Linear Polarization

The first special case is linear polarization. It highly dominates polarization signatures in the natural world with few exceptions. Two special cases of Equation 1 can result in a linearly polarized wave. First, if either the E_{xo} or E_{yo} component is zero, then the remaining nonzero term indicates that the electric field oscillates in the *y* or *x* plane, respectively. Figure 2.1 shows an example of a TEM wave where E_x is zero. The polarization angle is vertical (90° in standard *x*-*y* coordinate system) since there is no component of the electric field vector in the *x*-direction.

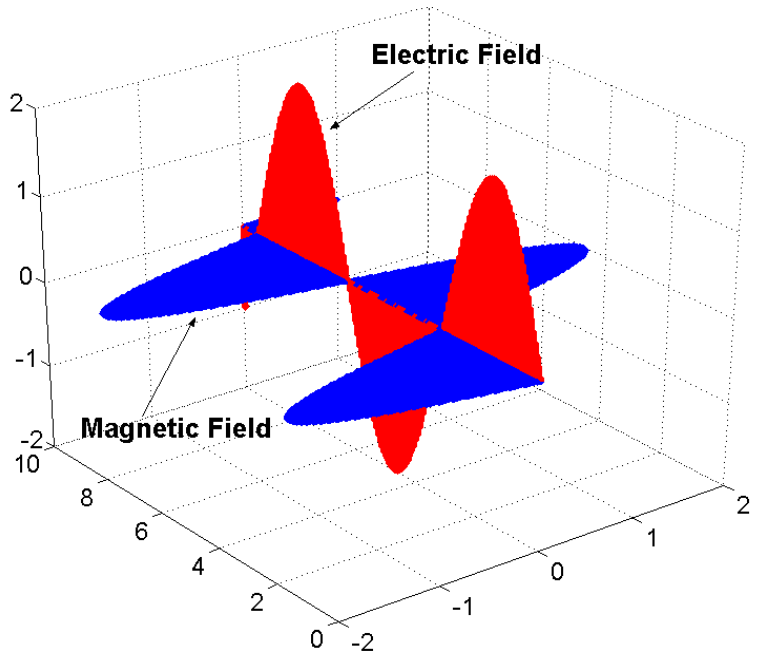

Figure 2.1. Light wave polarized in the E_y (vertical) direction.

In the second case, the light will also be linearly polarized if there is zero relative phase (ϕ) between the two orthogonally oriented electric field components. In this case, both components oscillate together in time. For example, if both components are exactly

out of phase with equal magnitude, they constructively add to form -45° polarization. Figure 2.2 shows the cross section of a -45° polarized wave. It should be apparent that when the magnitude of E_x is different from E_y the polarization angle will differ from 45°.

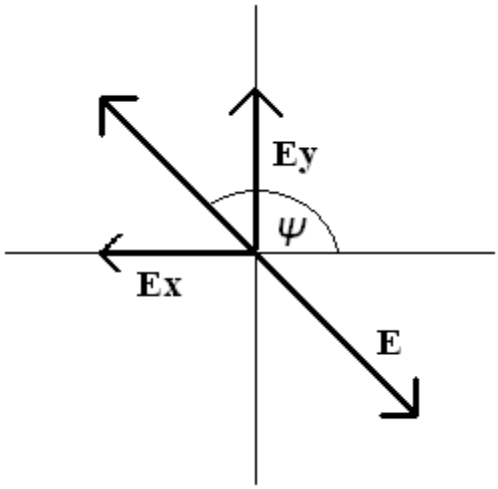

Figure 2.2. Linearly polarized light at -45° resulting from 180° phase difference between the *x* and *y* electric-field components. Ψ is the angle of polarization.

Circular Polarization

The second special case is circular polarization. Circular polarization occurs when both E_x and E_y are equal and have a ±90° phase shift, causing the total electric field to rotate through space and time in a circular pattern. This polarization is uncommon in nature because few materials have the property known as birefringence, which induces a phase shift between linear polarization components.

The general case of elliptical light in Equation 2.1 can be viewed as a superposition of circularly polarized light and any linearly polarized light vector. Instead of equal E_x and E_y components with exactly 90° phase shift, any combination of phase

and magnitude can occur. This polarization is generally a rotating ellipse in time and space. Therefore, in the general case, light is said to be elliptically polarized.

Quantifying Polarized Light

Until this point, the discussion has been restricted to one wave. In actuality, many different light waves are coming from several sources in any environment. Furthermore, single sources can emit light pulses randomly in time. Since each chance light wave pulse is polarized at a different angle from other pulses, the instantaneous polarization changes erratically in time. Light incident upon a detector is constantly changing in polarization state. Therefore, the detector measures only the *average* polarization of light over the time of the measurement. For random polarization a measurement of the confluence of many random waves over a detector's exposure time produces a reading that looks partially *unpolarized*. It should be apparent that an unpolarized light measurement is not an instantaneous property of the light itself, but a consequence of the time averaging of the detector across the random fluctuations of the instantaneous polarization.

Besides time averaging, there are two other types of averaging in polarization measurements. The first is spectral averaging. A wider-bandwidth filter can reduce sensitivities of a polarimeter to specific areas of high polarization within its spectral band. Materials often have spectrally dependent polarization characteristics. For example, as will be seen shortly, a sky free of clouds and dense aerosols has a higher polarization in the red end than in the blue end of the spectrum. A broadband filter that includes both the red and the blue would average the two regions and underestimate the polarization in the red. Sometimes a spectrally averaged signal is desired, while other times it is not. The

application governs the decision. The second type of averaging is spatial averaging. Signals from one point in a scene can only be measured to resolution limits determined by some combination of the optics and detector. Consequently, this limitation averages light over the instantaneous field of view (IFOV) of the detector. In the case of a CCD camera, the polarizations of all objects within the FOV of one pixel are averaged. Any polarization variation within a single pixel is necessarily lost.

An instrument designer cannot realistically achieve high resolution in all three of these areas—temporal, spectral, and spatial. For most applications these areas compete. Instruments that are designed to be precise for one area will sacrifice resolution in another. For example, by shortening the time of integration for a measurement, a wider spectral band or a larger pixel is needed in an imaging polarimeter to obtain a sufficient signal-to-noise ratio. For a given source brightness, temporal resolution is increased only by decreasing spatial or spectral resolution. These limitations need to be closely considered in instrument design.

Because of the averaging, unpolarized light adds a new dimension to polarization measurement. When only one wave was considered, the component magnitudes and phases were enough to describe the light polarization. When many waves are considered, the polarization of the light can appear to be *partially polarized*—that is less than 100% polarized. A better way of quantifying polarization is necessary—one that accounts for the unpolarized component of the measurement.

Stokes Parameters

Stokes parameters are an accurate means of describing partially polarized light. The Stokes vector was derived originally by Sir George Gabriel Stokes in 1852 (Collett, 1993, pg. 36). This vector contains four elements that entirely describe the polarization state in any measurement of light. Each of these elements—called Stokes parameters—describes a fundamentally different polarization property (Equation 2.2). (The two different standard representations are shown.) Together, the Stokes parameters completely describe a polarization measurement.

$$\text{Stokes Parameters} \equiv \begin{bmatrix} S_o \\ S_1 \\ S_2 \\ S_3 \end{bmatrix} = \begin{bmatrix} I \\ Q \\ U \\ V \end{bmatrix} \tag{2.2}$$

S_0, or I, is the total intensity of the light—or more appropriately, the total irradiance of light. This is the only Stokes quantity that our eyes can see. It describes a spatial power density (W/m^2). S_1, or Q, is the fraction of light that is polarized more in the horizontal or the vertical direction (0° and 90°). S_1 is negative if the light is polarized more in the horizontal than the vertical direction and S_1 is positive if vice versa. This quantity can be considered to be the total light polarized in the 90° direction minus the light in the 0° direction. S_2, or U, is the fraction of light that is polarized more in the 45° or -45° directions. Similar to S_1, it can be regarded as the total light in the 45° direction minus the light in the -45° direction. Since both 90° and 0° polarized light waves have equal components in the -45° and 45° directions, S_2=0 for these waves. Similarly, 45° and -45° polarized waves have no S_1 component. S_3, or V, indicates the amount of circular

polarization present in the measured light. Negative numbers represent right-hand circular, while positive numbers represent left-hand circular polarization (left-hand and right-hand refer to a polarization vector that rotates counter clockwise or clockwise, respectively, when an observer views an oncoming wave). It should be noted that the definition of what is left-hand and what is right-hand is arbitrary, and some disciplines define it oppositely (see Reference Angle below). Since light can be a combination of these polarized states plus potentially an unpolarized component, S_1, S_2, and S_3 are constrained by the total intensity S_0 (Equation 2.3).

$$S_0^2 \geq S_1^2 + S_2^2 + S_3^2 \tag{2.3}$$

The Stokes vector is also only valid for light that is incoherent. Light that is coherent could potentially interfere at the detector plane causing the Stokes representation not to be valid. This requires that the coherence time of the wavefront being measured be much shorter than the integration time of the instrument. In other words, the Stokes vector is only valid to describe a light wave in time-averaged sense. It measures a statistical average of the polarization of an instantaneously changing light wave that is fluctuating much faster than the measurement time.

Reference Angle

All polarization measurements are made relative to a reference angle. When a polarized beam is incident upon a device such as a waveplate or polarizer, the calculations involve projections of the polarization onto the reference axis of the device. For example, when polarized light moves through a waveplate, determination of the output beam involves calculations of the light interactions that are parallel to and

perpendicular to the fast axis of the waveplate. Since each polarization device in the same instrument may have a different primary axis, it is necessary to define a reference angle for all Stokes vectors in the entire system. This reference angle is chosen arbitrarily, but it is convenient to choose a reference angle that is parallel with the horizon (or floor for inside measurements). This references the Stokes parameters to the local environment or room coordinates. Care needs to be taken when comparing measurements between polarimeters, as different instrument designers may use different reference angles. Similarly, circular left- or right-handedness may also be chosen from the perspectives of either an observer viewing the wave as it approaches or as it recedes. Each of these perspectives will see a different direction of rotation. Therefore, a reference needs to be chosen and followed for S_3. For example, a positive S_3 can be picked to describe clockwise rotation of the polarization vector viewed at one point in space as the light wave recedes away from the observer. In this dissertation, this convention was used.

Mueller Matrix Transformation

Although it may not be apparent at first glance, Stokes parameters readily avail themselves to a transfer-function approach to optical propagation. When light travels through space, scatters through a medium, reflects off a surface, or propagates through optical components, its Stokes vector typically can change. The output Stokes vector is a function of the initial state and the interactions that occurred during propagation. It would seem plausible that each new Stokes vector would be a function of the old Stokes vector multiplied by constants associated with the material. We would then have four equations—each with four coefficients. This reasoning led H. Mueller to propose that a

four-by-four matrix of numbers could be used to describe the interaction of any input Stokes vector with a given medium (Mueller, 1948). The "Mueller" matrix, as it is called, is a mathematical tool for describing optical propagation of partially polarized light (Collett, 1993, pg. 68).

Mueller matrices are used to describe the effects of material reflection, propagation, and scattering on any polarized, unpolarized, or partially polarized light wave. Many of these matrices are invertible, allowing the scientist to infer from the output matrix the polarization state of the light before the reaction—if the Mueller matrix is known. Equation 2.4 shows the standard Mueller matrix representation of a transformation from an original state (1) to a modified state represented by the Stokes vector on the left-hand side (2).

$$\begin{bmatrix} S_o \\ S_1 \\ S_2 \\ S_3 \end{bmatrix}_2 = \begin{bmatrix} m_{00} & m_{01} & m_{02} & m_{03} \\ m_{10} & m_{11} & m_{12} & m_{13} \\ m_{20} & m_{21} & m_{22} & m_{23} \\ m_{30} & m_{31} & m_{32} & m_{33} \end{bmatrix} \begin{bmatrix} S_o \\ S_1 \\ S_2 \\ S_3 \end{bmatrix}_1 \tag{2.4}$$

The properties of each of the "*m*" parameters have been explained previously (Lu and Chipman, 1996), but several special properties should be noted. First, for free-space propagation, elements m_{00}, m_{11}, m_{22}, and m_{33} are equal to 1, while the others are equal to zero. This is expected as each Stokes parameter should not affect any other components except itself during free-space propagation. Second, the parameter m_{00} is the unpolarized transmittance of the system. By normalizing all other parameter to m_{00}, the system transmittance can be factored out of the equation. Third, m_{01}, m_{02}, m_{10}, and m_{20} all are related to diattenuation in a material. This property causes materials to allow one

polarization component to pass, while absorbing the orthogonal component. This property is critical to polarimeter design. (For definitions of other properties of polarizing components see Tyo et al., 2006.)

System Matrices

Polarimeters use the Mueller matrix to reconstruct the Stokes vector of a system. The difficulty of polarization measurement is that standard sensors cannot return a polarization value. They return a value that corresponds to the irradiance (brightness) of an object. Therefore, a novel approach must be used to determine the Stokes vector for an optical measurement. Since a Mueller matrix models an optical system, it was conceived that by measuring the irradiance of an object through different known Mueller matrices, the various pixel brightness values and the known Mueller matrix values could be used to find the polarization of the incoming light. (To extract a complete Stokes vector a minimum of four independent intensity measurements with different polarization settings on the polarimeter—each setting represented by a unique Mueller matrix—are required. For the designed polarimeter, only four polarimeter measurements were used. Using more than four measurements overdetermines the Stokes parameter extraction. Since the instrument in question uses the minimum of four measurements, the remainder of this paper discusses only these four measurements.) Imaging of the same scene through four different Mueller matrices is accomplished either by quickly changing polarization elements between images and assuming the scene is not changing (called a *time sequential* or *division of time* polarimeter) or by using different optical trains to obtain four simultaneous measurements. The latter case uses either *division of amplitude*,

division of aperture, *division of focal plane*, or *coboresighted* methods (Tyo et al., 2006). In either case, the unique Mueller matrix of the polarimeter associated with each of the four images must be known. For the sequential polarimeter it is helpful to refer to each of these time consecutive Mueller matrices as polarimeter states. Since the polarimeter design discussed here is a sequential polarimeter, these different polarimeter Mueller matrices will be subsequently called polarimeter states.

By inspection of Equation 2.4, the irradiance of a pixel is only dependent upon the first line of the Mueller matrix. Therefore, only the first lines of each Mueller matrix, along with the value of the pixel for that image, are used to extract the polarization of the pixel. The first rows of the Mueller matrix for each of the four polarimeter states form the system matrix (Tyo et al, 2006). An example of a system matrix is shown on the right side of Equation 2.5. (DN stands for digital number.) Each line of matrix corresponds to a different polarimeter state.

$$\begin{bmatrix} \text{Image1 pixel value}\,(DN) \\ \text{Image2 pixel value}\,(DN) \\ \text{Image3 pixel value}\,(DN) \\ \text{Image4 pixel value}\,(DN) \end{bmatrix} = \begin{bmatrix} .5 & -.43 & 0 & -.25 \\ .5 & .45 & .03 & -.21 \\ .5 & -.19 & .39 & .25 \\ .5 & .18 & -.42 & .21 \end{bmatrix} \begin{bmatrix} S_0 \\ S_1 \\ S_2 \\ S_3 \end{bmatrix} \tag{2.5}$$

The system matrix ideally is well conditioned and can be inverted and applied to the pixel values for each polarimeter state to reconstruct the input Stokes vector. The condition number of a matrix represents how errors propagate backwards during the inversion (Watkins, 1991, pg. 94). As an example, if any raw image has an error of 2% and the condition number (associated with the 2-norm) of the Mueller matrix is 2.5, then the expected typical error is ~5%. Many types of condition numbers exist. Each condition

number varies due to the norm used in its computation and determines a different type of error. For example, the 1-norm represents the sum of all errors in each element of the Stokes vector, while the ∞-norm represents the maximum possible error across all elements of the Stokes vector (Ambirajan and Look, 1995). For polarimetry the appropriate norm to minimize errors across all elements is the 2-norm (Tyo, 2000), which can be regarded as the RMS of the element errors. (The specific error of each element depends on which image contains the error, whether the error is negative or positive, etc.) For the best Stokes data, a low system matrix condition number is desired.

A general form of the system matrix is shown in Equation 2.6. As with any matrix, the accuracy of the elements of the system matrix determines the amount of error produced when it is inverted. For polarimeter design, errors in the measured values of the first line of the Mueller matrix for each state causes systematic errors in the measured Stokes vector. Therefore, the accuracy of the measured system matrix values ($a_{00}\ldots a_{33}$) considerably affect the accuracy of the system. ($S_{01}\ldots S_{04}$ are the irradiances (S_0)of each state from state 1 to state 4.)

$$\begin{bmatrix} S_{01} \\ S_{02} \\ S_{03} \\ S_{04} \end{bmatrix} = \begin{bmatrix} a_{00} & a_{01} & a_{02} & a_{03} \\ a_{10} & a_{11} & a_{12} & a_{13} \\ a_{20} & a_{21} & a_{22} & a_{23} \\ a_{30} & a_{31} & a_{32} & a_{33} \end{bmatrix} \begin{bmatrix} S_0 \\ S_1 \\ S_2 \\ S_3 \end{bmatrix} = A * S \tag{2.6}$$

Other Useful Representations of Polarization

Although Stokes parameters can accurately describe light fully, there are other methods of describing polarization that give a better conceptual understanding. Degree of

linear polarization, degree of circular polarization, and angle of polarization can also completely describe the polarization state of measured light.

Degree of linear polarization (DoLP) is the percentage of light that is polarized linearly (Equation 2.7). It can also be viewed as the probability of any wave over the course of the measurement time being polarized in the direction of the angle of polarization.

$$\text{DoLP} = \frac{\sqrt{S_1{}^2 + S_2{}^2}}{S_0} \tag{2.7}$$

Angle of polarization determines the primary orientation of the polarization ellipse (or line) in space. Horizontal polarization is typically 0°, depending on the reference angle definition. As expected, this parameter is undefined for completely circularly polarized measurements and unpolarized measurements. For partially polarized measurements, it is the angle of the polarized portion of the measurement.

$\psi = \frac{1}{2}\tan^{-1}\left(\frac{S_2}{S_1}\right)$, where ψ is the angle of polarization. (2.8)

Finally, the degree of circular polarization (DoCP) describes the degree to which the wave is elliptically polarized. Linearly polarized light carries a value of 0, while circularly polarized light has a value of -1 or 1, depending upon the direction of rotation.

$DoCP = \frac{S_3}{S_0}$, where DoCP is the degree of circular polarization (2.9)

Besides these parameters, it is also common to describe polarization in terms of degree of polarization (DoP), which is similar to degree of linear polarization (DoLP) but also includes the circularly polarized component. Also, it is common to normalize the

Stokes Parameters to S_0. This makes the Stokes parameters percentages similar to the degree of polarization quantities—with the exception that they can also be negative.

Polarization Sources

Sunlight outside the Earth's atmosphere is generally unpolarized because of the random nature of its thermal emission. Instances of polarized light in nature arise primarily by two different events: the scattering of light and reflection from surfaces. Both of these events directly apply to the research at hand. First, scattering of sunlight by particles in the atmosphere causes skylight to be partially polarized. Second, the reflection of this light from objects causes these objects to have polarimetric signatures dependent upon both Fresnel reflection and surface scattering.

Reflection on a Dielectric Boundary

The Fresnel equations govern the behavior of light upon an optically smooth dielectric boundary. Different polarization components are reflected and transmitted differently at a boundary. This boundary can be paint, metal, etc. Without going into great detail, the reflection causes incident unpolarized light to become partially polarized. Equation 2.10 shows the reflectance (for optical power, not electric field amplitude) for a dielectric boundary (Fresnel's Reflection Equations). These equations describe the amount of reflection experienced by the polarization components in the direction parallel and perpendicular to the plane of incidence (Hecht, 2002, pg. 350). The plane of incidence is defined as the plane that contains the unit normal to the surface and the direction of propagation. It is clear from the equations that the reflectances for each of the

polarization components can be significantly different. Therefore, unpolarized light—such as sunlight—will become partially polarized upon reflection from a dielectric surface.

$$R_{\perp} = \left(\frac{\eta_i \cos\theta_i - \eta_t \cos\theta_t}{\eta_i \cos\theta_i + \eta_t \cos\theta_t} \right)^2 \qquad R_{\parallel} = \left(\frac{\eta_t \cos\theta_i - \eta_i \cos\theta_t}{\eta_i \cos\theta_t + \eta_t \cos\theta_i} \right)^2 \tag{2.10}$$

η_i and η_t are the indices of refraction for the incident and transmitting media, respectively, and θ_i and θ_t are the angle of incidence on the material and the angle of transmission into the material (Hecht, 2002, pg. 114).

Boundary reflection can greatly change the polarization state of incident light. In fact, at one angle, all parallel polarization transmits into the material. This angle—called the Brewster angle—completely polarizes the reflected light.

Although Fresnel reflection greatly affects the polarization signatures of ground-based objects, polarization signatures are also heavily influenced by the polarization state of the incident light. Therefore, it is also necessary to understand skylight polarization signatures.

Sky Polarization from Rayleigh Scattering

Although skylight polarization changes with clouds, clear sky polarization is governed primarily by the phenomenon that makes the sky blue—Rayleigh scattering. Rayleigh scattering is the scattering of light by particles that are much smaller than the wavelength. For direct sunlight, small molecules in our atmosphere cause light to be scattered. Since Rayleigh scattering depends upon the inverse fourth power of wavelength, shorter wavelengths scatter more than long wavelengths. Therefore, blue

light is scattered more than red light. This, coupled with lower sensitivity of the human visual system to even shorter wavelengths (e.g. violet), causes a clear, clean sky to appear blue. With sufficient path length, such as at sunset or sunrise, enough short-wavelength light is scattered to cause the directly viewed sun to appear red/orange, while the sky above appears blue.

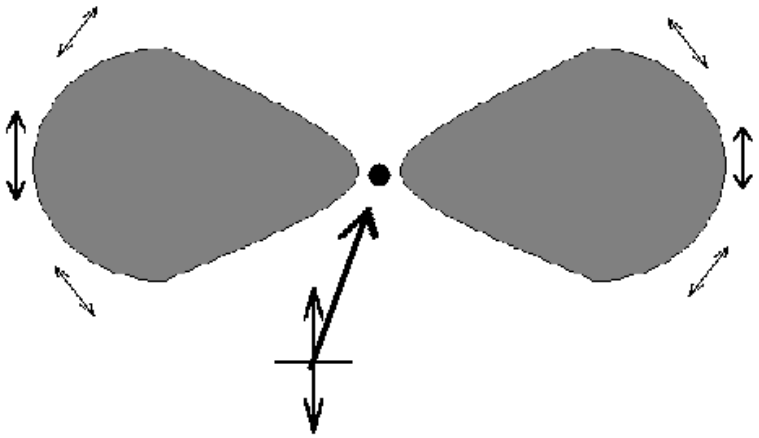

Figure 2.3. Dipole scattering of vertically polarized light.

Rayleigh scattering also causes skylight to be polarized. The polarized component of light is at maximum at all angles for which light is scattered by 90° to the direction of illumination. One way of illustrating the scattering is as a classical dipole radiator. As light encounters molecules—which are much smaller than a wavelength—the molecules absorb some of the photons. These molecules are excited in the direction of the wave's instantaneous polarization and act as dipole radiators—where the dipole would be in the direction of the polarization of the illuminating light. Because the scatterer acts as a dipole radiator, which radiates no energy along the dipole axis, the magnitude of the

scattered light falls to zero in the direction of the illuminating light wave polarization. Figure 2.3 shows how a vertically polarized illuminating wave will scatter at 90°.

All the scattered radiation from one polarization component is 100% polarized and the radiation falls off like a dipole radiator. (For the Figure 2.3 example, no radiation would be observed above or below the scatterer. This is called the Tyndall effect.) Figure 2.3 is only a 90° cross section. The polarization scattered in the forward and backward directions is also polarized in a similar fashion. The entire polarization pattern looks like a donut, with the polarization being parallel to the surface of the outside of the donut. For each individual polarized wave in an unpolarized merger of waves, the pattern shown is rotated to match the polarization angle. Superposition of all the patterns results in the polarization pattern expected for scattered unpolarized light. If unpolarized light were illuminating the scatterer, a plane of 100% polarized light would radiate from the scatterer at 90° from the incident light direction. Forward and backward scattered light would be completely unpolarized, but light scattered into all other angles would fall between the 100% and 0% degree of polarization extremes. Therefore, all scattered radiation has a maximum polarization at 90° to the illumination angle. Equation 2.11 shows the predicted Rayleigh scattering irradiance for optically small particles (Measures, 1984, pgs. 45 and 46).

$$I_{s\perp} = \frac{\sigma_\pi^R I_i}{2r^2} \qquad I_{s\|} = \frac{\sigma_\pi^R I_i}{2r^2}\cos\theta \qquad \sigma_\pi^R \equiv \frac{\pi^2 (n^2-1)^2}{N^2 \lambda^4} \tag{2.11}$$

θ is the scattering angle, σ_π^R is the backscattering cross section, I_i is the unpolarized illuminating irradiance, N is the number density of scatterers, n is the

complex index of refraction for the medium, and *r* is the distance from the observer to the scattering object. $I_{s\perp}$ is the irradiance of the scattered light that is polarized perpendicular to the scattering plane (defined by the incident light beam and the scattered light beam); $I_{s||}$ is the irradiance of the scattered light that is polarized parallel to the scattering plane.

Notice that the scattering cross section falls off with the fourth power of wavelength, causing longer wavelengths to be scattered less than shorter wavelengths. Also, notice the difference between the two components of polarization. For 90° scattering angles, the parallel component falls to zero and the scattered light is totally polarized in a direction perpendicular to the scattering plane—the plane defined by both the incident and scattered light beams. In actuality, the polarization of 90° scattering angles does not reach 100%. There are two primary reasons for this discrepancy. First, diatomic molecules, such as oxygen and nitrogen in the atmosphere, scatter light anisotropically (Coulson, 1988, pg. 174, 180). This causes the dipole radiator model to break down slightly. Second, multiple scattering in the atmosphere reduces the amount of polarization (Bohren, 1995, pg. 65).

A clear atmosphere will exhibit a high degree of polarization—on the order of 50-80 percent. Polarization falls off toward the sun and toward the anti-solar point. Because of aerosol (Mie) scattering and multiple scattering, the points of zero polarization are not directly at the solar and anti-solar points. Instead, four neutral points, located slightly above and below the solar and anti-solar point, exhibit zero polarization.

The neutral points were first discovered by Arago, Babinet, and Brewster (Barrall, 1858; Babinet, 1840; Brewster, 1847). These four points of zero polarization are located

about 20° above and below the sun and the anti-solar point. Their exact position can change depending upon aerosols and atmospheric turbulence (Horvath, 1998). These points move throughout the day with the sun and the clear-sky polarization signature.

Previous Investigation of Full-Sky Polarization

Although many researchers have studied visible-band atmospheric polarization, only a few have built full-sky measurement systems. For all types of polarimetric imagers, the polarimetric data are extracted from a series of intensity images. For a three-Stokes system that measures the first three Stokes parameters, a minimum of three images is necessary. For a four-Stokes polarimeter, a minimum of four images is needed for the reconstruction. These raw images can be taken either simultaneously with different detectors and optics trains, or sequentially with one detector and a changing optics train. The choice of the type of polarimeter is based on the application and the prerogative of the investigator. The strengths and weaknesses of the previous investigators' instruments were largely a consequence of the method of generating the raw images. All investigators used a three-Stokes polarimeter. This type of polarimeter does not measure the circularly polarized component. Skylight has no significant circular component, at least that is known (Kawata, 1978), so the fourth Stokes parameter was not considered necessary.

Horvath (1998-2002)

Over the last few years, the primary researcher in the field of full-sky polarization has been Gabor Horvath at Eotvos University in Budapest, Hungary. Horvath has used

full-sky polarimetry to measure polarization of skylight at night, neutral points during an eclipse, the fourth neutral point, and cloud depolarization (Horvath et al., 2003; 2002; 1998; Suhai and Horvath 2004).

Horvath primarily uses single-lens reflex (SLR) cameras as the method of measurement in his experiments. A train of three coboresighted cameras mounted next to each other is pointed toward zenith. Each camera has its own individually oriented polarizer (0°, 60° and 120°) and fisheye lens. Images are obtained by exposing all cameras simultaneously. The polarimetric data are extracted by scanning images after film development and processing.

The strength of Horvath's method is that images are taken concurrently. Therefore, no errors are produced by temporal scene variation. Also, by using color film three different band signatures are produced simultaneously.

Horvath's method also has some weaknesses. First, the process of exposing film, developing it, and scanning it for different cameras can produce uncertainties in the consistency of the detector response. Use of one detector—with several quick successive images—is preferable to this multiple-detector approach. By using one detector, the intra-detector response differences to brightness and polarization are eliminated. Errors from temporal variations in a single-detector instrument can be minimized by making the measurements quickly. Second, radiometric calibration is difficult or impossible because each new case of film can have a slightly different sensitivity. Third, the entire data extraction process is tedious and not well suited to large data sets or real-time analysis. Finally, using the wide-band response of the film to measure spectral information results

in broad spectral information. This causes more spectral averaging of polarization than is desired.

North and Duggin (1997)

A second set of researchers used a unique idea to measure skylight polarization. Using a 4-lens stereoscopic camera mounted on a tripod, North and Duggin viewed a dome mirror on the ground. The dome mirror reflected the whole sky back into the camera, allowing full-sky imaging but with some blockage by the camera.

This system had similar strengths to the Horvath imager. It provided simultaneous data and was portable. The stereoscopic camera helped with pixel alignment by using lenses that were machined to point in the same direction. It also had similar weaknesses to Horvath. First, the polarimetric response of the dome had to be calibrated out of the data. (Note: the fisheye lens in other systems also needs to be calibrated for similar reasons.) Second, the camera blocked a portion of the zenith sky. Problems with film and wide spectral bands similar to Horvath's problems were also exhibited. A system that is not limited by film development is more desirable. The most serious difficulty encountered with both this system and Horvath's system is the lack of automated measurements and the inability to obtain Stokes parameters quickly.

Liu and Voss (1997)

Several of the weaknesses of the film systems were solved by the development of a CCD fisheye system (Voss and Liu, 1997; Liu and Voss, 1997; and Liu 1996). Their system used a fisheye lens mounted on a CCD imager. Reimaging optics were used to reduce the image to the size of a smaller CCD. Polarimetric data were obtained by taking

three images through three different polarizers mounted in a rotating filter wheel. The angles of the polarizers were orientated in a manner that gave the best signal-to-noise ratio for the recovered Stokes vector—0°, 60°, and 120°. Three polarizers and a blank slot—for dark images—were used in the wheel. By rotating the polarizers in the wheel and by rotating spectral filters in another wheel in front of them, three Stokes parameters could be taken for four different wavelengths.

This system offered many advantages over the previously mentioned systems. First, data could be quickly taken and analyzed. There was little time delay between data acquisition and reproduction of the Stokes components. The single detector solved most calibration difficulties by eliminating concerns about multiple response curves. The same imaging optics were used for all images, so there was no concern about variance in their transmittances. They also used a true radiometric calibration. This helped with cloud identification problems and gave an extra degree of scientific capability. Finally, the spectral filters used a 10-nm bandwidth. These narrow bands gave the polarimeter the ability to better recognize unique polarimetric signatures across the visible spectrum.

Although it was a nicely developed instrument, one major problem with the Voss and Liu polarimeter was the long time required to expose and download the raw images. With this delay and the time required to rotate the polarizers, the total time necessary to acquire the four images for the Stokes reconstruction was 2 minutes (Pust and Shaw, 2006). This delay created large errors when moving clouds were in the sky. Therefore, Voss and Liu restricted their analysis to clear-sky measurements.

Unpublished cloud observations I made with the Infrared Cloud Imager (ICI) (Thurairajah, 2004; Thurairajah and Shaw, 2004; Shaw et al. 2005) have consistently displayed movements of clouds in excess of 3.5 degrees per minute. For an instrument such as Voss and Liu's, this cloud movement would correspond to a 40-pixel shift over the two minute acquisition time. This would produce large edge errors for clouds.

None of these previous researchers has considered the effect of full-sky polarization on target signatures or used a consistent measurement system to document clouds over long periods of time. A new design was desired to measure both full-sky polarization and target signatures quickly.

POLARIMETER DESIGN

As has been previously shown, former full-sky polarimeter designs allowed room for improvement. Even more, the need for target signature capabilities demanded further instrument capabilities. In response to this need, a polarimeter that meets and exceeds the limitations of previous instruments has been designed and built. Since film detection methods are not well-suited to large data campaigns and multiple detector systems are difficult to calibrate, difficult to align, and expensive to build, a single CCD-based design platform was chosen. This platform used the same basic design as Voss and Liu's instrument, but reduced the image acquisition time from 2 minutes down to 0.4 seconds. (This value depends on the exposure time, which can vary between 1 second and 0.4 seconds.) Important design criteria were used to build an instrument that improved upon the previous designs.

Design Criteria

Design of the instrument focused on four primary goals. (1) The acquisition time of the instrument must be reduced as much as possible. From the ICI observations mentioned previously, it is clear that clouds can move by more than 0.3 pixels per second. Since sub-pixel shifts can cause notable errors in Stokes image reconstruction (Persons, 2002), it was desired to keep the acquisition time for the entire measurement below 1 second. (2) The instrument must be quickly changeable between a full-sky field of view and a narrow target field of view. The full-sky requirement of the instrument dictated that the front lens be a fisheye lens. Unlike other polarimeters, this requirement

forced the polarization optics to be located behind the lens because of the large ray angles. Although this made calibration more difficult, it helped solve the problem of quick changeability. Since the front lens is the first optic in the system, the fisheye can be removed and replaced with a telephoto lens. The polarimetric optics stay behind these front lenses and were not disturbed by the quick changeability. (3) Incidence angles must be minimized on polarization-sensitive optics. Since many polarization optics, including achromatic waveplates and liquid crystal variable retarders (LCVRs), exhibit polarization properties that depend on incidence angle, the Mueller matrix of these optics will change with at different points on the image plane and at different focus settings and f/#s. This is discussed in the *Use of Mueller Matrices in Imaging Systems* section. Although separate calibrations for each setting are used to compensate for this effect, minimizing incidence angles both makes instrument design easier, and reduces these effects, which increase the system matrix of the system—and therefore the noise. (4) Aberration spot sizes must be reduced to the size of a pixel or smaller. Although a diffraction-limited design sounds rewarding, resolution of the instrument for spot sizes smaller than a pixel will be limited by the size of the pixel, not the optics.

Several different polarimeter designs could be chosen. A rotating-polarizer design was a simple solution, but lacked the capability of measuring circular polarization. Since few investigators have explored sources of circular cloud polarization—especially cirrus cloud polarization, a 4-Stokes polarimeter was desired. Both rotating quarter wave plate (RQWP) and liquid crystal variable retarder (LCVR) designs were considered. A RQWP design uses four images taken at four different quarter-wave-plate fast-axis angles to

reconstruct the Stokes vector. This requires the physical rotation of the quarter wave plate in front of a polarizer. The LCVR-based design also uses four images to reconstruct the Stokes vector, but voltages are used to adjust the retardance of two LCVRs in front of the polarizer rather than rotating the retarder. The rotating-plate design is limited by the rotation speed of the quarter wave plate, the exposure time, and the bandwidth of an achromatic waveplate, while switching time of the LCVRs and the exposure time limits the acquisition speed of the LCVR design.

An initial polarimeter design was based on the rotating quarter waveplate (RQWP) design. However, this instrument had an acquisition time of 5 seconds. The long acquisition time resulted in large errors from moving clouds (see Design Criteria #1). The speed of this system was primarily limited by the start/stop action of the waveplate rotation stage. This RQWP design was abandoned for a liquid crystal variable retarder (LCVR) based design. The LCVR-based design, which uses two LCVRs and a fixed polarizer, was chosen for its fast switching times and the capability of the LCVRs to optimize the system matrix of each filter band independently. The acquisition time of the LCVR-based system was limited by both exposure time and the switching time of the liquid crystals. Depending upon exposure time, the system could acquire an entire set of Stokes images in 0.4 to 1.2 seconds.

Polarimeter Design for LCVR-Based System

The optical design cannot be implemented without consideration of the polarimetric design of the instrument. The type of polarimetric imager chosen dictates many of the design choices in the optical design. The liquid crystal based design was

chosen to implement the quick image acquisition required by Design Criteria #1 above. Each of the remaining criteria apply to the optical design of the polarimeter, which is discussed in a later section. LCVR-based designs involve many subtleties, which make the design work nontrivial. Without an adequate understanding of the issues affecting LCVR polarimeters, it is not possible to achieve a well-calibrated polarimeter.

For any LCVR design, two LCVRs are placed in front of a fixed polarizer. For each of the four images in the image sequence, the driving voltage is changed to adjust the retardance of each LCVR. The brightness value of each image pixel depends on the polarization of the incoming light and the Mueller matrix of the polarimeter. For a given pixel, the four values of the brightness from the four images are used to reconstruct the Stokes parameters for that pixel. Both the retardance of each LCVR for each image and the permanent fast axis location of each LCVR can be chosen arbitrarily during the design. The question is: how are the LCVR fast axis position and retardance values selected?

Selection of the Ideal LCVR Parameters

As previously introduced, the system matrix is used to reconstruct the Stokes vector from the irradiance values of several images. To achieve a well-conditioned system matrix, the LCVR fast axis and retardance values must be chosen carefully. These values determine the system matrix. Conditioning an LCVR system is especially difficult since the retardance values for each image and the fixed fast axis values amount to 10 variables—8 retardances and 2 fast axis angles. Optimization of the system matrix condition number on the 10 variables required a constrained nonlinear function

minimization. This type of optimization requires an iterative solution such as the Gauss-Newton method. Also, since there are many variables, several different solutions that minimize the system matrix exist simultaneously.

Optimization for this instrument followed the work of Tyo (Tyo, 2000). The MATLAB (ver. 7.0.4) Optimization Toolbox (ver. 3.0.2) was used to optimize the fixed rotation angle and the set of four retardance angles—associated with each of the four images—for each LCVR simultaneously. The LCVRs were modeled as perfect retarders. Retardance values were constrained from 0 to 180º (half-wave retardance)—although not necessarily. The *fmincon* MATLAB function was used to minimize the condition number for the perfect two-LCVR system. As expected, many unique sets of rotation and retardance angles with equivalent condition numbers could be found by varying initial conditions. The set chosen is shown in Table 3.1, for which the 2-norm condition number was 1.82. This condition number is extremely close to the minimum possible 2-norm condition number of 1.73 (Tyo, 2002). Ideally, the two-LCVR system should be able to attain this value, but the constraint of the retardance values limited the condition number.

Table 3.1. Retarder settings for the LCVR polarimeter.

	Retarder1	Retarder2
Fast Axis Fixed Rotation Angle	115.0°	45.0°
Retardance Angles		
Image 1 (Polarimeter State 1)	150.5°	105.2°
Image 2 (Polarimeter State 2)	27.7°	180.0°
Image 3 (Polarimeter State 3)	180.0°	15.4°
Image 4 (Polarimeter State 4)	18.17°	64.77°
Condition Number (2 norm)	1.82	

The retardance and equivalent rotation angles for LCVRs have been shown to vary with incidence angle (Xiao, 2003). Therefore, in an imaging system using LCVRs, each ray that forms the image will have a different retardance and rotation angle. This causes depolarization in the system (see next section). Therefore, using a perfect retarder model for the LCVR is invalid. Still, this set of retardance and rotation angles was used as an approximate optimization. Depolarization in the imaging system will increase the condition number of the system from this ideal solution. In fact, since each ray in the imaging system is subjected to a different Mueller matrix, the question must be asked: is the Mueller matrix even a valid representation of a imaging system where elements in the system have significantly varying polarization effects across their apertures?

Validity of Using Mueller Matrices to Describe Imaging Systems

For most Stokes vector imaging systems using rotating polarizers and waveplates, the Mueller matrix of the system does not change significantly across the aperture of the optic. All ray paths to the image plane can be therefore summarized by one Mueller matrix. However, in LCVRs, the retardance and rotation angle of the birefringence can vary significantly according to the incident angle of the ray (Xiao, 2003). Also, depolarization is slightly induced by the LCVR crystal. Each ray path must be described by a unique Mueller matrix, which includes this angle-dependent LCVR retardance and rotation, and the LCVR depolarization. Therefore, in LCVR imaging system, even though the light incident on the imager may have a uniform polarization for all ray paths, each ray converging on an image point after passing through the imager will exhibit a slightly different Stokes vector. The superposition of these rays causes apparent

depolarization. Therefore, a LCVR used in an imaging system cannot be modeled as a perfect retarder. For a proper calibration, it is desired to use the Mueller calculus to describe the system with LCVRs. The question is: can an equivalent Mueller matrix for an imaging system be found?

We start by assuming geometric optics is a good approximation. (For optics that image well, using rays instead of field as an approximation is valid). Equation 3.1 shows the Mueller matrix for one ray (numbered 1) through the system.

$$\begin{bmatrix} S_0 \\ S_1 \\ S_2 \\ S_3 \end{bmatrix} = \begin{bmatrix} m_{00} & m_{01} & m_{02} & m_{03} \\ m_{10} & m_{11} & m_{12} & m_{13} \\ m_{20} & m_{21} & m_{22} & m_{23} \\ m_{30} & m_{31} & m_{32} & m_{33} \end{bmatrix} \begin{bmatrix} S_{0ray} \\ S_{1ray} \\ S_{2ray} \\ S_{3ray} \end{bmatrix} = M_1 S_1 \tag{3.1}$$

The left-hand Stokes vector represents the Stokes vector at the imaging plane. The Stokes vector at the image point is the addition of the product of Stokes vectors and Mueller matrices for each ray path (Equation 3.2). In Equation 3.2, 1,2, *N*, etc. represents each ray through the system.

$$\begin{bmatrix} S_{0total} \\ S_{1total} \\ S_{2total} \\ S_{3total} \end{bmatrix} = M_1 S_1 + M_2 S_2 + M_3 S_3 + ... + M_N S_N \tag{3.2}$$

Now if two conditions are met, an equivalent Mueller system matrix can be found. (1) If every object imaged by the system is at the same distance, then all the rays that traverse the system from one object point to an image point will have a static cone of ray paths no matter what the object is. Therefore, for various objects, the cone of rays will stay the same. (2) If the wavefront across the entrance pupil of the system is

assumed to be spatially uniform, the input Stokes vector of each object ray will be the same. Therefore, the irradiance of each ray, the Stokes vector of each ray, and the position of each ray in the imager will be constant for an object point. Equation 3.3 shows that, under these conditions, an equivalent Mueller matrix (M) can be found for each point in the image. ($S_1 = S_2 \ldots = S_N = S_{input}$ and M is the equivalent Mueller matrix for the image point.)

$$\begin{bmatrix} S_{0total} \\ S_{1total} \\ S_{2total} \\ S_{3total} \end{bmatrix} = (M_1 + M_2 + M_3 + \ldots + M_N) * S_1 = M * S_{input}, \tag{3.3}$$

Condition #1 is true in this system since the objects will always be approximately at infinite distance when compared to the focal length. Also, viewing the object as a collection of point sources, for an object at long distance, each point source approximately becomes a plane wave at the imager. Therefore, each wavefront associated with each object point within a pixel can be approximated as a constant across the entrance pupil (Condition #2). On the contrary, Condition #2 could be invalid for close objects because the difference between the BDRFs (bi-directional reflectance function) of two separately measured objects at the same position could potentially be significant. This would cause the magnitude of the wavefront across the aperture to be spatially non-uniform in intensity for each object point. It could also be different between two separately measured objects. Equation 3.3 would be invalid because $S_1 \neq S_2 \neq S_3$, etc. The consequences of this breakdown would potentially cause two separately measured objects at the same position with identical polarization signatures but differing BDRFs to be

measured as having different polarization signatures—which is clearly invalid. (Note: If all possible objects at one position measured by the instrument had BDRFs of the same shape—but potentially different overall reflectances—the instrument calibration would still hold, but I believe it is overreaching to make the assumption that all BDRFs for close objects are similar in shape over the FOV of a pixel. An investigator who wanted to use LCVRs for close objects would need to prove that for any close object, the shape of the BDRF is roughly the same over the pixel FOV for the Mueller calculus to be valid.) For objects far away from the imager, these issues are not concerns since the portion of the solid angle of the portion of the BDRF viewed is small and therefore the wavefront can be approximated as a uniform intensity wave across the aperture. Therefore, an imager that focuses at approximately infinity meets the conditions necessary to use the Mueller calculus. Another way of looking at this is that the apparent depolarization caused by the retardance-dependent LCVR apertures can be calibrated out as a systematic error.

Notice that these assumptions necessarily have three consequences. First, each image point can have a different equivalent Mueller matrix associated with it. Therefore, every pixel in the system must be calibrated separately. Second, the system must be calibrated separately for each f/# because changes in the ray cone will modify the calibration. Third, the focus of the instrument cannot be changed without altering the calibration. Therefore, only under certain constraints is a Mueller matrix—and therefore system matrix—representation valid for an imaging system.

Departure of the System Matrix Condition Number from the Ideal

Variation of polarization across all ray paths will cause an apparent depolarization at the image point. This variance will degrade the condition number of the system matrix from the ideal. The severity of this degradation depends upon the variance of the angle of incidence across the LCVRs' apertures. Therefore, restricting the angle of incident light onto the LCVR curbs the degradation of the condition number. Calibration of this instrument revealed that restricting the maximum incident angle at each LCVR to 5° allowed the condition number to remain between 1.85 and 2.3 for all pixels, wavelengths, etc. Still, inadequate attention to these issues could cause problems for LCVR imagers. Future designers of LCVR-based polarimeters should be aware of these issues.

Polarimetric Lens Aberrations

Since each front lens—whether the fisheye or the telephoto—is located in front of the polarization optics, the polarization of the incoming light can be corrupted by the refraction through the optics. This arises from the different refraction angles and optical path lengths seen by each ray in the ray cone. Like the LCVR problems mentioned in the previous sections, the unique ray paths in lenses cause apparent depolarization at the image plane. This phenomenon is called polarimetric aberration (Chipman, 1987).

For lenses with low incidence angles, such as the telephoto lens, this issue is small. However, for lenses with high incidence angles, such as the fisheye, reflection of some of the incident light from the front surface could potentially cause the polarization of the light transmitted into the lens to be significantly modified. In fact, without lens coatings, all reflected light from the fisheye at the Brewster angle would be completely

polarized perpendicular to the plane of incidence. For light rays incident at the Brewster angle, only a small portion of the perpendicular light is transmitted. Any input polarization state would be seen by the imager as mostly polarized parallel to the plane of incidence. This would make the inversion of the lens Mueller matrix difficult. In other words, the lens Mueller matrix would be ill-conditioned. With lens coatings, this problem is reduced as the anti-reflection coating allows transmittance of the perpendicular light into the lens. Still, the problem is not completely nullified. Both polarizations do not completely transmit into the glass. Even more, ZEMAX modeling of the fisheye and telephoto lenses showed that the standard antireflection coatings cause many linearly polarized rays in the pupil to become slightly elliptically polarized. The model predicted that linearly polarized waves would acquire ellipticities of about 1%. After calibration of the instrument, this problem was shown to be minor. (It did not significantly reduce the condition number of the entire system). Still, it was significant enough that the lens effects could not be ignored. Full measurement of the Mueller matrices for each lens was necessary. These Mueller matrices were then inverted and applied to the measured polarization to compensate for the effects of the lens.

Optical System Design

Once the polarization design of the LCVR-based polarimeter was accomplished, the optical layout of the system was planned. Optical design focused on first selecting the appropriate components for the polarization system, then selecting the camera, selecting each front lens, and implementing appropriate reimaging optics to reduce the image formed by the front lenses to the size of the camera image plane.

Selection of the LCVRs

Companies that produce high-quality liquid crystal variable retarders (LCVRs) are rare. Many companies make LCVRs that switch between two states at approximately 0 and 180° of retardance for industrial applications, but few make a high-quality LCVR that uses an adjustable voltage over the entire range of retardances.

Meadowlark Optics provides a research-grade LCVR that was chosen for this application. The Meadowlark LRC-300 temperature-controlled LCVRs are 50 mm (2") in diameter and provide a 41 mm (1.6") diameter clear aperture. Since narrow filters (discussed below) were selected, the large aperture was necessary to attain a high f/#. These LCVRs switch as quickly as 55 msec. (Although moving from low to high voltages is much quicker than 55 msec, the relaxation time of the crystals from high to low voltages was around 55 msec.)

Temperature control at 100°C was used to stabilize the liquid crystal material. Changes in the liquid crystal temperature cause changes in the Mueller matrix of the device. For outdoor applications, it is critical that the internal LCVR temperature remain steady. Heating up the liquid crystal also gave the advantage of causing the material to switch faster. For a cooler material, the switching time would be slower than 55 msec.

Selection of the Polarizer

The most important consideration for polarizing optics is the acceptance angle. The Newport and Meadowlark *Polarcor* polarizers will accept incident rays up to 15°, but have a very narrow band (Newport, 2006). The Newport *Precision* series polarizer has an extinction that is better than 1000:1 between 430-710 nm (Newport, 2006).

Meadowlark optics offers a similar polarizer (Meadowlark, 2006). These polarizers require a near-normal incidence angle. (There are no specifications for this, but it is assumed in the literature.) Newport and Meadowlark *Polarcor* lacked the large bandwidth needed in this system. Therefore, only the *Precision* series polarizers from each company were considered. It was assumed that the polarizers have an incident-angle-dependent polarization error that increases linearly with angle. Therefore, a small incidence angle has an acceptable error. The *Precision* series polarizers are rated for 0-15° incidence angles (Newport, 2006). Since incidence angle concerns for the LCVRs had already restricted the ray cone to under 5°, incidence angle does not create appreciable problems for the polarizer extinction.

Selection of Camera

Most CCD-based cameras use 8-bit quantization, which provides a best-case quantization error of 0.39%. (This reflects a pixel value that uses the entire dynamic range of the camera; the error will be worse for smaller pixel values.) For polarimetric observations, any quantization error will be amplified by the condition number of the system. This is discussed in *Selection of the Liquid Crystal Parameters*. The 2-norm condition number of a matrix gives the average expected error in a matrix inversion. In the case of the polarimetric imager, the error in the raw data will be amplified in the Stokes parameters by the condition number. For a typical condition number of 2, the 0.39% quantization error will be amplified to almost 1%. This restricts the accuracy of the instrument to a best-case scenario of 1% uncertainty, neglecting other error sources. To allow the instrument to have better accuracies, only cameras with quantization levels

greater than 8 bits were considered. Also, the fast image acquisition constraint demanded that the camera have a fast image download. Fast exposures are useless unless the images can be quickly retrieved from the camera.

To meet the radiometric quantization and speed requirements, a DALSA 1M30 camera was selected for the polarimeter. This 1 Mpixel device provides 12-bit resolution. It also uses a pixel format that is much larger (13 μm) than most CCD-based cameras. The large pixel format allows the aberration minimization to be accomplished easily. The camera is capable of producing 30 frames per second with 30-msec exposures. Most importantly, the camera is limited by exposure time, not download time. The integration time can be controlled manually from 5 μs to ∞. This makes it ideal for any light condition. Also, the camera has a quantum efficiency that is better than 5% at 900 nm, which makes it capable of near-infrared measurement. Finally, the dynamic range of the camera is 70 db, while noise is around 1.5 digital numbers (DN).

Selection of Filters

For the LCVR-based polarimeter, the retardance and rotation angles of each LCVR heavily depend upon wavelength. Therefore, narrow-bandwidth filters are necessary to ensure that the spectral shape of the calibration source does not change appreciably compared to the spectral shape of the measured light. If the calibration-light and measured-light spectra are sufficiently different, errors are introduced by the spectral dependence of the LCVRs. For this reason, the narrowest practical filters were chosen. Thermo-Oriel 10-nm visible-band filters were chosen at 450, 490, 530, 630, and 700 nm. The narrow bandwidth allowed high signal-to-noise exposures to be taken throughout the

day until sundown. The selected wavelengths were chosen to cover the blue end of the spectrum more thoroughly since the DoLP of the clear sky increases quickly with wavelength in this area of the spectrum. Above about 570 nm, the DoLP of the sky begins to flatten out through the near infrared. Therefore, fewer filters were needed above 530 nm.

Because of the wavelength dependence of the LCVRs, spectral response differences within the filter pass-band between the calibration source and the light measured could potentially cause errors in the calibration. For these narrow 10-nm filters, this effect was thought to be minimal. Still, spectral shape differences were known to exist between sunlight and the calibration standard used in the laboratory. It was impossible to model the induced error without being able to measure the retardance dependence on wavelength directly. Although modeling the effects of the problem was impossible, the severity of the problem was measured by rechecking the calibration performed using the laboratory lamp with a measurement of a reference polarizer using sunlight illumination. The calibration never faltered by more than 1% between the lab calibration using the laboratory standard lamp and the calibration check using sunlight. Therefore, this error source could not have caused more than 1% error. (This error was included in the final error analysis.)

Selection of Front Lens

To obtain a full-sky field of view, a fisheye lens is necessary. There are a few different manufacturers of fisheye lenses. I chose to use Nikon F-mount lenses for two reasons. First, Nikon has an esteemed reputation for offering high-quality lenses to the

general public. Second, since the Dalsa camera came with the Nikon F mount, Nikon reimaging optics (discussed in the next section) would be the best choice. For consistency to the reimaging optics, Nikon was chosen for both the fisheye and telephoto front lenses. Each lens in the Nikon line has already been designed to minimize aberrations. I would not be able to design a competitive solution. Therefore, several Nikon fisheye and telephoto lenses were considered for the front lenses.

Nikon makes several fisheye lenses. Two lenses in particular were considered: the older 10 mm f/5.6 OP (Orthogonal Projection) and the new 16 mm f/2.8D AF.

Nikon 10 mm f/5.6 OP Fisheye. The 10 mm fisheye projects a 20-mm-diameter image onto the film plane, as shown in Figure 3.1. (A 35-mm film frame is 24 mm tall.) Notice that the full frame is not filled.

An orthogonal projection lens causes the angles near the horizon to take up less area than the center image. This corresponds to an area projection much like that of irradiance upon a planar surface. As zenith angle increases, the projected area becomes smaller until it is zero at the horizon. Consequently, this lens is great for radiometrically measuring irradiance projected onto a surface from a hemisphere, but the losses of resolution at the image edges makes it ill-suited for this polarimeter design. Second, this lens creates a smaller image than the 16 mm fisheye discussed in the next section, so the image aberrations will be larger per sky solid angle. Third, this lens is not as new as the 16 mm fisheye. (It is assumed that the newer lens has better quality.) Therefore, the 10 mm OP lens was not selected for this project.

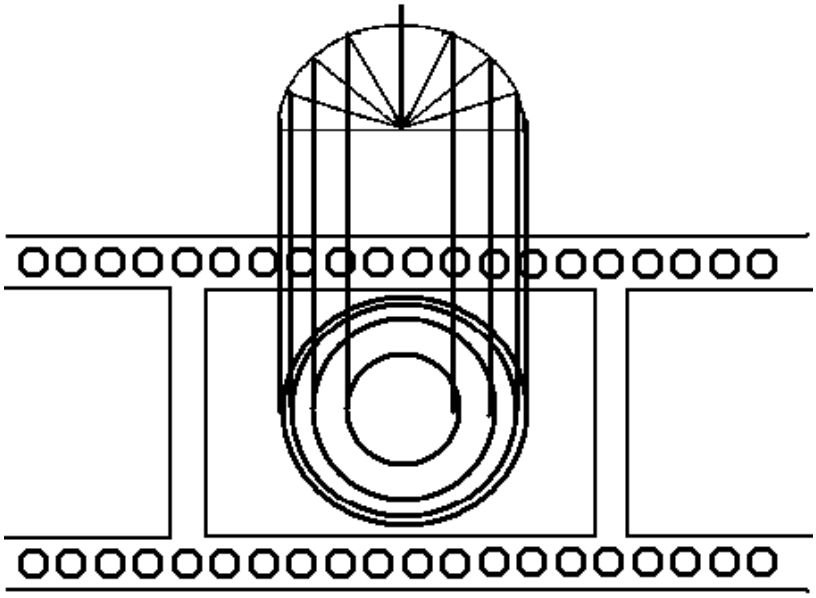

Figure 3.1. Orthogonal projection of 10 mm f/5.6 lens onto film. The top semicircle represents light in the sky dome. The center is the zenith, while the outside edges contain light from the horizons.

Nikon 16 mm f/2.8D Fisheye. The newer 16 mm f/2.8 lens has many advantages over the 10 mm f/5.6 lens. First, it uses an equidistance projection (Figure 3.2), which provides much better outside resolution than the orthogonal projection. Figure 3.2 shows the actual 43-mm image diameter projection onto the 35 mm film. This is a full-frame fisheye; therefore, it only views both horizons at the corners. To capture a full sky image, it was necessary to shrink this image to fit onto the smaller 13-mm Dalsa CCD array. Second, the lens has a great reputation for its sharp quality.

The ZEMAX optical design code was used to model the 16-mm fisheye lens using design data obtained from the United States Patent Office (Sato, 1995). Spot size diagrams for the lens model are smaller than the diffraction limit (Figure 3.4). The spot size for the center of the image is less than 8 μm, which is well within the airy disk. This

superb lens design is almost diffraction limited. For this reason and those described previously, this lens was chosen as the final fisheye lens for the polarimetric imager.

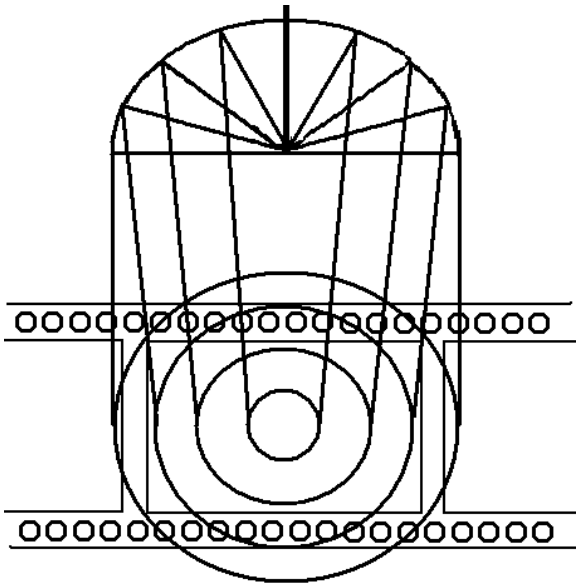

Figure 3.2. Equidistance projection similar to 16 mm f/2.8 fisheye. For this projection, the number of pixels across the image is linearly proportional to the angle traversed.

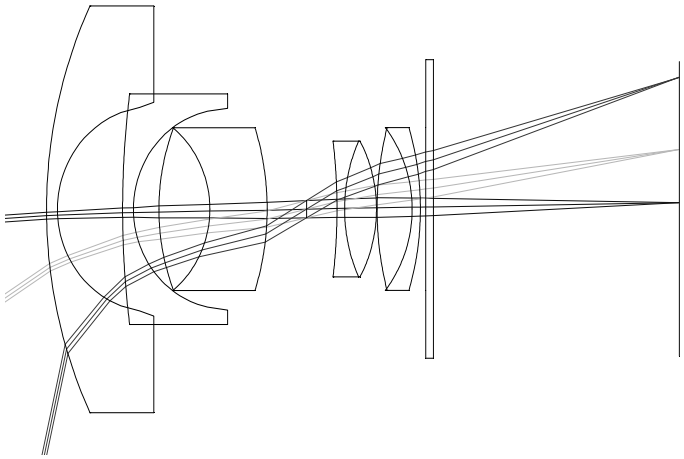

Figure 3.3. Ray trace of 16-mm fisheye lens at f/15.

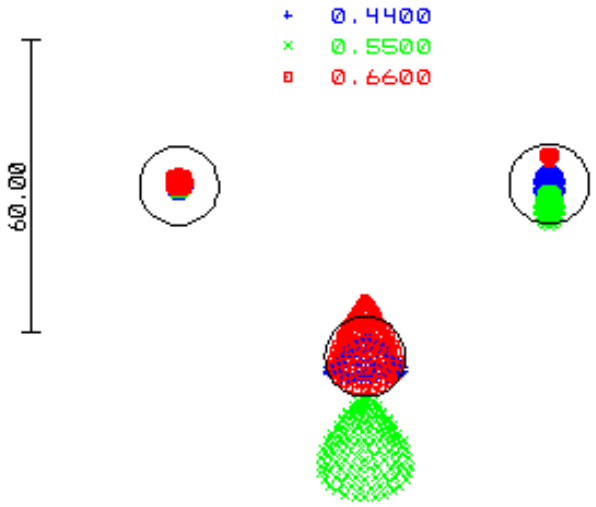

Figure 3.4. Spot size diagrams for the 16-mm fisheye lens. The spots for the 440, 550, and 660 nm wavelengths are shown in representative colors. The Airy disk (16.1 μm diameter), denoting the first minimum of the circular diffraction pattern, is shown in black. The upper-left spots are for the center of the image. The upper-right spot is for a point mid-way between the center of the image and the outside of the image. The lower-center spot is for the outside of the image.

Narrow FOV Lens Selection. A narrow-field lens was desired with a focal length between 200 mm and 400 mm. Many different Nikon lenses have been produced in this focal range. Because of the ZEMAX design work necessary for the project, only lenses that had patents available were considered. After a search of the patent information, many different telephoto and variable focal length lenses exhibited near diffraction-limited performance. The telephoto lens chosen from the candidates was the Nikon 300-mm telephoto lens.

Optical Component Order

For any 4-Stokes liquid crystal variable retarder (LCVR) design, two LCVRs are placed in front of a fixed polarizer. Since the fixed polarizer only transmits light

polarized in one direction, the polarization effects of all subsequent components are transparent to instrument calibration. For this reason, it is most desirable to place all optics and filters behind the polarizer. In the case of this full-sky polarimeter, the large field angles make this arrangement impractical. Therefore, all components except the front lens were placed behind the polarizer in the imaging train. This placed the LCVRs and polarizer after the front lens but before the filter, reduction optics (discussed below), and the Dalsa camera.

Reduction Optics

The ultimate goal of the reduction optics was to resize the 43-mm-diameter image from the fisheye into an image that fits on the 13-mm Dalsa CCD plane. Before serious optical design was attempted, it was reasoned that other Nikon lenses might be able to accomplish the task. By using another Nikon lens to reimage the image formed by the fisheye, reduction of the image size to the Dalsa CCD could be obtained. Many macro lenses can reduce an image by one half or more. These lenses could theoretically be used to shrink the image. For a fisheye image 43 mm in diameter and a 13-mm square CCD, an image reduction ratio of about 0.30 was needed.

To reduce an image by this amount, the macro lens needed to be located a long distance from the fisheye lens. This distance caused massive vignetting in the system. In fact, the outer edges of the final image would lose all light. Figure 3.5 shows the ray trace for this hypothetical system.

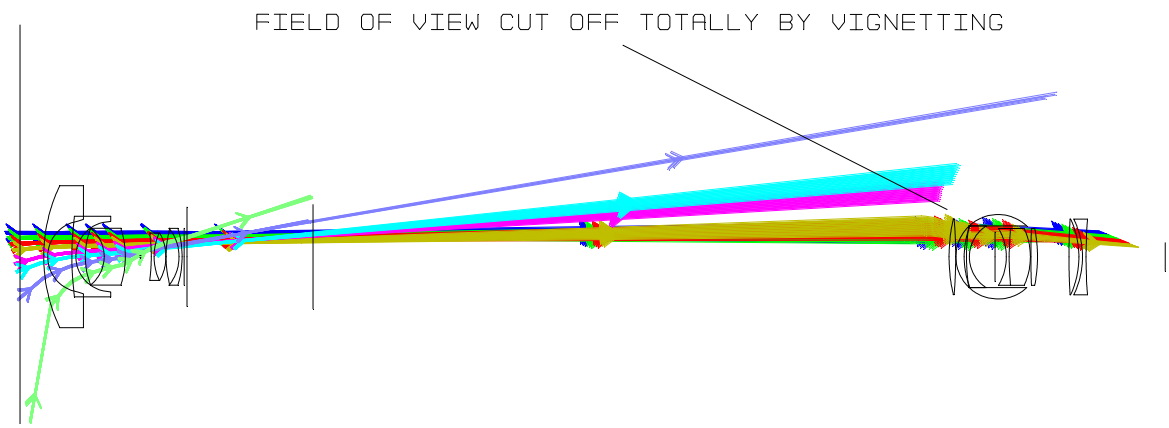

Figure 3.5. Vignetting in the optical train before addition of a field lens.

It was necessary to bend the rays back toward the optical axis to eliminate this vignetting. A field lens served this purpose. By inserting a lens at the fisheye image location, the light was bent toward the optical axis without changing the power or focus of the system. An example of this effect is shown in Figure 3.6.

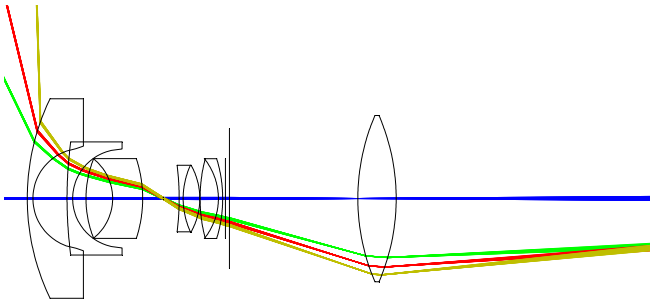

Figure 3.6. Field lens example.

Once the rays were bent back toward the optical axis, another lens reimaged the image at the field lens to a smaller CCD-plane image. To keep the imager small, the macro lens needed to have close focusing ability. Another consideration was the incidence angle constraint previously mentioned. If the fisheye and field lenses are located sufficiently away from the macro lens, the incidence angle upon the LCVRs

would be kept shallow. Lenses with a macro mode typically focus as near as 1 foot. The Nikon Micro lens class was perfect for this application. These lenses typically reproduce objects up to a factor of 1/1 and are specifically made for close focusing. They come in several different varieties: the 60-mm AF, the 105-mm AF, the 200-mm AF, and the 85-mm MF.

Although the 85-mm lens would be a good choice, no patent data could be found for it. Before modeling was initiated, some initial properties of the lenses were considered. The 200-mm lens focuses at ~50 cm for a 1:1 reproduction. This means that for a 0.3 reproduction, the distance would be about 30 cm. This would make the imager long and bulky. Therefore, the 200-mm lens was eliminated from consideration. Both the 60-mm and 105-mm lenses focus at 30 cm or less for 1:1 reproduction, so the resulting system lengths would be manageable. The 60-mm and 105-mm lenses were each modeled in ZEMAX using patent information (Suzuki, 1998). The model for each lens was used in a full system design with the fisheye models. Focusing was set in the model for a reproduction ratio of 0.3. Optimization was done according to the ZEMAX default merit function. The minimum-spot-radius optimization was used (as apposed to wavefront or centroid optimization). This function effectively minimizes the total spot size for all wavelengths. The wavelengths used for this design were 430, 550, and 600 nm. These values represented the visible band of the spectrum. After initial optimization, several different field lenses were tried with the 60-mm Micro and 105-mm Micro lens designs. Finally, one of these designs was selected.

60-mm Micro Lens Designs. The 60-mm designs were plagued with field lens problems. The field lens needed to be selected with a very specific focal length. Choosing too much field lens power caused the large-field-angle rays to be vignetted by the top of the 60-mm lens aperture. Too little power caused the mid-field-angle rays to be vignetted by the bottom of the Micro len's aperture. Either problem resulted in a non-uniform image. Figure 3.7 shows the mid-field vignetting (yellow lines) for a field lens with too little power. (The vignetting of the yellow rays is on the aperture stop inside the 60 mm Micro lens.) Finding a field lens that did not have vignetting for any field at low f/#'s proved to be impossible. Also, the aberrations in these 60-mm systems seemed to be worse than the aberrations in the 105-mm systems. Overall, the 105-mm systems seemed to have slightly smaller spot radii. Therefore, the 60-mm designs were abandoned.

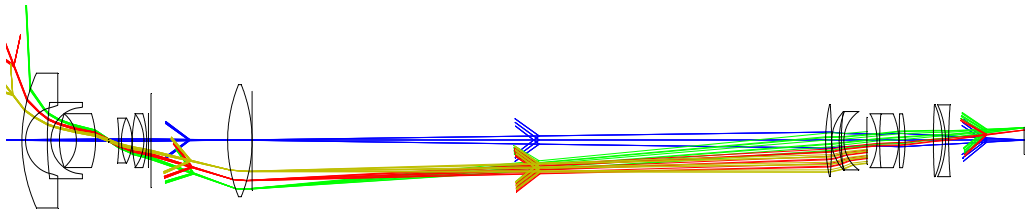

Figure 3.7. Vignetting problems for a 60-mm Micro design with a field lens of insufficient power. The yellow lines represent mid-field rays that are vignetted by the aperture stop inside the 60-mm Micro lens shown on the right.

105-mm Micro Lens Designs. The polarimeter system design with the 105-mm Micro Lens was very similar to that with the 60-mm design. Many different system designs resulted from trial-and-error type modeling. Nevertheless, several methodical steps were used to obtain the final design.

First, the patent information for the 105-mm lens was entered into ZEMAX (Suzuki, 1998). This information was only provided for certain focusing distances. It was

necessary to optimize the focus of the 105-mm lens to the location of a 43-mm-diameter virtual image formed by the fisheye lens. (This is the diagonal of a 35-mm SLR image.) The object distance was set to approximately 400 mm to achieve a 13-mm image of the 43-mm virtual image. Figure 3.8 shows the 105-mm lens model optimized for observing a 43-mm-diameter object. With the image reduction achieved, the fisheye/telephoto and field lens were added to the front of the imaging system in the model.

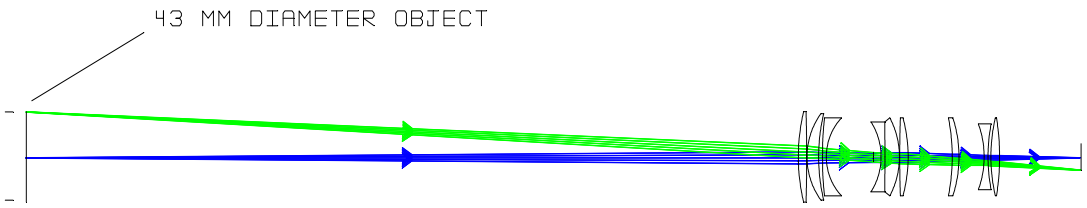

Figure 3.8. Optimized 105-mm Micro lens configured to create a 13-mm-diameter image from a 43-mm diameter object.

Choosing a field lens for the polarimeter system was a nontrivial task. First, the field lens power and position proved to be slightly different for the 300-mm telephoto lens and the fisheye lens. Also, aberrations were different in the two designs. The telephoto resolution was selected as the limiting factor for aberration design, since high resolution of the sky is not as critical. Thus, telephoto aberrations held priority. Many different types of field lenses were considered in models, including bi-convex, plano-convex, and achromatic types. Also, multiple field lenses were tried within these designs. Using two field lenses seemed to perform the best for most designs. An example of a design with three plano-convex field lenses is shown in Figure 3.9. Designs with more than three field lenses did not see any improvement over their less complex counterparts.

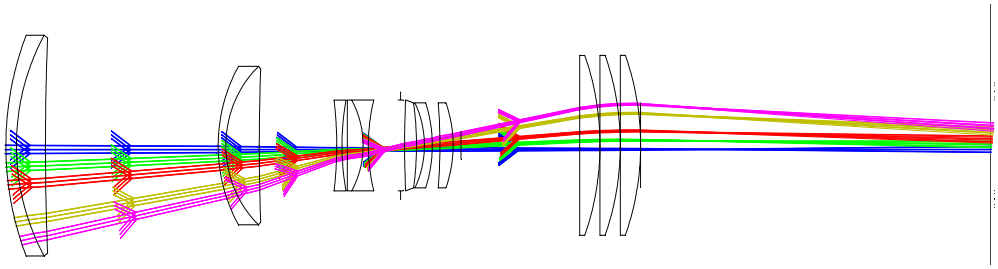

Figure 3.9. 300-mm telephoto lens with three plano-convex field lenses.

The single-lens achromatic doublet system was the best performer. The JML DBL14075 lens was chosen for the field lens in this case. The lens prescription used for this lens was obtained from the ZEMAX lens catalog and inserted directly into the system model. Since the fisheye lens used a different power than the 300-mm telephoto front lens, separate field lens designs were necessary for each lens. For this system, a dual set of JML DBL14075 field lenses also performed the best. Therefore, the two front lens assemblies (fisheye and telephoto) each contained their own appropriate field lens(es).

Final System Performance

The final design exhibits low aberrations across the entire field of view. The spot sizes were very close to the size of the pixel (13 μm). The worst aberrations were wavelength-dependent defocus and distortion. However, since the final instrument was to use narrow-band filters and an automatic focuser to image each color, spot sizes could be analyzed on a per-wavelength basis. When each wavelength was separately analyzed, the spot sizes were smaller. Figure 3.10 shows the ray trace for the telephoto and for the fisheye lens.

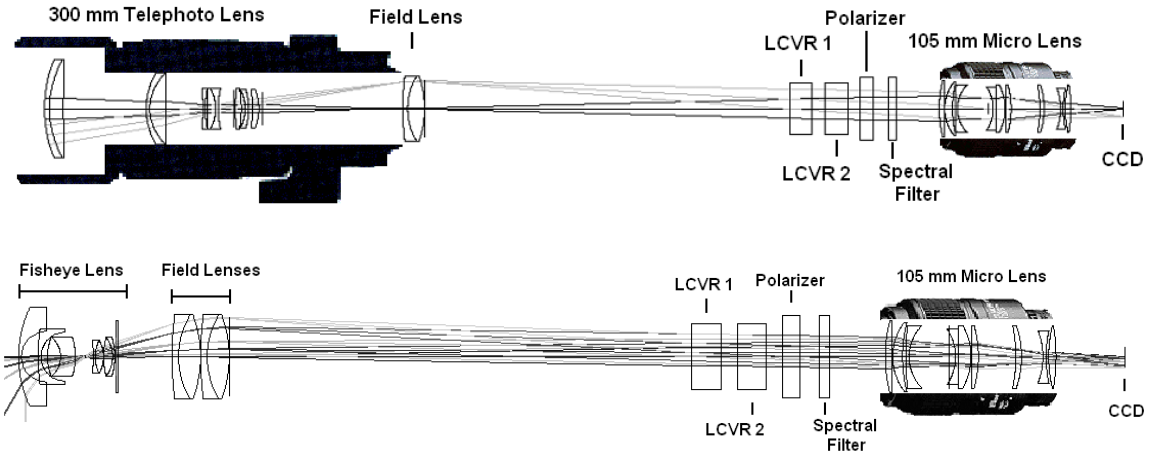

Figure 3.10. Final telephoto and fisheye designs with encasings shown for reference. Since the telephoto system is longer, the scale is not the same for each system version.

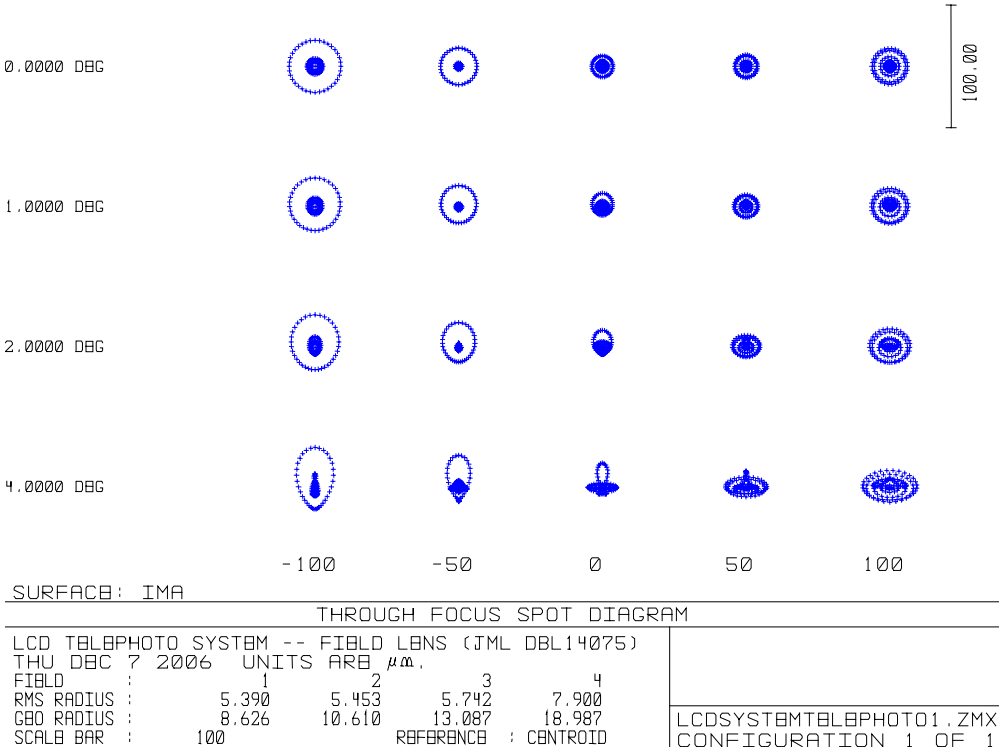

Figure 3.11. Through-focus spot diagrams for the polarimeter system with the telephoto front lens at 450 nm and f/4.0. All units are in micrometers (μm). The degree markers on the left side denote the field angles in object space. Each column shows the spot size when it is at a given point from the paraxial focus. The distance from focus is listed below the spots in μm . The center column is the best focus. The RMS radius is the spot size of the root mean radial size of all rays. The geometrical radius only reflects the radius of the ray farthest from the centroid.

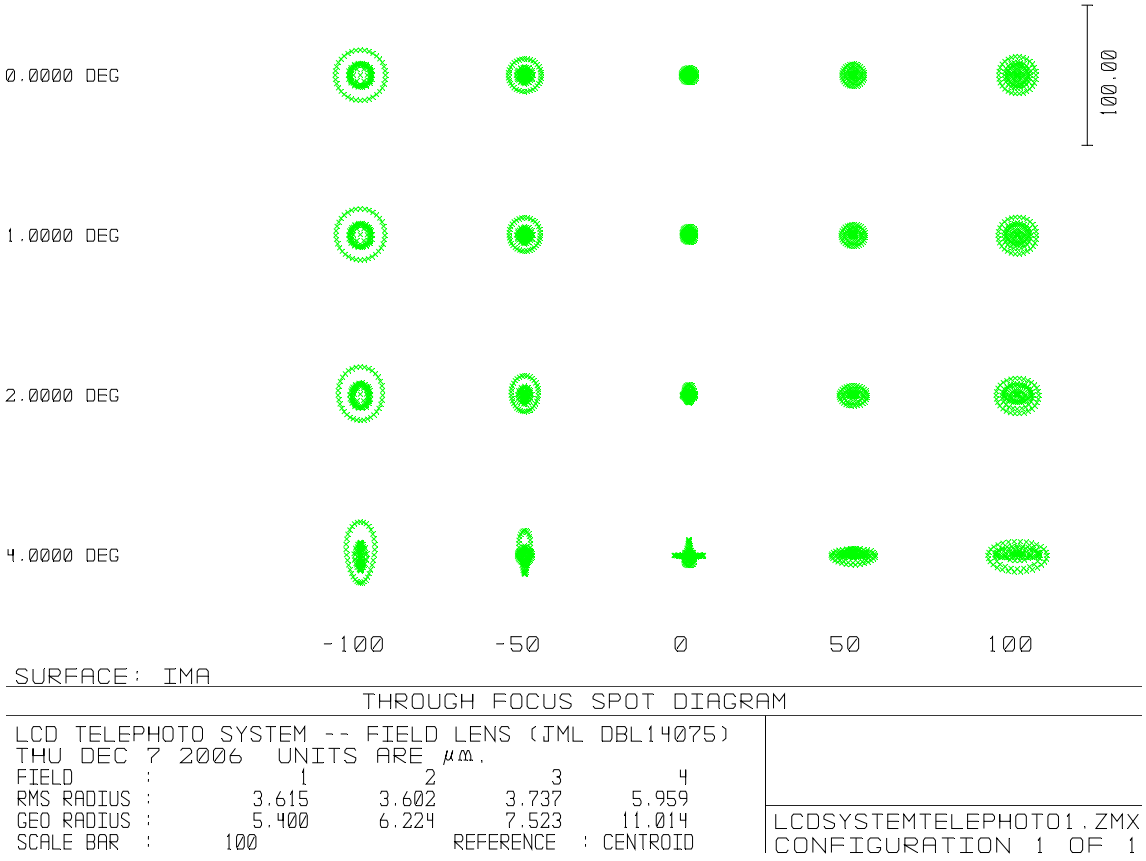

Figure 3.12. Through-focus spot diagrams for the polarimeter system with the telephoto front lens at 530 nm and f/4.0. All units are in micrometers (μm). The degree markers on the left side denote field angles in object space. Each column shows the spot size when it is at a given distance from the paraxial focus. The distance from focus is listed below the spots in *u*m. The center column is the best focus. The RMS radius is the spot size of the root mean radial size of all rays. The geometrical radius only reflects the radius of the ray farthest from the centroid.

Figures 3.11-3.13 show the telephoto aberrations at three wavelengths—450, 530, and 700 nm—at their truest foci. For clarity, the spot diagrams are shown only at the center wavelength. When the upper and lower band wavelengths were added, the spot sizes did not increase appreciably. With the exception of the 450-nm wavelength at 4° FOV—which exhibited large coma—all RMS spot sizes fit within the 13-μm Dalsa CCD pixel. Real Nikon lenses will have manufacturing-induced aberrations that depart from

the ideal patent attributes. Still, these models show that—if the imager is designed correctly—the instrument resolution can be nearly limited by the CCD pixel size.

The through-focus spot diagrams show that the focus must be finely tuned to obtain the desired resolution. The Finger Lakes DF-2 electronically controlled focuser used for positioning the focal plane provides 2.5 µm step resolution (calculated using DF-2 specifications, Finger Lakes, 2005). Therefore, adjustments within 20 steps will give satisfactory results. Design implementation has proven this to be true.

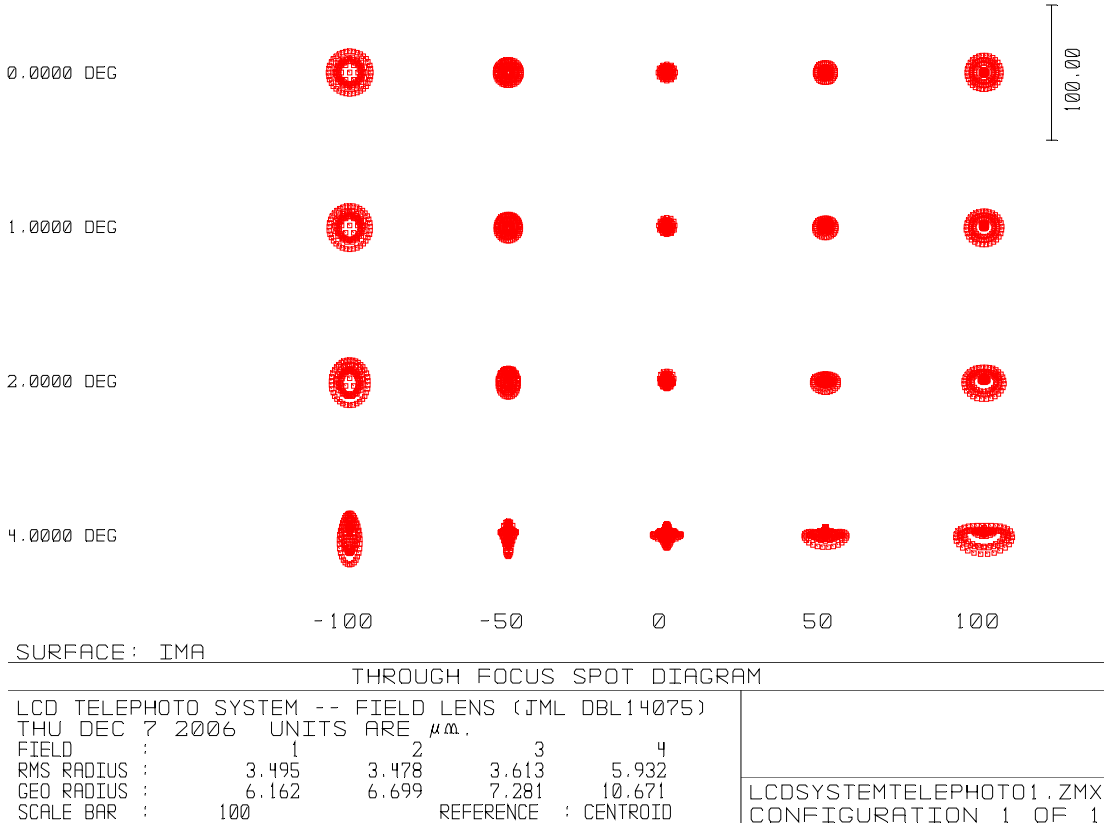

Figure 3.13. Through-focus spot diagrams for the polarimeter system with the telephoto front lens at 700 nm and f/4.0. All units are in micrometers (µm). The degree markers on the left side denote the field angles in the object space. Each column shows the spot size when it is at a given distance from the paraxial focus. The distance from focus is listed below the spots in µm .The center column is the best focus. The RMS radius is the spot size of the root mean radial size of all rays. The geometrical radius only reflects the radius of the ray farthest from the centroid.

Although the telephoto resolution was the priority, the fisheye properties were not ignored. Figures 3.14-3.16 show through-focus spot diagrams for the polarimeter system with the fisheye lens.

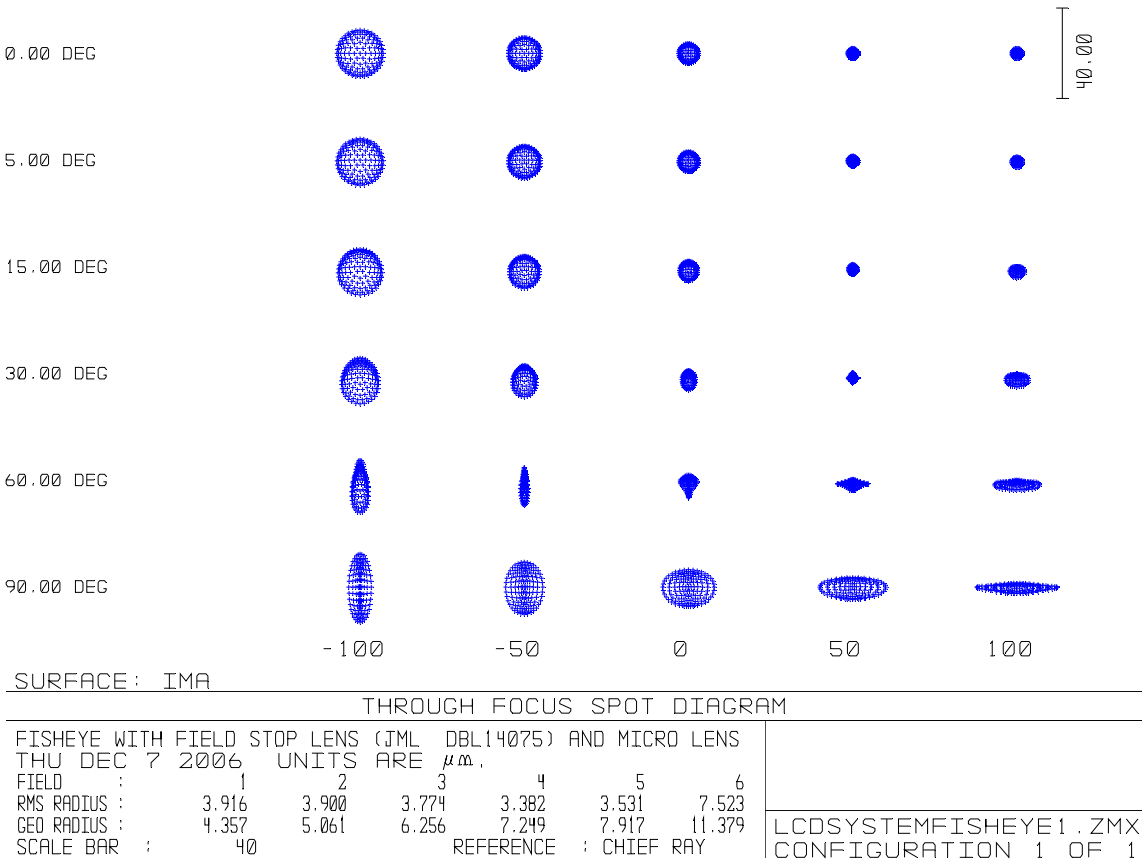

Figure 3.14. Through-focus spot diagrams for the polarimeter system with the fisheye lens at 450 nm and f/4.0. All units are in micrometers (μm). The degree markers on the left side denote the field angles in object space. Each column shows the spot size when it is at a given distance from the paraxial focus. The distance from focus is listed below the spots in μm .The center column is the best focus. The RMS radius is the spot size of the root mean radial size of all rays. The geometrical radius only reflects the radius of the ray farthest from the centroid.

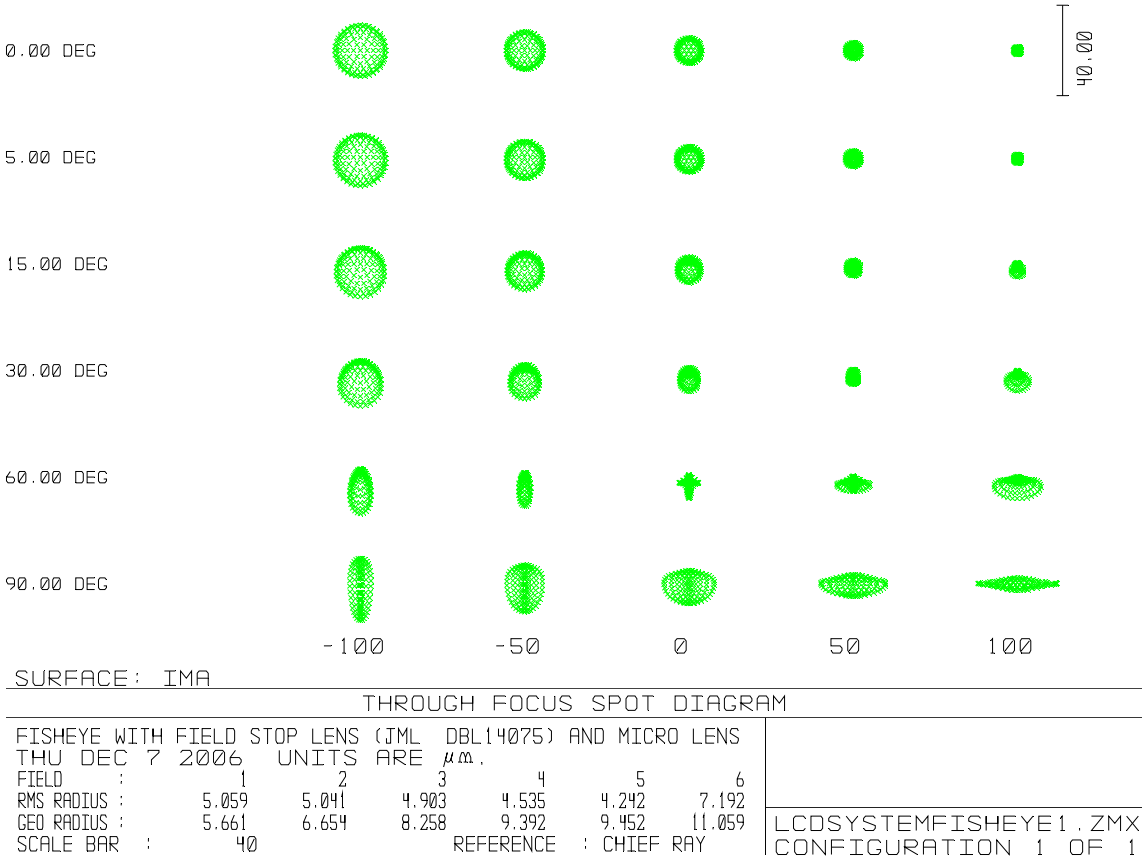

Figure 3.15. Through-focus spot diagrams for the polarimeter system with the fisheye lens at 530 nm and f/4.0. All units are in micrometers (μm). The degree markers on the left side denote the field angles in object space. Each column shows the spot size when it is at a given distance from the paraxial focus. The distance from focus is listed below the spots in μm .The center column is the best focus. The RMS radius is the spot size of the root mean radial size of all rays. The geometrical radius only reflects the radius of the ray farthest from the centroid.

The fisheye spot diagrams displayed similar performance to the telephoto lens. In fact, only the far outside field angles had RMS spot sizes that were greater than the pixel diameter. These outside field angles were plagued by astigmatism. Most importantly, the results show that the imager will have resolution for both the fisheye and the telephoto that is nearly limited by the size of the pixel.

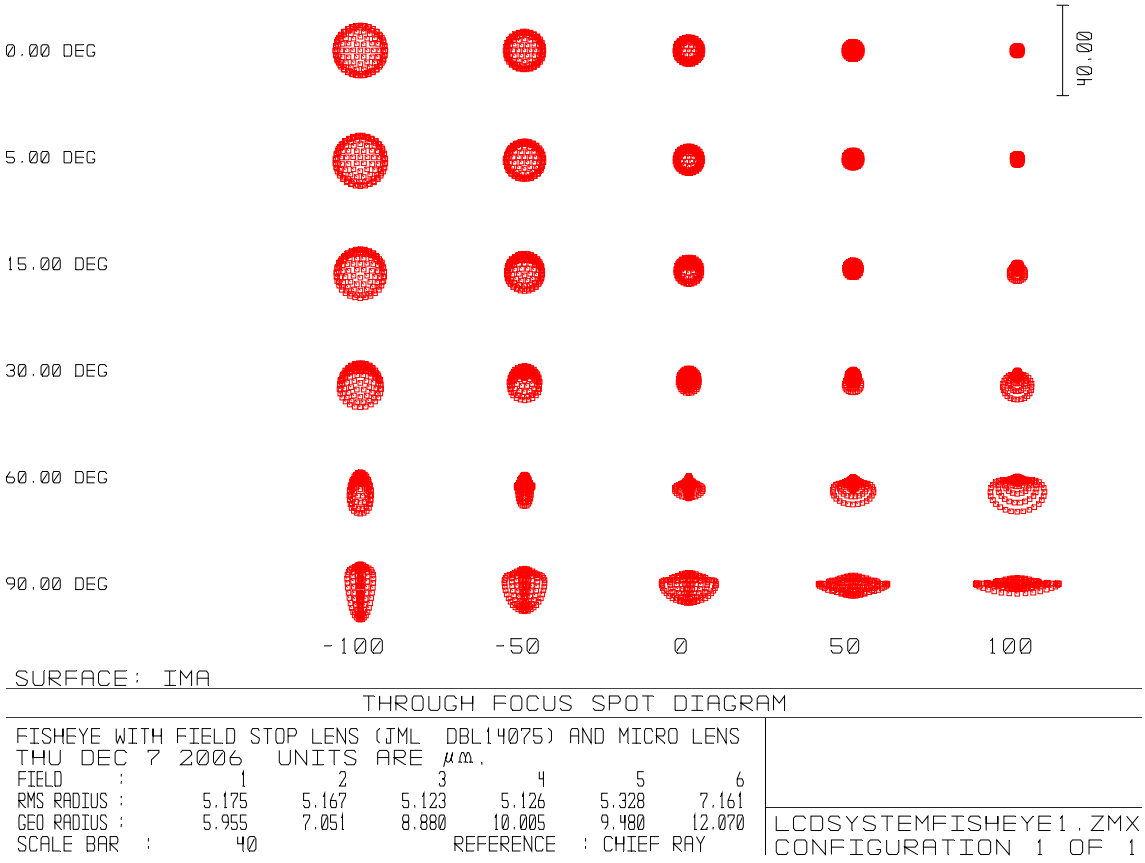

Figure 3.16. Through-focus spot diagrams for the polarimeter system with the fisheye lens at 700 nm and f/4.0. All units are in micrometers (μm). The degree markers on the left side denote the field angles in object space. Each column shows the spot size when it is at a given distance from the paraxial focus. The distance from focus is listed below the spots in μm .The center column is the best focus. The RMS radius is the spot size of the root mean radial size of all rays. The geometrical radius only reflects the radius of the ray farthest from the centroid.

System Implementation

To add the ability to automatically focus the camera, a focuser was added to the front of the Dalsa camera. The Finger Lakes DF-2 was chosen. This focuser allows 2.54 μm resolution through 5 mm of travel. The focuser is controller through the computer USB port. A C++ software development kit was also included with the focuser. Since the DF-2 provided its own F-mount for the 105-mm Micro lens, the F-mount front plate was

removed from the DALSA 1M30 camera and holes were drilled into the DF-2 to allow mating to the 1M30. The holes in the DF-2 were drilled slightly oversize to allow for image alignment on the CCD array.

After the 1M30 was mounted to the DF-2, the 105-mm Micro lens could be mounted directly to the camera and focuser assembly. It was found that 2" Thorlabs lens tubes will screw directly into the 105-mm Micro lens. For the remainder of the design, these tubes enclosed the optical train. Thorlabs also makes F-mount adapters and focus tubes for these lens tubes. The versatility of the line made the rest of the design considerably easier.

To mount each of the five spectral filters, the Finger Lakes CFW-1 filter wheel was selected. This filter wheel holds five 2" filters and is automatically controlled through USB. The same C++ software development kit (SDK) that controlled the DF-2 also controlled the CFW-1. I ported this software routine to MATLAB so that the entire system could be run from within MATLAB. At the time of this writing, both the SDK and my port were available from Finger Lakes Instruments (FLI) at http://www.fli-cam.com/software.htm.

Using Thorlabs lens tube compression holders (Part Number: SMR2C), the filter wheel was retrofitted to clamp onto the tube held by the 105-mm lens. For the remainder of the design, these tube holders were used to join the LCVRs, polarizer, and lenses (Figure 3.17). Extraneous holes and gaps in the filter wheel, focuser and mounts were taped off with electrical tape and sealed to eliminate light leakage. To allow the heaters to maintain a constant temperature, the LCVRs were heavily insulated with polystyrene

foam building insulation (not shown in Figure 3.17, but seen in Figure 1.1). This insulation allowed the instrument to be operated down to an outside air temperature of 50°F, at which point the camera passed out of specification.

A Newport F-mount holder was used to join each of the tubes containing the field lenses to the specific Nikon front lenses. The front lens assemblies each contained their own appropriate field lens. To change front lenses, the front lens assembly is removed at a Thorlabs lens tube joint by screwing it from the rest of the instrument. This joint is located just above the insulation (see in Figure 1.1).

The entire polarimeter system was mounted to a piece of aluminum channel iron using 8-32 hardware. Slots were machined into the channel iron to allow adjustment of the focus of the 105-mm Micro and the center of the optical axis. (The focus of the 105-mm Micro needed to be adjusted coarsely before the DF-2 could make fine adjustments.)

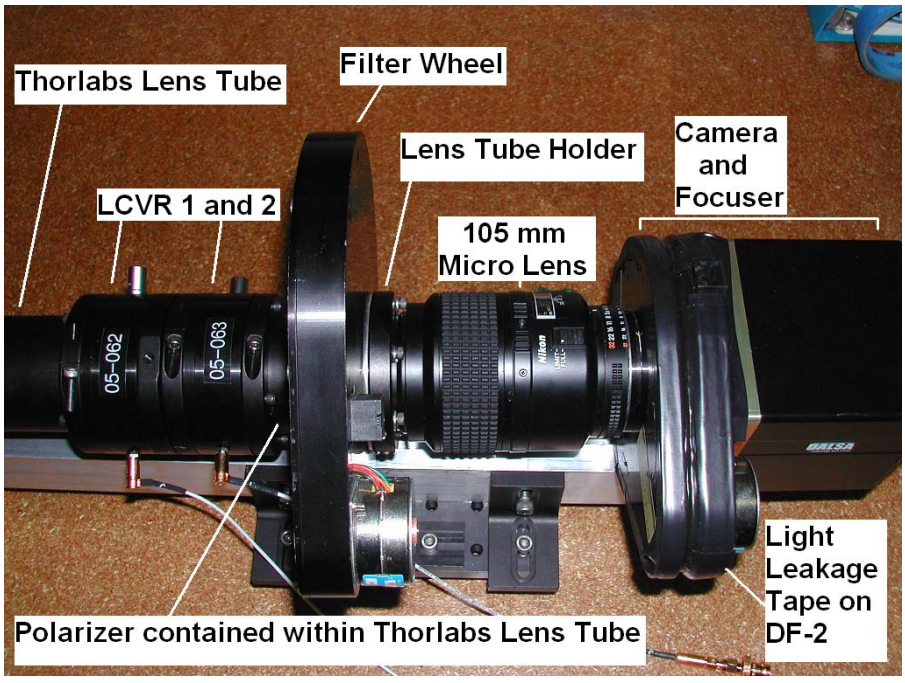

Figure 3.17. Back section of the polarimetric imager.

All data acquisition and some processing steps were run by a graphical user interface designed in MATLAB. This software merged C++ data acquisition of the camera with MATLAB data processing. Explanation of the intricacies of this complex piece of software (currently > 3500 lines) is beyond the scope of this dissertation. A summary of the software is given in Appendix II: *Operating Instructions for the Polarimeter.*

POLARIMETIC CALIBRATION

Camera Calibration

Dark Current Correction

The Dalsa 1M30 collects dark current pixel values that are substantial. (Dark current is imager noise that causes non-zero values of the images while under zero light conditions.) Typical values of the dark image average are around 46 digital numbers (DN). To correct for the dark current, a predetermined laboratory dark image is subtracted from every raw image taken with the polarimetric imager. This image is fairly uniform, but some noise is organized into higher-DN vertical stripes (Figure 4.1). This image was obtained by averaging five dark images while the imager was sealed from outside light. To ensure that the imager was light tight, dark images were taken with both room lights on and off. No change was observed.

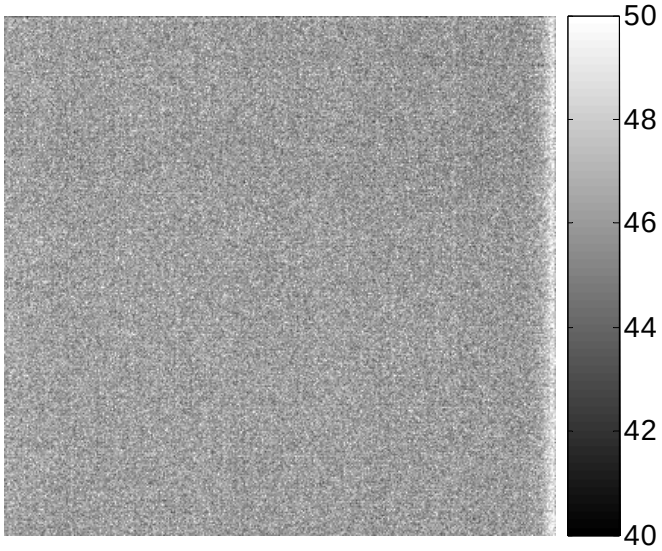

Figure 4.1. Dalsa 1M30 dark image.

The dark image average was found to depend on the exposure time. Exposures that were 250 msec exhibited dark noises that were about 2 DN larger than 50 msec exposures. To compensate for this, an exposure-dependent uniform correction was added to the standard dark image. Temperature dependence was not investigated thoroughly, but in the one instance that information was available, dark images that were taken at 55° F were only 0.25 DN different from the laboratory calibrated dark images at 70°F.

The dark image exhibited variation of both the average dark noise across the image from exposure to exposure and individual pixel variation between exposures. For 50-msec exposures, the average image dark noise deviated by ±0.176 DN (standard deviation), while for 250-msec exposures the average image dark noise varied by ±0.437 DN.

Most individual pixels varied by less than ±15 DN over 5 images (Figure 4.2). Without pixel averaging, this variability of the dark noise would cause high errors in the polarization for dimly exposed images. In fact, to reduce the Stokes parameter error from this source to 0.3%, the minimum exposure of the pixel must be at least 1000 DN. Median pixel averaging removes most of this concern. Still, an underexposure mask was created for pixels below a 100 DN threshold. During data processing, areas where any raw image values were below this threshold were considered unreliable.

It was observed that after the imager remained on standby, the first two images taken displayed higher digital numbers than average. At a 250-msec exposure time, the first image was 1.5 DN higher than the average, while the second image was about 0.4 DN higher. For this reason, two dummy images are always exposed before any

polarization data. (The average dark image calculation also ignores these first two images.) Slow dark current build up in the CCD probably caused this additional noise.

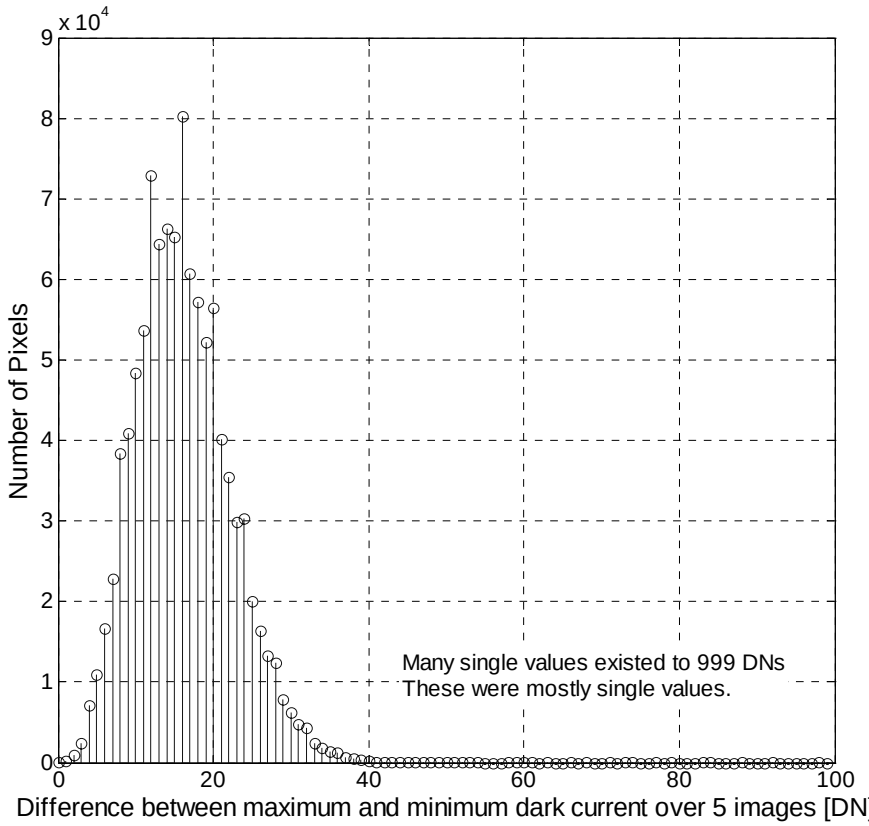

Figure 4.2. Histogram of the dark current difference between the maximum and minimum of each pixels dark current over 5 images. (The vertical axis range is 0 to 90,000 pixels.)

Linearity Correction

The DALSA 1M30 is also slightly nonlinear at the top of its dynamic range by about 4%. (The lower half of the dynamic range was sufficiently linear.) The source of this error is probably nonlinearity in the readout amplifier. The error is systematic, so it is removed by calibration. Using a *Sphere Optics* integrating-sphere luminance standard, the linearity response of the camera was calculated after dark image subtraction (Figure 4.3). Using a cubic regression, an equation that linearizes the data points was calculated.

The exposure jitter in the nonlinear data—typically 0.1%—is not significantly amplified by the linearization of the data. To show the variability of the linearization process, fifteen different linearity curves were taken and linearized (Figure 4.4). After linearization, the zero radiance point was checked for accuracy. This point was within 0.2 DN of zero for all 15 zero-radiance readings.

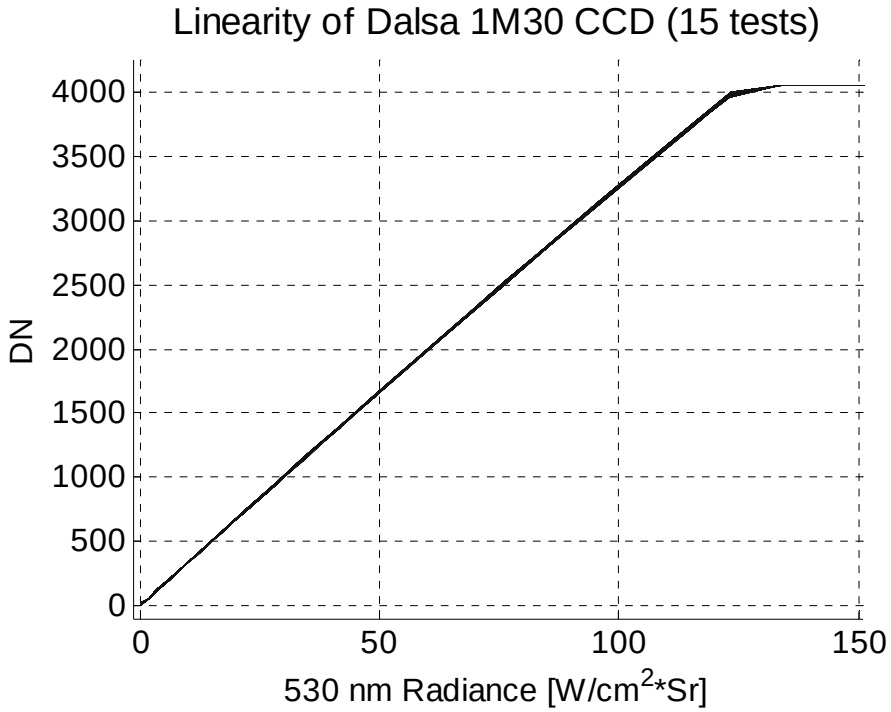

Figure 4.3. Linearity response of the Dalsa 1M30 camera. The response is limited by the maximum digital number of the 12-bit amplifier at 4095 DN.

Because of the sharp roll off above 3950 DN, pixel values above 3900 DN are considered unreliable. An overexposure mask was created to indicate areas where the raw images are overexposed. Furthermore, overexposure of any pixels is avoided because pixel bleeding causes large areas of unreliable data. For most data sets used in the current study, the maximum exposure of any pixel was limited to 3800 DN.

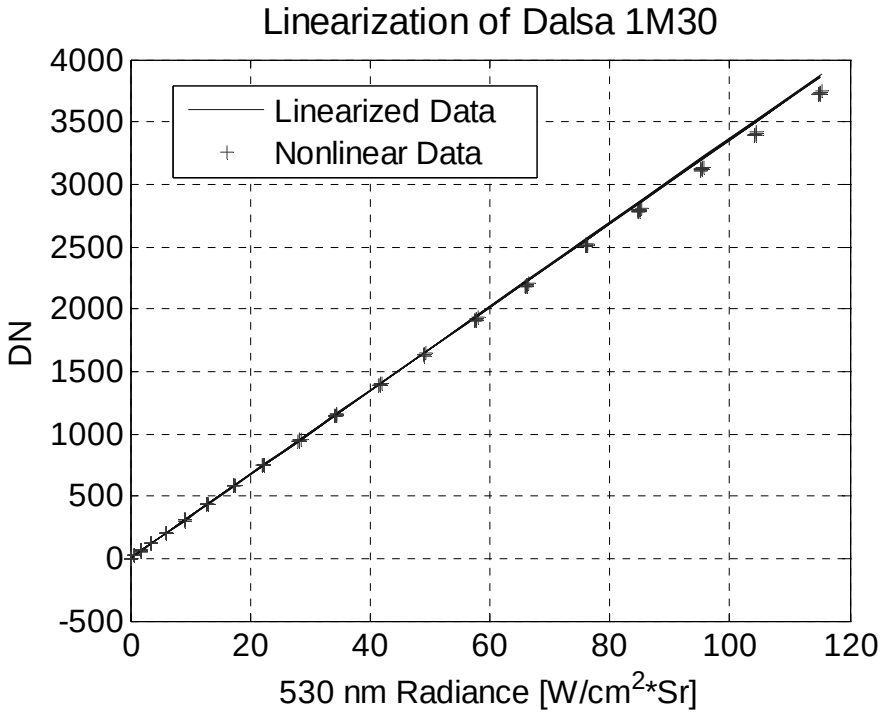

Figure 4.4. Results of the linearization of the camera.

Determination of LCVR Modulation Voltages for Each Retardance

To implement the retardance sets found in the system optimization (Table 3.1), modulation voltage values for the LCVRs were found. As mentioned before, retardance and rotation angles of the LCVR vary significantly with incidence angle and wavelength. For this reason, graphs of the retardance vs. voltage from Meadowlark would not be accurate for the imaging system. A method of measuring an equivalent retardance for each wavelength for the center of the image was devised.

One LCVR was measured in the system at a time. For each voltage, four input light states corresponding to –90°, -45°, 0°, and 45° linear polarization states were used to measure m_{01} and m_{02} of the system. Using the determined m_{01} and m_{02}, a nonlinear solver was used to find the values of the retardance and rotation angle that corresponded

to these values—assuming a pure retarder. For each wavelength, a voltage vs. retardance curve was developed (see Figure 4.5 for example). Then, the appropriate modulation voltages for the retardance values in Table 3.1 were found. Table 4.1 gives the selected voltages for each image in the sequence.

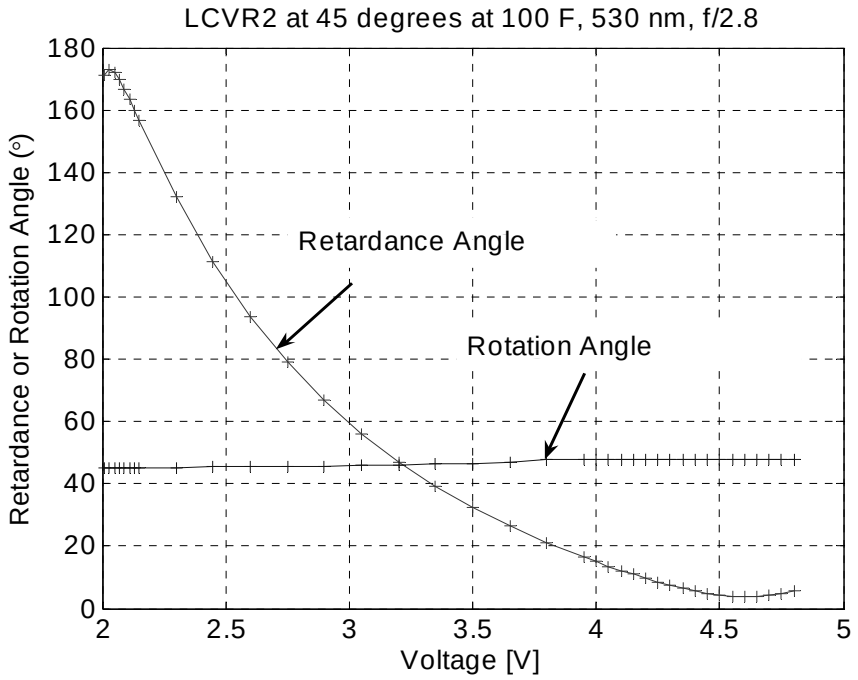

Figure 4.5. Example voltage vs. retardance curve for LCVR at 45° retardance.

Table 4.1. Final Control Voltages for LCVR1 and LCVR2.

	Voltages (V)	Image 1	Image 2	Image 3	Image 4
450 nm	LCVR1	2.272	3.647	2.12	3.908
	LCVR2	2.73	2.26	4.168	3.163
490 nm	LCVR1	2.162	3.527	2.025	3.802
	LCVR2	2.607	2.14	4.065	3.037
530 nm	LCVR1	2.107	3.504	1.98	3.77
	LCVR2	2.501	2.042	3.985	2.927
630 nm	LCVR1	1.88	3.242	1.73	3.526
	LCVR2	2.309	1.85	3.866	2.736
700 nm	LCVR1	1.78	3.19	1.645	3.515
	LCVR2	2.177	1.72	3.815	2.607

Calibration Methodology

By taking exposures of a polarizer at several different angles in front of an unpolarized light source, the instrument system matrix could be determined. As mentioned previously, separate calibrations were necessary for every pixel, for every filter, at every f/#. Calibration of the polarimeter with each front lens could have been accomplished by rotating the polarizer in front of the system including each front lens. This method would only return the first three columns of the system matrix. Retrieving the fourth column of the system matrix could only be accomplished by generating a circular wave. Lack of availability of quarter-wave plates made generating the necessary circular light impossible. (These large aperture waveplates are expensive and a specific plate for each wavelength would have been required.) Without these waveplates available for calibration the polarimeter would consequently be restricted from measuring the circular component of polarization (S_3). Using knowledge of the system components allowed a creative solution to this problem. By making two assumptions about the properties of the lenses and the LCVRs, the fourth column of the system matrix could be modeled. A roundabout calibration was used that initially calibrated the system without the front lens (Figure 4.6). Later, the system was calibrated with the front lens.

First, the first three columns of the system matrix were measured with only LCVR2 installed in the system. Then it was assumed that each LCVR could be modeled as an ideal retarder. Using the measured elements of the first three system matrix columns of LCVR2, the LCVR2 retardance and rotation angles were modeled using a nonlinear solver. Then, LCVR1 was added to the system. Again, values of the first three

columns of the system matrix were taken. By using the measured values of the first three columns of the system matrix for each pixel, the modeled values of LCVR2, and an ideal model, the retardance and rotation angles of LCVR1 were modeled using a nonlinear solver. The fourth column of the system matrix was generated using the modeled retardance and rotation values of both LCVRs. At this point, the polarimeter without the front lens was calibrated fully. Herein, this is called the near-field polarimeter calibration.

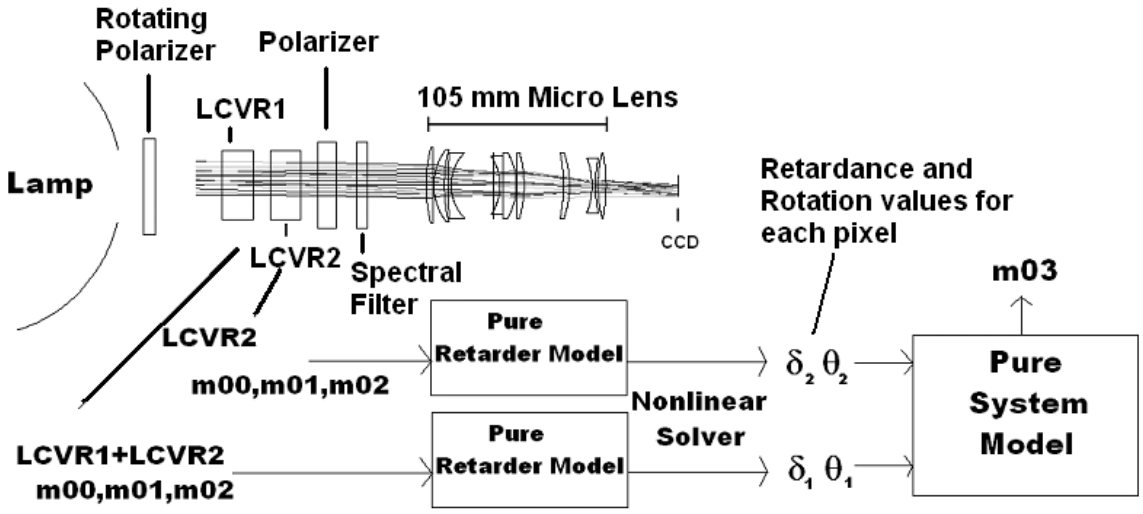

Figure 4.6. Modeling of the first row of the 4th column of the system matrix. The elements *m00, m01*, *and m02* are the measurements of the first three elements of this row of the system matrix. The element *m03* is the modeled component. LCVR1 is removed from the system to obtain the LCVR2 values of *m00, m01, and m02*.

After the near-field calibration, each front lens was attached to the system for calibration. The first three columns of the Mueller matrix of each front lens were measured using the near-field calibration. Again, the fourth column of the Mueller matrix could not be measured without specific quarter-wave plates for each filter wavelength. The lens Mueller matrix was assumed to be non-depolarizing (Chipman, 2005) and

symmetrical (Xing, 1992). Using these assumptions, the fourth column of the lens Mueller matrix was determined from the values of the first three columns.

Although the lens matrices could have been included with the system matrix measurement and the whole system could have been calibrated as a single unit by sacrificing the S_3 parameter, use of the model for the fourth column of the system matrix and the use of the symmetrical model for the lens allowed a reasonable estimate of S_3. This method proved to be useful for determining a modeled fourth component of the system matrix. Although the assumption of the ideal retarder caused circular polarization to be under-predicted—with the exception of the fisheye at large incidence angles—the method produced fairly accurate measurements of S_3 (discussed below).

Calibration of the Polarimeter without a Front Lens

The first three elements of each row of the system matrix (a_{x0}, a_{x1}, and a_{x2}) can be found by use of a linear polarizer. (Remember that each row is associated with one set of retardances for both LCVRs of the polarimeter. This is also referred to as a polarimeter state in this dissertation.) Images were taken with a large-aperture linear polarizer (extinction ratio better than 10^{-3}) oriented at 0°, -90°, 45°, and -45° for each polarimeter state with the instrument looking into a 10-cm-aperture uniform luminance standard. This corresponds to the normalized Stokes vectors, [1 1 0 0], [1 –1 0 0], [1 0 1 0], and [1 0 -1 0]. The image values measured at each of these settings were used to determine the first three components of the row. For example, in row 0, a_{00}, a_{01}, and a_{02} were determined, according to Equation 4.1.

$$\begin{aligned}
\text{Image}_{0} &= 1a_{00} + 1a_{01} + 0a_{02} + 0a_{03} \\
\text{Image}_{-90} &= 1a_{00} - 1a_{01} + 0a_{02} + 0a_{03} \\
\text{Image}_{+45} &= 1a_{00} + 0a_{01} + 1a_{02} + 0a_{03} \\
\text{Image}_{-45} &= 1a_{00} + 0a_{01} - 1a_{02} + 0a_{03}
\end{aligned} \tag{4.1}$$

Inspection of Equation 4.1 shows that a_{00}, a_{01}, and a_{02} can be determined from these images. Each of the other three rows (a_{1x}, a_{2x}, and a_{3x}) was measured in a similar fashion. The last column of the system matrix could not be measured using only a linear polarizer, as mentioned previously. Instead, the last column of the system matrix was modeled according to the retardances and equivalent rotation angle of each LCVR, assuming they were pure retarders. This measurement of the elements in the first three columns of the system matrix and the modeling of the last column was done for every pixel and every spectral filter at four different f/#s (2.8, 4.0, 5.6, and 8).

Accuracy Assessment

Four different polarizer positions—22.5°,-67.5°, –22.5°, and 67.5°—were used to validate the calibration. These states were chosen because they were different than the calibration settings. Unpolarized light was also measured. Finally, circular polarization was created using a 2.5-cm achromatic waveplate. There is uncertainty in the exact Stokes vector generated by the achromatic waveplate, as the retardance is dependent upon the incidence angle of light and the wavelength, and the exact position of the fast axis changes with wavelength. Nevertheless, an estimate for the accuracy of the fourth column model could be found by measuring light from the achromatic waveplate. Table 4.2 shows the maximum errors recorded through all four f/#s.

The model of the last column of the system matrix seems to cause under-estimation of the magnitude of the circular Stokes parameter at 90%. This is probably attributed to the fact that the retarders are not ideal. Even with the uncertainties in the achromatic waveplate, higher values of the circular component were expected. For all foreseeable measurements, the light will be partially polarized linear light. If circular light in nature is found, the instrument will measure a circular signature, but not necessarily be quantitatively accurate until a circular polarization calibration is completed with a large-aperture achromatic waveplate. This is acceptable since circular polarization is not expected to be found in either sky or targets. Overall, the linear polarization and unpolarized accuracies seem to be limited by slight exposure jitter in the camera.

Table 4.2. Summary of maximum errors without front lenses.

Error	Linear Input (100 %)	Unpolarized Input	Circular Input
S_1 and S_2	+/-1.1%	+/-0.4%	unknown
S_3	+/-1.5%	+/-0.3%	-10%

Calibration of Polarimeter with Telephoto and Fisheye Lenses

The front lenses were calibrated separately from the polarimeter. Since their Mueller matrices are well conditioned, the Mueller matrix of the front lens is inverted and multiplied by the measured Stokes vector to obtain the input Stokes vector. Calibration of the lenses followed a method that is similar to the near-field calibration. Using the calibration of the near field with the front lens added, a Stokes vector was measured with a linear polarizer set to -90º, 0º, -45º, and 45º. Using the measured Stokes vectors and the known input Stokes vectors, the first three columns of the lens Mueller matrix were

found. Equation 4.2 shows an example of this calculation for the second row of the Mueller matrix.

$$\begin{aligned} S_{1\,(0)} &= 1m_{10} + 1m_{11} + 0m_{12} + 0m_{13} \\ S_{1(-90)} &= 1m_{10} - 1m_{11} + 0m_{12} + 0m_{13} \\ S_{1(+45)} &= 1m_{10} + 0m_{11} + 1m_{12} + 0m_{13} \\ S_{1(-45)} &= 1m_{10} + 0m_{11} - 1m_{12} + 0m_{13} \end{aligned} \tag{4.2}$$

Once the first three columns were found, the matrix was assumed to be a symmetric, non-depolarizing Mueller matrix and the last column calculated. Since the lens is not perfect, these assumptions induce some error into the circular component. Most optics have little depolarization (Chipman, 2005), so the measurement of a near-unity matrix is not surprising. A typical Mueller matrix (normalized to m_{00}) is shown in Equation 4.3. Notice that calibration errors in the near-field polarimeter cause some matrix elements to be slightly greater than unity and the lens matrix measurement compensates for these errors.

$$\begin{bmatrix} 1.0000 & -0.0006 & -0.0018 & -0.0081 \\ -0.0008 & 1.0083 & -0.0047 & 0.0320 \\ 0.0009 & -0.0019 & 1.0012 & 0.0089 \\ -0.0081 & -0.0320 & -0.0089 & 1.0047 \end{bmatrix} \tag{4.3}$$

Fisheye Calibration Methodology

The fisheye lens is also close to an identity matrix at the center, but slightly worse at the high-incidence-angle fields. Calibration of the fisheye was accomplished with piecewise measurements across the field of view of the instrument. The luminance standard and polarizer were rotated in a plane defined by the optical axis and the polarimeter base (as shown in Figure 4.7 looking down). The setup shown only calibrated

a horizontal (0°) slice across the center of the fisheye image. To calibrate the whole image, the polarimeter itself was rotated -45º, 0º, 45º,and 90º, while the luminance standard and polarizer were left in place to obtain slices that covered the whole image area.

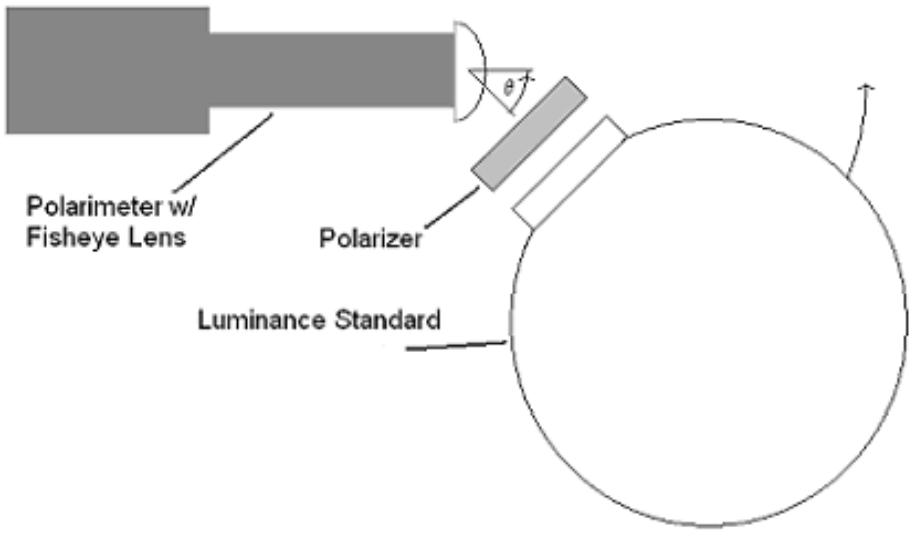

Figure 4.7. Setup used in the fisheye lens calibration. The luminance standard and the polarizer rotate together in the direction of the arrow for each calibration piece.

One problem with the fisheye calibration is the issue of reference plane. The fisheye itself rotates the polarization vector. As an example, consider a fisheye lens viewing the sky dome with the horizon at 90º from the optical axis (because the imager is looking up). The orientation of the polarizer sets the zero–azimuth angle. Horizontal polarization is defined as parallel to the horizon. Light incident from the horizon at 0º azimuth with a *vertical* polarization vector will be measured to have an angle of polarization of 0º by the polarimeter; however, light incident from the horizon at 90º of azimuth with *horizontal* polarization also will be measured to have an angle of

polarization of 0º. Finally, a field incident upon the fisheye from the horizon at 45º of azimuth with a 45º polarization will also be measured to have a polarization angle of 0º.

To verify that the fisheye was truly causing this problem, an inverse experiment was devised. A vertically polarized laser beam was expanded to fill the aperture of the fisheye lens from the image side, rather than the object side. Then, a polarizer was used to extinguish the dome of polarized light that emanated from the fisheye lens in all directions. In the center of the lens, the polarized light from the fisheye lens acted just like its telephoto counterpart: it was vertically polarized. On the horizon, though, the polarization angle was continuously changing with position at all points along the horizon. The measurements confirmed the polarization orientation issues described above.

Should an incident ray from the horizon that has polarization parallel to the horizon always be measured as the same polarization angle? This is a matter of choice. If all horizontally polarized light at the horizon is measured to have the same polarization angle, there will be a discontinuity at the center, as indicated in Figure 4.8. If the rotation of the fisheye is maintained, there will not be a discontinuity, but interpreting angle-of-polarization data is more challenging. Even with this challenge, the latter method was chosen to avoid an additional rotation in the fisheye lens calibration matrix. Post-processing algorithms could be used to convert between the two types of referencing (i.e., change between horizon reference and instrument-polarizer reference).

Because the fisheye lens rotated the polarization vector, the images of the calibration polarizer have a polarization angle that varies across the aperture. Therefore,

for each piecewise slice, the only accurate angle of polarization was at a line across the center of the slice. For each of the slices, a line was extracted across the accurate part of the calibration slice. Calibration data were then linearly interpolated between each of these calibration lines. In the center of the image, all the slices converged upon the same calibration so the center was calibrated in a block without interpolation. The accuracy of the interpolation was of concern, but validation discussed below shows that the calibration worked well.

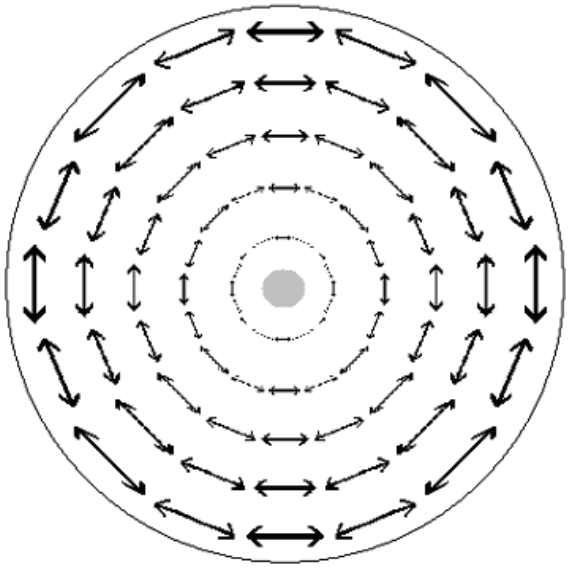

Figure 4.8. A discontinuity occurs at the center of the image if all rays with polarization parallel to the horizon are measured as the same polarization angle as shown.

Since the Mueller matrix is obtained for each lens, problems in the lenses could be investigated. For the 300-mm telephoto, the Mueller matrix image was nearly unity. The only deviations from unity are attributed to errors in the near-field calibration. For the fisheye lens, the Mueller matrix of the central parts of the lens was always near unity (Figure 4.9). At high incidence angles (>45°), the fisheye lens induced moderate amounts

of circular polarization (~15%) into a 100% polarized linear input. This is seen in the *m31* and *m32* images (bottom row, center two images) and their corresponding symmetric components *m13* and *m23*. Slight amounts of diattenuation were also seen (<1.5%). This is more difficult to see, but is exhibited in *m10, m20, m01, and m02*. It was unclear whether the diattenuation came primarily from real lens diattenuation caused by the large reflection angles, or errors in the near-field polarimeter system matrix. At any rate, the Mueller matrix image of the fisheye image is nearly unity and therefore well conditioned for inversion.

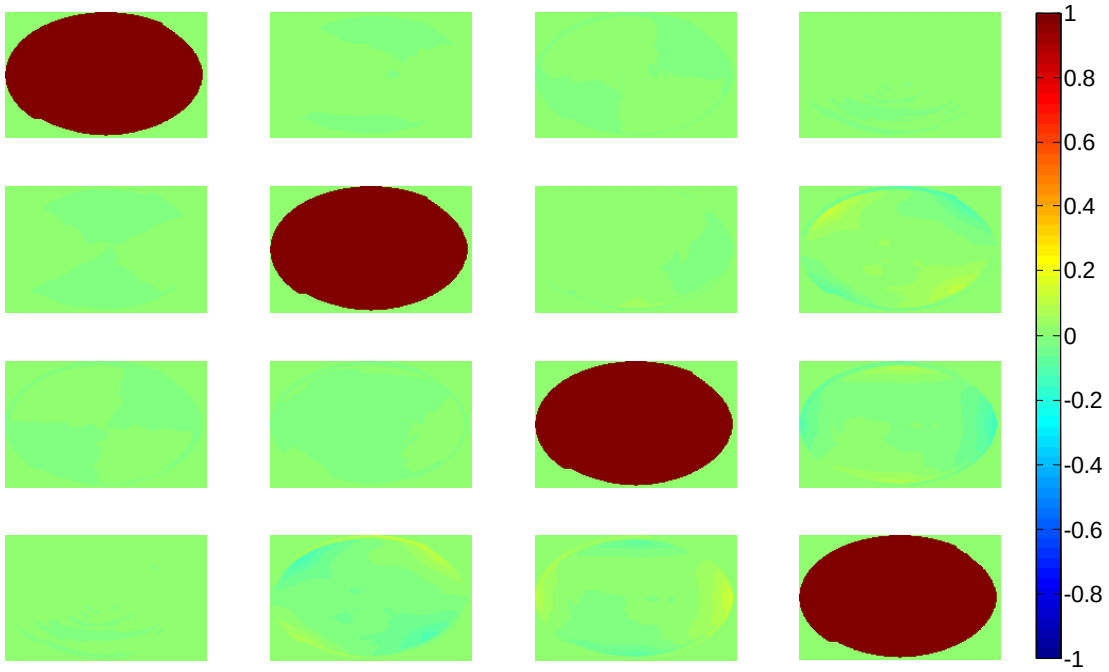

Figure 4.9. Normalized Mueller matrix image of the fisheye lens. Each image corresponds to the appropriate "m" parameter in the Mueller matrix. For example, the upper left image is the *m00* parameter. Portions outside the image circle are unused in the polarimeter. For the major axis elements, the values are between 0.98 and 1.005 for nearly all elements. (Elements that are measured greater than unity are caused by near-field calibration errors.) An ideal lens with a unity Mueller matrix would be unity in all images down the primary diagonal (this is close) and be zero in all other images.

Lens Calibration Accuracy Assessment

After calibration of the telephoto lens, validation was performed identically to the system-matrix validation using 22.5º, -22.5º, 67.5º, and -67.5º polarizer angles. None of the errors in circularly polarized, linearly polarized, or unpolarized light changed significantly. Expected Stokes-vector reconstruction error in the telephoto lens is less than ±1.5% except for S_3.

Fisheye validation used the same method, but multiple validation images were taken across the field of view. For images that were in the interpolated areas, it was difficult to know the exact angle of polarization as it changed across the image of the luminance standard. Nevertheless, the angle of polarization did not seem to depart from what was expected across the center of each image. Errors in the degree of polarization were ±1.5%. Circular polarization errors were significantly worse (±5%) because the circular polarizer models were not entirely valid. Angle-of-polarization error in the center of the fisheye image was ±0.3º. The condition number for the whole imager varied from 1.85 to 2.3 across all f/#s, wavelengths, and pixels. Therefore, depolarization in the LCVRs and polarimeter lens aberrations did not seem to significantly reduce the conditioning of the system matrix.

Performance Assessment and LCVR Calibration Concerns

Pixel-to-Pixel Variation

In light of the variations in the dark current, the variation of individual pixels was analyzed. The question was: For an area with one polarization, what variation is seen in the image area? For the degree of linear polarization, the variation of most pixels over

small areas (less than 50 x 50 pixels) was less than ±1% (Figure 4.10). Individual Stokes parameters behaved similarly. Similarly, the majority of individual angle-of-polarization pixels were distributed over about ±0.2° (Figure 4.11). As mentioned before, these effects can be reduced by pixel averaging.

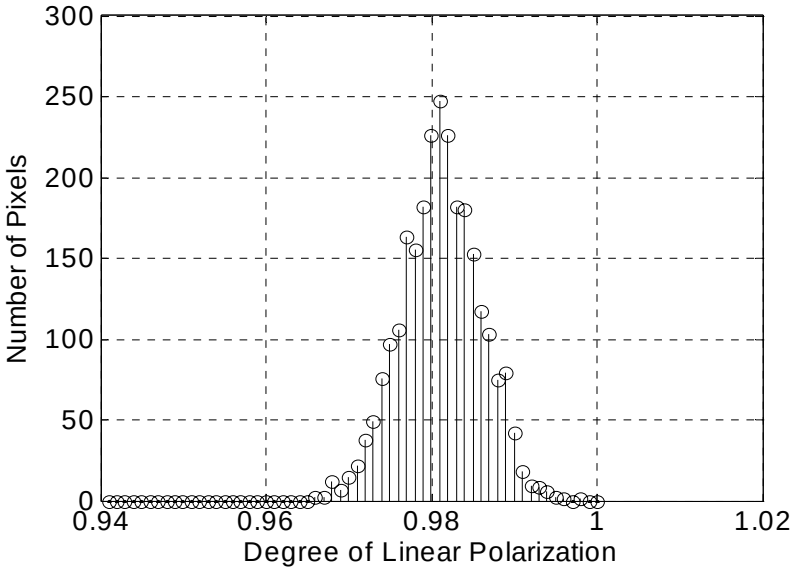

Figure 4.10. Example of DoLP pixel distribution over a 50 pixel x 50 pixel area.

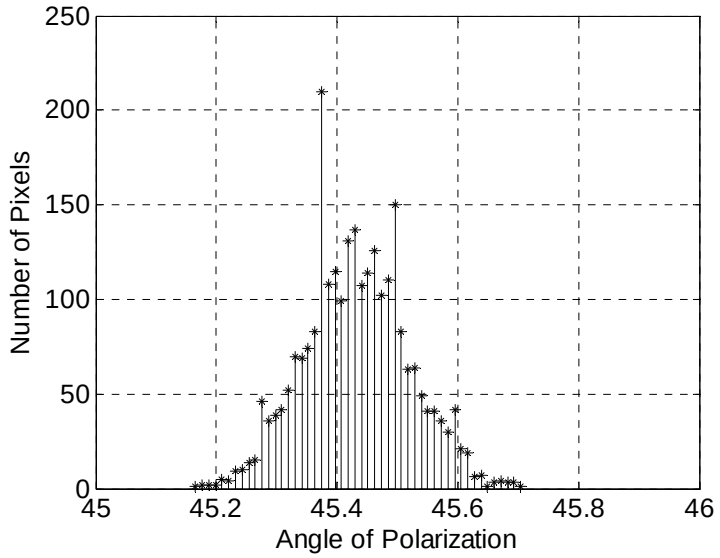

Figure 4.11. Example of AoP pixel distribution over a 50 pixel x 50 pixel area.

Effects of Using the Wrong f/# Calibration

As mentioned previously, the calibration was not expected to remain valid if the f/# of the system was changed. To verify this idea, I made measurements at f/2.8, f/4.0, f/5.6 and f/8.0, using the calibration for the f/4.0 setting. Table 4.3 shows the average degree of polarization for fisheye measurements obtained with the instrument viewing a linear polarizer oriented at -22.5º for 490 nm as an example. There is clearly a rise in the degree of polarization determined with the f/4.0 calibration as the imager is stopped down. This is expected because setting the instrument at a larger aperture creates more depolarization in the LCVRs. Therefore, for a set calibration, the lower f/#s should measure a lower degree of polarization. This confirms the conclusion that each f/# should be calibrated separately, although in this imager it does not seem to be an excessively large problem. Adherence to the low incidence angle (<5º) design constraint probably minimized the problems of depolarization in the LCVRs.

Table 4.3. Measurements of degree of polarization over all f/#s using the f/4.0 Calibration.

f/#	Measured Degree of Polarization
F2.8	99.4%
F4.0	99.9%
F5.6	100.3%
F8.0	100.3%

Spurious Reflection Effects

One concern for the instrument calibration is the problem of multiple reflections of light inside the instrument. During the fisheye calibration, only the piece of the image that needed to be calibrated was illuminated. This is equivalent to a scene that is dark

everywhere except in the area of interest. In field measurements, the full scene will illuminate the imager. If multiple reflections inside the instrument lens system are significant, then the light from the other areas will effectively cause the degree of polarization to be reduced in the area of interest. Still, the anti-reflection coatings of Nikon's high-quality optics should minimize any spurious reflections. The question is: how significant is the problem of spurious reflections?

One method of answering the problem is to look at the effects of lens flaring in images that directly view the sun. Figure 4.12 shows the reduction of the degree of polarization between two images that are within 1 minute of each other at the same exposure. One directly images the sun; one does not.

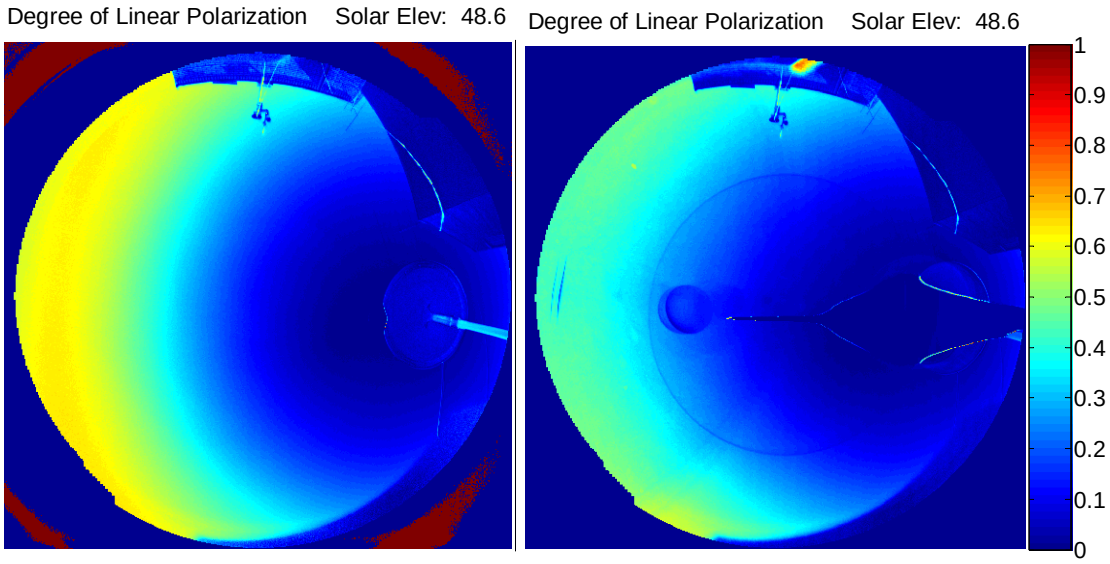

Figure 4.12. Effects of directly imaging the sun on the DoLP at 530 nm on 13:04 MDT, September 11, 2006. The image on the left side is taken with the sun blocked. The image on the right side directly images the sun. The peculiar data on the right of this image arise from blooming in the CCD. Both the area of maximum DoLP and the lens flare area are reduced by ~20% (DoLP) when the sun is directly imaged.

The approximate 530-nm spectral irradiance of the direct sunlight was obtained from MODTRAN as 4.28e-6 W/(cm^2 cm^{-1}). The scattered spectral radiance for 530 nm at zenith was 4.94e-9 W/(cm^2 cm^{-1} sr). Assuming the worst- case scenario is when the entire sky dome radiance corrupts the area of interest, the projected solid angle for the hemisphere projected onto the sensor is $\Omega = \pi$ sr. Therefore, the maximum irradiance from other areas of the sky, when the sun is blocked, is 1.55e-8 W/(cm^2 cm^{-1}). (The irradiance is the radiance times the projected solid angle.) This means that the difference between the ratio of the irradiance from all points in the sky to the sun is ~275. For a given sky, the degree of polarization reduction will be linearly dependent upon the radiance from the other areas of the sky. For direct sun illumination, the DoLP is reduced by 20%. When the sun is blocked, only the remaining sky dome will reduce the DoLP for a given area. Using the fractional difference between the two effects, the reduction of the DoLP by the remaining scattered light could only be ~0.069%. Therefore, sporadic scattering of light in the optics does not reduce the degree of linear polarization sufficiently to cause concern (as long as the direct sun is blocked).

Calibration Stability of the LCVR Polarimeter

Because of the complexity of the calibration, the entire process could last several days. Repeated recalibrations were therefore undesirable and calibration stability of the instrument was a concern. Repeated validation of the instrument calibration over the short term (less than 2 days) showed a very stable instrument. Variation in the degree of linear polarization (DoLP) over the short term was as low as 0.3%, while the angle of polarization varied by less than 0.1° (Figure 4.13). The high-frequency variations

displayed in Figure. 4.13 come from exposure jitter in the individual images, while the lower-frequency oscillations come from the temperature oscillations caused by the heating control.

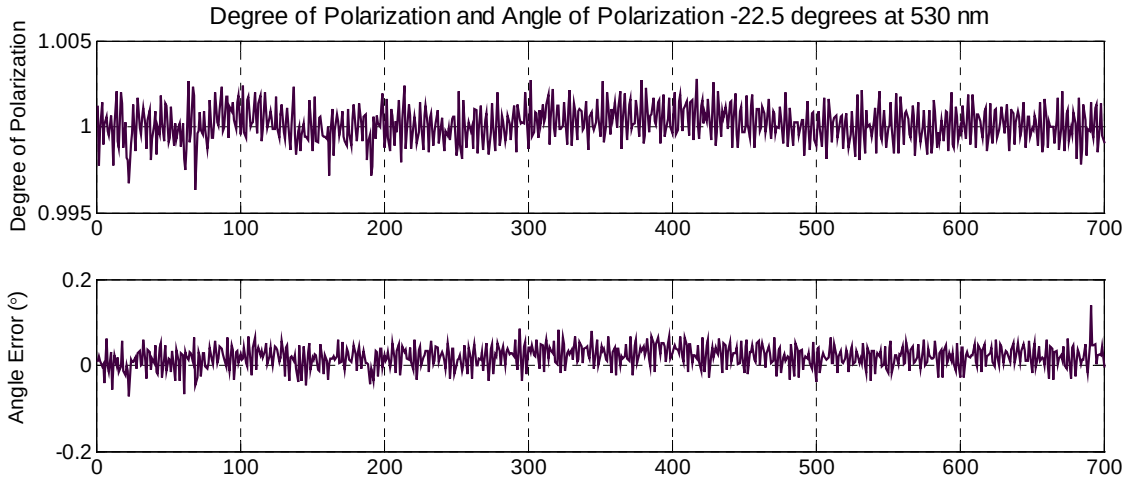

Figure 4.13. Short-term stability of the polarimeter. All data were averages of the center 200 x 200 pixels while looking at a –22.5° reference linear polarizer at 530 nm. The 700 iterations were taken over approximately 3 hours.

In contrast to the short-term stability, analysis of the long-term stability unveiled problems. First, when the LCVRs remain at one temperature, the ions within them tend to reach equilibrium in the steady state. This causes the polarization properties of the LCVRs to remain stable. Temperature cycling of the LCVRs causes slight changes of the ions in the LCVR alignment layer. These changes cause errors in the polarimeter calibration. After cycling the temperature, errors as large as 10% were observed in the Stokes parameters. To eliminate this problem, a battery backup system was added to the LCVR heater system. This system keeps the LCVRs at one temperature, even when the system is unplugged or when power fails. Even with this problem eliminated, the calibration of the instrument has been seen to vary by about 2% DoLP over periods of

weeks. For this reason, the near-field calibration was always checked in the field before data were acquired. A polarizer was attached directly to the near-field polarimeter and measurements of several polarization angles were taken. After calibration in March 2006, the calibration remained stable within 2% until the end of September 2006. At this time, a move of the instrument to take target data caused the LCVRs to slightly jump calibration. Target data were taken after this time (see the next section). Before all the desired target data acquisition was completed, a heater failure caused the calibration to be completely lost. As a result of the cold temperatures when the heater failed, the LCVR states were modified beyond the typical 10% error and DoLP errors were above 25%. Subsequent target data collection was abandoned. Therefore, only two days of target data were recorded. Once calibration stability issues were considered, the overall instrument calibration through the entire summer was ±3.5% for 100% polarized light. All of the calibration errors and stability errors are less severe for partially polarized light than for fully polarized light, so all errors should be considerably less than 3.5%.

EFFECTS OF CHANGING SKYLIGHT ON GROUND-BASED PLATES

Although it is known that a few investigators have looked at visible-band polarization signatures (Egan and Duggin, 2002; 2000), no published literature on changes in target DoLP caused by different sky conditions was found. (Much of this shortage is attributed to the sensitive nature of the military component of the field.) To understand the severity of the atmospheric effects on targets, measurements were taken of four different metal plates during two successive days with dissimilar sky conditions.

Experimental Setup

Four plates measuring 1 m by 1 m were made of standard 3/16" steel. Two of these plates were sandblasted with 60-grit sand to roughen the surface. The four plates were then painted with Krylon flat black and flat tan spray paints so that there was a smooth plate and a rough plate of each color. After initial painting, it was observed that the paint itself did not smoothly coat, so the two smooth plates were iteratively wet sanded and repainted until a consistent smooth coat was obtained. These plates were placed on the top penthouse of the Engineering and Physical Sciences building at Montana State University. The polarimetric imager was placed on the top of a neighboring building looking down at the plates at an angle of 21° and nearly straight south.

Images were taken on September 27 and 28, 2006. September 27 started completely overcast and then the clouds began to break up around 11:40 am Mountain Daylight Time (solar elevation of 38°). By early afternoon the sky was completely clear

and remained clear until sunset. September 28 was in many ways exactly opposite. In the morning, the sky stayed clear until late afternoon. At this time, partial cloud cover began to form and remained in place until after sunset. For each plate, all raw images over each day were aligned to one image using an automated correlation algorithm. For all plots, a region encompassing the center of the plates was averaged to give the DoLP measurement.

Figure 5.1. Clouds breaking up around 12 pm MDT on September 27, 2006.

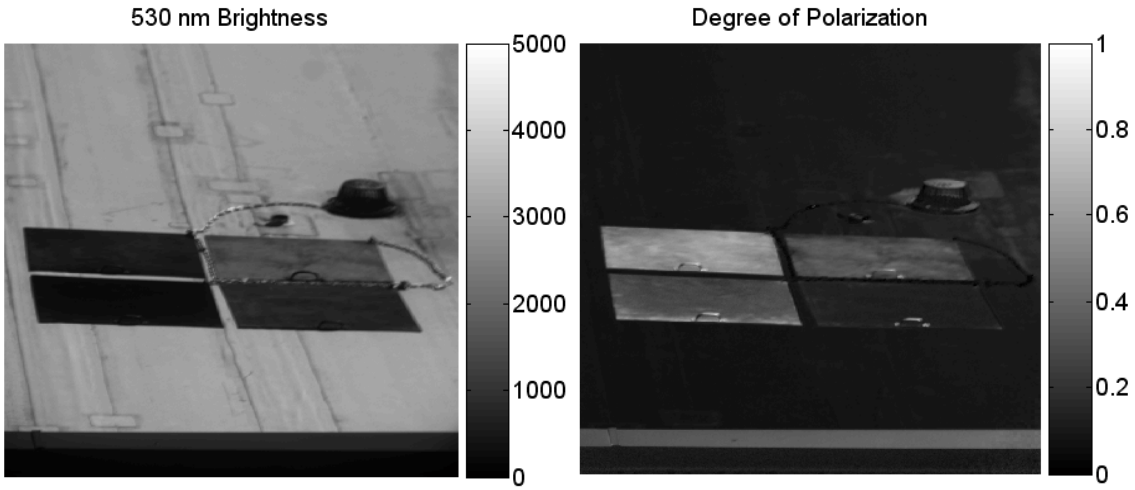

Figure 5.2. Sample images of four Krylon painted plates. The smooth black plate is in the upper left-hand corner, while the rough black plate is in the lower left-hand corner. The smooth tan plate is in the upper right-hand corner, and the rough tan plate is in the lower right-hand corner.

Figure 5.2 shows a sample image from the data. Notice the different polarization signatures for the different plates. Also, the plate handles are more highly visible in the DoLP image. The band at the bottom of each image is the roof railing, which is a flat aluminum cap. This cap exhibits a strong degree of linear polarization.

Comparison of Target Signatures

An important note about the data presented in this section is that the data may have large absolute calibration errors (possibly as much as 10%). Data in this section are precise between the two days (September 27 and 28), but should not be taken as accurate. For this reason and the possibility of significantly different atmospheric aerosols, comparisons to data from other instruments should be made loosely. This problem exists because of a LCVR calibration shift. Still, the calibration was stable between the two days and is profitable for comparison.

Figure 5.3 shows the DoLP for the four different plates at 630 nm on September 27. This plot illustrates the usefulness of the DoLP to differentiate between materials. The smooth and rough surfaces exhibit significantly difference polarizations. In fact at most points in the graph, each plate could be easily classified only by its DoLP. Interestingly, the DoLP for the darker black plates is much higher than the respective (in terms of roughness) tan plates. This suggests that dark targets would be distinguished more easily from the background by considering DoLP instead of brightness. Figures 5.7 and 5.8 illustrate this for other wavelengths as well.

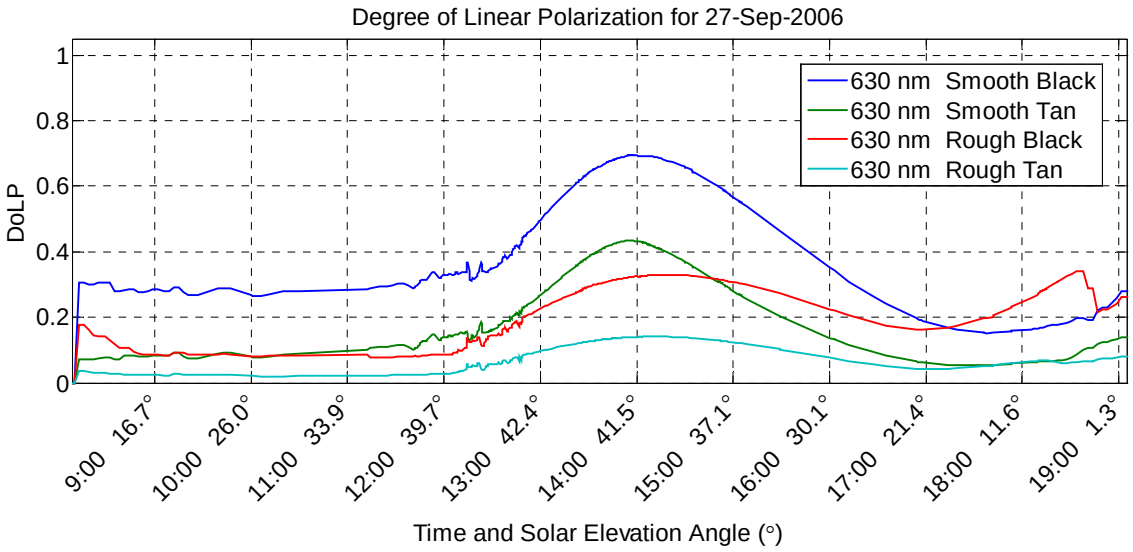

Figure 5.3. Degree of linear polarization for different plates at 630 nm on September 27, 2006, plotted as a function of local time (MDT) and solar elevation angle.

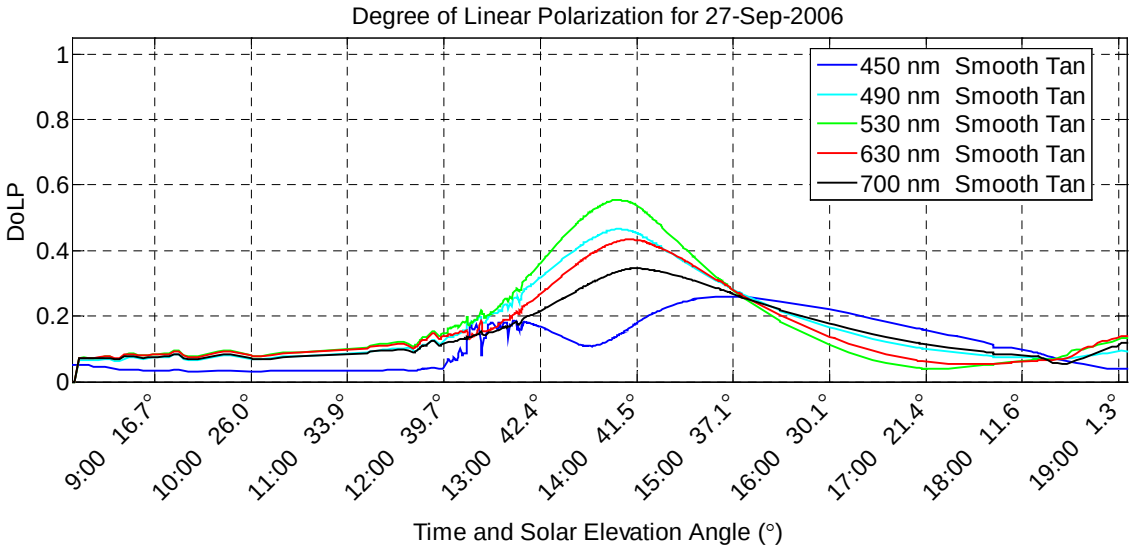

Figure 5.4. Degree of polarization for smooth tan plate for different wavelengths on September 27, 2006, plotted as a function of local time (MDT) and solar elevation angle.

Figure 5.4 shows the complexity of degree of polarization signatures through the course of the day for the smooth tan plate. DoLP is dependent upon plate color, plate roughness, sky conditions, solar zenith/azimuth, and wavelength. Since DoLP depends on

solar elevation, comparison plots of the degree of polarization between days are plotted against the solar elevation angle, not time. The early afternoon of both days exhibited a clear sky. (In this dissertation, clear sky means a sky free of clouds.) This region was expected to exhibit the same degree of polarization on both days. Any differences in the early afternoon DoLPs are attributed to slight differences in solar azimuth between the two days and slight aerosol differences. Using two successive days minimized changes in these variables. Figure 5.5 shows the differences for the same smooth tan plate at 450 nm between the two days. The early afternoons compare well, as expected. Notice that in the early morning the DoLP for the overcast day is more than 10% lower than for the clear day. Also, as clouds began to move in on the afternoon of September 28, the DoLP dropped considerably below that of the clear afternoon of September 27. Late in the afternoon, these differences were not as substantial.

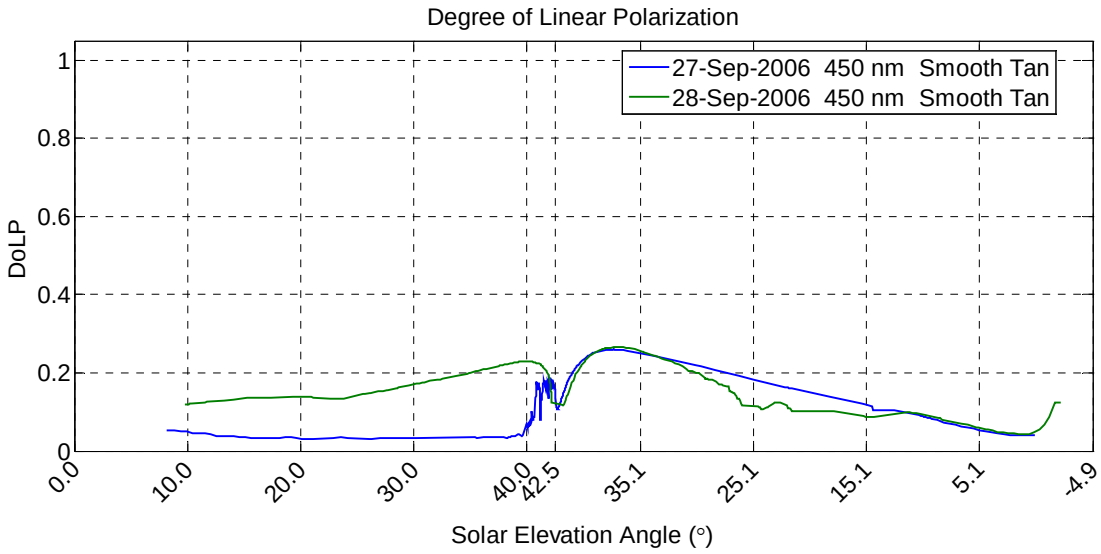

Figure 5.5. Degree of polarization comparison for the smooth tan plate at 450 nm on two days. September 27, 2006 (blue line) was cloudy and then clear, while September 28, 2006 was clear and then partly cloudy.

For the same plate at 630 nm, different effects are seen for the scattered clouds on the afternoon of September 28 (Figure 5.6). When clouds are introduced into the scene, the degree of polarization is up to 10% higher than the clear sky. Therefore, clouds do not necessarily always reduce the degree of polarization. Accurate modeling of the scattering and reflection are needed to better understand the problem. This work is beyond the scope of this research—which is to plainly show the differences of DoLP that can occur with different sky conditions.

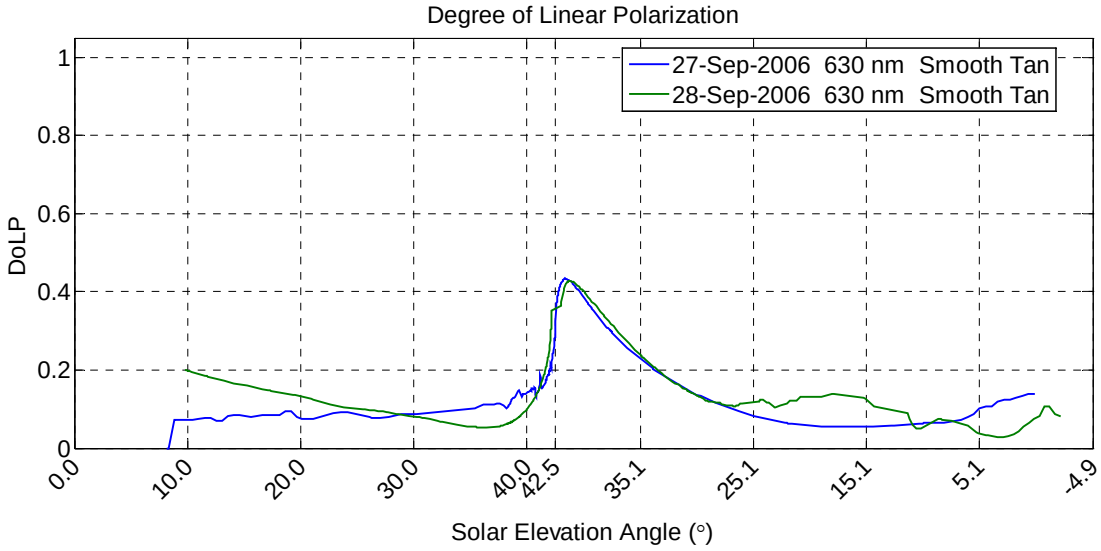

Figure 5.6. Degree of polarization comparison for the smooth tan plate at 630 nm.

Similar DoLPs to those at 630 nm were exhibited at 490, 530, and 700 nm (not shown), but with less variance between the two days. Another interesting feature is that the 450-nm DoLP has a dip near the 42.5° solar zenith angle, while the other wavelengths spike at this point. (Note: The flat spot in the September 28 data at this point is due to the sun not going as high as on September 27. There are no data available for solar elevation angles above 42° on September 28.) Without knowing the index of refraction of the paint,

this is impossible to model. Both wavelength dependence of the paint index of refraction and the large contribution of background polarized light in the blue end of the spectrum are probable causes for this dip. (The red end is dominated by the direct sunlight.)

Shadow Effects on Targets

On September 27, 2006, the 450- nm data exhibited strong spikes during the time that the clouds were breaking up (between 1200 and 1300 MDT). These spikes show the strong difference that can occur in the DoLP when the target is in the shadow of a cloud as opposed to in the direct illumination of the sun (Figure 5.7). This behavior was displayed by all the plates and is less severe for longer wavelengths. The blue end of the spectrum is most adversely affected by the target being in the shadow for a high solar elevation (Figures 5.7 and 5.8). At 450 nm, the cloud shadowing of the sun causes the DoLP to change by up to 13% from direct solar illumination, while at 700 nm, the shadowing only caused a 4% change from the direct illumination.

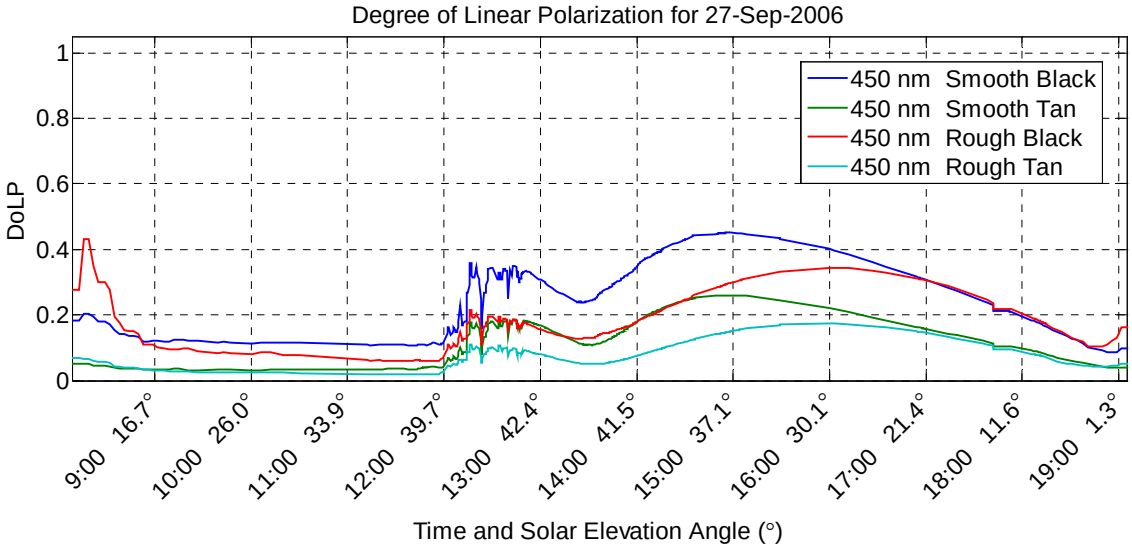

Figure 5.7. DoLP for all plates at 450 nm on September 27, 2006.

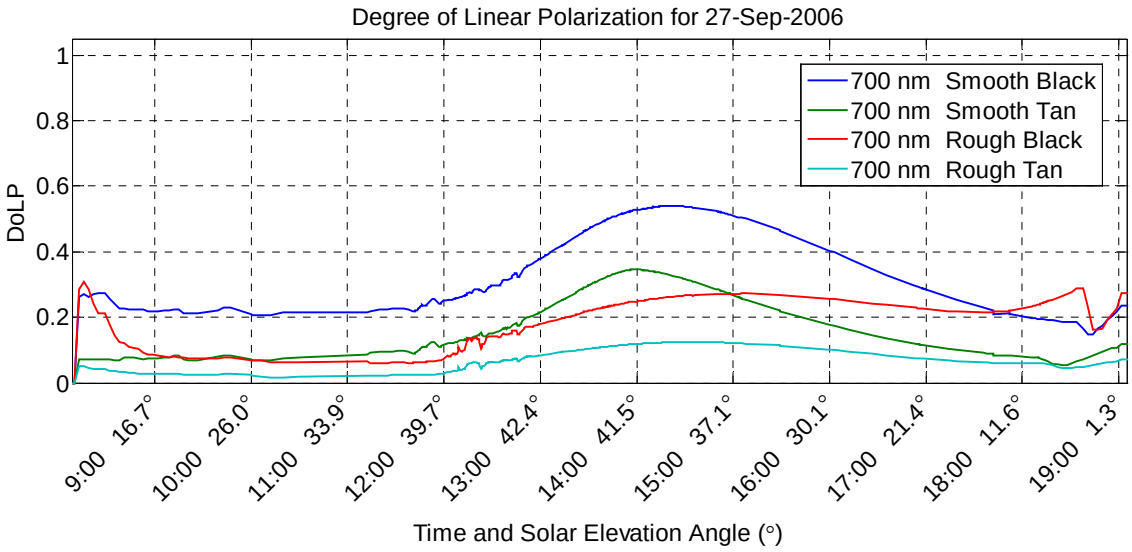

Figure 5.8. DoLP for all plates at 700 nm on September 27, 2006.

This behavior is also shown late in the day when the east railing of the building begins to shadow the plates from direct sunlight. This behavior is dominant at the longer wavelengths (Figure 5.9). At 450 nm, the shadow in the DoLP is barely visible since there is little direct blue light illuminating the target at sunset (Figure 5.10). Therefore, when the sun was high, cloud shadows affected the 450 nm DoLP, but when the sun was low, the railing shadows were insignificant at 450 nm. (It should be noted that all data in the above plots—Figures 5.3-5.7—are contaminated by the shadow effect after the sun moves below 9° of solar elevation. In the morning the plates were far enough away from the west railing that this was not a problem.)

These effects may cause large problems for aircraft surveillance during partly cloudy skies. Ground objects in cloud shadows will need to be treated differently from objects that are directly illuminated by the sun. This effect alone could possibly make

longer wavelengths more desirable for surveillance. For high altitude data collection, reduced scattering into the path at longer wavelengths should also make them preferred.

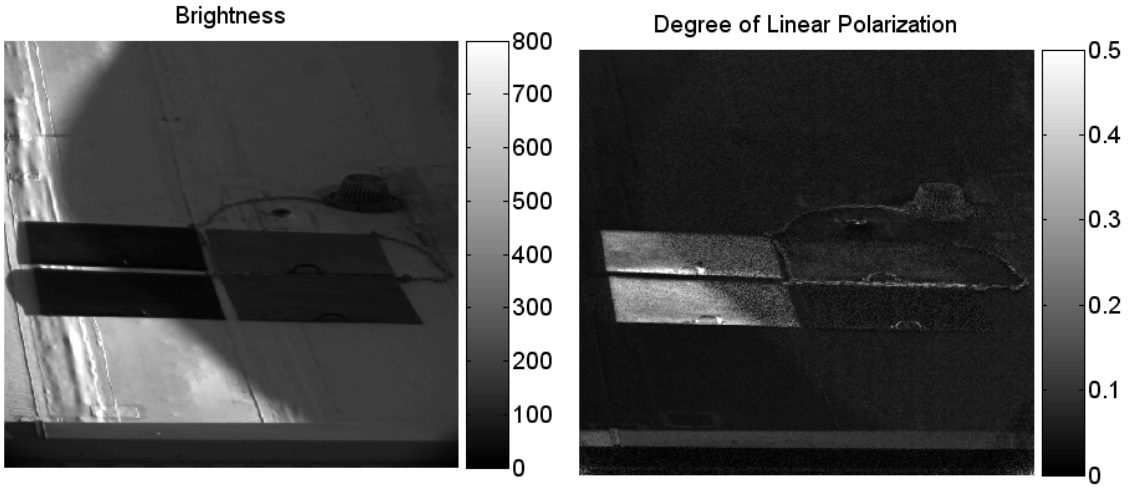

Figure 5.9. More pronounced shadow effect on the black plates (left-hand side) than on the tan plates (right-hand side) at 700 nm (Sept. 27 18:41 pm MDT).

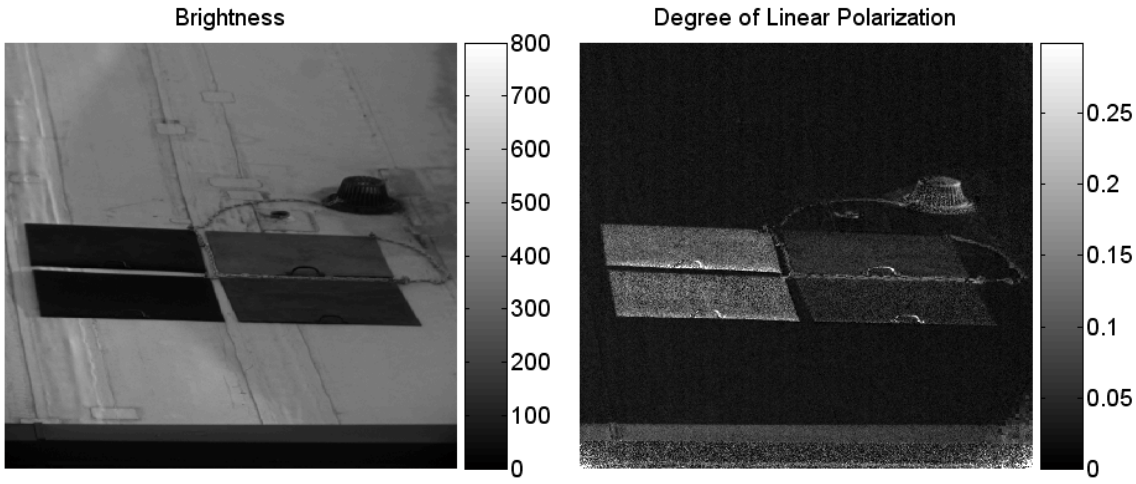

Figure 5.10. More pronounced shadow effect on the black plates (left-hand side) than on the tan plates (right-hand side) at 450 nm (Sept. 27 18:41 pm. MDT).

Dew Effects on DoLP

On the morning of September 28, dew formed on the penthouse roof and the

plates. The dew did not significantly affect the tan plate polarizations, but significantly affected the DoLP and AoP of the white roof. The black plates were also affected until they completely dried at 9:35 am MDT (22° solar elevation). Compared to a dry roof, the dew modified the reflective properties (Figure 5.11), the DoLP, and AoP (Figure 5.12).

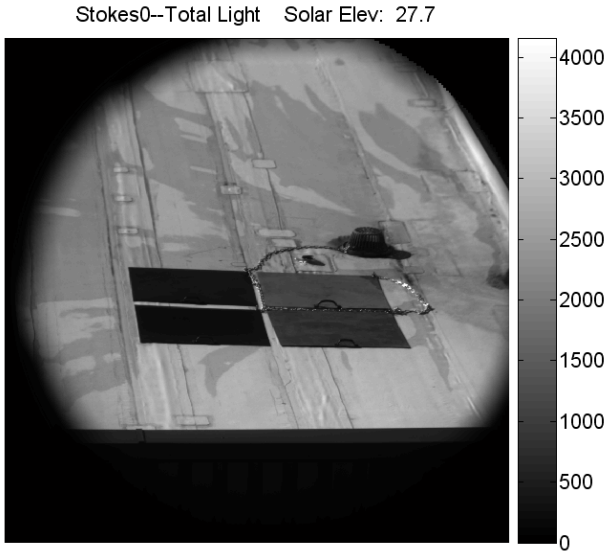

Figure 5.11. Brightness at 530 nm (September 28, 2006 10:13 am MDT).

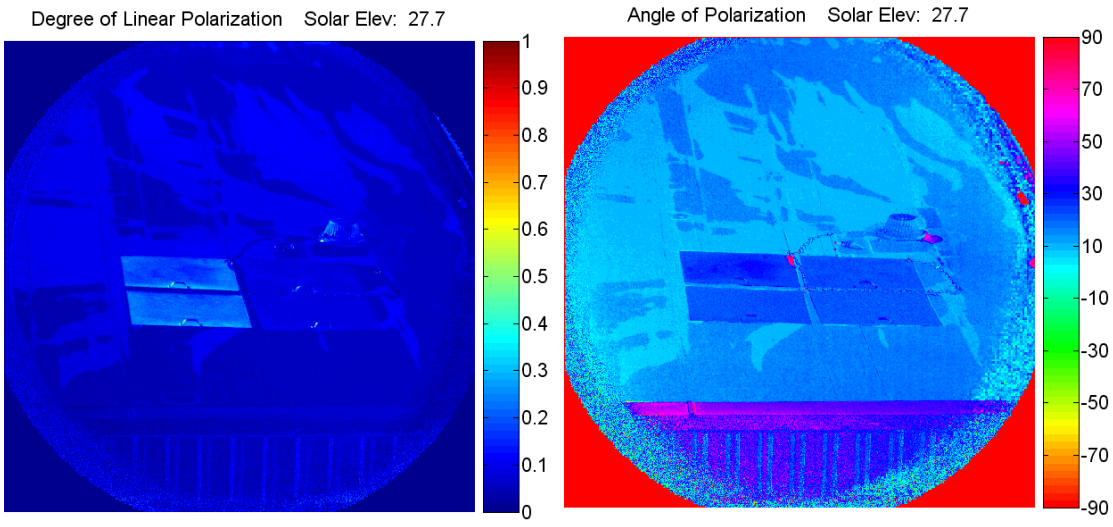

Figure 5.12. DoLP and AoP at 530 nm (September 28, 2006, 10:13 MDT).

The smoothing effect of the water caused the DoLP to jump considerably at all wavelengths. This also caused a change in the AoP, which is attributed to a different index of refraction for the water than for the roof material.

Conclusions – Effects of Changing Sky on Targets

1. Changes in the sky can affect targets by changing their DoLP upwards of 20%. For this data set, the changes in the target due to changing skies are slightly more pronounced for the shorter wavelengths than the longer wavelengths.
2. Sensitivity to clouds seems to be dependent upon many variables including solar zenith and wavelength. Clouds do not always cause higher or lower target DoLPs. Reduction of the DoLP depends on the solar zenith, and possibly other variables.
3. When the sun moves behind an object such as a cloud, the targets can change AoP and DoLP. For the surfaces measured, this effect was highly dependent on wavelength, but not target color or smoothness. For low sun elevations, the longer wavelengths were affected more by shadows. At these low solar elevations, little short-wavelength radiation comes from the direct illumination, so shadowing does not significantly change the illumination of the object. (This is seen by the near absence of the shadow in the brightness image of Figure 5.10.) For high sun elevations, the shorter wavelengths were affected more by shadows. This is expected since the scattered light at shorter wavelengths is a large fraction of the illuminating light. For the longer wavelengths, even when the sun is blocked, the majority of the illuminating light comes from forward scattering of the cloud particles, as little light is Rayleigh scattered.

4. Surface roughness reduces the DoLP. This is expected from the more random scattering of the surface.
5. Understanding target signatures requires knowledge of the index of refraction of the material, modeling the roughness of the material, and modeling sky illumination. It is not a trivial task.

FULL-SKY POLARIMETRIC MEASUREMENTS

Clear-Sky Polarization

For a given location, three primary variables affect sky Degree of Linear Polarization (DoLP): solar elevation (or zenith) angle, clouds, and aerosols. Each of these variables can reduce the DoLP from a Rayleigh atmosphere (the atmosphere described by a pure molecular column). Because of a varying amount of atmosphere above a location, the density of the molecular column can affect the DoLP. This is from the reduction of multiple scattering for a thinner atmosphere. Still, this effect is minor compared to the effects of the three primary variables, and does not change for a set location. Each of these variables is discussed at length below.

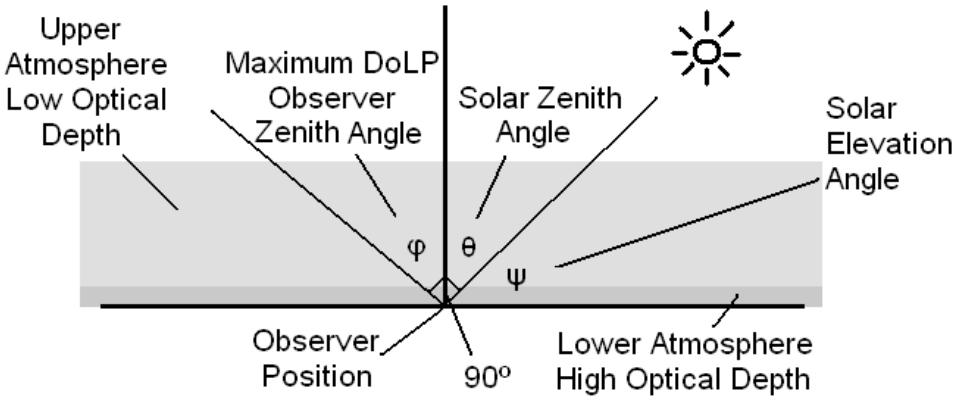

Figure 6.1. Relationship of solar zenith angle to the maximum DoLP observer zenith angle. Unscaled upper and lower atmospheres are shown to illustrate the increased optical depth of the observed atmospheric path in the direction of maximum DoLP as the solar elevation angle increases. (The lower atmosphere is shaded darker to indicate higher extinction, especially in the aerosol-laden boundary layer.)

Solar Zenith Angle Effects and Airmass Correction

Since the area of maximum degree of polarization is always ~90° from the solar position, changes in solar elevation angle throughout the day concurrently change the

maximum DoLP observer angle (i.e., as the sun rises higher in the sky, the region of maximum DoLP moves to larger zenith angles). As the maximum DoLP observer angle changes, the optical depth of the atmospheric column that is observed increases with the sun height (Figure 6.1). (Optical depth is a measure of the transparency of a medium. Reduction in transparency is caused both by scattering and absorption. Looking through an atmosphere with a high optical depth is difficult. For a low optical depth atmosphere, the atmosphere is nearly unnoticeable to the observer.) Since longer paths cause the light to experience more multiple Rayleigh scattering and more aerosol scattering before being observed, longer paths cause the DoLP to be reduced for higher solar elevation angles (Figure 6.2). For this reason, comparing measurements at the same time on different days is irrelevant due to dissimilar solar positions from day to day. All data comparisons between days must be made according to solar elevation angle.

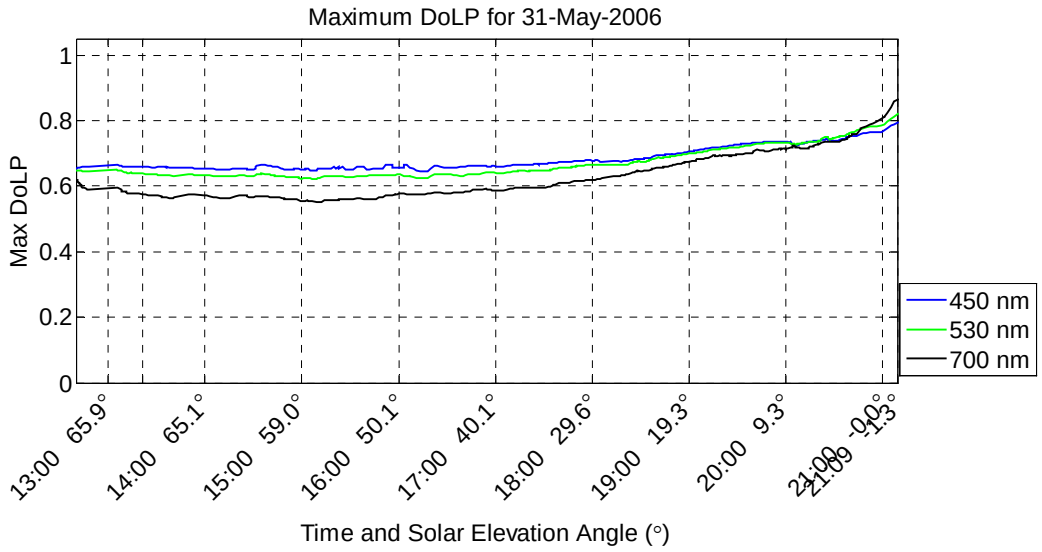

Figure 6.2. Effect of solar elevation angle on DoLP. The colors used to plot the wavelengths represent their actual color as perceived by a human observer. 700 nm is plotted as black since it is not visible to the human eye.

Although longer column length is one process that adds to multiple scattering, Coulson has shown that reduction of the DoLP at high solar elevation angles is exacerbated by the column illumination by molecules on the horizon below the region of maximum degree of polarization (Coulson, 1988). During mid-day the molecules on the horizon below the area of maximum degree of polarization are directly illuminated, so they contribute more to this multiple scattering. As the sun moves lower, these molecules become engulfed in the Earth's shadow, so they no longer contribute to the multiple scattering. Surface reflection from the horizon also is eliminated, so multiple scattering is at a minimum around sunrise and sunset. Therefore, at sunrise and sunset, the maximum degree of polarization is closer to the higher single-scatter approximation.

Still, a portion of the reduction in DoLP during the mid-day is caused by the increase in optical depth of the column. This effect looks very similar to the effect seen on the optical depth as the sun moves through different elevation angles. For solar radiometer measurements, optical depth readings are always adjusted from the measured optical depth to the zenith optical depth by dividing the reading by the secant of the solar zenith angle—also called airmass (see Equation 7.1). I investigated whether DoLP data could also be corrected by dividing by the airmass at the observer angle—which is ~90° from the zenith angle. This would give an effective DoLP that could be compared to DoLPs at sunrise and sunset. Figures 6.3 and 6.4 show the DoLP before and after the airmass correction.

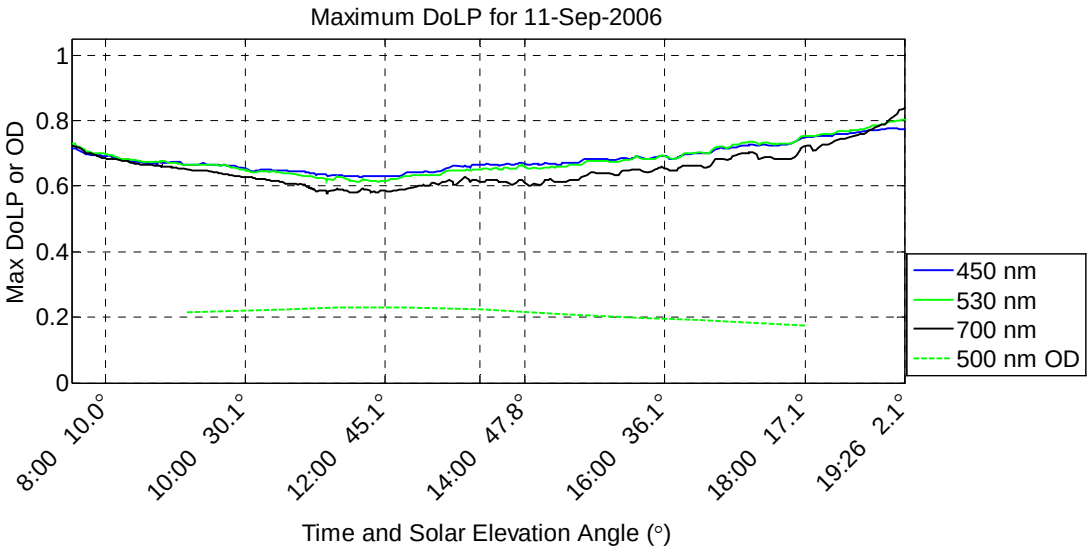

Figure 6.3. September 11, 2006 DoLP without airmass correction (the green dashed line at the bottom shows the 500-nm optical depth measured by a solar radiometer).

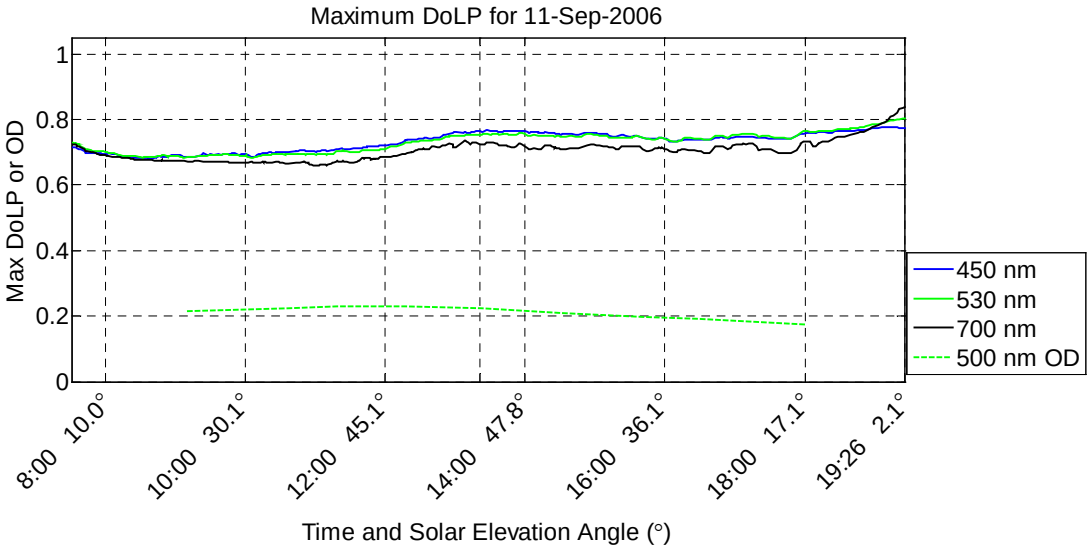

Figure 6.4. September 11, 2006 DoLP with airmass correction.

Although at first glance the correction seems to flatten the DoLP over the day, deeper analysis shows problems with the correction. First, near sunset the DoLP is still higher. This is expected as the earth shields more of the molecules below the horizon at

this time. The secant correction does not correct for this multiple scattering effect. Secondly, optical depth at the zenith does not seem to be highly correlated to DoLP after correction. For example, although the zenith optical depth is similar at 10:00 and 14:00, the corrected DoLP does not even closely match. Even worse, the original data seem to be more closely correlated to the optical depth (Figure 6.3, 530 nm). This suggests that the dependence of the maximum degree of polarization on path optical depth is not a significant variable for these high solar elevation angles (30.1 and 47.6° respectively).

These problems are explained by the fact that correcting the DoLP for the airmass is not as simple as correcting the solar radiometer optical depth for airmass. The optical depth depends only on the multiple scattering in and out of the direct path, while the DoLP is dependent upon the multiple scattering in the observing path and the illuminating path. Therefore, using an airmass correction does not provide any significant benefit compared to using the original data.

Aerosol Effects

The DoLP is very sensitive to the aerosol content of the atmosphere. These scatterers significantly reduce the DoLP. Figure 6.5 shows data for 3 days with widely varying optical depths. The aerosol optical depth (AOD) for September 25, September 11, and September 5 was roughly 0.05, 0.10, and 1.05, respectively.

The separation of 700 nm from the group for September 5, 2006 demonstrates the wavelength dependence of the effects of aerosols. Although aerosols tend to affect all wavelengths similarly, there is a wavelength dependence of the magnitude of DoLP reduction. This reduction appears to depend on aerosol type and size distribution. Also,

notice that when compared to sunset data, the mid-day 700-nm DoLP remained higher than the other wavelengths, yet for lower optical depths it always moved lower during the mid-day. The cause of this difference may be unrelated. For the low aerosol days, the drop of the 700-nm DoLP below that at shorter wavelengths is attributed to the fact that Rayleigh scattered light falls off with wavelength. For any wavelength, the polarization measured is a merger of the highly polarized light from the upper atmosphere and the lower polarized light from Mie scattering in the aerosol-laden boundary layer. Since very little light is Rayleigh scattered at 700 nm, the increase of the observed optical depth, especially in the boundary layer, as the sun moves higher in the sky causes the 700-nm DoLP to be more affected by the aerosols than the DoLP at shorter wavelengths. For high aerosol days, the polarization signature is dominated by both single and multiple aerosol scattering in the boundary layer. Polarization effects are highly dependent upon the Mie scattering phase function of the aerosol type and size distribution. Therefore, the fact that the 700-nm DoLP is higher in this case could possibly be a chance property of the forest fire aerosols present. For other aerosols, the 700-nm DoLP could possibly be lower than at shorter wavelengths.

Also, notice that as the optical depth approaches zero, the degree of polarization does not approach 100%. Multiple scattering of the molecular column reduces the DoLP even for an aerosol-free sky. Previous investigators have taken readings of the DoLP for the cleanest skies in the world, such as at Mauna Loa, Hawaii. Several papers show that the maximum degree of polarization measured at 700 nm never exceeds about 87% at 3° solar elevation in these clean skies (Coulson, 1983; 1988). In fact, multiple scattering,

molecular asymmetries, and the random distribution of particles will cap the DoLP at ~94% for the cleanest atmosphere (Bohren, 1996). My data taken during the clearest days of September 25 and May 31, 2006 found maximum degree of polarization values of about 88% at 700 nm for 3° solar elevation. Considering that the instrument has an error estimate of ±3%, the data taken in Bozeman is not unreasonable--although it does seem impressive that Bozeman occasionally reaches the level of purity as found at Mauna Loa. (For this instrument, data beyond about -2° of solar elevation is too noisy to be trusted. To create a buffer, 3° was taken as the minimum reliable solar elevation for a clear sky.) To obtain reliable data at lower solar elevation angles, much wider bandpass filters are necessary to provide a stronger signal on the detector.

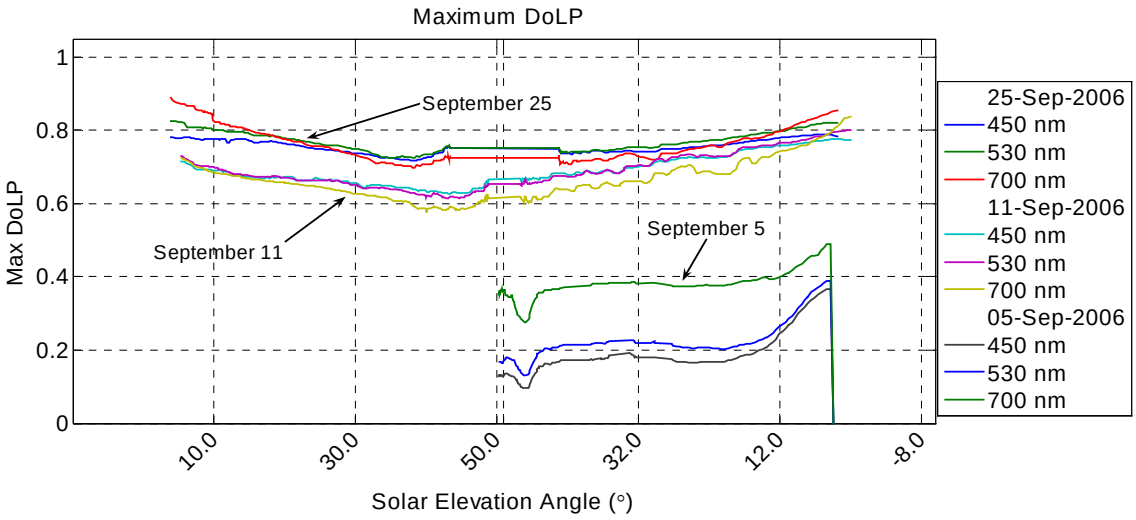

Figure 6.5. Effect of aerosols on DoLP.

Cloud Effects on Polarization

Clouds severely reduce the degree of polarization since the intense multiple scattering in them causes them to look like large unpolarized sources. Figure 6.6 shows

an example of what a cloud will do to the DoLP. In fact, when looking at a thick cloud, typically the only measurable DoLP is the Rayleigh scattered light between the observer and the cloud.

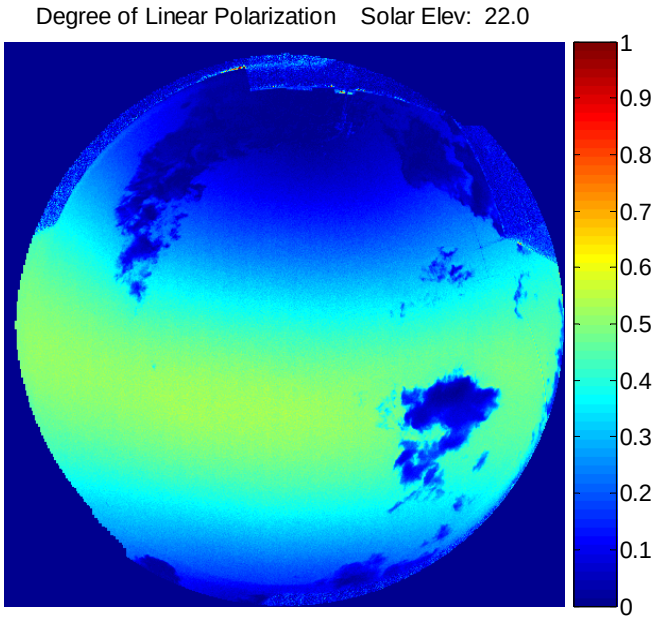

Figure 6.6. Example of cloud effects on DoLP at 450 nm. The clouds appear as largely unpolarized sources that reduce the otherwise relatively highly polarized skylight.

Because MODTRAN-P is a single point code, it does not model anything outside of the scattering geometry of the observed column of air. The effects of clouds (or clear sky) in other areas of the sky upon the observed column are totally ignored in the model. This generates two important questions concerning the viability of the sky to be modeled by a single-point code such as MODTRAN. (1) Will clouds in a partially cloudy sky affect surrounding clear sky polarization? Since these clouds act as unpolarized sources in a similar yet reduced magnitude as the sun, they will cause the reduction of the degree of linear polarization. An important sub-question is, how significant is this reduction? (2) How much will the polarization measured looking at one cloud be affected by the

presence of clouds around it? If either of these issues is significant, then MODTRAN-P may need to be modified to account for these effects. The second question will be addressed first.

Overcast-Sky Polarization

For all overcast skies that have clouds thick enough not to allow the light above the cloud through, the DoLP is zero within the error margin of the instrument. Figure 6.7 shows an overcast sky on April 11, 2006 at 18:00 MDT for 700 nm. Notice that, with the exception of some slight (<2%) DoLP that is generated by errors in the fisheye lens Mueller matrix, the DoLP of the entire sky is zero. The buildings on the top and right of the image are slightly polarized. The clouds act as a uniform source from all directions, thereby eliminating any polarization from Rayleigh scattering. This is consistent for all wavelengths.

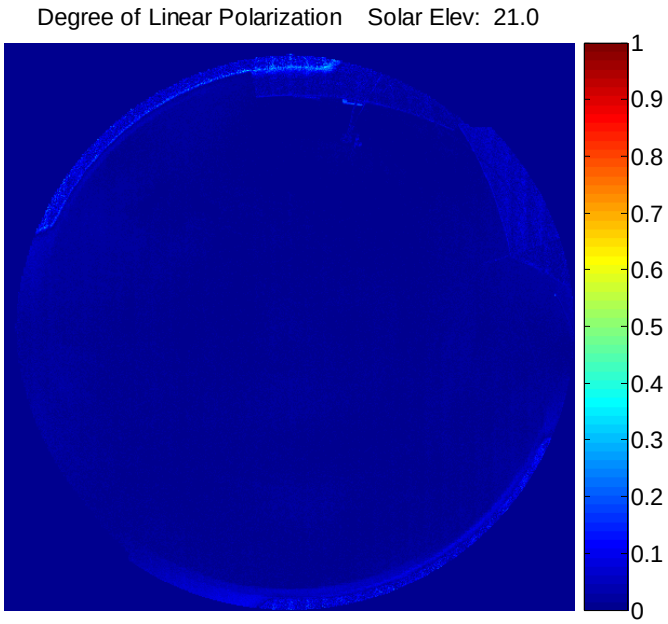

Figure 6.7. DoLP for an overcast sky.

Partially Cloudy Sky Polarization

For skies that are only partly cloudy, the measured polarization is dependent on both the thickness of the cloud and whether or not the column below the cloud is illuminated directly by the sun. If the cloud is thin, polarized light from scattering above the cloud is seen by the instrument. If the column below the cloud is not illuminated directly by the sun, the illumination of the column from other clouds and the sky will reduce DoLP underneath the cloud. Significant DoLP can only be generated by illuminating the column primarily from one direction. For an overcast sky with optically thick clouds, the most extreme scenario occurs and the DoLP is zero. The question of greatest interest is: For a thick cloud surrounded by clear sky, how much polarization is generated below the cloud? To answer this question, a thick cloud must first be found. For all cases, only clouds that had nearly zero polarization at 700 nm were considered to be thick. Since Rayleigh scattering falls off with wavelength, very little light at 700 nm is scattered into the path between the cloud and the observer. It has been observed in the data that the DoLP can be nearly zero at this wavelength. Using this as a criterion, a thick cloud can be found. Once a cloud is found, the DoLP generated at 450 nm under the cloud was analyzed.

For the first example, a mid-day DoLP value was analyzed. Figure 6.8 shows the cloud in the band of maximum polarization. Only areas where the DoLP for the 700-nm wavelength was effectively zero were considered. The 450-nm DoLP was as high as 4% in these areas (Figure 6.9).

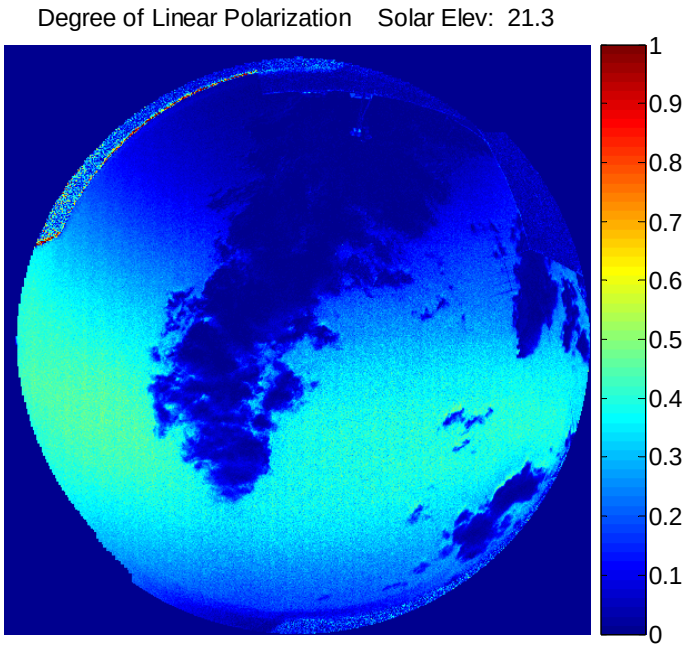

Figure 6.8. DoLP for a cloud using the fisheye April 27, 2006 18:17 MDT at 700 nm.

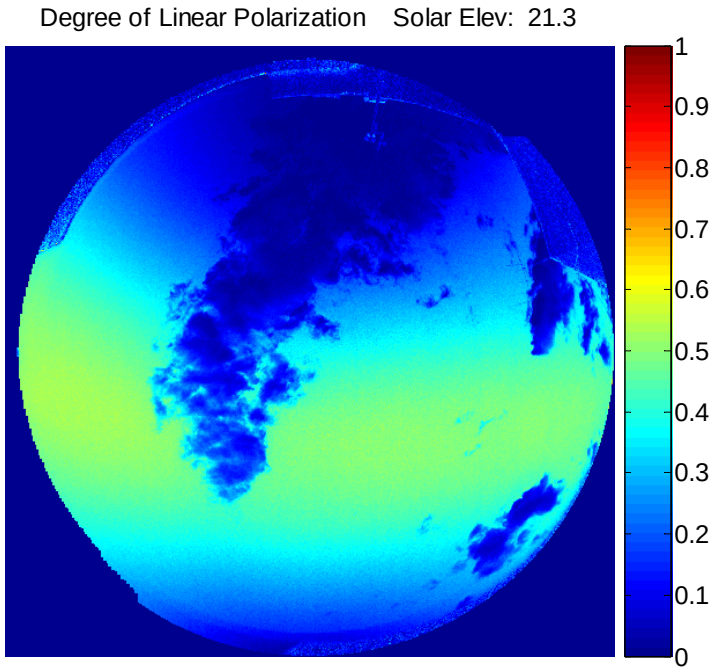

Figure 6.9. DoLP for a cloud using the fisheye lens on April 27, 2006, 18:17 MDT at 450 nm.

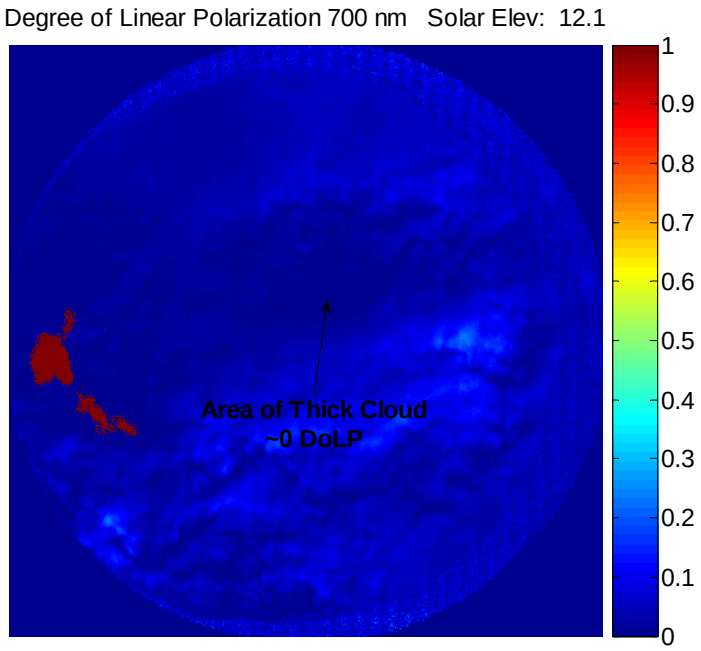

Figure 6.10. DoLP for a thick cloud observed with the telephoto lens on October 20, 2005 at 700 nm. The areas of red on the left side of the 700 nm data show an area of over exposure.

One factor that cannot be ignored is the brightness of the cloud. If a cloud is extremely bright, it will effectively reduce the DoLP much more than a very dark cloud. For this reason, several cloud pictures were inspected to find clouds with the highest DoLP. Using telephoto lens data from October 20, 2005, some large DoLPs were found below clouds at 450 nm. One case is shown in Figures 6.10 and 6.11.

For the images shown in Figs. 6.10 and 6.11 clouds fill the entire image. In reality, the entire sky was partially clouded. For these low solar elevation angles, the sun directly illuminated the column underneath the cloud. In the 450-nm image (Fig. 6.11), the area of the thick cloud is not physically in the same place as the 700-nm image owing to the ~25 seconds between the two images. Although this DoLP may not be considered

to be an absolute maximum for the amount of DoLP generated underneath a cloud, it does show that significant DoLPs of at least 15% are possible.

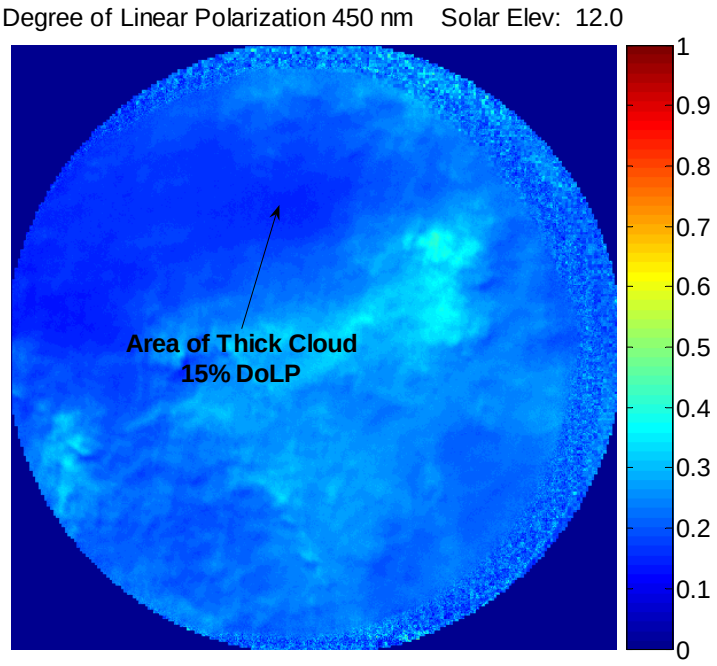

Figure 6.11. DoLP for a thick cloud observed with the telephoto lens on October 20, 2005 at 450 nm.

Using the minimum polarization in each image finds the spots with the thickest clouds. Since many images are taken successively, the minimum in each 700-nm image will be in either the 450-nm image that precedes or follows it. Therefore, a plot of successive minimum DoLP measurements for all three wavelengths shows the amount of polarization that can be generated underneath a thick cloud (Figure 6.12). Thick clouds have near-zero 700-nm polarization.

For 450 nm, the cloud polarization under the thick cloud areas—places where the 700-nm line is near zero—seems abnormally high. This suggests that the calibration might be suspect. This suggestion is improbable, however, because the two clear-sky

areas on both the left and right edges of the plot compare well to previous clear-sky data. In fact, the data seem lower than typical clear-sky data for a sky of low aerosol content—not higher. The probability of thin clouds even in the clearest portions of the sky makes this expected. Therefore, the calibration problem explanation is not reasonable.

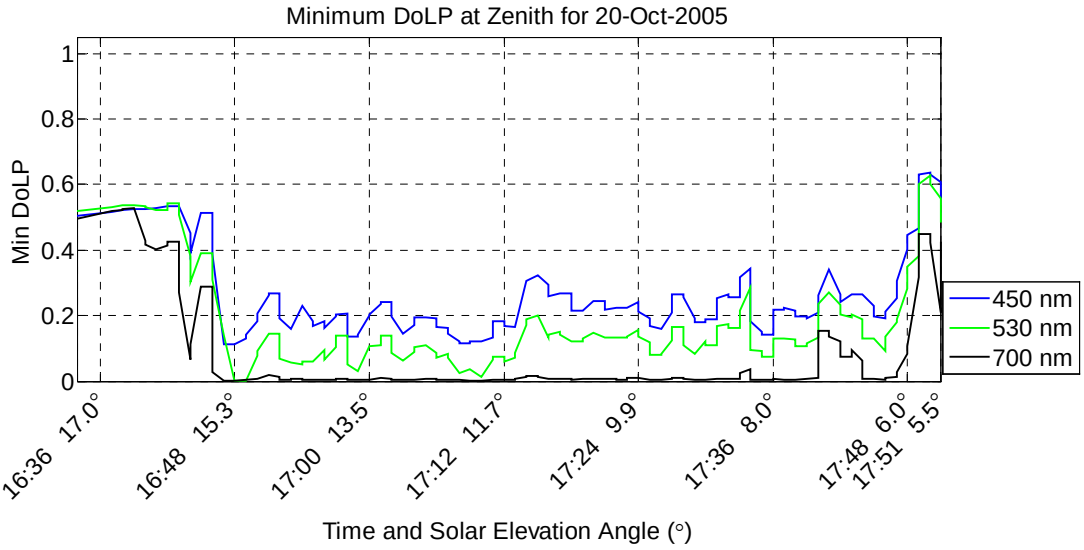

Figure 6.12. Minimum DoLP at zenith using the telephoto lens on the afternoon of October 20, 2005.

When only the areas where the 700-nm DoLP is near zero are considered, the DoLP at 450 nm is as high as 23%. DoLPs at 450 nm of this magnitude for thick clouds were never reproduced in any subsequent data—although this was the only set that used the telephoto lens. Most DoLPs generated under thick clouds measured by the fisheye lens were near 5-6% at 450 nm. The wider field of view of the fisheye does reduce the resolution to a point where the thickest cloud areas may not be seen. Local shadowing of the areas under the clouds can cause small parts of the cloud bottom to be dark and thus have a higher DoLP. Some of these areas could be missed by a combination of the lower resolution of the fisheye and the 9x9 median filtering used to reduce noise in the

minimum DoLP. Without reasonable explanation for the irregularity, it is determined that the 450-nm DoLP generated under clouds can rarely reach upwards of 22%.

Effects of Clouds on Surrounding Clear Sky

It is clear from the above section that the partially cloudy skies have different DoLPs than skies that are completely overcast, but what about the opposite problem? Specifically, do clouds reduce the degree of polarization in clear-sky portions between the clouds? To further understand the question, it is helpful to think of the clouds as sources—just as the sun is a source—that illuminate the column of air above the observer. To understand the degree of polarization, the observer must understand where the light illuminating the column is coming from. For a clear sky, the sun is the primary illumination source of the column above the observer. Each molecule in the column scatters light from the sun back to the observer (Figure 6.13). Although the sun is the primary source, other molecules and aerosols can also scatter light from the sun, which is again scattered by the column. This minor contribution is called multiple scattering.

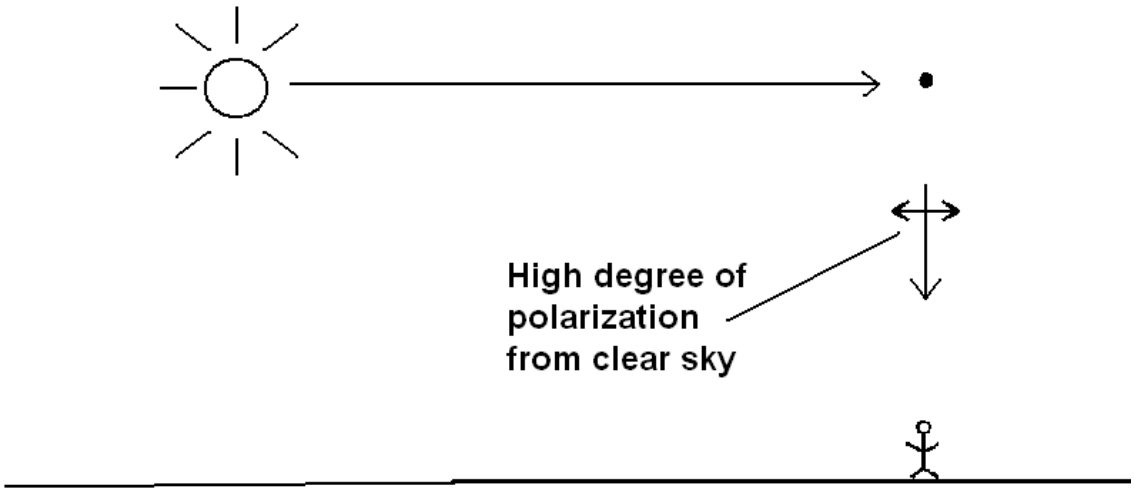

Figure 6.13. Clear-sky scattering from sunlight only.

Since clouds are scattering sunlight, they are a more extreme form of multiple scattering. Because of their size and optical depth, clouds cause much brighter multiple scattering than small aerosols and molecules. For this reason, it is helpful to view them as extra-solar illumination sources. These sources reduce the DoLP since their illuminating light is coming from different directions than the sun (Figure 6.14). Since clouds are much dimmer than the sun, these effects are small enough that they never completely wipe out the polarization generated by the sun, but the degree to which they reduce the DoLP is a mystery. The question is: How much do clouds affect the degree of polarization in the clear-sky areas between them?

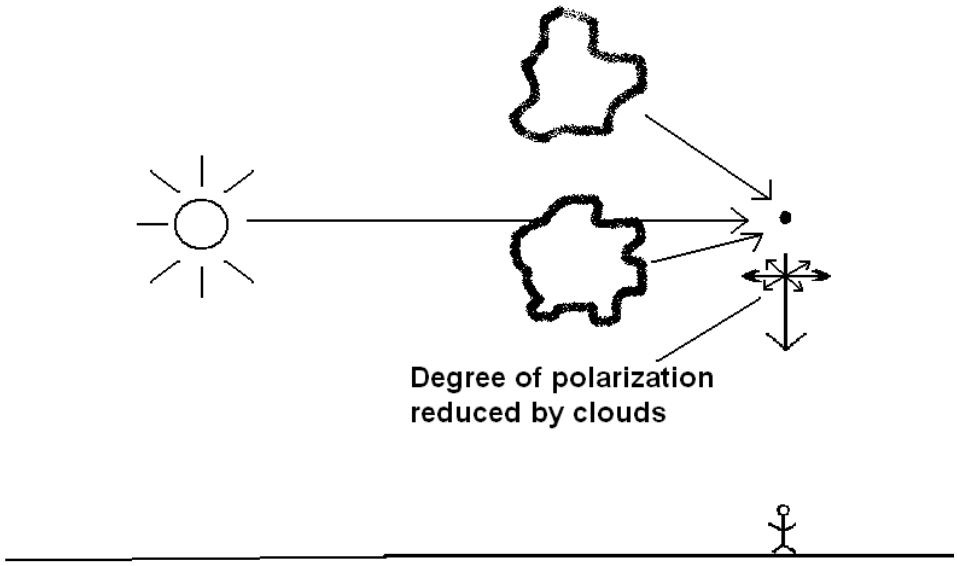

Figure 6.14. Reduction of clear-sky degree of polarization by clouds.

Because of its full-sky capability and short acquisition time, the polarimeter described here is uniquely suited to study this problem. Because of instrument limitations, previous investigators were confined to either single-pixel measurements of the sky or full-sky images of only clear skies. This instrument can measure skies with

moving clouds at full-sky resolution. Several images of the effects of clouds have been taken over the 2006 summer. Consistently these images have shown that the degree of polarization is severely reduced in the areas of the sky between the clouds. Examples of this are shown in Figures 6.15 and 6.16. The large cloud on the left of the June 23 image is over the Bridger mountain range, while the small scattered clouds to the right are forming over the Gallatin mountain range. In both images, it is clear that the maximum degree of polarization is much lower in the clear center area when clouds are present (left image) than when clouds are not present (right image). Also, this example illustrates a feature that is common to all the partially cloudy data: The 700-nm DoLP is reduced more severely than the 450-nm DoLP. Since aerosols have a large effect on the degree of polarization, it is reasonable to ask: Were the aerosols similar on both days?

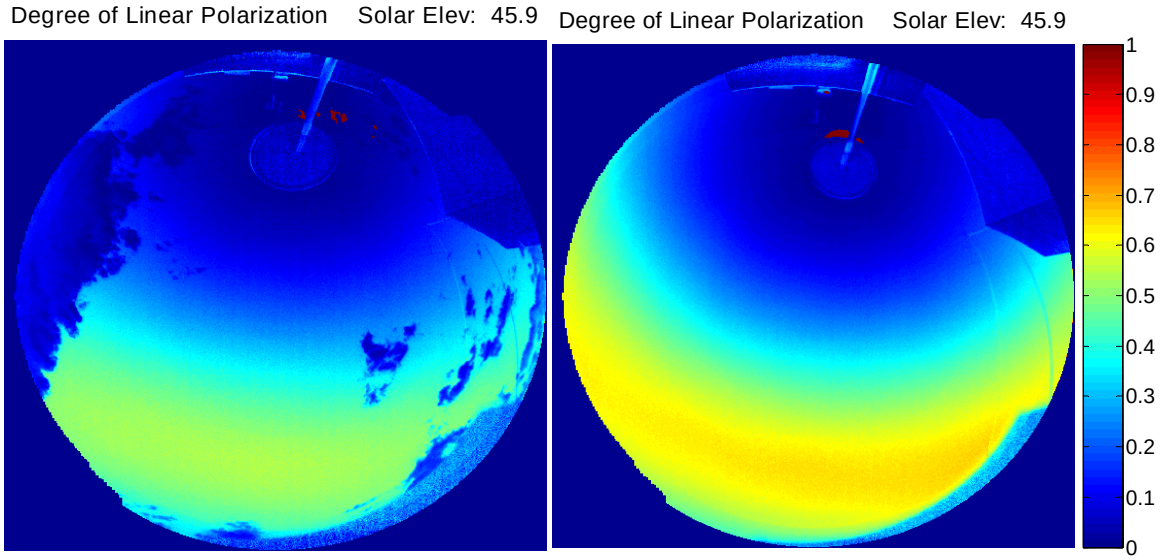

Figure 6.15. Comparison of a partly cloudy sky on June 23, 2006 (left) at 16:36 MDT and a clear sky on June 26, 2006 (right) at 16:36 MDT (450 nm). Areas in red are overexposed.

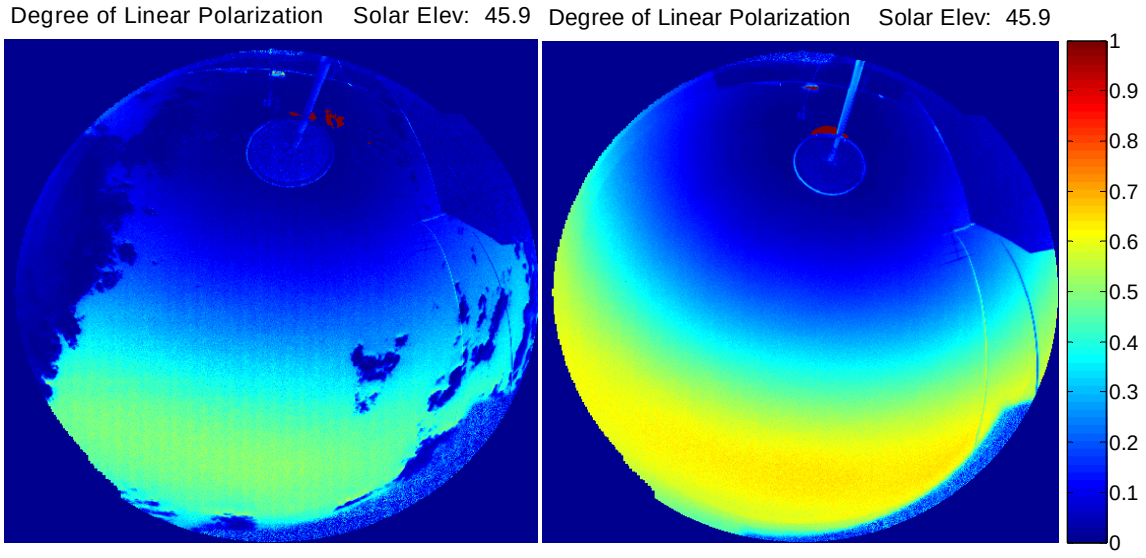

Figure 6.16. Comparison of a partly cloudy sky on June 23, 2006 and a clear sky on June 26, 2006 (700 nm).

Aerosols were expected to be similar for June 23 and 26 for two reasons. First, there were no significant aerosol events, such as forest fires, in the area at the time. Second, although solar radiometer data were unavailable for either day, it is reasonable to assume that the optical depths were similar because the degree of polarization in the morning of both days was nearly identical (Figure 6.17-19). Since aerosols rarely change quickly in areas (without significant industrial sources) that do not have a strong aerosol event, it is assumed that the aerosols did not significantly change between the morning and the afternoon (furthermore, the measurements were taken from within the boundary layer, so diurnal variations of boundary layer thickness should not be a significant contribution). (September 11 is shown for comparison to June 26. Although the optical depth in the afternoon is dropping—causing the maximum DoLP to be slightly lower—both the morning and evening of September 11 compare well to June 26. The difference between these days gives a reference to how well two clear skies with similar optical

depths will track each other.) Notice that June 23 has some special features. First, it has a clear-sky region for most of the morning that compares well to both June 26 and September 11, 2006. At some point near the time of maximum solar elevation (65.7°), the maximum DoLP begins to drop significantly. Then, around 41° solar elevation angle (16:30), large clouds move into the sky. These clouds cause a large drop in the maximum degree of polarization between the clouds (Figure 6.17-19). This is most pronounced for the 700-nm wavelength (Figure 6.19)—as was seen in Figures 6.15 and 6.16. Finally, after the majority of clouds clear the sky at 31° solar elevation angle (18:00), the maximum degree of polarization increases but remains significantly lower than both September 11 and June 26. From 31° to 16° (18:00 to 19:27), the sky is clear in most images, but a few small clouds are seen sporadically. Since aerosols are an unlikely cause, the reduction of the maximum DoLP during the late afternoon is likely caused by something other than aerosols.

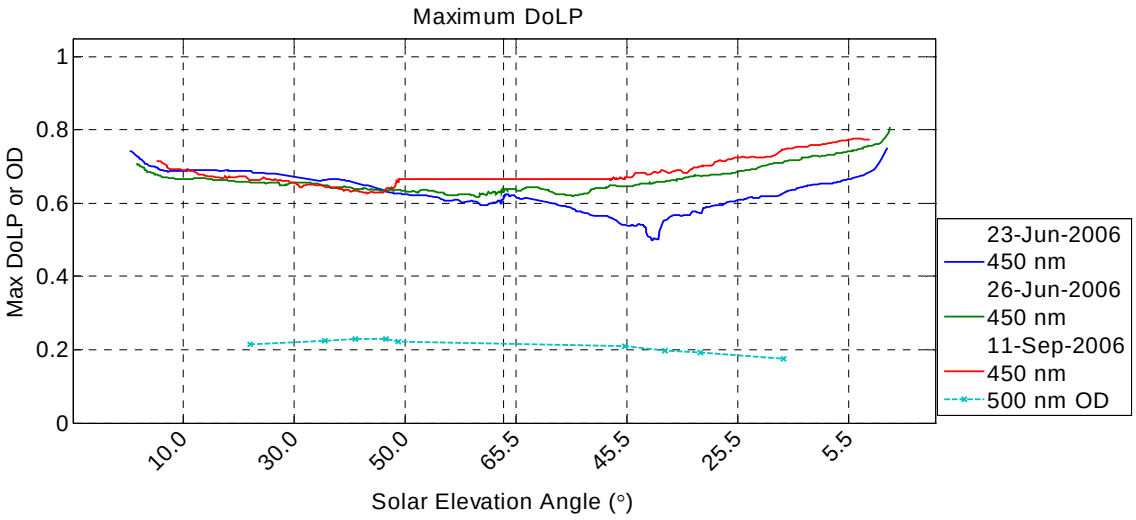

Figure 6.17. Maximum degree of polarization for June 23, 26 and September 11, 2006 at 450 nm. The extra x-axis hash shows the maximum solar elevation for June 23.

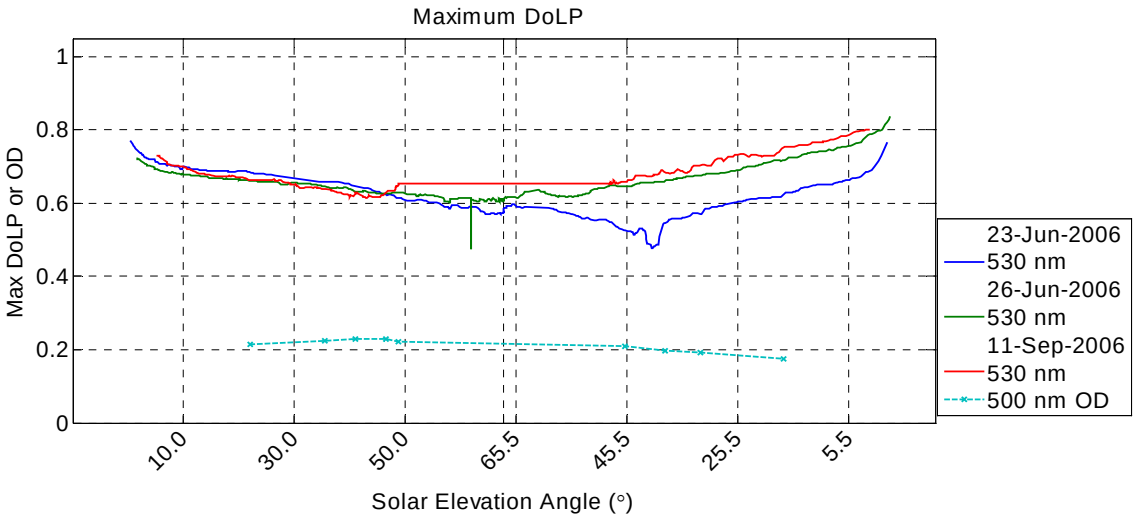

Figure 6.18. Maximum degree of polarization for June 23, 26 and September 11, 2006 at 530 nm. The flat spot in the September 11 data occurs where the sun never attained that height. The extra x-axis hash shows the maximum solar elevation for June 23.

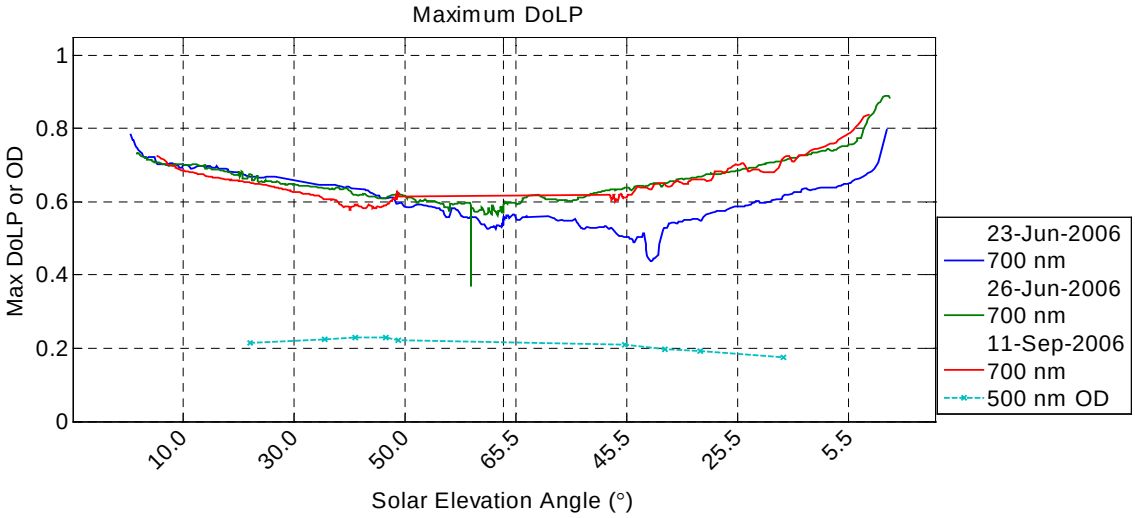

Figure 6.19. Maximum degree of polarization for June 23, 26 and September 11, 2006 at 700 nm. The flat spot in September 11 data occurs when the sun never attained that height. The extra x-axis hash shows the maximum solar elevation for June 23.

It is clear from the data that the large clouds are highly correlated to a drop in the degree of polarization in the surrounding clear sky. The reason for this reduction is not as clear. Look at the late afternoon data. Observations during this time and inspection of the

images show few clouds. Still, the maximum degree of polarization is considerably lower than for September 11 and June 26. Since changing aerosols are not likely the primary origin for this reduction, cloud droplets that are beginning to form on the aerosols are the probable cause of the reduction. These droplets—though not visible to the naked eye—significantly affect the polarization. (In fact, since cloud droplets grow on the aerosols, it begs the question: What is a cloud and what is an aerosol?) This conclusion is supported by the presence of the few small clouds between elevation angles of 31° to 16° (18:00 to 19:27). These clouds are just large enough to become visible. This conclusion is also supported by the reduction of the maximum degree of polarization before the clouds are visible in the mid-afternoon. Cloud droplet formation is beginning as the sun moves below 60°, long before the observer perceives clouds.

Therefore, the question must be asked of a partially cloudy sky: Is the sky between the clouds really clear? Although, the sky appears to be clear, this could possibly be a false perception. Thin clouds could be causing the reduction of the DoLP. Therefore, it is uncertain whether the DoLP reduction is caused by either large clouds acting as illumination sources or by thin sub-visual clouds in the apparent clear sky region. Therefore, the optical depth between the clouds needs to be known. For a clear sky, the atmosphere is fairly homogenous. The optical depth measured by a solar radiometer can give an accurate estimate for the whole sky. For obvious reasons, when clouds are present, solar radiometer data cannot predict optical depths across the whole sky. For thin cloud droplet layers seen between the clouds, the same spatial variability problem occurs. To attack this problem, a method of measuring optical depth away from the path to the

sun is needed. The best resource for this measurement is a calibrated and steerable LIDAR that can measure extinction. This LIDAR would need the capability to be scanned between clouds. Such instrumentation is not currently available at MSU, but may be available eventually. Until this instrument is available, it will be impossible to separate the portion of the reduction in DoLP that comes from the illumination of the column by the nearby clouds from the portion that comes from increased optical depth between the clouds. An exact cause for the DoLP reduction is uncertain.

In spite of the difficulties in producing an exact answer to the cause of the DoLP reduction, it is concluded that clouds are highly correlated to a decrease in the degree of polarization between the clouds. One important outcome of this research is the fact that sensors that are used to look down at ground objects through partly cloudy skies will be affected by this reduction of DoLP. The same process that reduces the DoLP between the clouds while looking up will likely reduce the DoLP of a target viewed by a down-looking surveillance instrument. Surveillance aircraft will not be able to look between clouds in a partially cloudy sky without taking into account path scattering between the target and the sensor. Even if other factors are ignored, ground-target signatures will vary considerably between a measurement taken during a clear sky and a measurement taken between clouds in a partially cloudy sky.

Clouds with non-Zero Polarization

As was seen in the *Partially Cloudy Sky Polarization* section, any measurable DoLP seen when looking at a thick cloud normally reflects only Rayleigh scattering between the cloud and the observer. For the shorter wavelengths, this is much more

pronounced. The Rayleigh scattering into the path overcomes any polarization that a cloud exhibits. Therefore, the angle of polarization (AoP) seen is identical to that of a clear sky, but the bright cloud at the end of the observation path reduces the DoLP (Figure 6.20-21). Notice that in most areas of the sky, clouds are not even visible in the AoP image. (Areas in black mask areas where the DoLP is under 1%. Since the AoP of unpolarized light is not defined and calibration errors in the fisheye matrix cause errors in the AoP for low DoLP values, these areas show places where the AoP data are unreliable.) At longer wavelengths, Rayleigh scattering into the path is minimal. Although the DoLP of the cloud at 700 nm is very low (<5%), the AoP image shows that the polarization angle for some clouds is different than the Rayleigh scattering in the adjacent clear sky (Figure 6.21). Since a completely unpolarized cloud would reduce the DoLP but not change the AoP, this polarization must come from the scattering of the cloud particles themselves. These data show that clouds themselves can scatter partially polarized light. The typical value of this light is less than 5% DoLP. One possible explanation is the presence of ice crystals in the cloud, which would reflect light in ways described by the Fresnel equations. If these crystals are well organized, they could cause measurable DoLPs. For the day in question, this explanation is suspect, since the outside temperature was 23 °C. With a typical lapse rate of 7 °C/km and cumulus cloud heights of 3 km, the cloud bottom probably was not below freezing. Even if it was a higher cloud, it would be expected that the cloud would super cool before freezing. A more likely cause of this DoLP is Mie scattering polarization.

For any single scattering geometry, the scattering plane includes both the direction of incidence light and the direction of the scattered light. For scattering by particles much smaller than a wavelength, the scattered light will always have a polarization that is perpendicular to the scattering plane. For larger particles, Mie theory predicts that the single-scattered light is polarized in one of two directions: either parallel to the plane of scattering or perpendicular to the plane of scattering. Multiple scattering models have shown little departure from the single-scatter case (Kattawar, 1972). For a line of observation to a cloud, every particle in the line of sight (LOS) will have the same scattering plane, because the plane includes the observer's LOS and the sun. Therefore, all measured polarization angles will either be parallel or perpendicular to this plane.

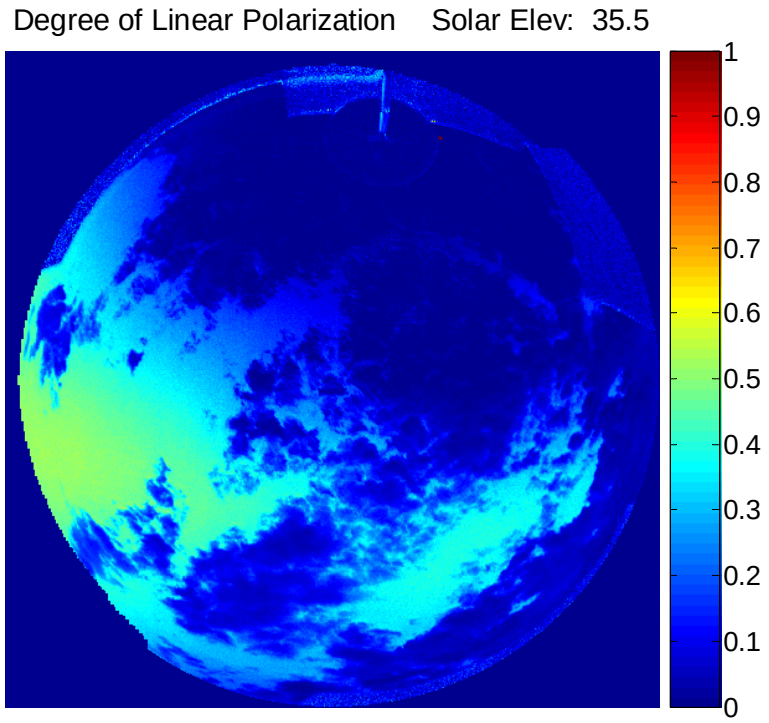

Figure 6.20. DoLP for a cloudy sky on May 24, 2006 at 17:21 MDT (450 nm).

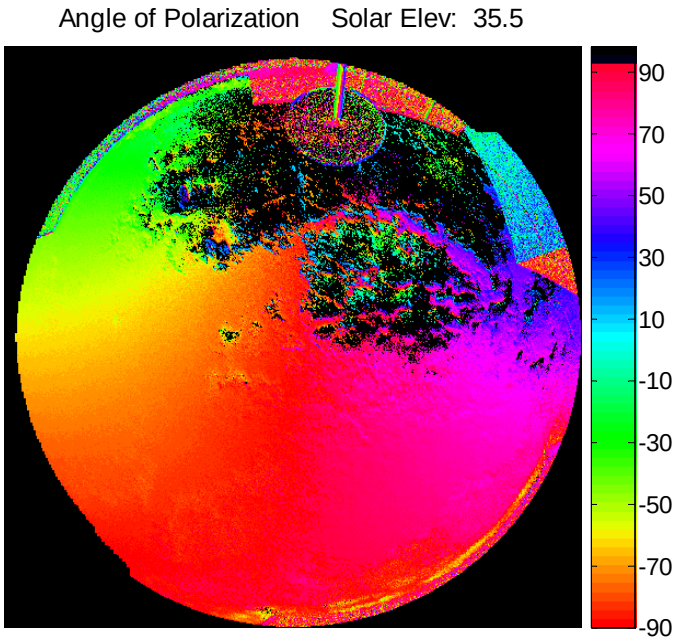

Figure 6.21. AoP for a cloudy sky on May 24, 2006 at 17:21 MDT (450 nm). Areas in black show areas where the AoP data are unreliable owing to a combination of the AOP being undefined at DoLP = 0 and calibration errors. Areas in black show places where the DoLP is lower than 1%.

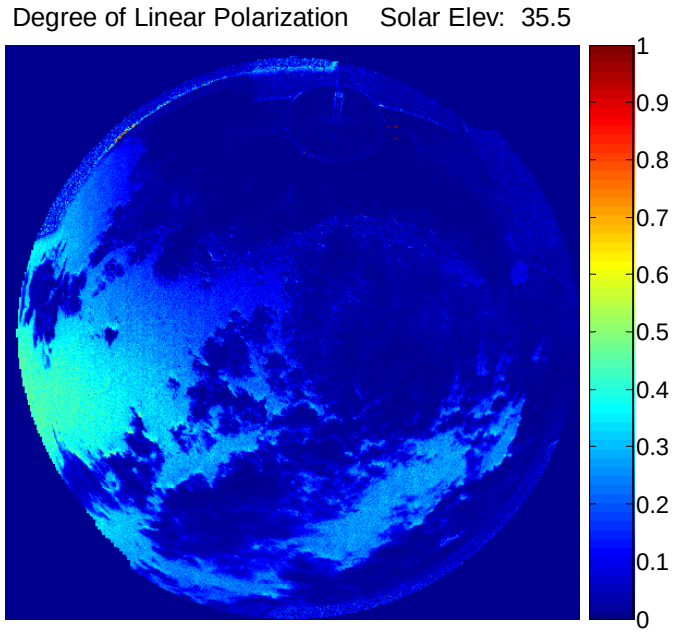

Figure 6.22. DoLP for a cloudy sky on May 24, 2006 at 17:21 MDT (700 nm).

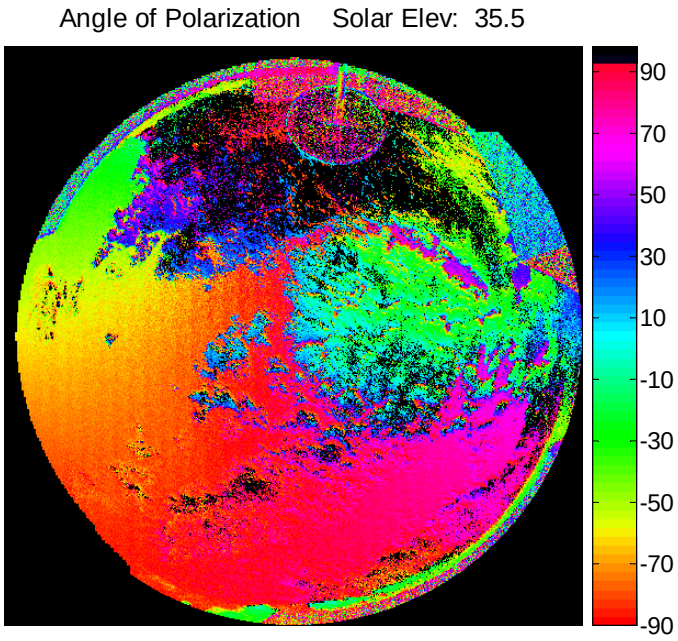

Figure 6.23. AoP for a cloudy sky on May 24, 2006 at 17:21 MDT (700 nm).

Therefore, the observer sees three primary types of scattering light: (1) The Rayleigh scattering between the observer and the cloud, which is always polarized perpendicular to the scattering plane; (2) the multiple-scattered light from the cloud droplets, which is primarily unpolarized; and (3) the single-scattered light from the cloud droplets which can either be polarized in a perpendicular direction to the scattering plane or in a direction parallel to the scattering plane.

If the single-scattered light from the cloud droplet is perpendicular to the scattering plane, it is in the same direction as the Rayleigh scattering. For this case, the angle of polarization image will look the same as the clear sky. When the single-scattered light from the cloud is parallel to the scattering plane and is dimmer than the Rayleigh scattering into the observation path, it will reduce the DoLP as it partially cancels the

polarization of the Rayleigh scattering. Still, the AoP will not change. Either of these cases could describe what is seen in the 450-nm image (Figure 6.21).

If the scattered light from the cloud droplets is both parallel to the scattering plane and brighter than the light scattered into the path, the cloud polarization will overcome the polarization of the light scattered into the path and a 90° change in the angle of polarization will occur. This is much more likely to happen at the longer wavelengths since the Rayleigh scattering into the path is low. Inspection of the AoP image confirms this explanation, since the clouds are always polarized roughly 90° from the adjacent clear sky (Figure 6.23). For both images, though, the degree of polarization is very low because the multiple scattering from the cloud is much brighter than both the single-scattered light from the cloud droplets and the Rayleigh scattering between the cloud and the observer.

This piece of information could be used to check cloud droplet size distributions from other instruments. A Mie scattering code could be used with the predicted droplet size and scattering geometry to predict whether the scattering is at 90° to the Rayleigh scattering or not. This prediction could then be compared against the actual AoP measurement from the polarimeter. Because Mie scattering is strictly valid only for spherical particles, this argument begins to break down in ice clouds.

Halo Polarization

On April 12, 2006 between 11:23 and 11:26 MST, a 22° halo happened to be viewed while taking data. The polarimetric pictures provide a rare opportunity to confirm work done over the last 25 years into the polarization of halos (Können et al., 1983; 1991;

2003; Lynch, 1979). Although this halo was not complete in any of the three images taken, almost the entire halo could be assembled from the fusion of the images. The best image taken at (11:24:13 MDT) is shown for 450 nm (Figure 6.24). The sun occulter blocks the direct sunlight.

One outcome of the previous research into the polarization of halos has been the assertion that 22° halos will always have a polarization angle that is parallel to the scattering plane—that is the plane that includes the sun, the observer, and the scattering crystal (Können, 1983; 1991). Since the background Rayleigh scattering of the sky will always scatter light polarized perpendicular to the scattering plane, the angle of polarization of the halo will always be oriented 90° from the skylight behind it. Even though noise slightly corrupts the halo AoP image, this characteristic is very clear in the 450-nm image (Figure 6.25).

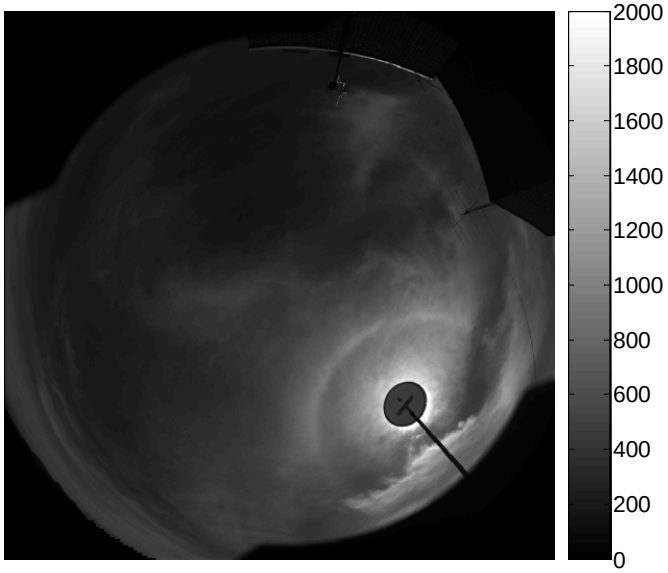

Figure 6.24. Intensity image of a 22° halo at 11:24:13 MDT on April 12, 2006 (450 nm).

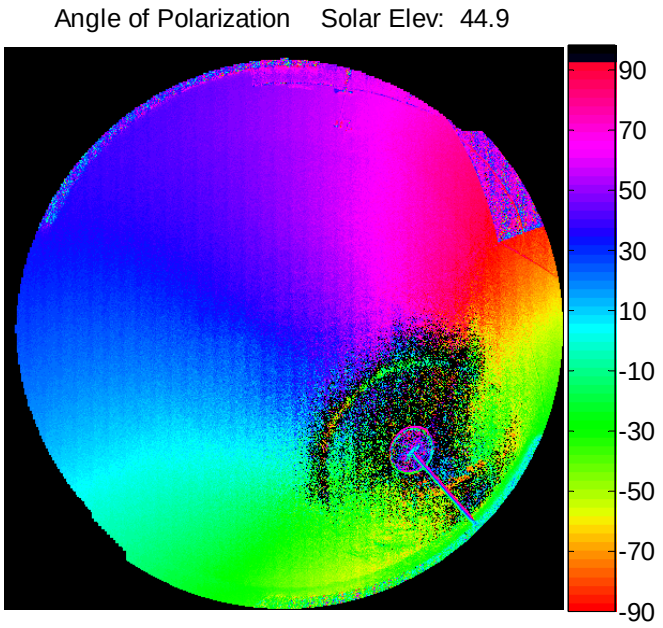

Figure 6.25. Angle of polarization image of a 22° halo at 11:24:13 MDT on April 12, 2006 (450 nm). Areas of low DoLP (<0.8%) are masked in black.

Other wavelengths have similar angle of polarization images. Because of the low exposure needed to suppress bright areas near the sun from overexposure, noise is seen in all DoLP and AoP images. Rescaling of the DoLP images is necessary to see the very low polarization of the halo. No halo DoLP was above 2%. This was consistent with previous predictions of DoLPs of 4% for 22° halos (Können, 1983) and previous measurements that were below 3% for all wavelengths (Können and Tinbergen, 1991). The lower values in these measurements can be accounted for by the brightness of the background clouds. One difference between the intensity image and the polarization image is the width of the polarized ring. For 450 nm (Figure 6.26), the ring is much narrower than at 700 nm (Figure 6.27). This is consistent with previous measurements (Können and Tinbergen, 1991).

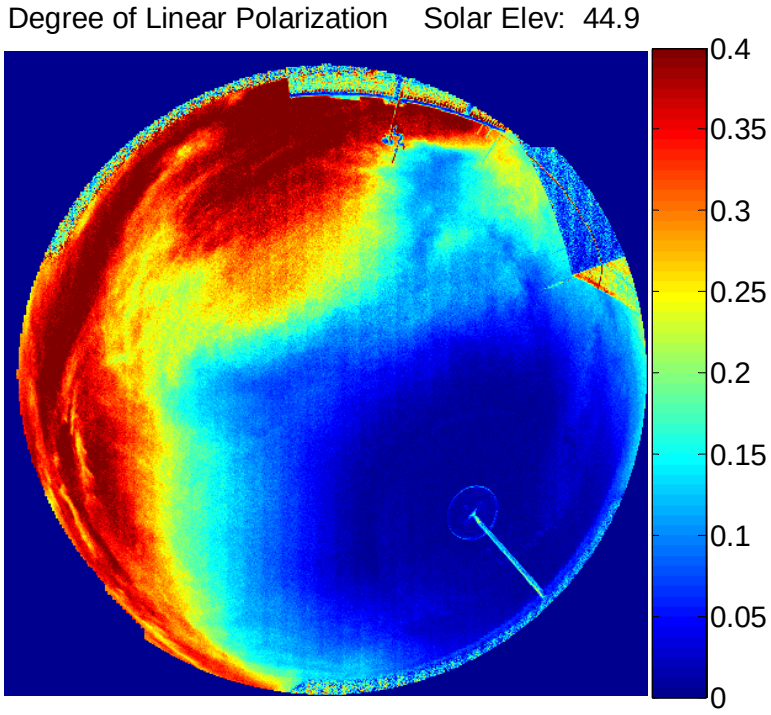

Figure 6.26. DoLP of 22° halo at 11:24:13 MDT on April 12, 2006 (450 nm).

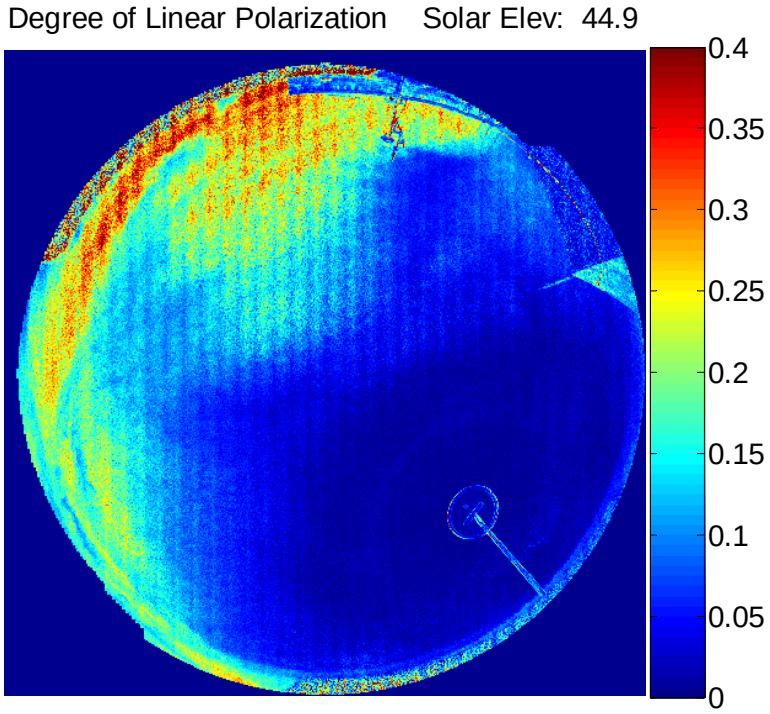

Figure 6.27. DoLP of 22° halo at 11:24:13 MDT on April 12, 2006 (700 nm).

Because of the temporal variability of the halo, there were no data that had the same halo piece in all wavelengths. Therefore, it is difficult to compare the DoLP across wavelengths. Still, the maximum degree of polarization in the ring for each wavelength was found by inspection. The results—although lower than previous investigation—show a similar trend in DoLP across wavelength. The values for each wavelength are shown in Table 6.1. Besides the scattering crystal themselves, the degree of polarization also depends on the clouds behind the halo and the Rayleigh scattering between the observer and the ice crystals. Therefore, a direct quantitative comparison to other investigators results is nearly impossible. A consistent full halo with simultaneous ice crystal sampling is needed to give significantly new contributions to the established halo science. Still, these polarization images of the full halo provide valuable confirmation of previous predictions that the halo angle of polarization will be parallel to the scattering plane.

Table 6.1. Maximum Degree of Polarization in the 22° Halo Ring. The previous investigator data come from Können, 1991.

Wavelength (nm)	Measured DoLP	Previous Investigator's DoLP
450	.010	.026
490	.007	
530	.0091	
630	.0106	
700	.0132	.029

VALIDATION OF POLARIZED MODTRAN

No known investigator has considered the accuracy of the new MODTRAN-P model in the visible spectrum. Investigation into the model validity in the near infrared is ongoing (Conant, 2005). Validating the model involves many measured variables. Each of these variables must be accurate for the validation to be reliable. The validation performed here focuses on the maximum degree of polarization in the clear sky.

Model Input Selection for MODTRAN-P

MODTRAN-P is a versatile tool for modeling atmospheric radiative transfer. It can be used to find atmospheric transmittance spectra, solar irradiance on a surface, effects of surface reflection on satellite measurements, atmospheric thermal emission spectra, etc. Because of its vast applications, the input deck is very complicated with a slew of "cards," optional cards, and optional variables. For this reason, many variables have no bearing on the polarization modeling, but errors in important variables can significantly affect the model. With so many variables, it is easy to lose the important ones among the insignificant ones. Appendix A documents the settings that were used in the polarization models given in this dissertation. Refer to it for specific variable names and reasons for selecting them. The parameters listed below describe the most important variables to the models and limitations of the current version of MODTRAN-P.

MODTRAN-P Input Overview

Clouds, aerosols, and molecular composition are the three variables that most

influence the polarization of scattered light in the atmosphere. Each of these variables must be modeled appropriately to predict the polarization of the sky. MODTRAN uses a maximum of 32 layers in its atmospheric model. The limitation of 32 layers makes modeling fine vertical structures impossible.

Vertical profiles of atmospheric humidity, temperature, and pressure are directly inserted into the MODTRAN model. Obtaining measurements for the molecular composition of species other than water vapor (i.e. CO, CO_2, N_2, etc.) is not practical. Fortunately, the standard models of molecular composition adequately model the Earth's atmosphere for molecules that do not significantly change in the atmosphere. These standard models include mid-latitude summer, mid-latitude winter, 1976 standard model, etc. Sensitivity of the degree of polarization to changes in the standard model for species other than water vapor was found to be below 0.5%.

Aerosol type and extinction are modeled using four different profiles of separate aerosol classes. These four profiles correspond to the boundary layer aerosol, the tropospheric aerosol, the stratospheric aerosol, and high-stratospheric aerosol. These aerosol classes are each defined with extinction profile, wavelength dependence, and scattering phase function. For each aerosol class, the extinction profile is defined at 550 nm and other wavelengths are determined with a scaling factor from the 550-nm definition. Scattering phase functions for the aerosols can also be defined by the user. In addition, default aerosol profiles for each standard aerosol class are available. These extinction profiles exist for the standard Rural aerosol at 23-km visibility, for the standard Urban aerosol at 5-km visibility, and for the standard Troposphere aerosol at 50-km

visibility. Other models are also available. Each standard visibility model contains four typical extinction profiles for each of the four aerosol classes. It is possible to use these standard aerosol models with user-defined extinction profiles for each aerosol class, or even define your own aerosol properties. Also, phase functions can use Mie-generated phase functions, Henyey-Greenstein phase functions, or user-defined phase functions. For this study, aerosol profile extinction information was obtained from solar radiometer and LIDAR data (see the next two sections for details). Dependence of the model on aerosol type was one of the variables tested in the clear-sky models. Without a solar radiometer with more channels or other instrumentation, accurate representations of the aerosol size distribution and phase function could not be derived. Some of these aerosol capabilities are not available in MODTRAN-P anyway. Therefore, the standard models were used for the aerosol type and the standard Mie-generated database for these models was used for the phase functions, while the extinction profile came from the LIDAR and solar radiometer data. Selecting different standard aerosol models tested the dependence of the model DoLP on the aerosol type.

For clear-sky models, cloud variables were completely turned off in the model. Care was taken to collect data on days that were completely clear of clouds throughout the day for this part of the study—with the exception of September 5, 2006 which had some clouds in the afternoon. For cloudy models, cloud extinction, cloud thickness, and cloud height are necessary inputs to MODTRAN. Cloud extinction is impossible to measure without more sophisticated instrumentation and/or aerial collections. Thickness

was modeled according to LIDAR measurements if the cloud was penetrable. Otherwise, the cloud model was not run. Cloud height was obtained from the LIDAR.

MODTRAN-P Limitations

The developers of the first release of MODTRAN-P have elected to remove certain capabilities from the original MODTRAN input deck. Since MODTRAN-P is not in full release, these limitations are not consistently documented, yet. The limitations listed below have been found in a few papers and by word of mouth from people close to the project.

Multiple scattering apparently is not properly implemented for polarization. All multiple scattering is modeled as totally unpolarized (Fetrow, 2006). Therefore, inclusion of proper multiple scattering—which is necessary to an accurate model—is impossible. Using multiple scattering in the current code reduces the overall degree of polarization, as it should, but it does so at a rate that is not realistic. The magnitude of this problem is tested in the clear-sky models section.

Only a sub-set of the default aerosol models is available (PPS V4.3 Command Line Usage, 2005). The Navy maritime model, the two fog models, and the desert model are not implemented in the current version. For the simulations here, the Urban, Tropospheric, and Rural models were used for the standard aerosol type.

Finally, this version of the code uses a standard scattering phase function that does not allow the user to achieve realistic modeling for the aerosols present in a particular measurement. Furthermore, it has been shown that improved phase functions

will gain nothing for the accuracy of the model until the multiple-scattering algorithms are implemented properly (Conant et al., 2005).

Radiosonde Data – Molecular Extinction Profile

Radiosonde (weather balloon profile information) data were obtained from atmospheric soundings using RS-92 sondes and a Vaisala PP21 Sounding Processor. These soundings provided height, pressure, temperature, and relative humidity profiles. All of these values were directly input into MODTRAN after sampling to the 32 layers used by MODTRAN. These values affect the molecular extinction of the atmospheric profile. Values of molecular components other than water vapor used the defaults of the Midlatitude Summer model. (See Appendix 1 for more details on the MODTRAN inputs.) Layer resampling used an algorithm that sampled for regions of large change in both the relative humidity profile and the aerosol extinction profile extracted from the LIDAR. (Temperature and pressure data did not significantly change compared to the other variables.) Most of the balloons popped at an altitude near 22-27 km. Therefore, the stratosphere was not entirely sampled for relative humidity, pressure, and temperature. Models that ignored the stratosphere consistently under-predicted the degree of polarization in the atmosphere. Because the light scattered from the stratosphere is nearly pure single-scatter Rayleigh, it has a much higher degree of polarization than light scattered in the aerosol-laden troposphere. Since stratospheric Rayleigh scattering proved to be critical to the degree of polarization in the models, a dynamic number of layers (typically around 6 layers dependent upon the altitude that the balloon popped) were

reserved for a default stratosphere. The remaining layers were reserved for the radiosonde data.

One surprise found while validating the MODTRAN-P model was that humidity has little effect on the model. When humidity was changed by 10-60%, the degree of linear polarization (DoLP) was affected by less than .01%. Therefore, humidity is not a significant variable--except that it swells the aerosols, but this is accounted for in the optical depth measured by the solar radiometer. It is also possible that changes in the temperature and pressure profile could also be insignificant to the DoLP. Still, using a standard 1976 model as compared to an actual radiosonde profile was shown to cause differences of up to 0.4%. This suggests that using the actual radiosonde data is best, but that standard models may be sufficient in the future. For certainty, the models used here continued to use the real radiosonde data.

Solar Radiometer Data – Total Extinction

Solar radiometry uses measurements proportional to the radiance coming through the atmosphere along with the known detector response for the constant top-of-atmosphere solar radiance to derive the optical depth—or total extinction—of the atmospheric column. A calibrated detector is used to obtain voltages looking directly at the sun. This voltage is then compared to the voltage that the radiometer would see at the top of the atmosphere (determined during calibration) to calculate optical depth. Since the optical depth depends on solar angle, the optical depth calculations are always corrected to an equivalent optical depth for a zenith view. Equation 7.1 shows the calculation for optical depth (Shaw, 1983).

$$\mathrm{OD} = \frac{\ln(V) - \ln(V_0)}{\sec(\theta_z)} \tag{7.1}$$

V is the voltage measured, V_0 is the calibration voltage—that is the voltage the radiometer would see while viewing the sun from the top of the atmosphere—θ_z is the solar zenith angle, and OD is the calculated optical depth at zenith.

In addition, the voltage (V) is corrected for the earth-sun distance on the day of the year the measurements were made. All measurements are corrected to an equivalent distance of one astronomical unit (using the square of the Earth-sun distance for r^2 falloff). Adjustments for temperature variation of gain could also be applied, but these sub-percent adjustments were not necessary. Other factors, such as the assumption of atmosphere homogeneity, will contribute more to errors in the models than these small temperature errors.

The solar radiometer, obtained from Dr. Glenn Shaw at the University of Alaska - Fairbanks, measures three different channels—425, 500, and 790 nm. None of the wavelengths exactly matched the 550 nm extinction profile needed for MODTRAN. However, using the 500- and 790-nm data, the 550-nm optical depth was obtained through linear interpolation. Although the assumption of linear fall off of the aerosols is not valid, aerosol extinctions do change slowly (Schuster, 2006). Also, 550 nm is sufficiently close to 500 nm that the value of the optical depth did not change significantly from the longer wavelength. For most model runs, the correction from optical depth at 500 nm to optical depth at 550 nm was around ~10%. MODTRAN models of transmittance with Rural, Urban, and Troposphere aerosol types showed that the maximum error from linear interpolation would be around 0.3% transmittance. This is

a small error compared to other sources of error in the model. The derived 550-nm optical depth was then used to obtain the 550-nm aerosol extinction profile by inverting the LIDAR signal.

LIDAR Inversion – Aerosol Extinction Profile

Although the molecular extinction profile comes from the radiosonde data, aerosol information was also needed to complete the atmospheric profile information. Being one of the key components of depolarization in the atmosphere, aerosol extinction needs to be accurately modeled in MODTRAN-P. The MAML LIDAR system designed and built by Nathan Seldomridge at Montana State University was used to gather backscatter signal profiles for the aerosols (Seldomridge et al., 2006; Seldomridge, 2006). This LIDAR system uses a laser, a detector, and a sampling analog-to-digital (AD) card to measure the backscatter from the atmosphere. Since the LIDAR sees backscatter from both the molecular components and aerosol components of the atmosphere, an algorithm that both extracts the total extinction of the atmosphere from the signal and separates the aerosol and molecular components of the extinction is necessary. Several methods of LIDAR inversion can be used to extract extinction from a single-color LIDAR signal. Most of these methods are various derivations from the Fernald method introduced in 1972 (Fernald et al., 1972) or the Klett method introduced in 1981 (Klett, 1981). Each of these methods uses the range-corrected LIDAR signal (RCS) with a boundary condition to start the inversion. The boundary condition is a point in the signal range where the extinction of the signal is known or can be accurately assumed. (The “boundary condition” should not be confused with the “boundary layer.” The boundary condition is

a mathematical term for the initial condition that finds a specific solution to a problem. The boundary layer is a layer of high aerosol distribution close to the earth's surface caused by various human and nature interactions.) Using the signal and extinction at a known point, calculations extract the extinction for all other signal profile heights. Two particular methods of selecting a boundary condition were considered: the far-end solution and the optical-depth solution (Kovalev and Eichinger, 2004).

In the far-end solution, the extinction is assumed to be known for a point in the far end of the LIDAR range. Particularly, it is useful to assume that no aerosols are at a point far above the earth's boundary layer and the LIDAR signal at that range comprise only pure molecular backscatter. In practical inversions, this point is normally taken to be more than 5 km above the earth's surface. Since molecular extinction is easily modeled by a combination of radiosonde data and standard models for the major molecules in the earth's atmosphere, the molecular extinction provides a value for the "boundary"—that is the point of known extinction. The major assumptions associated with this method are: (1) there are really no aerosols at the boundary point far above the earth's boundary layer, (2) the molecular model represents the molecular extinction profile well, (3) the backscatter-to-extinction ratio is known over the profile, and (4) the LIDAR return has a high signal-to-noise ratio (SNR) at the boundary condition point. (If SNR is low at this point, the entire extinction profile can be corrupted by the noise at the range of the boundary condition.) Some of these assumptions may be questionable. For example, without information from other LIDAR wavelengths, the backscatter-to-extinction ratio cannot be known over the profile. For a single-color LIDAR, the backscatter-to-

extinction ratio must take on an assumed value, constant over the LIDAR range. Multi-wavelength lidars can provide additional information (Cattrall et al., 2005) that can be used to improve the estimate of extinction-to-backscatter ratio, but still it nearly always must be assumed to be constant over the entire measurement range unless multiple-angle measurements are made (Spinhirne et al., 1976). Even more, for optically thick aerosols—such as forest-fire smoke—the LIDAR may not penetrate the high aerosol layer. Even if it penetrates the aerosol layer, the SNR can be reduced enough that an accurate boundary condition cannot be formed in the aerosol-free region. Experimentation with this method showed that using different boundary ranges with a given molecular profile resulted in aerosol profiles that could vary by a factor of 1.5. Noise in the upper ranges caused problems with the boundary condition. For these reasons, this Klett algorithm variant was not used for any of the clear-sky aerosol profile extractions. (A near-end variant of this solution was used for retrieving cirrus extinction. The only difference between these variants is that the boundary value is taken below, not above, the extinction profile of interest in the near-end solution.)

The optical-depth solution uses solar radiometer data to provide the total extinction over the LIDAR range. (Optical depth is the integrated extinction over range.) Since the total LIDAR signal can be integrated and the total extinction is known from the solar radiometer, a relationship is formed between signal and extinction. Using this relationship, the atmospheric extinction profile is determined from the LIDAR signal. If molecular extinction is known, the aerosol extinction profile is then extracted from the atmospheric extinction. Like the far-end solution, the optical-depth solution uses a few

assumptions. (1) The optical depth measured by the solar radiometer looking at the sun is the same as the optical depth of the LIDAR looking toward zenith. This assumption equivalently assumes that the atmosphere is homogenous. For models run over the course of a day in areas free of significant aerosol dispersion events, this assumption may lead to a random model error since the aerosols in the direction of the sun will not be systematically higher or lower than the aerosols at zenith. Therefore, it adds to the random noise of the model over the course of the day, but does not induce a systematic error. (2) The optical depth over the LIDAR range is known. This assumption is not trivial since the solar radiometer measures the total extinction to the top of the atmosphere, while the LIDAR only measures up to its maximum reliable operating range (MRR). This range varies and depends upon the amount of path attenuation. For the MAML system, this height could be as low as 2-3 km for extremely optically thick aerosols and upwards of 15 km for clear skies in the daytime. Also, the LIDAR transmit and receive beams are not in full overlap until roughly 70 meters above the surface, so the bottom portion of the profile does not contain accurate signal information. (3) The molecular extinction profile model is accurate. The molecular extinction profile was obtained from the radiosonde data and MODTRAN modeling of the atmosphere without aerosols. (4) Molecular absorption at the LIDAR wavelength is negligible. This assumption is valid at the 530 nm wavelength (Kovalev and Eichinger, 2004). (5) The backscatter-to-extinction ratio is constant over the range and the constant is known. The backscatter-to-extinction ratio for all clear-sky data was set to a constant of 0.016. This value was obtained from Table 7.1 of *Elastic LIDAR* (Kovalev and Eichinger, 2004, pg.

229). Although the backscatter-to-extinction ratio could vary slightly from this value, the optical depth caused the LIDAR inversion to be bounded. An error in backscatter-to-extinction ratio does not affect the overall extinction of the column, only local variations in the aerosol extinction. Figure 7.1 shows the influence of varying the backscatter-to-extinction ratio between 0.020 and 0.010. Notice that there are some local problems with extinction, but in most regions the variation is minimal. After the coarse MODTRAN sampling of the aerosol profile into 32 layers, these local errors become insignificant compared to the sampling errors. (6) There are no thin clouds affecting the solar radiometer measurement. To minimize this affect, clear-sky comparisons were only taken during clear-sky conditions.

Implementation of the optical-depth solution was as follows. A molecular extinction profile was obtained from a MODTRAN model using the radiosonde data. LIDAR data were first processed for offset and range correction. The first dip below zero in the range-corrected signal was used as an indicator of the maximum reliable range (MRR) of the LIDAR. The extinction profile above this range was modeled as a standard Rural 23 km aerosol model. Then, the optical depth above the MRR was integrated from the model results and subtracted from the 550-nm optical depth derived from the solar radiometer data. The resulting optical depth matched the optical depth effectively viewed by the LIDAR.

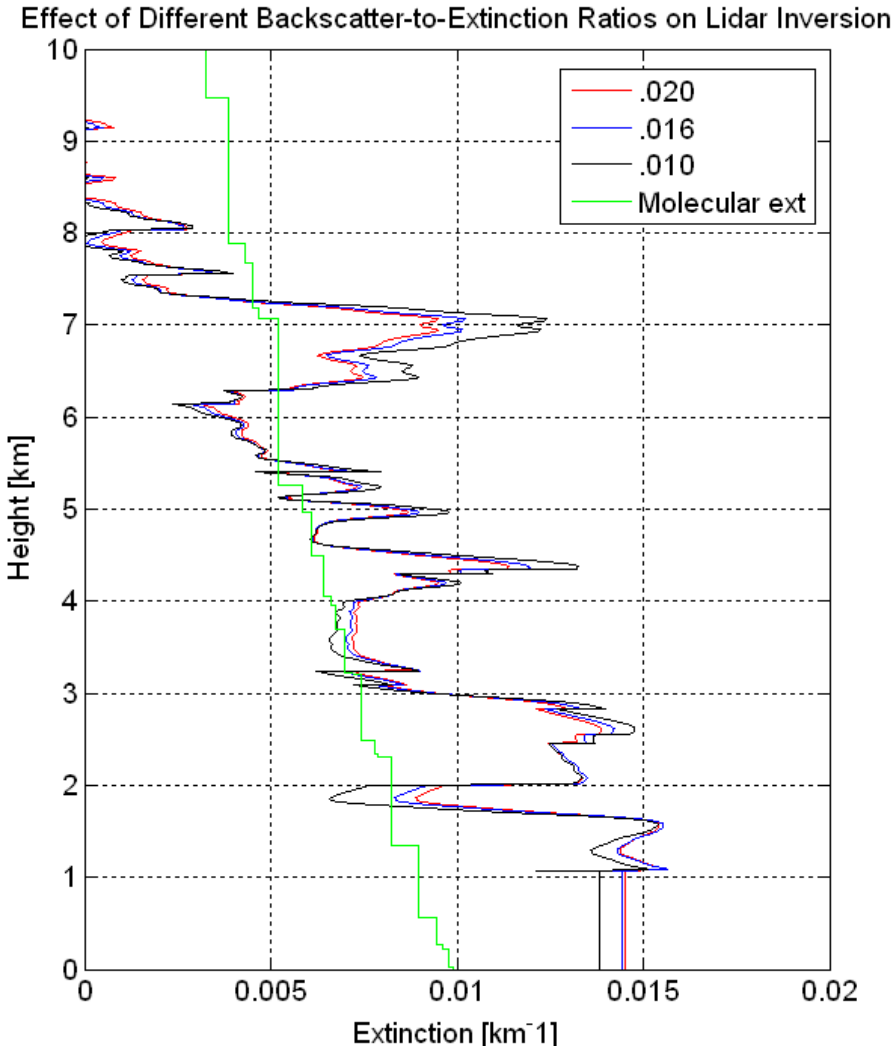

Figure 7.1. Effect of background-to-extinction assumption on aerosol extinction profile.

For the LIDAR inversion, the 550-nm backscatter was assumed to be the same as the 532-nm backscatter. Although this is not exactly true, the more important variable to the MODTRAN model was the total extinction interpolated from the solar radiometer data at 550 nm, not the exact placement of the extinction in the profile. Since the profile is a secondary variable, this is a secondary error and not highly influential on the model. Finally, the ~80 m region below full LIDAR overlap was considered small compared to

the ~3 km boundary layer. Therefore, the optical depth measured from the ground level by the radiometer was sufficiently close to the optical depth seen by the LIDAR. In post-processing, the extinction below full overlap was fixed to be the same as the extinction value measured at the first range bin with full overlap (~80 m). LIDAR data inversion followed the forms given in Kovalev and Eichinger, 2004, pg. 175-179. Equations 7.2-7.5 give the procedure for inverting the signal.

$T_{\max} = e^{-\mathrm{OD}_{550}}$, where OD_{550} is the optical depth at 550 nm. (7.2)

$$V_{\max} = T_{\max} e^{-(a-1)\int_{r0}^{\mathrm{MRR}} \kappa_m(r)dr} \quad a(r) = \frac{3/(8\pi)}{\pi_p} \tag{7.3}$$

π_p is the backscatter-to-extinction ratio (set at 0.016), $\kappa_m(r)$ is the molecular extinction profile obtained from the radiosonde and MODTRAN, $r0$ is the range at which overlap starts, and the MRR is the maximum reliable range from the LIDAR processing.

$$Z(r) = r^2 P(r) e^{-2(a-1)\int_{r0}^{r} \beta_m(r')dr'} \tag{7.4}$$

$$\kappa_p(r) = \frac{Z(r)}{\frac{2I_{\max}}{1-V_{\max}^2} - 2\int_{r0}^{r} Z(r')dr'} - a(r)\kappa_m(r), \tag{7.5}$$

$r^2P(r)$ is the range-corrected LIDAR signal, and β_m is the molecular backscatter coefficient. If molecular absorption is zero, this is equal to the molecular extinction coefficient, κ_m. κ_p(r) is the aerosol extinction profile.

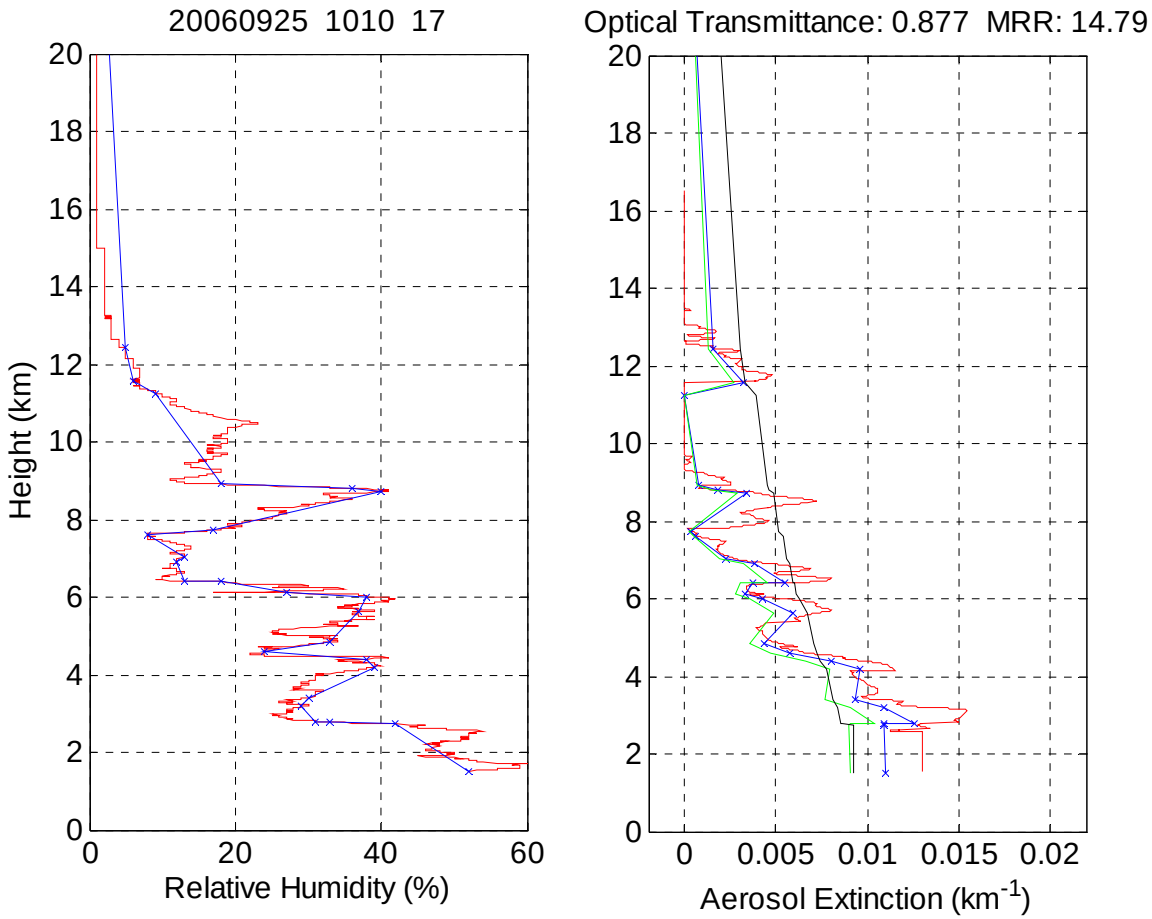

Figure 7.2. Example humidity and aerosol resampling for the 32 layers input to MODTRAN. For the left plot, the red line shows the humidity from the radiosonde. The blue line shows the final sampled humidity profile. For the right plot, the black line shows the molecular extinction profile obtained from the MODTRAN model and the radiosonde data. The red line shows the LIDAR extinction extracted from the inversion. The blue line shows the sampled extinction, while the green line shows the extinction after rescaling the profile to maintain the total extinction.

After the aerosol extinction profile was determined, it was resampled to 32 points along with the humidity, temperature, and pressure data using an algorithm that selected ranges with either high humidity or high aerosol extinction changes (Figure 7.2). An initial MODTRAN model was run and the total optical depth of the molecular and aerosol extinction was calculated from the output. The model optical depth was compared

to the 550-nm optical depth derived from the solar radiometer. If the modeled optical depth and the optical depth interpolated from the measured data differed by more than 0.5%, the aerosol extinction profile was rescaled by this factor. Therefore, the optical depth of the MODTRAN model and the solar radiometer always agreed to within 0.5%. This was very important since total extinction (optical depth) seems to be the most important driving variable for polarization. Exact representation of local aerosol extinction in the column is secondary to the inclusion of the true optical depth in the whole model. In fact, other researchers who have done MODTRAN-P validation have completely ignored the column information, using only solar radiometer data to create a homogenous boundary layer model (Conant, 2005). When the LIDAR could not penetrate the boundary layer (~ 3 km above ground), the model was built following a similar approach to these researchers. For altitudes above the boundary layer, the standard Rural 23 km model was used. The remaining optical depth was spread over a homogenous extinction layer from 3 km down to ground level in the model. The flowchart for the MODTRAN input process is shown in Figure 7.3. This flowchart only includes the most important steps and ignores minor model variables. See *Appendix A: MODTRAN Input Selection* for information.

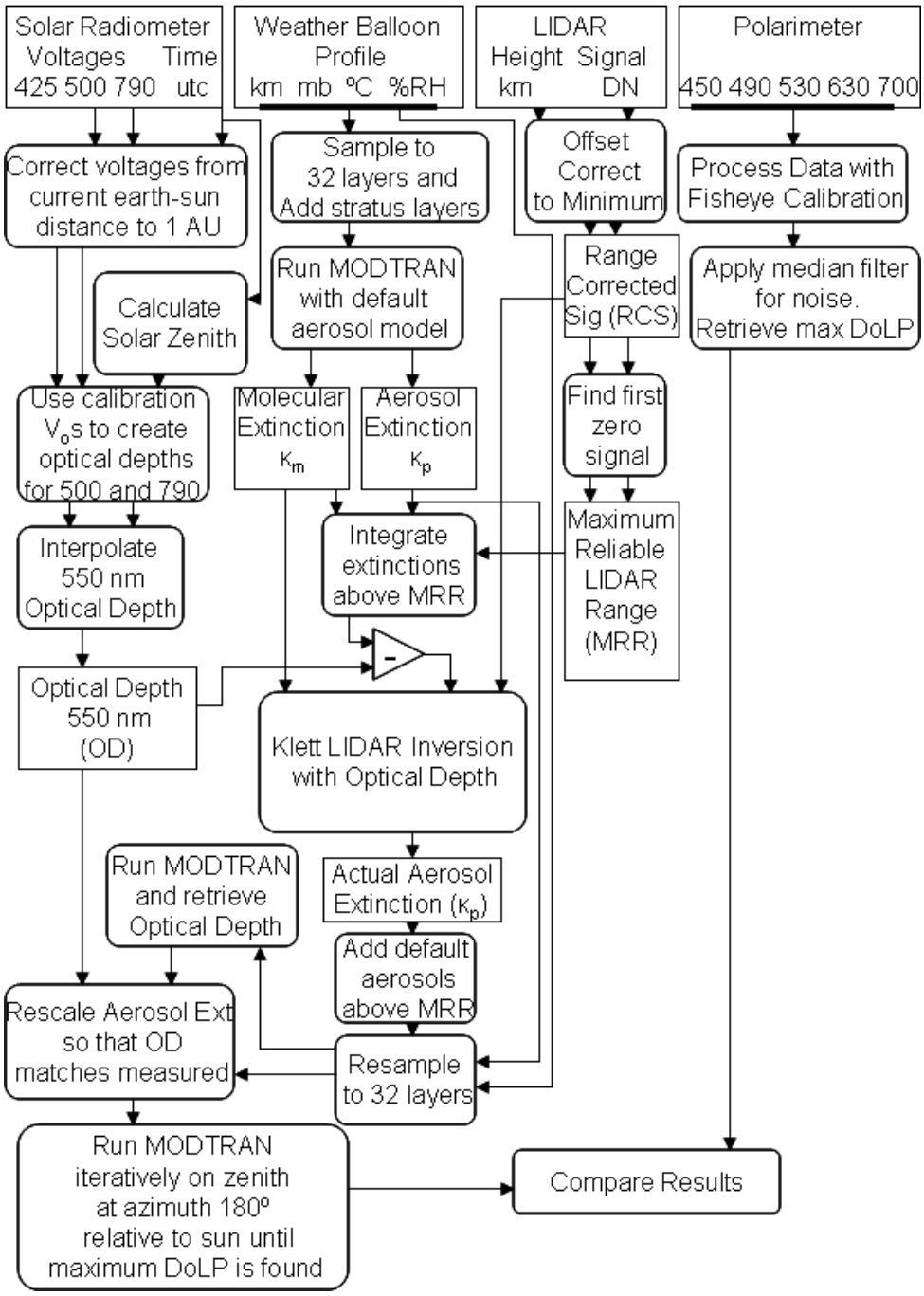

Figure 7.3. Flowchart of clear-sky MODTRAN-P maximum DoLP comparisons.

Clear Sky Maximum Degree of Polarization Models

While the maximum clear-sky DoLP is not the only parameter than must be validated in the MODTRAN-P simulation, its value is of primary importance to other sky regions. (Clear sky means a sky free of clouds in this dissertation.) If the maximum DoLP at approximately 90° from the sun is not accurate, the polarization of no other observed zenith and azimuth angles can be expected to be valid. For this reason, the primary focus of this validation work rested upon the maximum DoLP. For both the model and the actual data, the maximum degree of polarization was found. Image processing was used to find the maximum DoLP in the measurements, while an iterative search algorithm found the maximum DoLP for the model. (The maximum model DoLP was always within a few degrees of 90° from the solar zenith angle.)

The model was validated under three different sky conditions: optically thin boundary-layer aerosols, medium-optical-thickness boundary-layer aerosols, and optically thick boundary-layer aerosols. For all sky conditions, the total optical depth (OD) at 500 nm is listed (i.e. the optical depth that includes both aerosol and molecular scattering.) For each sky, MODTRAN-P was run with each of three different standard aerosol types—Rural, Urban, and Tropospheric. The current version of MODTRAN-P only models multiple scattering as completely unpolarized. Therefore, models using multiple scattering were expected to predict a lower degree of polarization than reality. Similarly, single-scatter models were expected to predict a higher DoLP since they do not accurately account for the DoLP reduction by multiple scattering. For each aerosol type, both single-scatter and multiple-scatter models were run to test these hypotheses.

The standard Rural aerosol type represents the closest standard aerosol model to the actual aerosols found in Bozeman during the summer months. These aerosols reflect agricultural processes and a general lack of nearby industrial sources. Still, forest fire smoke in the early part of September lingered during all the days chosen. This smoke, which may contain significant black soot content, may be closer to the standard Urban aerosol than the Rural type. For this reason, these two standard aerosol types—along with the standard Tropospheric aerosol—were chosen for the modeling.

Four questions need to be answered about the MODTRAN-P models. (1) How accurate are the models? (2) How dependent are the models on aerosol type? (3) Do any of the standard aerosols accurately model all aerosol densities? (4) How accurate are the single-scatter and multiple-scatter versions of the model?

Note: for all plots in this section, the color of the plotted line closely represents the color corresponding to the wavelength of light for both degree of linear polarization (DoLP) and optical depth (OD)—only total optical depth is reported. Black represents the invisible 700-nm wavelength. All times are Mountain Daylight Time (MDT = UTC-6 hours).

Sky with Low Aerosol Content (OD ≈ 0.16)

On September 25, 2006, the sky was one of the clearest of the year. By visual inspection of neighboring mountains, only May 31 seemed clearer over the entire summer. Since solar radiometer data were not available for May 31, September 25 was chosen for low-aerosol-content MODTRAN-P validation.

Rural Aerosol Models. Rural aerosol models for the multiple-scatter model are shown in Figure 7.4. Notice that, when compared to the single-scatter models (Figures 7.5 and 7.6), the multiple-scatter models are better at preserving the shape of the maximum DoLP curve over the day, especially for the longer wavelengths. Still many problems occur. First, the models for all wavelengths consistently under-predict the maximum degree of polarization in the sky. Secondly, the 700-nm instrument data exhibit the highest DoLP near sunrise and sunset, while in the model the 630-nm data are slightly higher. Finally, during mid-day the model results across the different wavelengths are separated by a larger gap than the measured data, and are ordered differently. Absolute differences between model and instrument results are between 9 and 22% (the instrument calibration uncertainty is approximately ±3%).

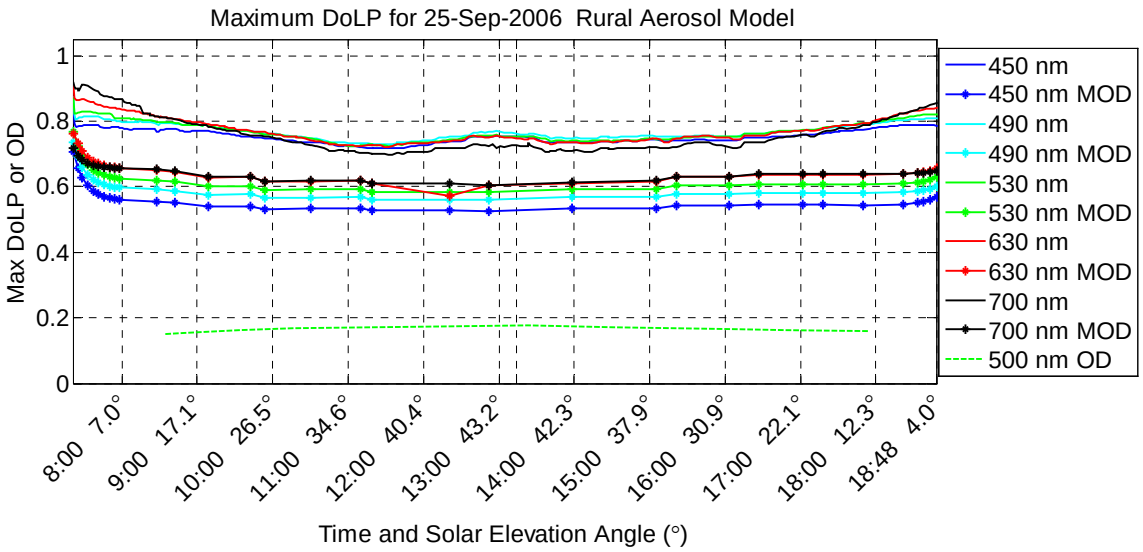

Figure 7.4. Low-aerosol max DoLP with Rural aerosol multiple-scatter model. Each wavelength is shown using a line color that is similar to the actual color seen in the sky. Dotted lines show the model results (MOD). The 500-nm optical depth measured with the solar radiometer is shown with a green dashed line.

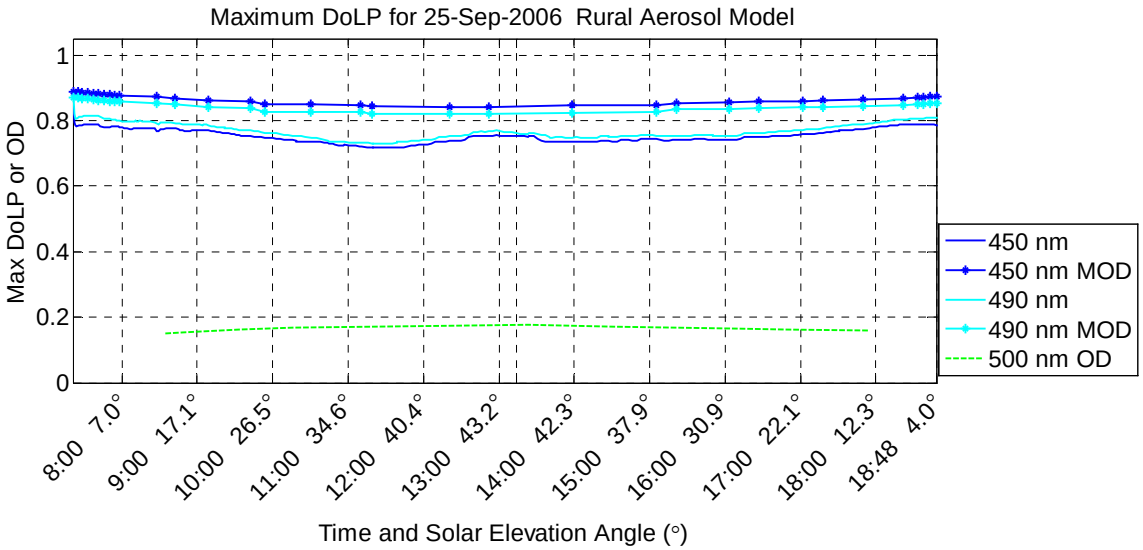

Figure 7.5. Low-aerosol max DoLP with Rural single-scatter model 450 490 nm.

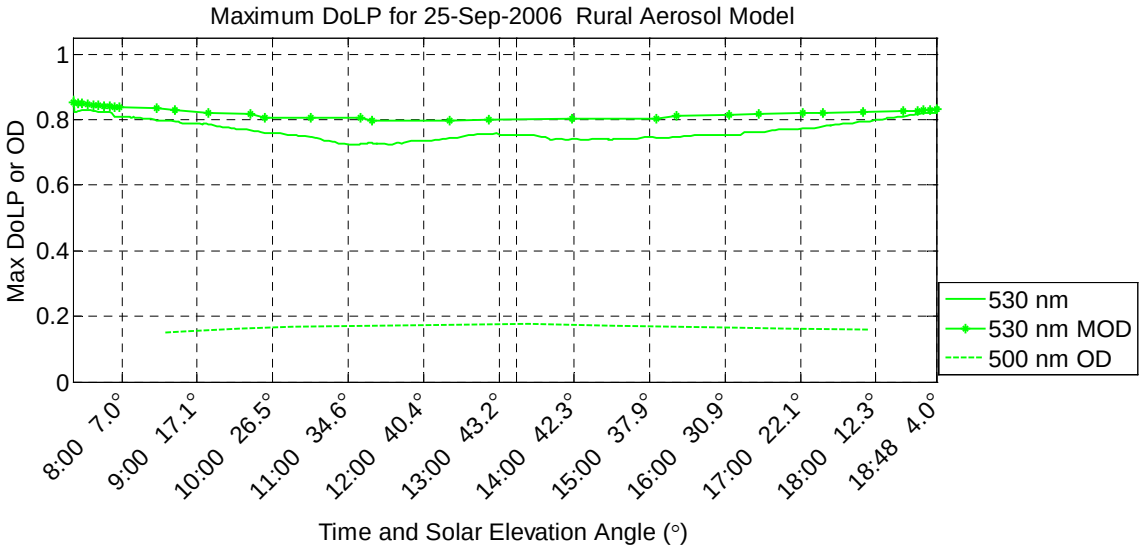

Figure 7.6. Low-aerosol max DoLP with Rural single-scatter model 530 nm.

For the single-scatter Rural aerosol models, the 450- and 490-nm models are much closer to the measurements with maximum errors around 13% (Figure 7.5). The line shape over all solar elevation angles also tracks well. The 530-nm model is even closer with a maximum error of 8% (Figure 7.6). During mid-day readings, both the 630-

and the 700-nm models are within the instrument accuracy (Figure 7.7 and 7.8). Still, near sunrise and sunset the model severely under-predicts the values by up to 13%.

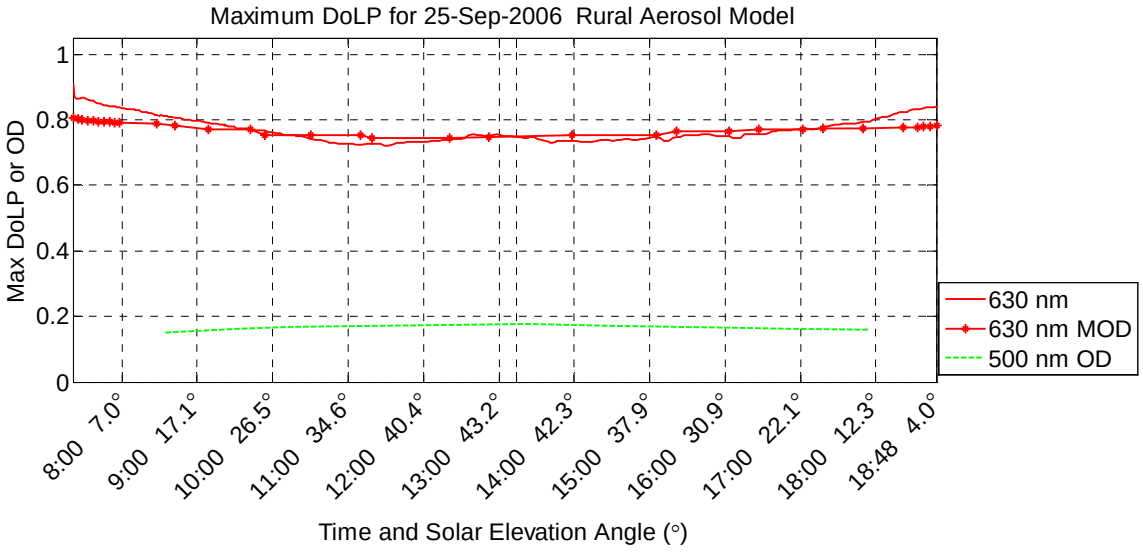

Figure 7.7. Low-aerosol max DoLP with Rural single-scatter model 630 nm.

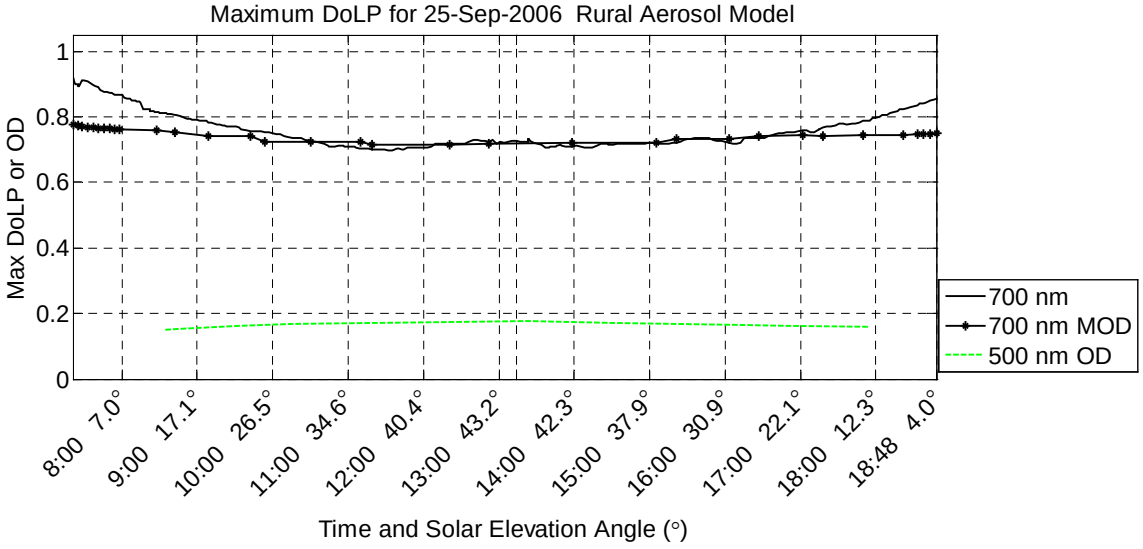

Figure 7.8. Low-aerosol max DoLP with Rural single-scatter model 700 nm.

Urban Aerosol Models. Urban multiple-scatter models exhibit maximum DoLPs that are nearly identical to the Rural aerosol model, except with a 4% shift toward the

instrument data (Figure 7.9). This may support the assertion that the Urban aerosol model is a better representation of the forest fire smoke seen in the Gallatin valley during September. Similarly, the Urban single-scatter models also increased by about 4% for the long wavelengths and about 2% for the shorter wavelengths. This increase pulls the Urban single-scatter models away from the actual data (Figures 7.10-7.13).

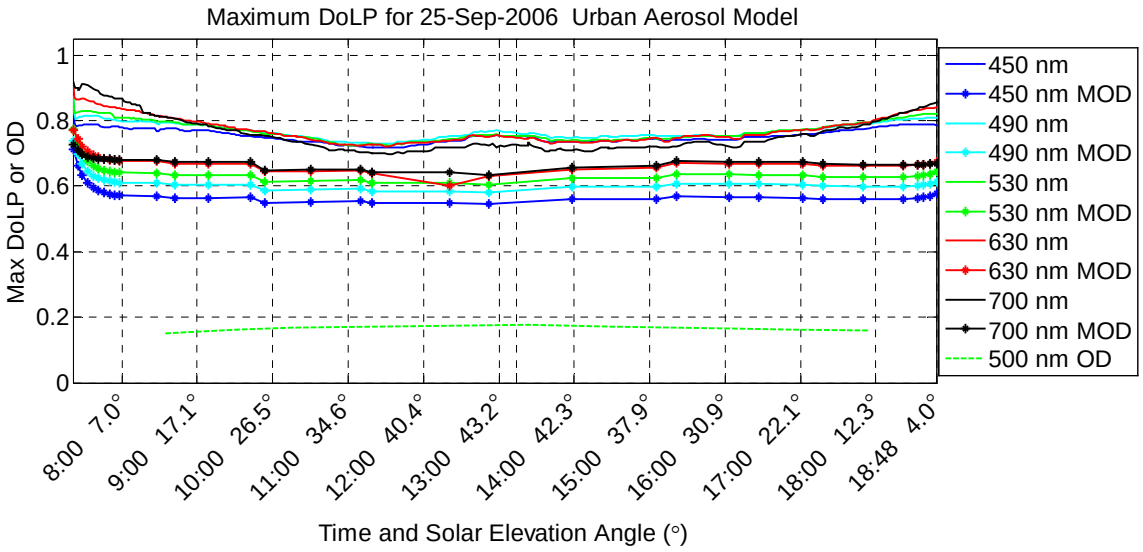

Figure 7.9. Low-aerosol max DoLP with Urban multiple-scatter model.

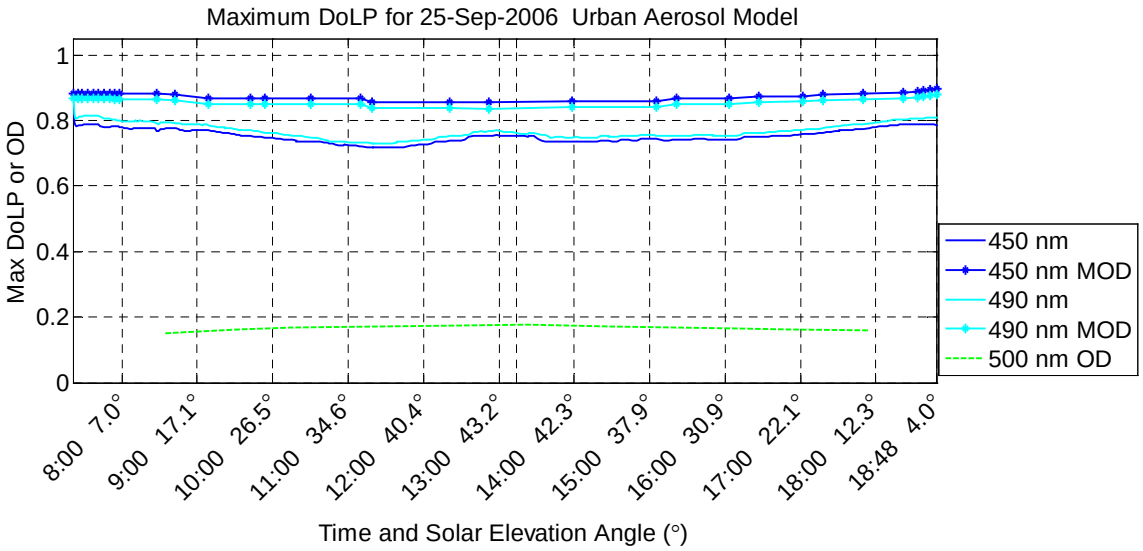

Figure 7.10. Low-aerosol max DoLP with Urban single-scatter model 450, 490 nm.

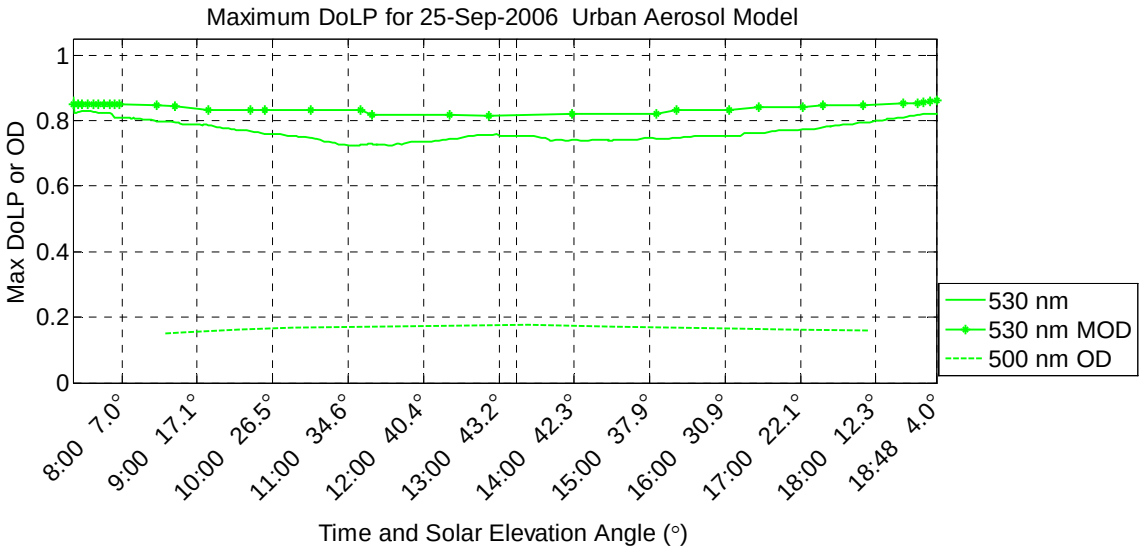

Figure 7.11. Low-aerosol max DoLP with Urban single-scatter model 530 nm.

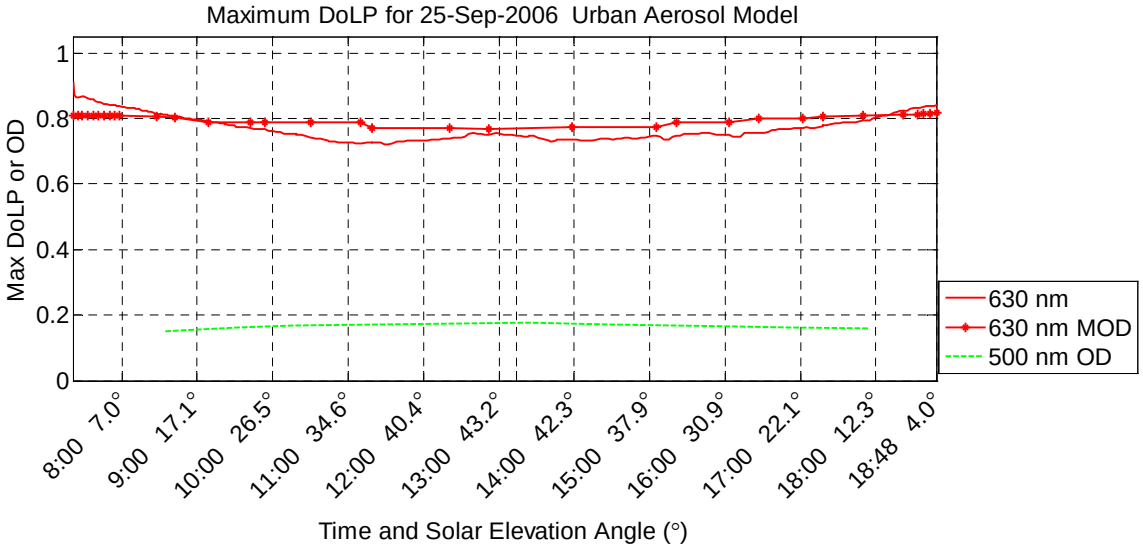

Figure 7.12. Low-aerosol max DoLP with Urban single-scatter model 630 nm.

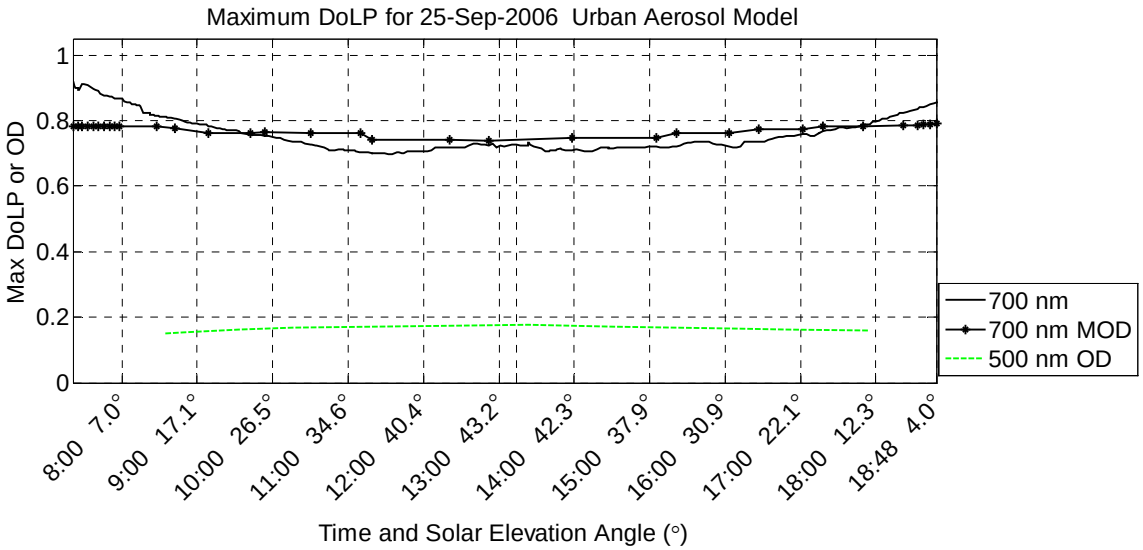

Figure 7.13. Low-aerosol max DoLP with Urban single-scatter model 700 nm.

Tropospheric Aerosol Models. For most MODTRAN standard models, the boundary layer (< 3km) uses the standard aerosol (Urban, Rural, Maritime, etc.), while the troposphere above the boundary layer uses the standard Tropospheric aerosol. In the standard Tropospheric model, this aerosol type is extended through the boundary layer. Although it may not be as representative as the Urban or Rural aerosols, this model is included as another alternative.

Compared to the other two multiple-scatter models, the Tropospheric aerosol type bunches the wavelengths in a more realistic way, but the overall accuracy of the model decreases by ~5% from the Rural model (Figure 7.14). For the clear sky, this standard aerosol is the worst model for multiple scattering.

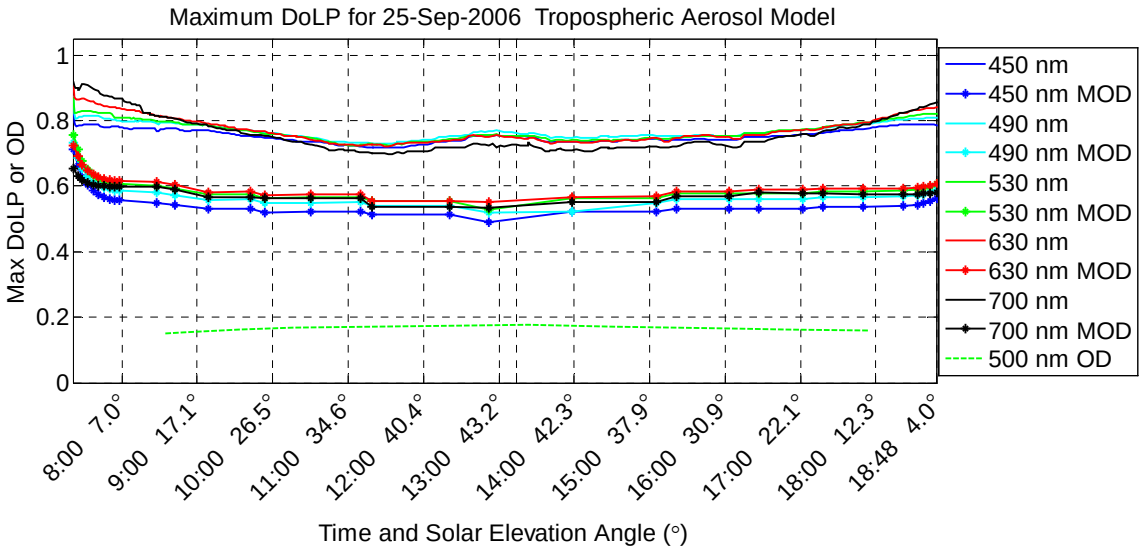

Figure 7.14. Low-aerosol max DoLP with Tropospheric multiple-scatter model.

For the single-scatter models, the shorter wavelengths move the DoLP about 1.5% lower than the Rural model, while the longer wavelengths actually move away from the instrument data. Therefore, the Tropospheric models are worse than both the Urban and the Rural aerosol models for the low-aerosol sky.

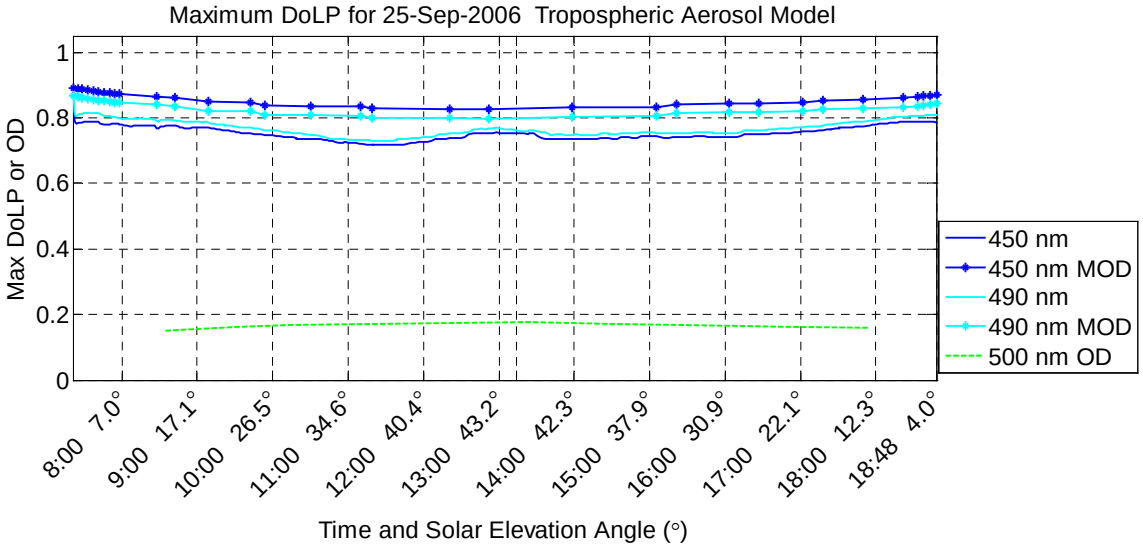

Figure 7.15. Low-aerosol max DoLP with Tropospheric single-scatter model 450, 490nm.

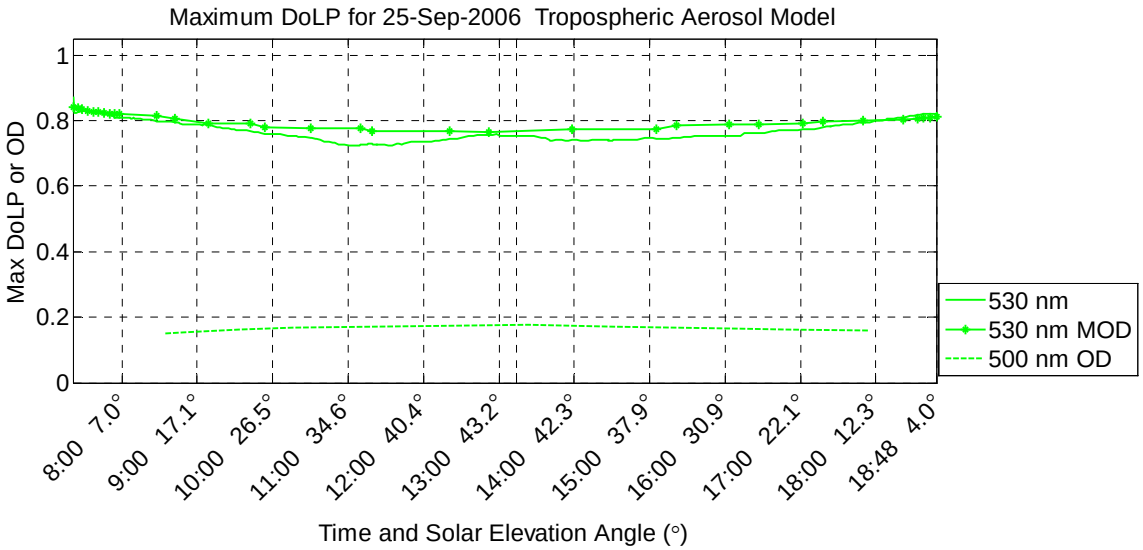

Figure 7.16. Low-aerosol max DoLP with Tropospheric single-scatter model 530 nm.

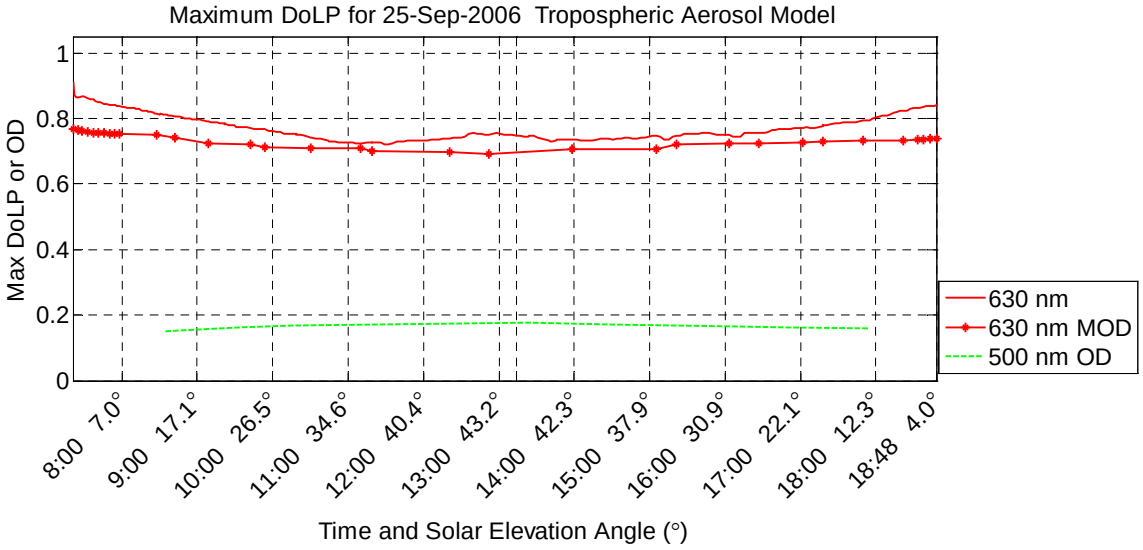

Figure 7.17. Low-aerosol max DoLP with Tropospheric single-scatter model 630 nm.

The low-aerosol sky models show that the accuracy of the model is greatly dependent upon the type of aerosol used in the model. Although each model has problems with multiple scattering, the single-scatter model is surprisingly accurate when used with the Rural or Urban aerosol type. With the exception of the 450 and 490 nm

wavelengths, both of these models predict values during the mid-day that were within the accuracy of the instrument. To better understand the exact accuracy of the model, more instrumentation is needed to measure the aerosol size distribution and MODTRAN-P needs to be upgraded to handle this information. Currently, MODTRAN-P is not capable of handling custom aerosol phase functions (Conant, 2005).

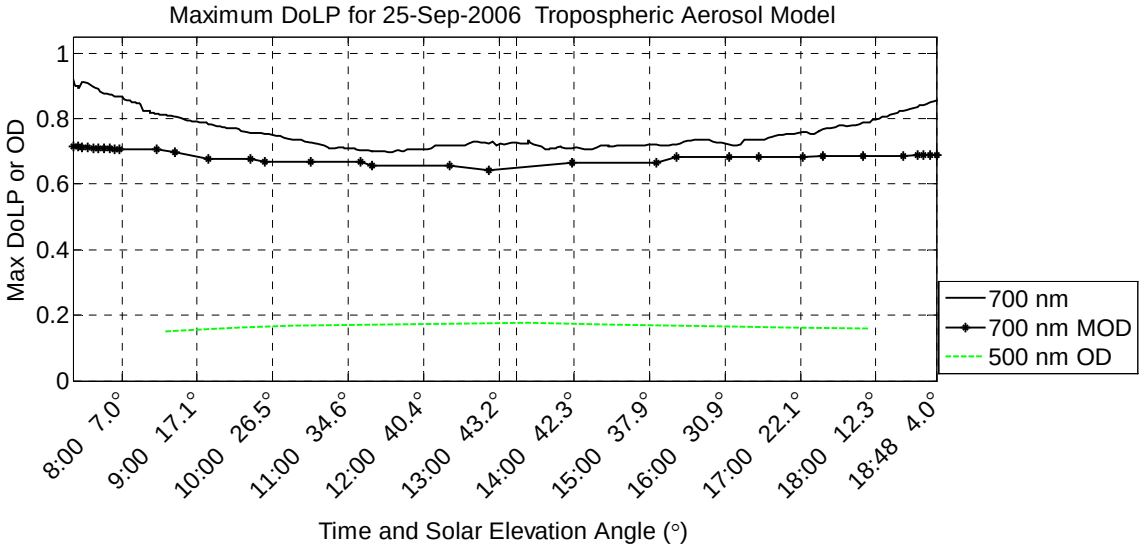

Figure 7.18. Low-aerosol max DoLP with Tropospheric single-scatter model 700 nm.

Long-Wavelength Single-scatter Problems. For all standard aerosols, the single-scatter model consistently under-predicts the DoLP near sunset and sunrise. It is hypothesized that the aerosols cause the model to reduce the DoLP too much. To better understand the problem, the single-scatter model was run again without any aerosols. The exclusion of all aerosols and multiple scattering provides an absolute upper limit to the maximum DoLP that can be expected from MODTRAN-P for each wavelength. After the new model was run, the maximum degree of polarization attained from the models was 94%. This was true for all wavelengths, not just the longer wavelengths shown (Figure

7.19). When multiple scattering and aerosols are removed from the model, only the asymmetries and random distribution of the molecules will reduce the degree of polarization from the 100% value predicted for an ideal spherical Rayleigh scatterer. The value attained by this model is identical to the 94% maximum predicted previously (Bohren, 1996).

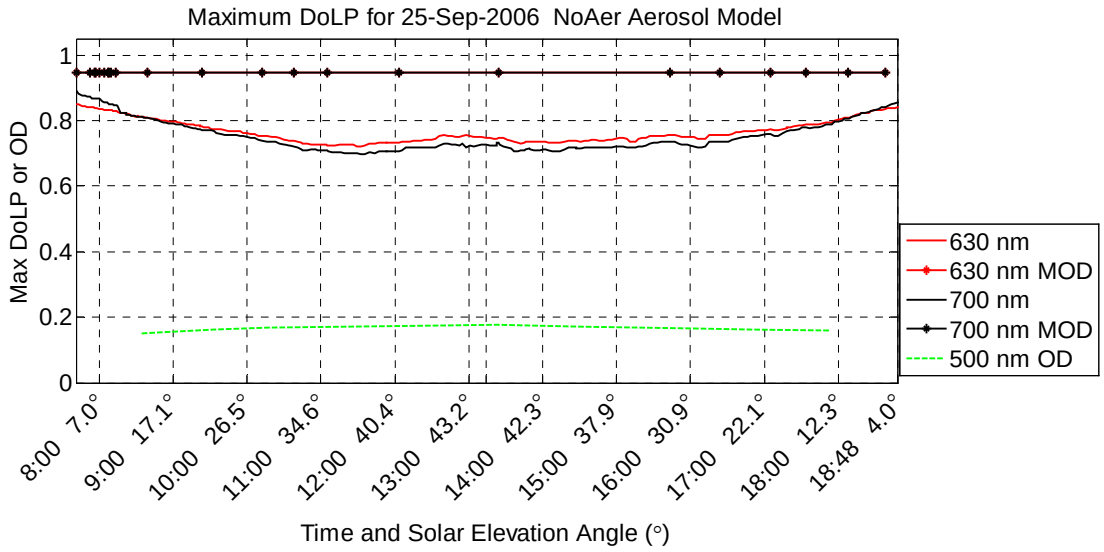

Figure 7.19. Long-wavelength model without multiple scattering or aerosols

The above data show that the single-scatter model is capable of predicting DoLPs over 90%, so the aerosols in the single-scatter model are reducing the DoLP by too much near sunrise and sunset. The model appears to be too sensitive to total extinction near these points, and may need to be adjusted for this error.

Sky with Moderate Aerosol Content (OD ≈ 0.22)

In late August and early September 2006, forest fires burned in both eastern and western Montana. In particular, fires burned in the Paradise Valley southeast of Bozeman in early September. These fires created some of the worst visibility ever seen in Bozeman

on September 5, 2006 (see the next section for data from this day). By September 11, the smoke had cleared considerably and the Tobacco Root Mountains (~70 km away) were barely visible on the horizon. This day provided moderate aerosol data.

Rural Aerosol Models. Figure 7.20 shows the results of the aerosol models with multiple scattering. For this day, the aerosols dropped significantly over the course of the afternoon and the model tracks appropriately. Still, the multiple-scatter model consistently under-predicts the DoLP. Also, notice that the order of the different wavelength plots is still inverted—with the 700-nm wavelength staying the highest during mid-day.

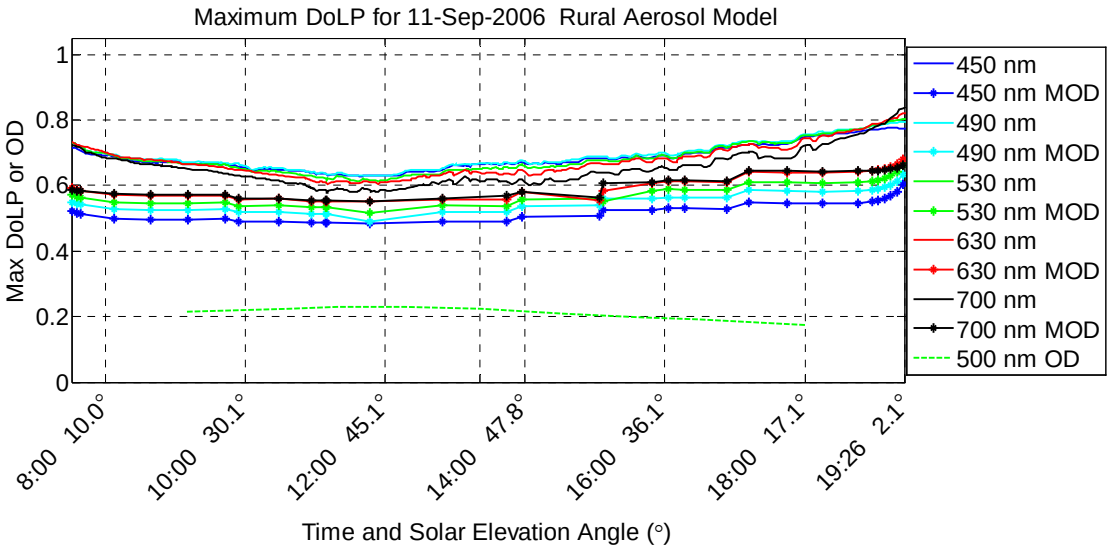

Figure 7.20. Moderate-aerosol max DoLP with Rural aerosol multiple-scatter model.

With moderate aerosols, single-scatter models over-predict the DoLP for all wavelengths (Figures 7.21-7.22). This is a departure from the low-aerosol Rural models, which predict the longer wavelengths well.

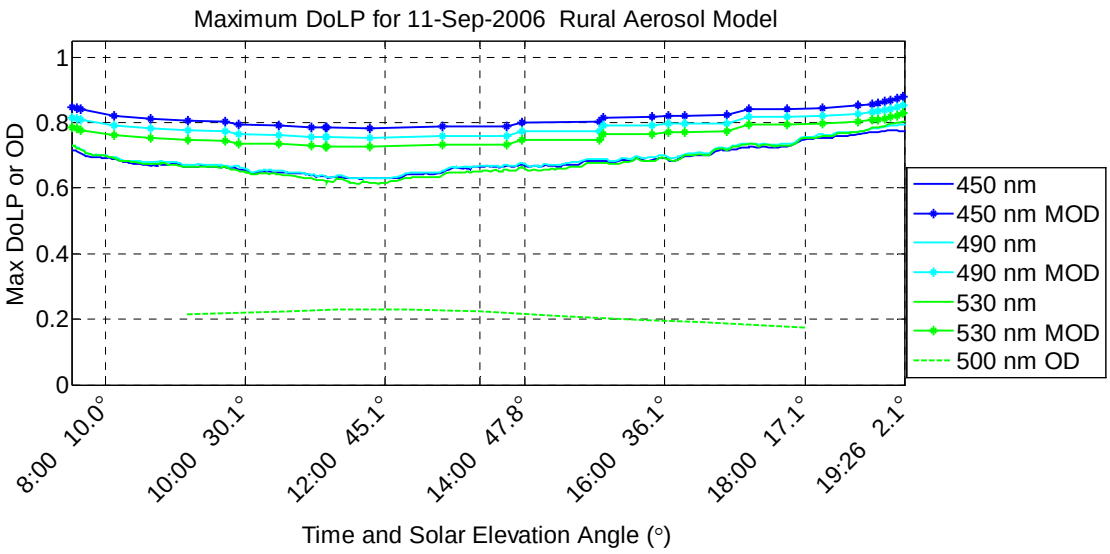

Figure 7.21. Moderate-aerosol max DoLP with Rural single-scatter model 450-530 nm.

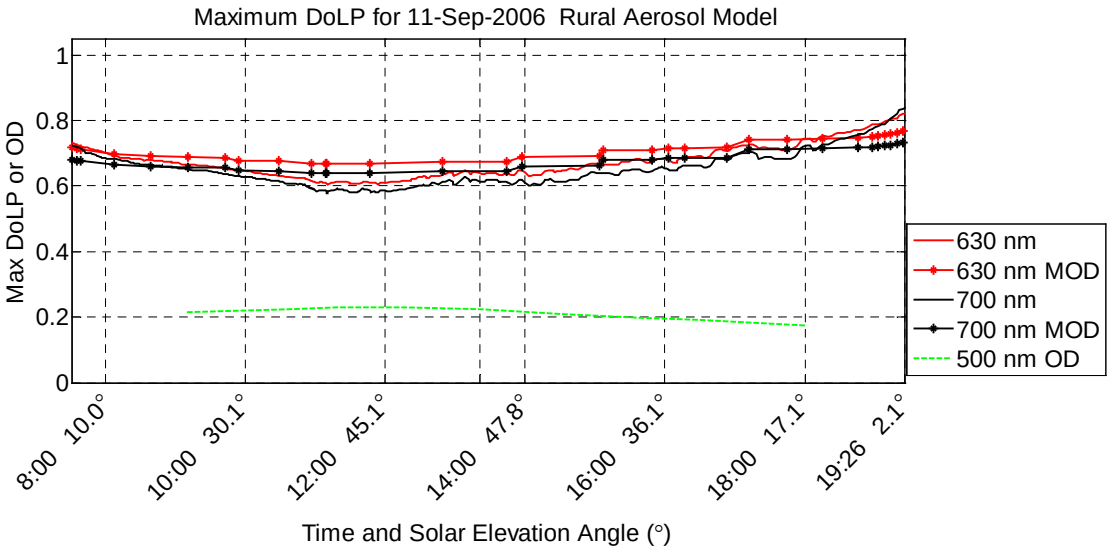

Figure 7.22. Moderate-aerosol max DoLP with Rural single-scatter model 630, 700 nm.

For the mid-day clear sky, a single-scatter model seems to be adequate for the longer wavelengths, but as aerosols increase, the scattering in the boundary layer causes the model to separate from the actual data. Notice that as the optical depth at 500 nm begins to drop below 0.20, the single-scatter 630-nm and 700-nm models become

accurate to within the instrument accuracy, but above this point they diverge from the instrument. The errors for 630 and 700 nm have now become as much as 7% during the mid-day, while the shorter wavelengths are worse than the low-aerosol models.

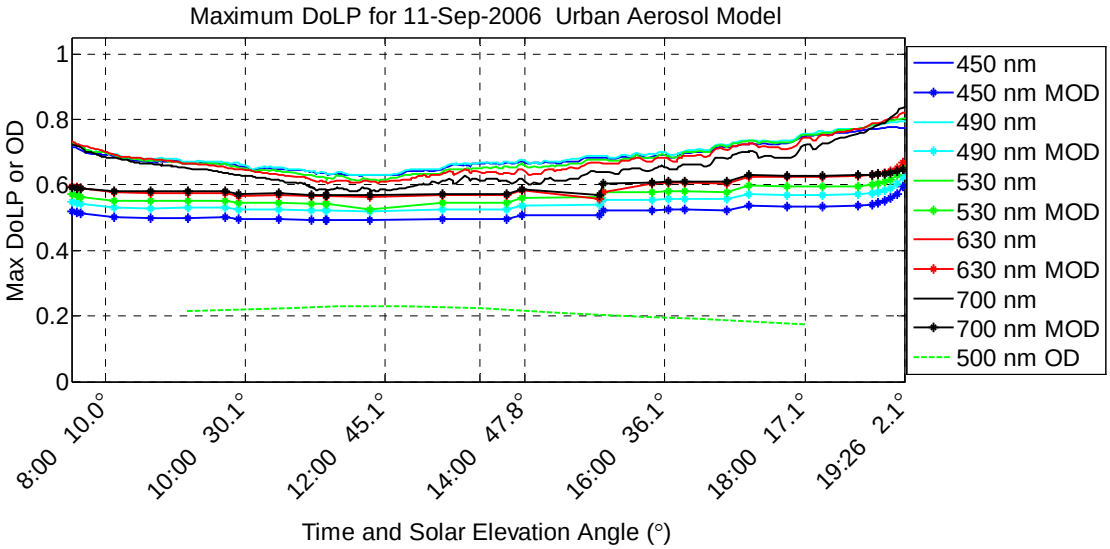

Figure 7.23. Moderate-aerosol max DoLP with Urban aerosol multiple-scatter model.

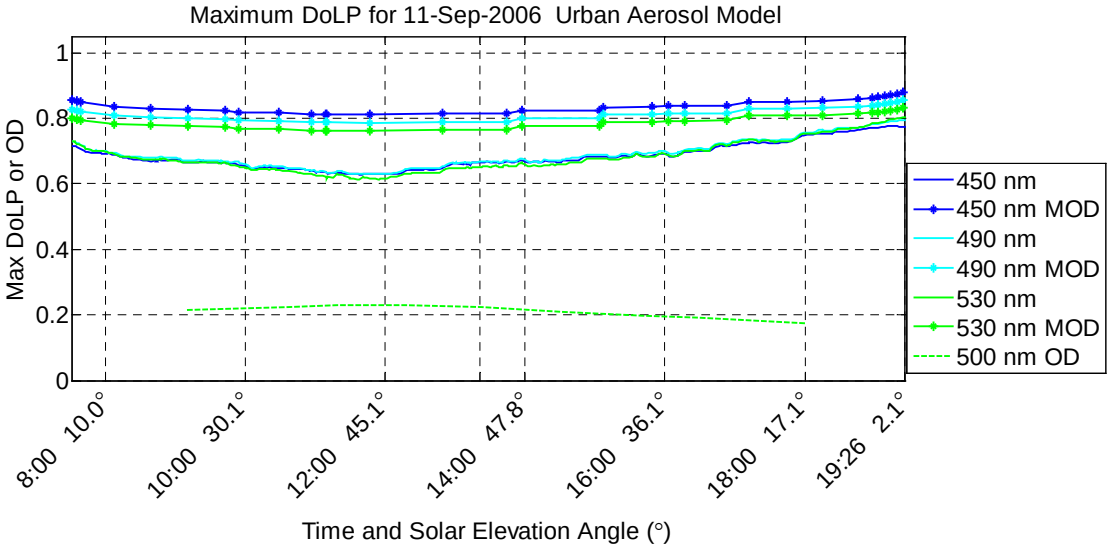

Figure 7.24. Moderate-aerosol max DoLP with Urban single-scatter model 450-530 nm.

Urban Aerosol Models. Urban models are shown in Figures 7.23-7.25. For the multiple-scatter model, the results are almost identical to the Rural model. The Urban model runs about 1% lower than the Rural model for most wavelengths. The single-scatter Urban models are similar to their Rural counterparts, but in all cases, they over-predict the measured DoLP to a larger extent than the Rural models.

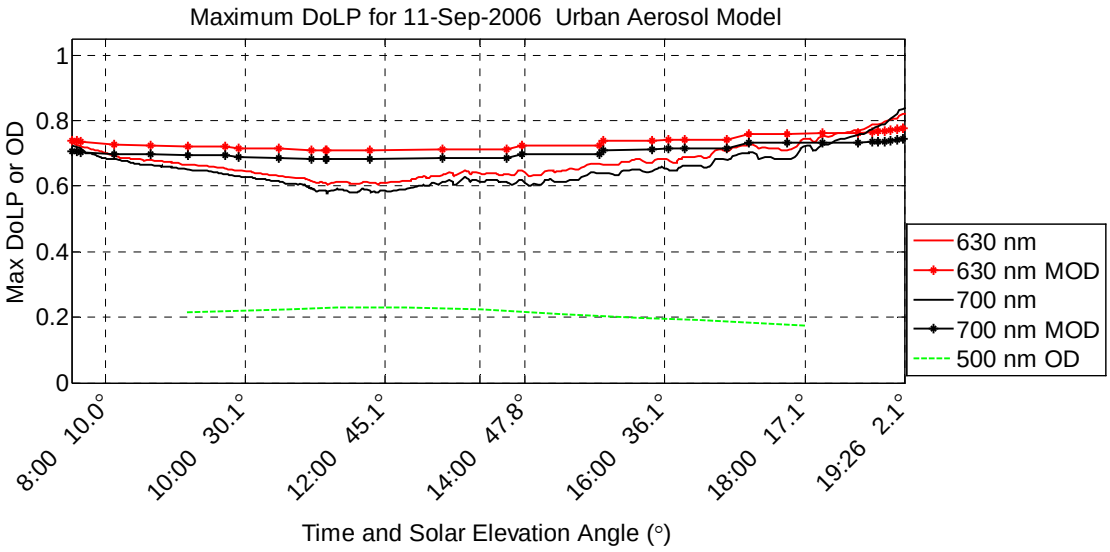

Figure 7.25. Moderate-aerosol max DoLP with Urban single-scatter model 630, 700 nm.

Tropospheric Aerosol Models. Finally, the Tropospheric models are shown in Figures 7.26-7.28. Similar to the low-aerosol sky case, the Tropospheric aerosol type produces much lower model maximum DoLP than the Urban and Rural types for the multiple scatter models.

For the single-scatter models, the Tropospheric aerosols ran closer than the other aerosol types. The better accuracy of the single-scatter Tropospheric aerosol type is probably coincidence, not a reflection of the overall accuracy of the model. The higher

reduction of the DoLP by the Tropospheric aerosol model is compensating for the over-prediction of the single-scatter model.

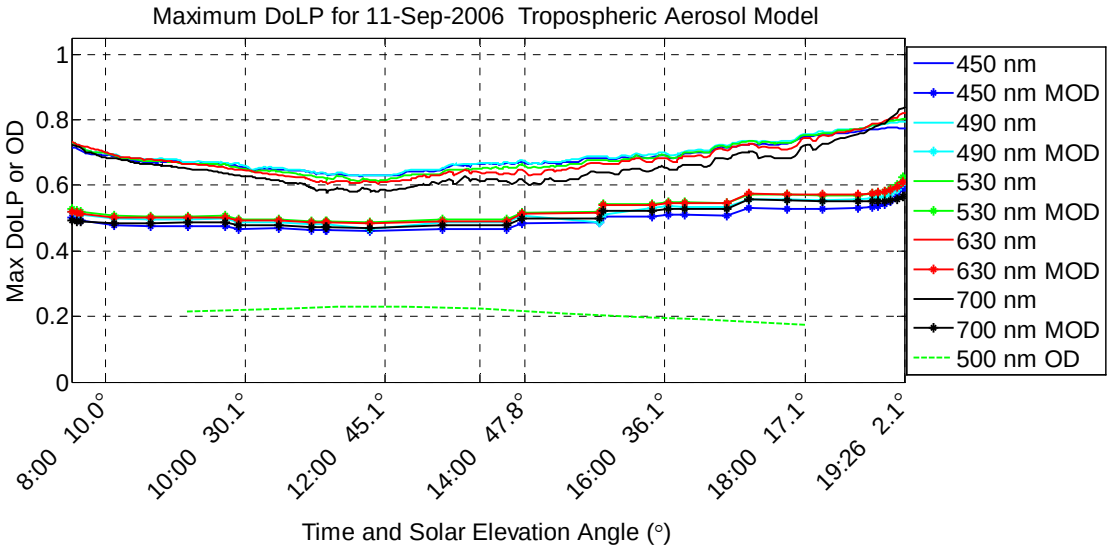

Figure 7.26. Moderate-aerosol max DoLP with Tropospheric multiple-scatter model.

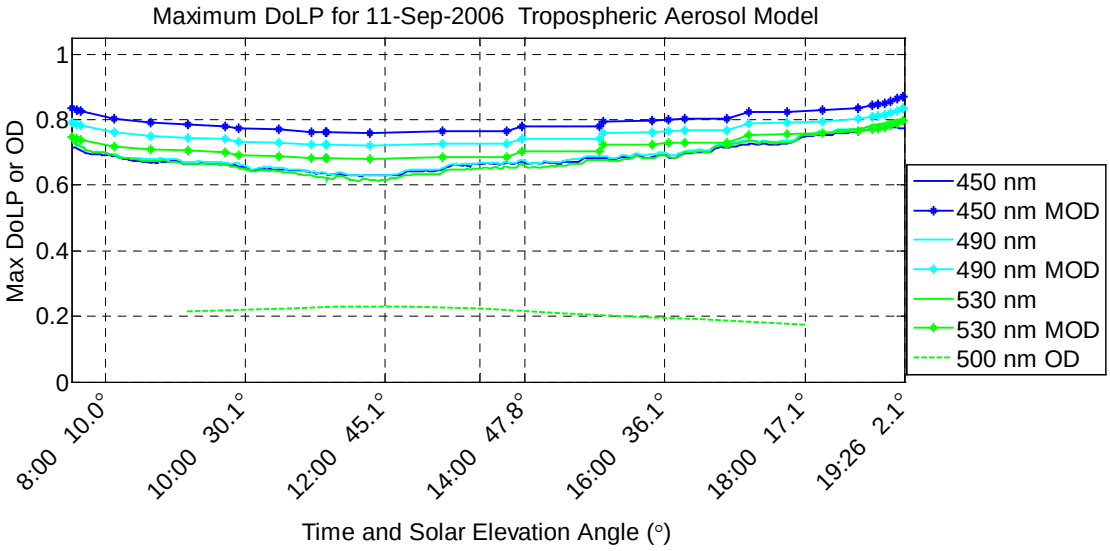

Figure 7.27. Moderate-aerosol max DoLP with Tropospheric single-scatter model 450-530 nm.

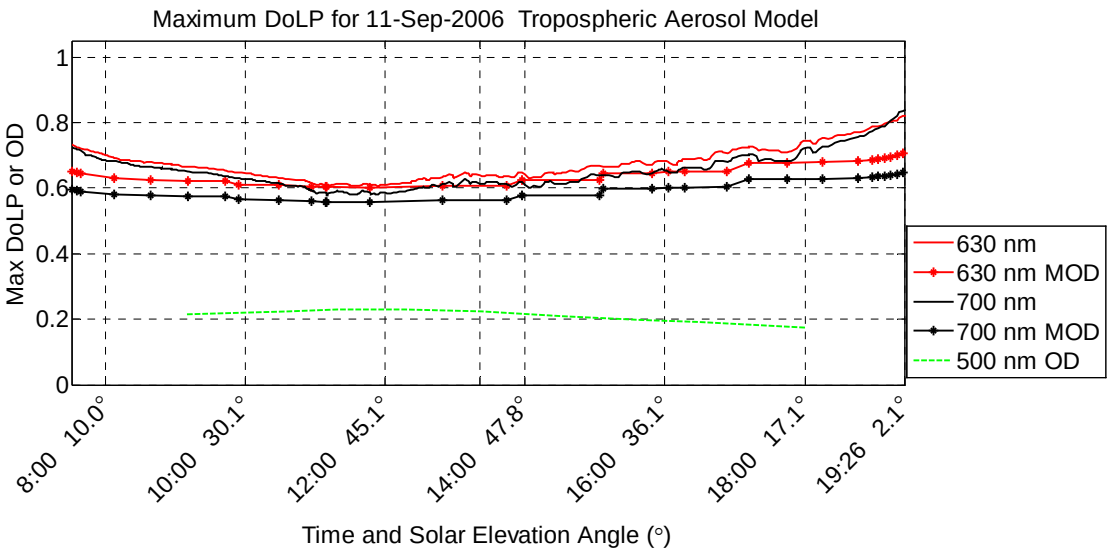

Figure 7.28. Moderate-aerosol max DoLP with Tropospheric aerosol single-scatter model 630-700 nm.

Sky with High Aerosol Content (OD ≈ 1.2)

September 5, 2006 provided a very dense aerosol layer—one of the worst Bozeman has ever seen. At some points in the afternoon, visibility on the ground was below 1.5 km. Only afternoon data were taken on this day. The bump in the data around 14:30 is from clouds that formed in the early afternoon. These clouds are seen in the data taken around this time. It is assumed that even the thinnest clouds went away later in the afternoon, but visibility was bad enough that it is unknown how many thin clouds were really above the aerosols. The optical depth is not shown in the figures since it is off scale. It slowly moved from 1.34 at 12:50 to 1.00 at 16:39. Later in the day it slowly increased to 1.25 at 18:10.

Rural Aerosol Models. Figures 7.29 and 7.30 show the multiple-scatter models for the high-aerosol day. For clarity, the shorter wavelengths have been separated from the longer wavelengths. The multiple-scattering model consistently under-predicts the

DoLP. During the mid-day, the long-wavelength errors are as much as 20%, while the shorter wavelengths are inaccurate by 10%.

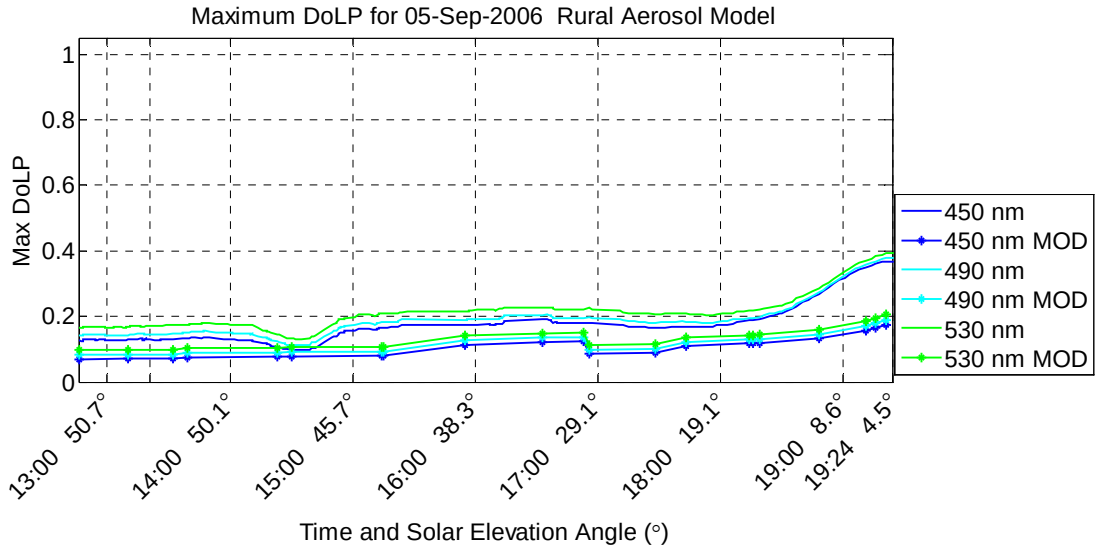

Figure 7.29. High-aerosol max DoLP with Rural aerosol multiple-scatter model 450-530 nm.

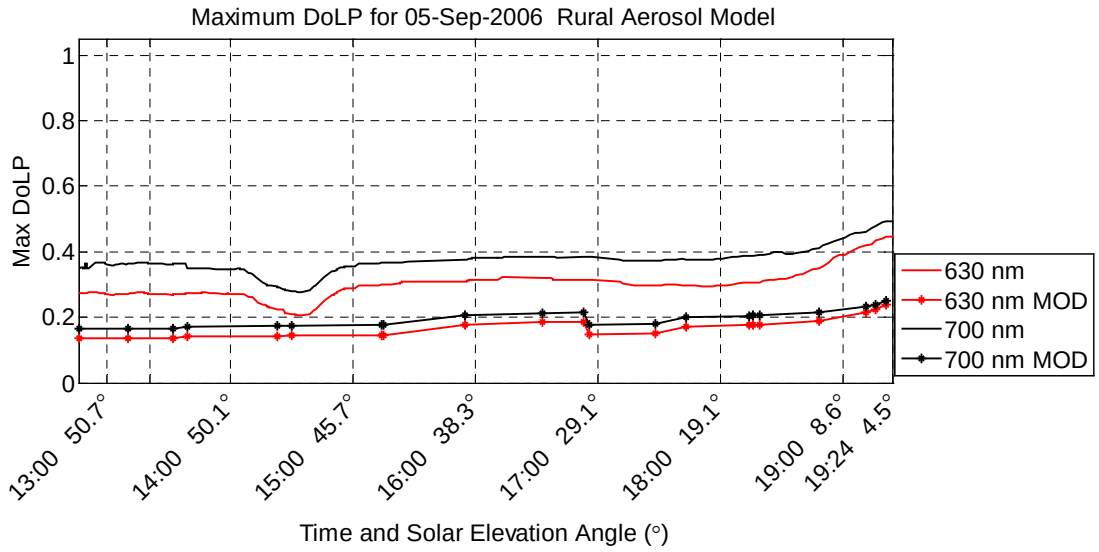

Figure 7.30. High-aerosol max DoLP with Rural aerosol multiple-scatter model 630, 700 nm.

Single-scatter models exhibit characteristics similar to the other models. Short wavelengths are not even close (Figure 7.31). Surprisingly, the largest error in the 700-nm wavelength model is only 6% (Figure 7.32).

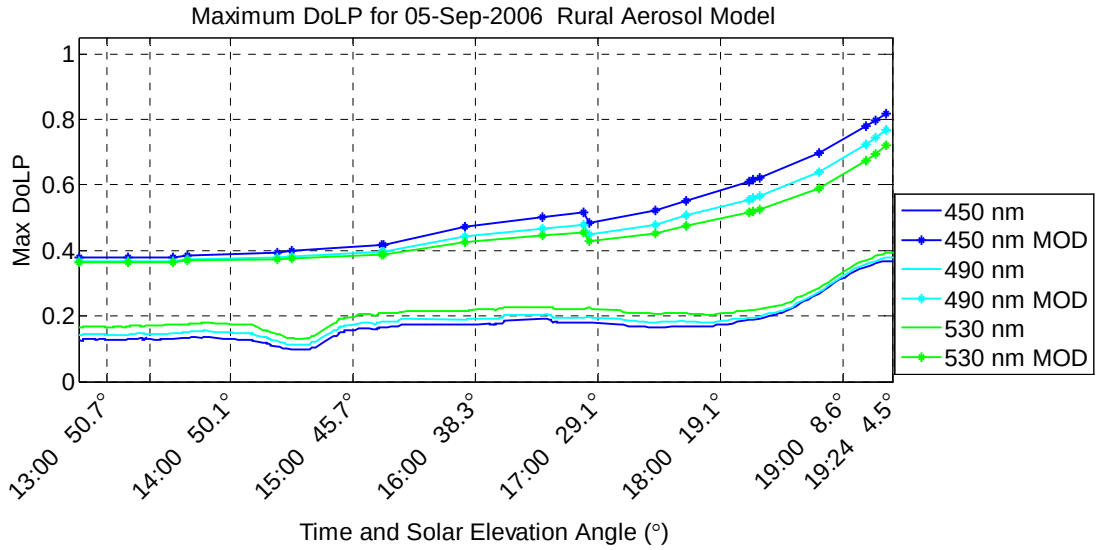

Figure 7.31. High-aerosol max DoLP with Rural aerosol single-scatter model 450-530 nm.

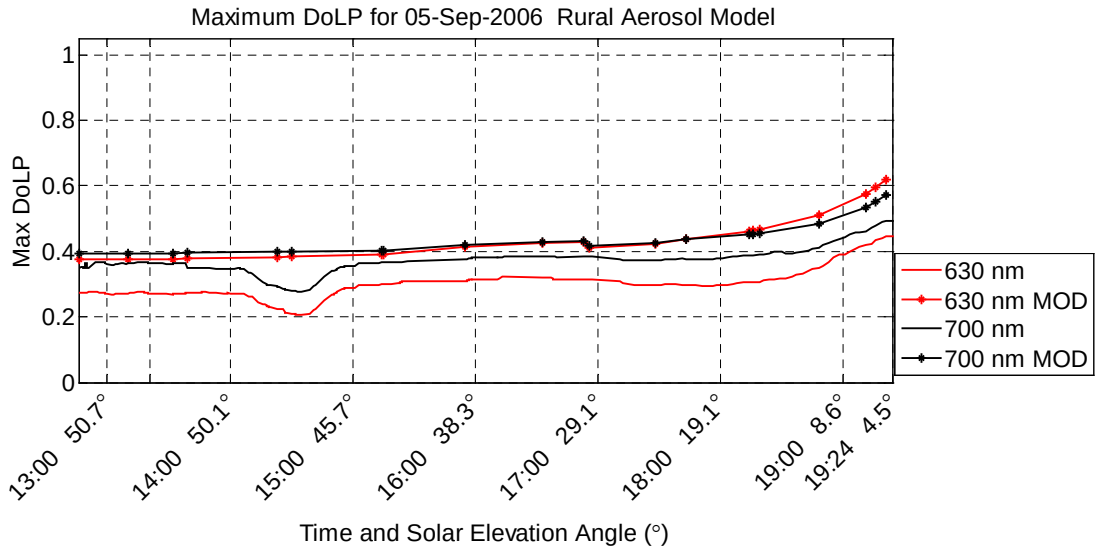

Figure 7.32. High-aerosol max DoLP with Rural aerosol single-scatter model 630, 700 nm.

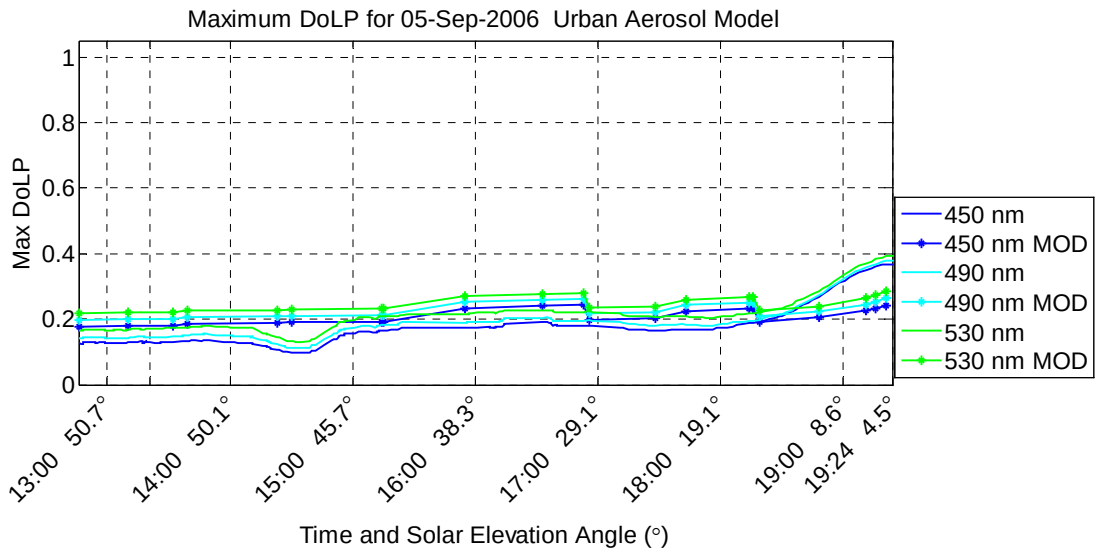

Figure 7.33. High-aerosol max DoLP with Urban aerosol multiple-scatter model 450-530 nm.

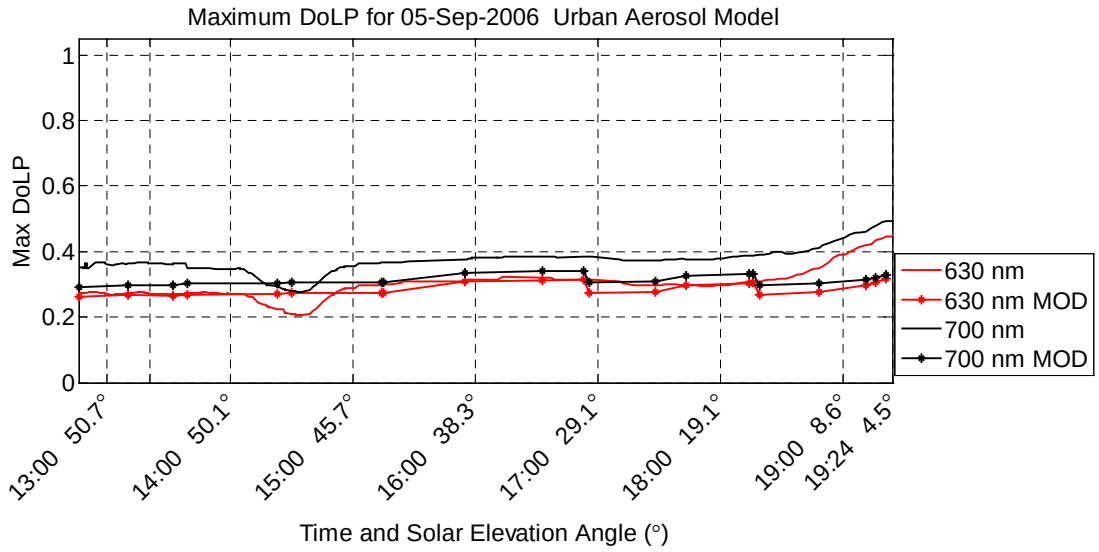

Figure 7.34. High-aerosol max DoLP with Urban aerosol multiple-scatter model 630, 700 nm.

Urban Aerosol Models. For all Urban multiple-scatter models, data were within 6%, except near sunset (Figure 7.33-7.34). These short-wavelength Urban cases are the only ones across all the models for which the multiple-scatter model is above the measured DoLP. Since the multiple scattering is modeled as unpolarized, all models

should be below the actual data. This suggests that either the Urban aerosol is a bad representation of the September 5 forest fire aerosols or another problem with the MODTRAN-P code exists. As with the Rural models, the single-scatter Urban models are always very bad (Figures 7.35-7.36).

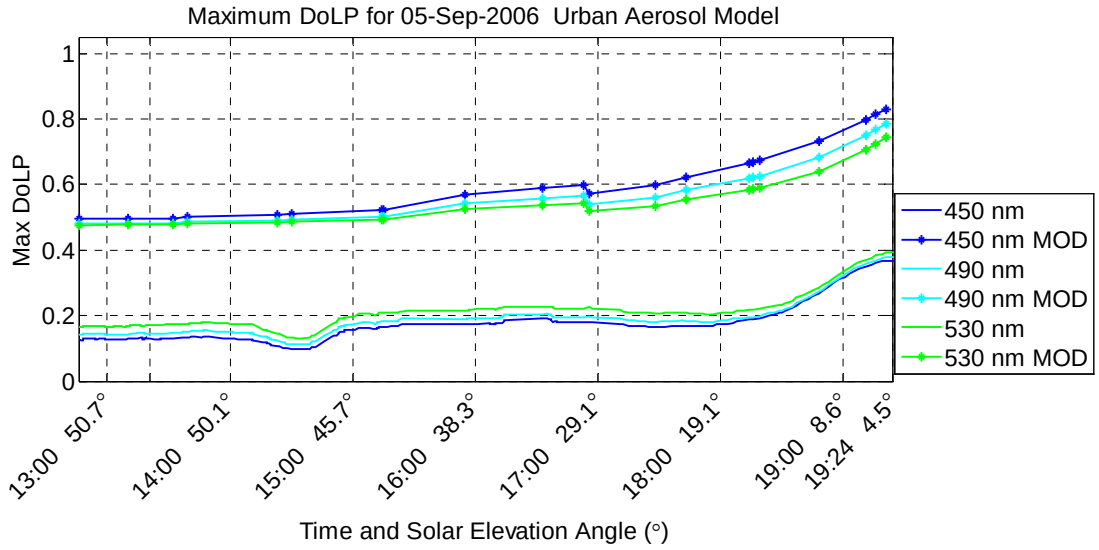

Figure 7.35. High-aerosol max DoLP with Urban aerosol single-scatter model 450-530 nm.

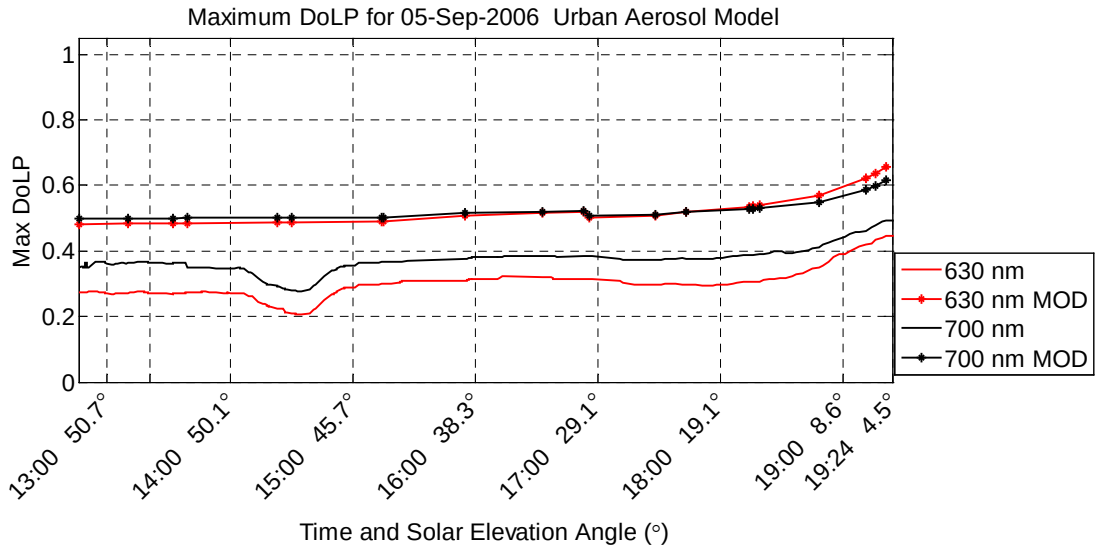

Figure 7.36. High-aerosol max DoLP with Urban aerosol single-scatter model 630, 700 nm.

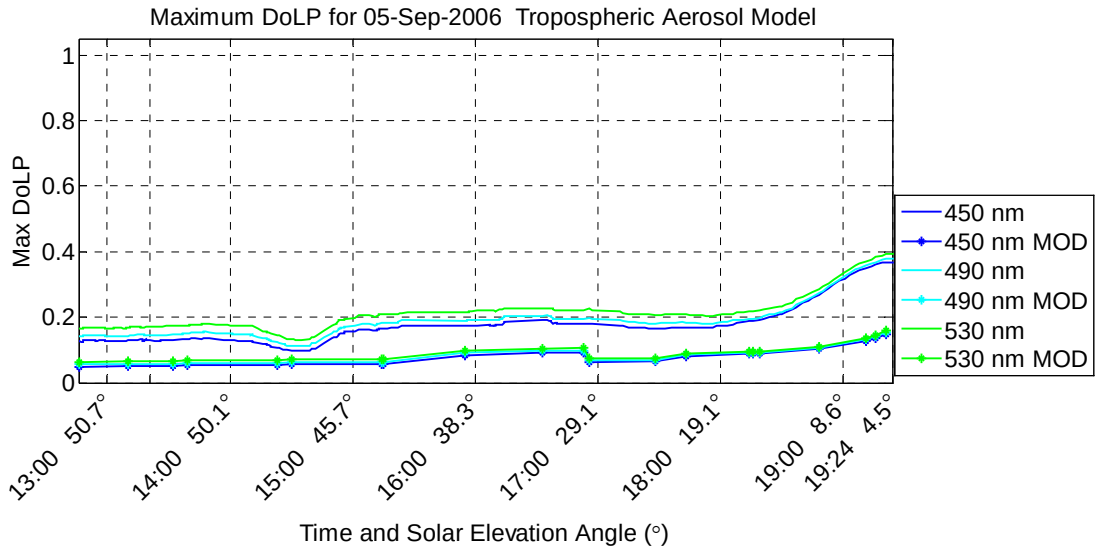

Figure 7.37. High-aerosol max DoLP with Tropospheric aerosol multiple-scatter model 450-530 nm.

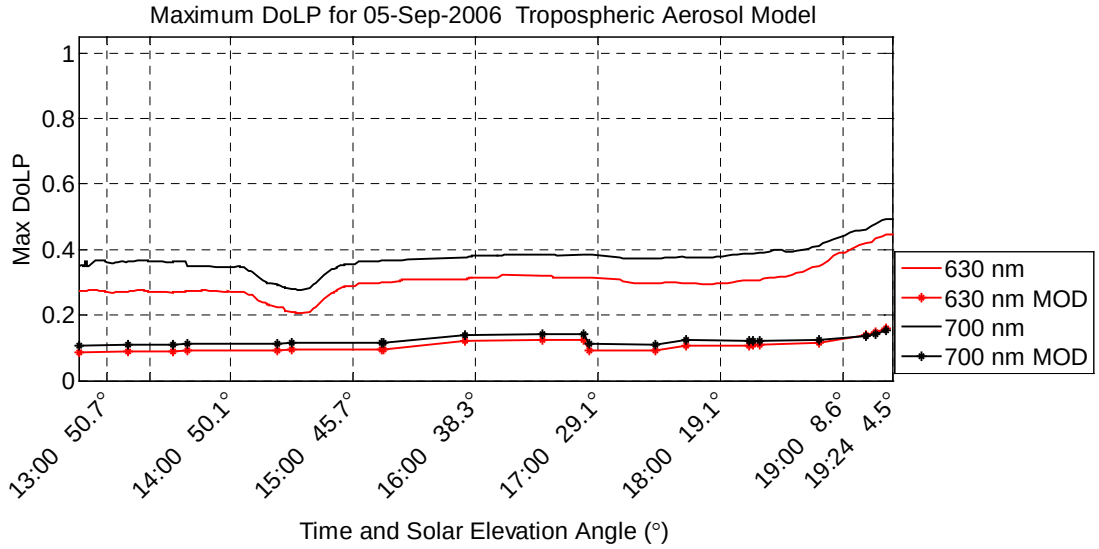

Figure 7.38. High-aerosol max DoLP with Tropospheric aerosol multiple-scatter model 630, 700 nm.

Tropospheric Aerosol Models. Tropospheric aerosols did not perform any differently than the previous Tropospheric models (Figures 7.37-7.40). Multiple-scatter predictions were too low. Single-scatter short wavelength predictions were very bad, but

the longer wavelengths were within 5%. Again, this is probably a result of the competing processes—the high polarization prediction of the single-scatter model against the too-severe DoLP reduction by the Tropospheric aerosol.

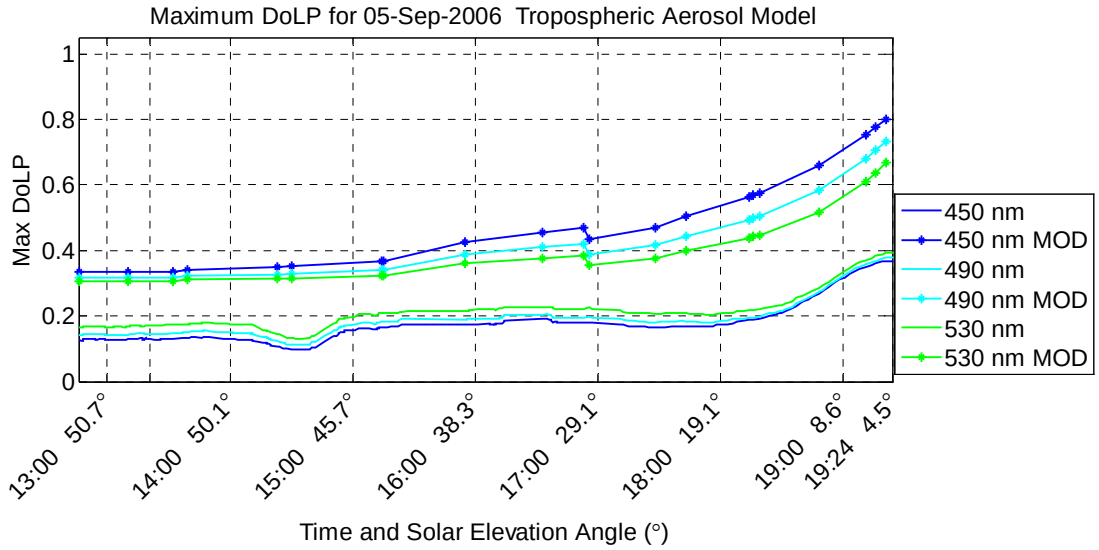

Figure 7.39. High-aerosol max DoLP with Tropospheric aerosol single-scatter model 450-530 nm.

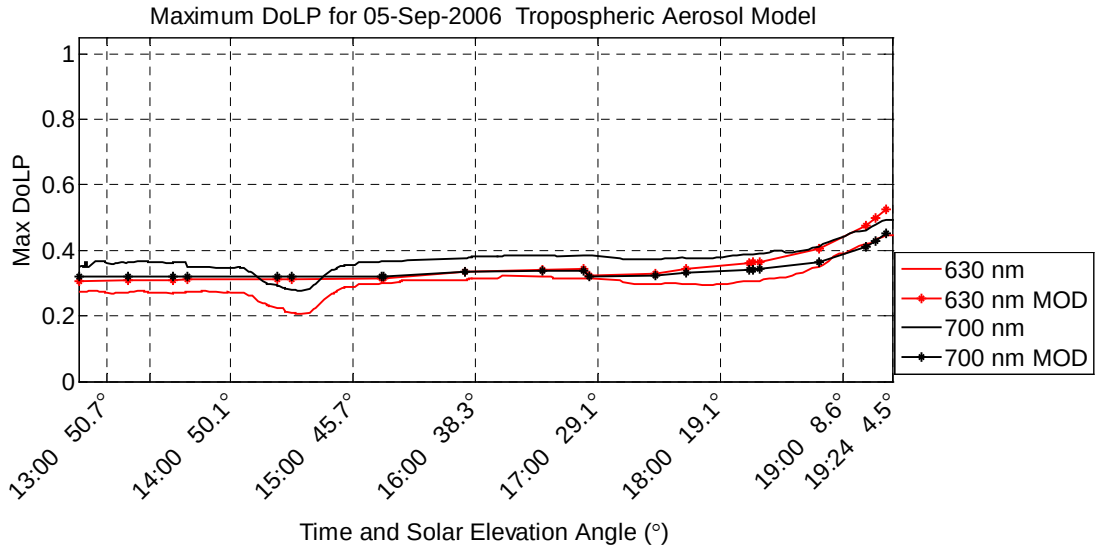

Figure 7.40. High-aerosol max DoLP with Tropospheric aerosol single-scatter model 630, 700 nm.

Zenith Slice Comparisons with MODTRAN-P

Although the maximum degree of polarization is the primary variable to be validated in the clear sky model, it was also desired to compare the model with measurement s made in sky regions away from the maximum degree of polarization. Since the mid-day September 25, 2006 clear-sky data seemed to be accurately modeled for 630 and 700 nm with a single-scatter model using the Rural aerosol type, these cases were used to assess the DoLP accuracy through a slice of the sky that included the solar position and zenith. The time of both slices was picked to be 13:00. Figures 7.41 and 7.42 show the results for both scattering models at 700 nm.

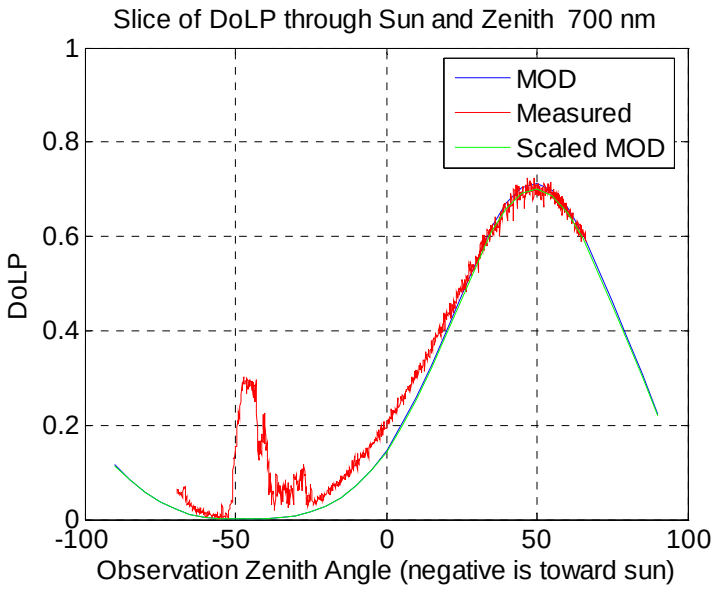

Figure 7.41. DoLP image slice at 13:00 MDT on September 25, 2006 with single-scatter model 700 nm. The green line shows the results of the model if it were to be scaled to have identical maximum DoLPs as the data. The bump in the measured data near the model zero is caused by the sun occulter. (This is the reflected DoLP of the back of the sun occulter.)

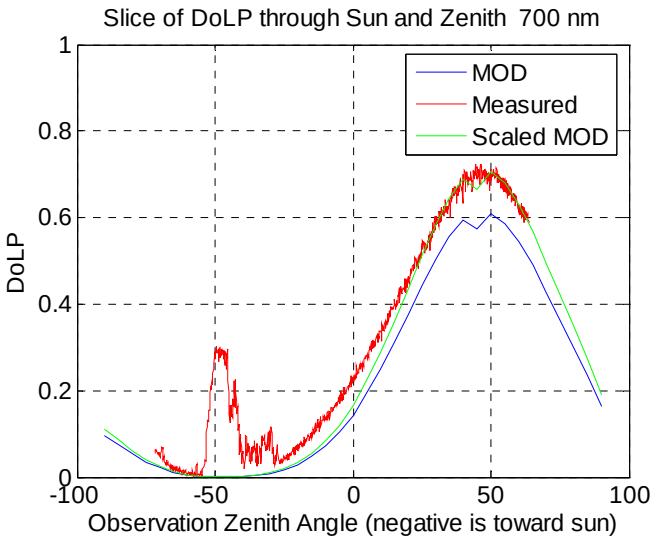

Figure 7.42. DoLP slice at 13:00 MDT on September 25, 2006 with multiple-scatter model 700 nm. The green line shows the results of the model if it were to be scaled to have identical maximum DoLPs as the data. The bump in the measured data near the model zero is caused by the sun occulter. (This is the reflected DoLP from the back of the sun occulter.) The bump in the model near the maximum appears to be a problem with the MODTRAN model itself, not input parameters.

Since the exact observation zenith angle for each pixel in the image is not known, the plot of the actual data was obtained by the following procedure: First, the angle of polarization image was displayed. Using the contour lines of the angle of polarization, the confluence of these lines (which happens at each neutral point) was used to approximate the exact position of the sun behind the solar occulter. The center of the image was estimated and the DoLP was extracted from a line that included these two points. The spike in the DoLP (red line) is not actual sky data, but displays the DoLP of the underside of the occulter. Visual fitting of the data confirms that the minimum DoLP of the model aligns with the solar position estimate. Second, the maximum DoLP was found for both the model and the actual data. Third, the data slice was stretched linearly to align the minimum of the data to the estimated solar point and the maximum of the data to the

maximum of the model. This linear stretching is valid only if the 16-mm fisheye lens actually uses a true equidistance projection—which Nikon claims it does. Finally, to allow comparison of the model to the actual data, the entire model was scaled to match the model maximum DoLP with the actual maximum DoLP (green line).

Inspection of the plots proves that near the point of maximum DoLP, the model accurately predicts the DoLP. Near the sun, neither model predicts the two neutral points, but instead shows one neutral point at the solar point. This is due to the invalid treatment of multiple scattering. In spite of the uncertainties in the exact location of the sun under the occulter, it can be confidently concluded that between 25° and 50° from the sun the DoLP is under-predicted by both models. (This is the area of the plot around 0° of observation zenith angle.) This conclusion is also supported by the 630-nm slice, which shows similar characteristics (Figures 7.43 and 7.44).

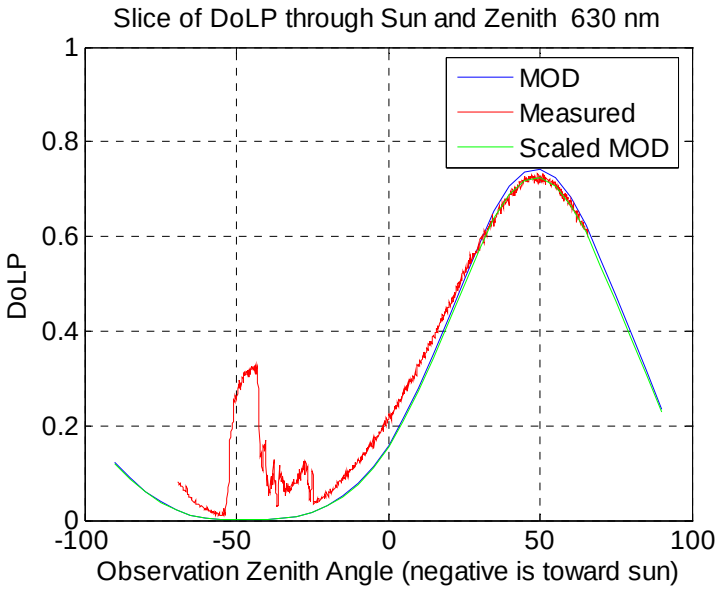

Figure 7.43. DoLP Slice at 13:00 MDT on September 25, 2006 for 630 nm with Single-scatter Model. The bump in the measured data near the model zero is the sun occulter. (This is the reflected DoLP from the back of the sun occulter.)

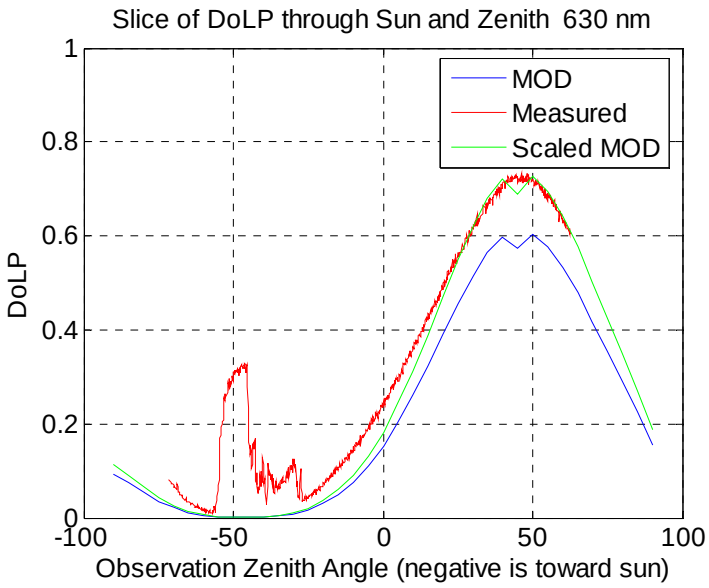

Figure 7.44. DoLP Slice at 13:00 MDT on September 25, 2006 for 630 nm with Multiple-scatter Model. The green line shows the results of the model if it were to be scaled to have identical maximum DoLPs as the data. The bump in the measured data near the model zero is the sun occulter. (This is the reflected DoLP from the back of the sun occulter.)

For both wavelengths, the single-scatter model is a slightly better model with maximum errors being about 5%, while the multiple-scatter model had errors as much as 6%. Close inspection of the plots reveals that the observed zenith angle of maximum degree of polarization for the multiple-scatter models is about 2° closer to the sun than the single-scatter models. Since this is a significant difference, absolute calibration of the angle of observation for the instrument should be considered for future MODTRAN-P validation work.

MODTRAN-P Clear-Sky DoLP Validation Conclusions

1. Multiple-scatter models—with one exception—consistently under-predict the DoLP for all wavelengths because of the inappropriate modeling of the multiple scattered

component as completely unpolarized. For low-aerosol skies, these models preserve the shape of the maximum DoLP near sunrise and sunset, but for larger optical depths they begin to lose their shape. Single-scatter models perform exactly opposite. They are too flat for low-aerosol skies, but for high optical depths they match the shape of the sunset/sunrise data almost exactly.

2. For all wavelengths above 600 nm, the multiple-scatter and single-scatter models can be used as a bound on the DoLP. The multiple-scatter model is lower than the measured data, while the single-scatter model is always higher than the measured data.
3. For a low-aerosol sky, single-scatter models are accurate to within instrument accuracy during the mid-day for wavelengths greater than 600 nm when either the Urban aerosol type or the Rural aerosol type is used. As the total optical depth at 500 nm increases above 0.20, the accuracy of the model moves above the error bounds of the instrument. For shorter wavelengths, the single-scatter model consistently over-predicts the maximum DoLP. This is expected because the wavelength dependence of Rayleigh scattering causes multiple scattering to be larger at shorter wavelengths.
4. For solar elevations near sunrise and sunset, single scatter models are less than adequate for the long wavelengths. The models consistently under-predict the DoLP in these regions. This suggests that the dependence of the DoLP reduction on aerosol extinction may be too extreme. The model seems to be too sensitive to total extinction in the boundary layer.

5. The standard Tropospheric aerosol type performs worse than the Urban and Rural types for all multiple-scatter models. Conversely, when used in the single-scatter model, the Tropospheric aerosol type performs the best overall for the three days. For mid-day data, maximum errors of 10% could be expected for 630 and 700 nm. Since multiple scattering is not a driving variable at these wavelengths, this suggests that the aerosol content from the forest fires most closely matched this standard aerosol model in the long wavelengths.
6. Aerosol type is a highly important variable. For high-aerosol-content skies, the difference between the models can be as much as 20%. For low aerosol content skies, the difference between models can be as much as 10%. For some special cases, these problems are not severe. For example, any of the standard aerosol models predict a fairly accurate polarization above 600 nm when used with the single-scatter model. Nevertheless, a complete MODTRAN-P validation will need instrumentation and software that can generate aerosol phase functions from an aerosol size distribution and complex refractive index. (MODTRAN-P also needs to be updated to handle this information.)
7. Modeling of the zenith slice through the sun showed than the DoLP in the region of the sun and the region of maximum degree of polarization was accurate. Still, the neutral points are not seen in the model because of the improper implementation of multiple scattering. Also, model regions that were 25° to 50° from the sun exhibited DoLPs of about 5% less than the measurements.

Cirrus Cloud Models

For cloud model validation, only partially cloudy skies were used. As stated before, a completely overcast sky will not have significant polarization. To verify the cloud models, four variables are needed for initializing the MODTRAN-P model: cloud type, cloud height, cloud thickness, and cloud extinction. It was difficult to be certain of the cloud type with the lower-altitude clouds: cumulus, stratus, etc. Also, the high extinctions of the cumulus clouds quickly attenuated the LIDAR signal. It was impossible to be confident that the LIDAR was penetrating the entire cloud. Therefore, the cloud thickness measurement was always suspect.

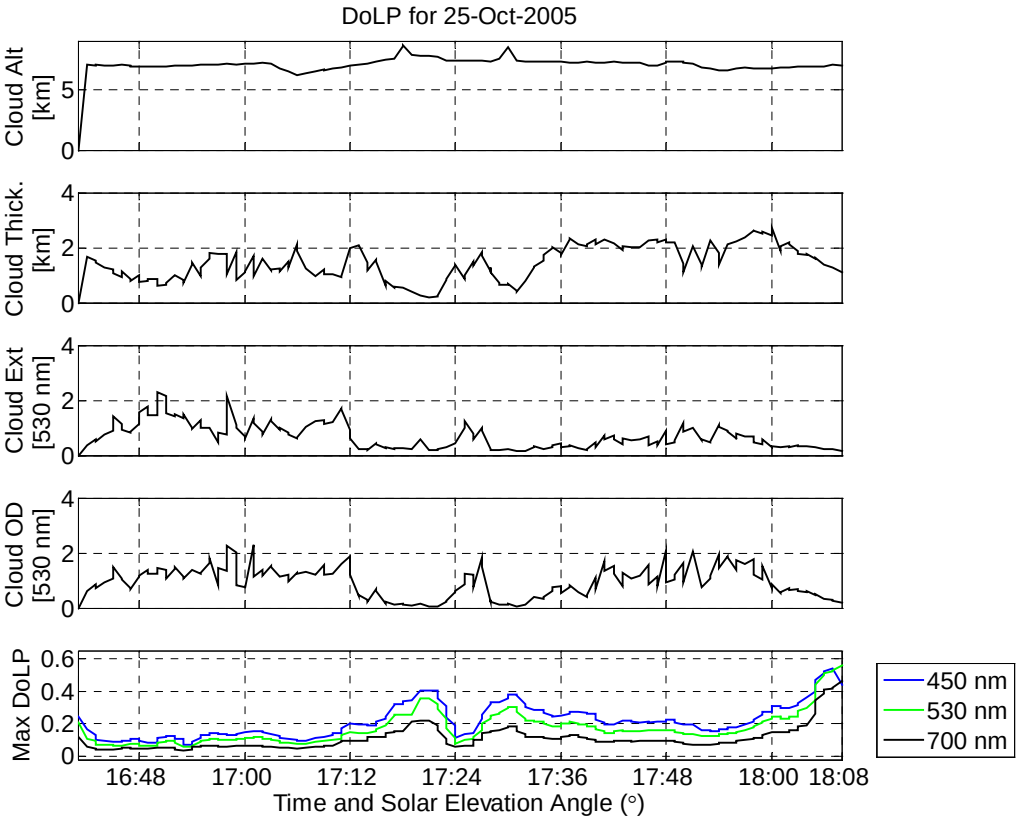

Figure 7.45. Cloud Statistics and DoLP for October 25, 2005. Cloud extinction units are km^{-1} and DoLP colors represent the colors of the actual wavelengths.

For cirrus clouds, the cloud type was easier to determine based on the depolarization ratio given by the LIDAR and the cloud heights over 7 km. The thin layers found over the late afternoon of October 25, 2005 gave a perfect scenario for testing the MODTRAN-P cirrus cloud model. DoLP readings were taken by the polarimeter while looking at zenith beside the LIDAR. Because of the broader FOV of the polarimeter, the center of the region of overlap between the polarimeter and the LIDAR was found by correlating the reduction of all DoLP readings with the total signal return from the cloud. A 40x40 pixel area was selected around this point. Figure 7.45 shows the cloud statistics and measured DoLP. The DoLP inversely tracks the optical depth of the cloud.

The MODTRAN cloud variable was set to visual cirrus clouds (ICLD=18). Since various cloud thicknesses were viewed, it can be confidently asserted that—with the exception of the thickest cloud—the cloud thickness measurements were accurate. Cloud extinctions were extracted using a Klett boundary algorithm similar to the far-end Klett solution described in the *LIDAR Inversion – Aerosol Extinction Profile* section. The new version of the algorithm used a near-end instead of far-end boundary solution. The optical depth solution (using a solar radiometer) was not considered since spatial variability in the cloudy sky makes it invalid. This near-field inversion used a point below the cloud to start the process. To reduce the sensitivity of the model to a static range, the boundary altitude was randomly selected between 5 and 6.5 km. These selected altitudes were sufficiently above the aerosol boundary layer to assume a boundary point. For this region, backscattered signal was assumed to come exclusively from molecular scattering. The extinction of the backscattered signal at the randomly selected altitude formed the

boundary condition for the Klett algorithm. With this condition in place, the extinction-to-backscatter ratio was assumed in the LIDAR inversion.

For retrieval of aerosol extinction, measurements by previous investigators were used to assume a backscatter-to-extinction ratio. A summary of previous research showed that the ratio varies little over a given aerosol type (Kovalev, 2004, pg. 229). However, in the case of cirrus clouds, large variations in the extinction-to-backscatter ratio complicate the ratio assumption. Preliminary modeling displayed a strong dependence of the modeled DoLP upon the value of the backscatter-to-extinction ratio selected for the LIDAR inversion. Still, extreme values of the ratio within the literature were used to determine the bounds of the model. Previous investigators reported values between .020 and .050 for all cirrus cloud investigations (Chepfer, 1999; Platt, 1987; Young, 1995). These values reflected an equivalent backscatter-to-extinction ratio that accounts for multiple scattering. An equivalent ratio is important because multiple scattering cannot be neglected in cirrus clouds (Platt, 1981). Although Young did not report a FOV, Platt and Chepfer reported FOVs of 2.5 and 3.5 mrad, respectively. Both researchers reported equivalent backscatter-to-extinction ratios of .02-.050. Although multiple-scattering should be dependent upon FOV, comparison of these two investigators shows little dependence between the equivalent backscatter-to-extinction ratio—which includes multiple scattering—and the FOV (Table 7.1). For the MAML system with Aperture #10, the half-angle FOV is 4.41 mrad. Although slightly larger than previous investigators, the slightly larger FOV is not expected to significantly increase the multiple scattering component. If anything, the backscatter will be increased, so the backscatter-to-extinction

ratio will be slightly higher than these values. This fact is important for interpreting the models shown.

Table 7.1. Equivalent backscatter-to-extinction ratios for cirrus clouds reported with receiver FOV for previous investigation (Chepfer, 1999; Platt, 1987; Young, 1995).

Investigator	Receiver half-angle FOV (mrad)	Backscatter-to-extinction ratios reported
Chepfer, et al.	3.5	.022-.051
Platt, et al.	2.5	.020-.050
Young	Not reported	.026-.050

Previously it has been reported that the near-field Klett algorithm is unstable for clouds (Kovalev, 2004, pg. 182). This instability can be caused by an erroneous boundary condition or invalid backscatter-to-extinction ratio. When this algorithm was used with large backscatter-to-extinction ratios (K), the algorithm remained stable. For this specific data set, backscatter-to-extinction ratios below 0.030 caused the algorithm to become unstable—the algorithm returned negative values. Figure 7.46 shows an example of this instability.

Because of the inversion instability below K=0.020, the LIDAR-derived data of cloud height, cloud extinction, and cloud thickness were used with three different backscatter-to-extinction ratios to model the DoLP—0.060, 0.050, and 0.030. The 0.060 ratio was added to account for any possible increase in the multiple scattering by the larger field of view of the MAML system. Figures 7.47-7.49 show the results of the cirrus cloud models.

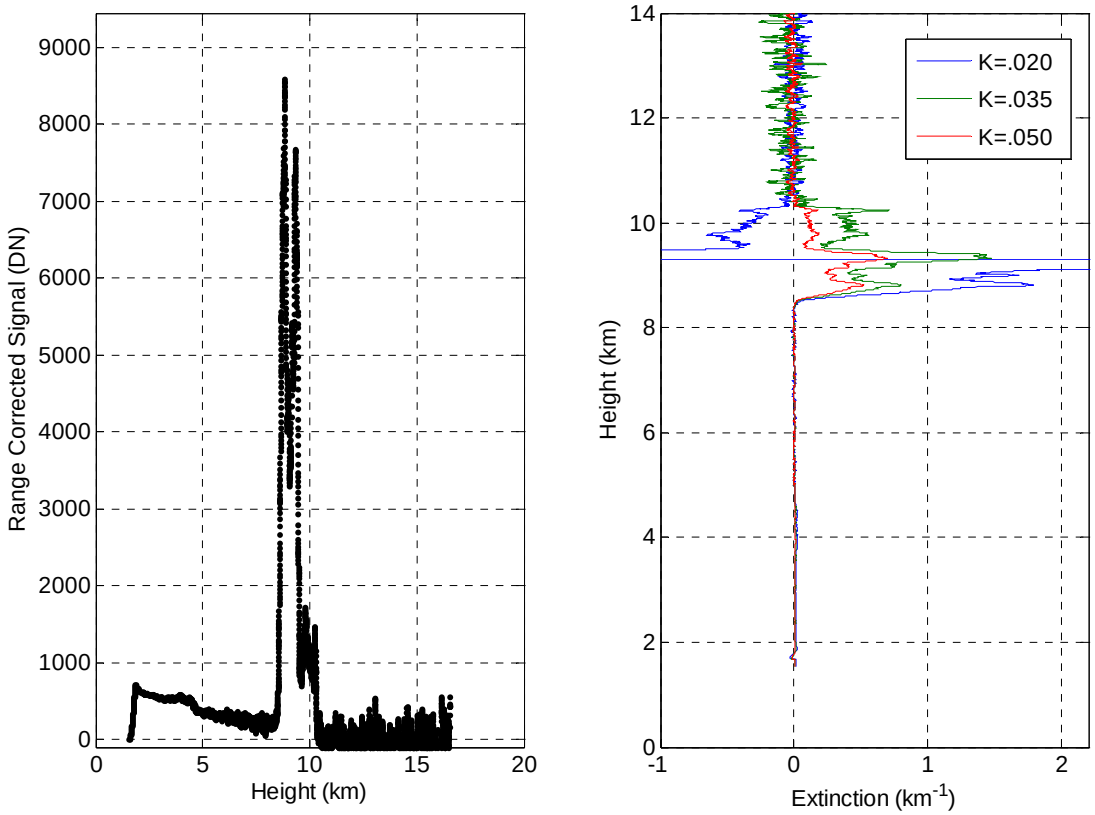

Figure 7.46. Instability in the near-field Klett algorithm. *K* represents the backscatter-to-extinction ratio. Notice that the blue line shows the instability for the cirrus cloud extinction when *K*=0.020.

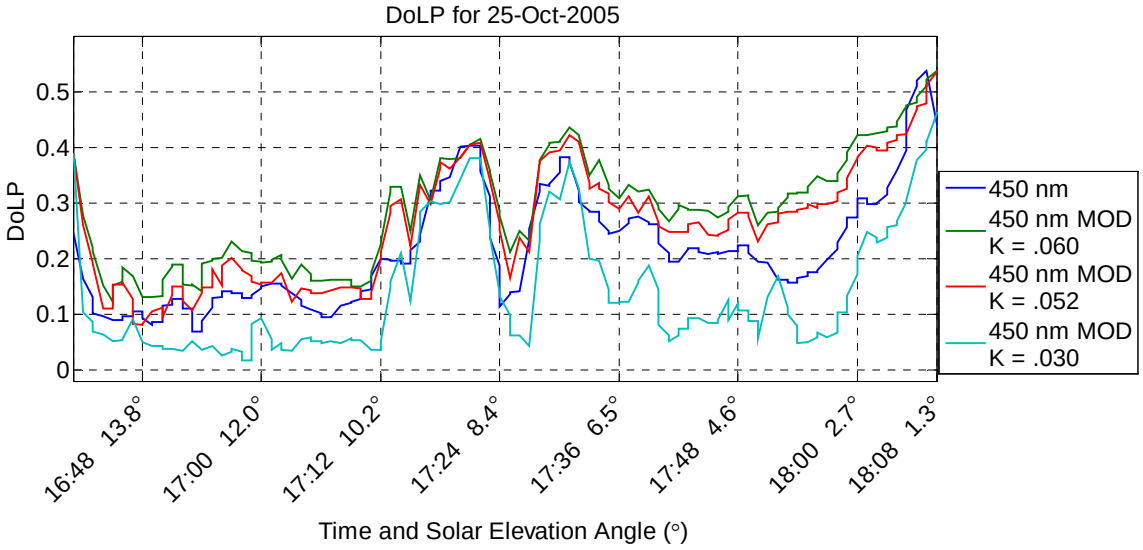

Figure 7.47. Cirrus cloud models for October 25, 2006 at 450 nm. MODTRAN-P models are designated by 'MOD'.

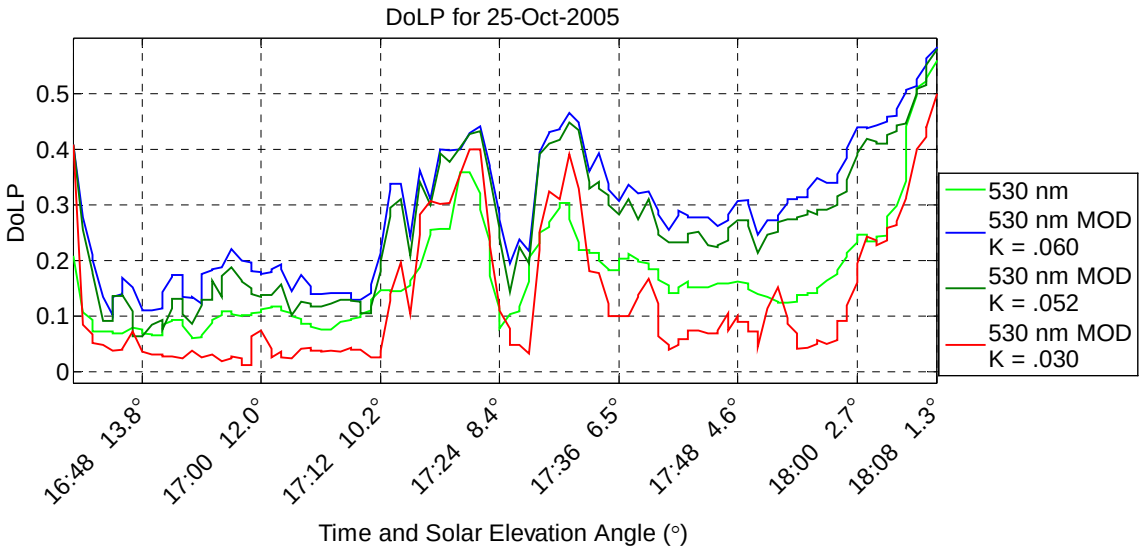

Figure 7.48. Cirrus cloud models for October 25, 2006 at 530 nm. MODTRAN-P models are designated by 'MOD'.

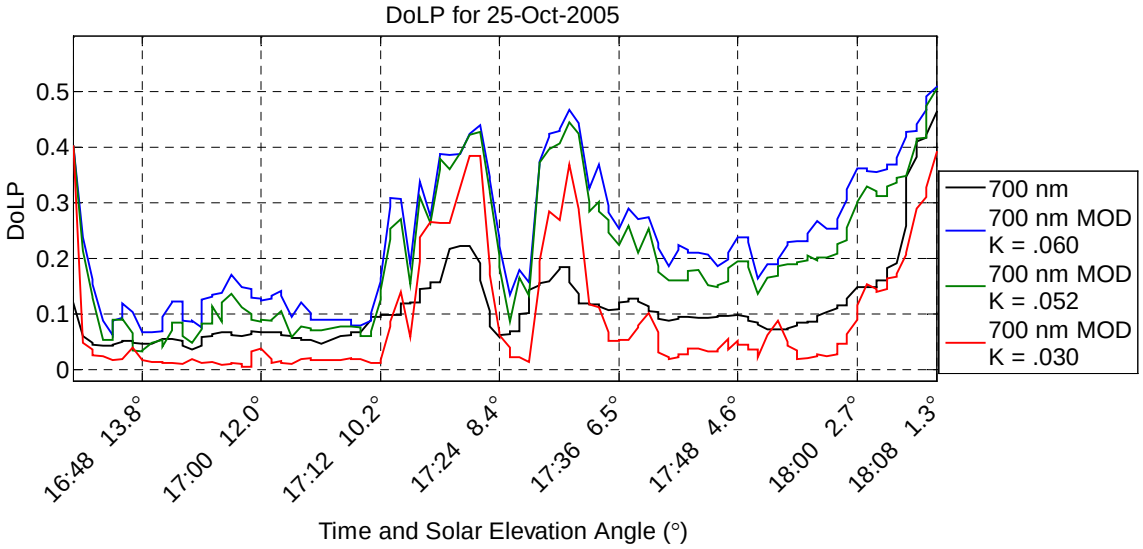

Figure 7.49. Cirrus cloud models for October 25, 2006 at 700 nm. MODTRAN models are designated by 'MOD'.

Each of these cirrus cloud models is a multiple-scatter model. Single-scatter models did not reduce the degree of polarization until large extinctions (> 50 km^{-1}) were used in the model. At this point, the model erred because of the high extinction.

Therefore, none of the single-scatter models worked correctly. Single scattering is not appropriate for cloud modeling, regardless. The multiple scattering is the primary effect that causes the reduction of the degree of polarization. The current multiple-scattering version of MODTRAN-P models the multiple scattering as completely unpolarized. For large optical depths, this model is expected to be fairly accurate. Any degree of polarization will come from the Rayleigh scattering in both the atmosphere above the cloud and the atmosphere below the cloud. Since the model does not accurately account for the Rayleigh scattering below the cloud (see the next section), model results are expected to be lower than the actual data.

The resulting models are surprising accurate. In fact, the 450-nm models are limited in accuracy by the range of the assumed backscatter-to-extinction ratios. Without knowing the true ratio, validation of the model cannot progress further. For the other wavelengths, the predicted DoLP is also highly dependent upon the assumed backscatter-to-extinction ratio; but regardless of the chosen backscatter-to-extinction ratio, all the models over-predict the degree of polarization during periods of thin clouds. For 530 nm, this error is approximately 5%; for 700 nm, approximately 18%. Since multiple-scatter models are always expected to perform lower that the actual DoLP, these numbers reflect possible errors in either (1) the model ice particle phase function for the visual cirrus cloud type, or (2) the calculated boundary extinction. The second possibility is highly likely since the assumption of a particle-free area underneath the cloud may not be valid. Although aerosol extinction may not be significant between 5 and 6.5 km, falling ice particles from the cirrus clouds could be present. If this were the case, the extinction at

the boundary would be much higher than previously assumed. Higher boundary extinction will cause the extinction of the entire profile to increase. This increase would increase the multiple scattering of the model and reduce the DoLP. Without knowing the exact extinction of the boundary, further modeling cannot proceed.

To eliminate the boundary extinction concern, a calibrated LIDAR would be useful to this project. A calibrated LIDAR would return a measurement of the atmospheric backscatter coefficient as a function of altitude. The backscatter-to-extinction ratio assumption would still be necessary, but questions about the clarity of the atmosphere underneath the cloud would be eliminated. Also a multicolor LIDAR system could potentially be useful to obtain a bound on the backscatter-to-extinction ratio or a high spectral resolution lidar could be used to completely separate the molecular and aerosol components of the lidar signal (Eloranta, 1991).

Cloud Polarization and the Validity of One-Point Models

In chapter 6, it was shown that the significant DoLP is generated underneath a cloud in a partially clouded sky. It was also shown that for an overcast sky, the DoLP is zero. MODTRAN-P does not allow the user to specify whether the column under the cloud is illuminated by a uniform cloudbank covering the entire sky, whether it is illuminated by only the sun, or whether it is illuminated by a partially cloudy sky. Therefore, either the case of the column illuminated by the overcast sky or the case of the column illuminated by the sun will be completely wrong. The question is: what illumination source is MODTRAN-P using?

Sample runs of the data show that for any thick cloud, the DoLP of the model is zero. Therefore, MODTRAN-P models the sky as an overcast sky for a thick cloud input. In other words, the model assumes every point in the sky to be the same—effectively an overcast sky. Any DoLP for a real cloud measurement is an error to the model. Using the results from Chapter 6: *Partially Cloudy Sky Polarization*, all DoLPs that were measured below the thick clouds are errors to the model. Therefore, the error in the model for the cloud in Figure 6.8 and 6.9 is 4%. The error for the thick portion of the cloud shown in Figure 6.10 and 6.11 is 15%. Although this may not be the maximum error possible for any cloud—since error depends on brightness of the cloud—these results show that significant problems occur in using a single-point model to predict the DoLP for a sky that has both clouds and clear sky. Most of these problems occur because large differences exist between the scattering that occurs when the sun is in a clear portion of the sky and the scattering that occurs when the sun is blocked by a cloud. For partly cloudy skies with the sun behind a cloud, the 450-nm DoLP measured when looking at a thick cloud can be as low as 0%, while for a scenario where the sun illuminates the entire column underneath the cloud; the DoLP can be as high as 20%.

To more accurately reflect the realities present in a partly cloudy sky, MODTRAN-P needs to be modified to allow illumination of the column underneath the cloud with the given solar scattering geometry. In fact, since an overcast sky DoLP is known to be zero always, it is not useful to model one cloud point as an overcast sky—as the current formulation does. It would be more useful to illuminate all clear-sky layers of the model below the cloud directly with the sun using the input scattering geometry.

Further modification to the code to allow for scenarios where the sun is behind a single cloud in a partially cloudy sky would also be useful. In such a case, each cloud could be modeled as a source at a different position in the sky dome. The contribution of each cloud to the Stokes vector of the column could be calculated. MODTRAN-P would need to be run to find the brightness of each cloud at each position. Then, for each position the Stokes contribution to the observed path would be calculated. After all cloud contributions were calculated, the superimposed results from each "cloud source" would give a model of the actual polarization measured by the observer. This model could potentially be used with or without direct solar illumination, to model any distribution of clouds in the sky.

Recommendations for Future MODTRAN-P Validation

1. The MODTRAN-P code should be updated to properly implement polarization of multiple scattering. Single-scatter models are nearly sufficient for long (> 600 nm) wavelengths in clear skies, but all short-wavelength models are inaccurate because of this shortcoming. This restraint severely reduces the value of this model. Until a revised version of the model which properly implements multiple-scattering is available, validation should not proceed. (This model is currently being produced and should be available soon (Fetrow personal communication, 2006).
2. MODTRAN-P needs to be updated to account for the scattering underneath the cloud in a cloudy model. For any cloud model that is sufficiently thick, the DoLP is zero. In reality, when the sun illuminates the atmosphere below a cloud, the DoLP is not zero. Therefore, the scattering geometry needs to be changed to account for the Rayleigh

scattering below the cloud. Also, MODTRAN-P also needs to be adapted to account for clouds in other portions of the sky. One potential solution is to simulate the polarization contribution of each cloud piecewise in a partially cloudy sky. By removing the sun from the scattering geometry and replacing it with each cloud, the Stokes vector contribution of each cloud could be modeled. The results could then be superimposed. Until the scattering geometry below the clouds is updated, this method cannot be implemented.

3. Aerosol type is a highly significant variable for the clear-sky validation. Without further aerosol information, model validation will ultimately be limited by the choice of standard aerosol type. Accurate aerosol phase function information is necessary for a complete validation. Before this phase information can be derived, the aerosol size distribution profile must be measured. Obtaining a complete aerosol size distribution profile is a nearly impossible procedure, but can be approximated from multiple-wavelength LIDAR data (Rajeev and Parameswaran, 1998). A 2-step approach should be considered. For the first step, multiple-wavelength solar radiometer should be obtained to extract aerosol size distribution and indices of refraction for the integrated column. This aerosol size distribution is then inserted into a Mie code to obtain aerosol scattering, absorption cross-sections, and the phase matrix (Conant, 2005). This phase matrix only models the integrated column. Still, the vast majority of the aerosols are in the boundary layer. Therefore, the boundary-layer aerosols could be modeled with the scattering phase matrix derived for the entire column, while upper-tropospheric and stratospheric aerosols could use the standard

Tropospheric model. For the second step, a multiple-wavelength LIDAR should be designed and built to obtain another measure of the aerosol size distribution and optical properties. This step would also allow continuation of the cirrus cloud model validation, which cannot be pursued further until better backscatter-to-extinction ratio information is obtained (see point 5 below). Still, building a multiple wavelength LIDAR system is not trivial and would probably involve another entire doctoral dissertation.

4. Once these issues have been addressed, the maximum degree of polarization in the sky could potentially be accurate in the MODTRAN-P models. Continued clear-sky validation would focus upon the DoLP in other points in the sky. Therefore, accurately calibrating the fisheye images for zenith angle would simplify these comparisons. Levels also need to be added to the system to make the zenith point in the image consistent between instrument setups.
5. Both the validation of the cirrus cloud models and the investigation into the origin of the DoLP reduction between clouds were limited by the uncalibrated LIDAR system. Without knowing the extinction between the clouds, a conclusion cannot be made about the question of whether the DoLP reduction is caused either by adjacent cloud illumination or by sub-visual swollen aerosols between the clouds. For the cirrus cloud models, a calibrated LIDAR will eliminate the uncertainty in the assumption of the profile backscatter at the boundary point. Once this assumption is removed, only the remaining backscatter-to-extinction ratio assumption will be a concern. Further research cannot proceed effectively until the MAML LIDAR is calibrated.

6. All cirrus cloud models were highly affected by the assumed backscatter-to-extinction ratio. In fact, 450-nm models were accurate within the range of assumed backscatter-to-extinction ratio values. Without knowledge of this ratio, further validation cannot continue. Even with the addition of a calibrated single-wavelength LIDAR, the backscatter-to-extinction ratio will be an important parameter in cirrus cloud models and, to a lesser extent, the clear sky models. If feasible, the development of a calibrated multiple-color LIDAR should be pursued to constrain the backscatter-to-extinction ratio.

CONCLUSION AND UNIQUE CONTRIBUTIONS

Validation of the MODTRAN-P atmospheric radiative transfer model in the visible region of the spectrum necessitated the development of a new full-sky polarimeter that could accurately measure the polarization of both clear skies and quickly-changing cloudy skies. This polarimeter has been developed using Liquid Crystal Variable Retarders (LCVRs). This instrument has an accuracy of ±3.5% (while the LCVRs remain stable). It has been used to measure clear-sky polarization, ground-based object polarization changes, halo polarization, and cloudy sky polarization. Contributions from this research that, as far as the author is aware, are novel to the overall scientific community are as follows:

- Initial validation of the MODTRAN-P atmospheric radiative transfer model in the visible bands has been accomplished. Most of this work focused upon maximum Degree of Linear Polarization (DoLP) for clear skies. Recommendations for both the improvement of the current MODTRAN-P model and direction for future validation are given in the previous section: *Recommendations for Future MODTRAN-P Validation*.
- A time-sequential visible-band full-sky polarimeter has been developed that incorporates both fast acquisition (up to 400 msec) and reliable digital data processing. This is a great improvement over previous designs.
- A set of necessary constraints has been established for use of a polarimeter that has variable aperture polarization components. These constrains must be followed to accurately measure polarization. Ignoring these constraints will cause errors in

polarization measurement. This is especially critical to future polarimeter developers that use Liquid Crystal Variable Retarders (LCVRs).

- It has been shown that the calibration accuracy of a polarimeter using LCVRs can remain within 2% for long periods (on the order of months) if the LCVRs are well insulated and temperature controlled (within 1° C) over long periods. Allowing the LCVRs to cool causes the instrument to lose calibration.
- Initial quantification of ground-based object DoLP change with changing skies has been accomplished. Objects can vary DoLP by up to 20% for different sky conditions in the visible and near infrared bands. This highlights the need for better understanding of the illuminating atmosphere. Also, for aerial surveillance, the problem of thin clouds and aerosols between the observer and the ground-based object cannot be ignored in interpretation of the object DoLP.
- The polarization of single scattering from cloud particles has been verified. This DoLP is very low because it is nearly drowned out by the dominant multiple scattering in the cloud.
- Previous measurements of halo polarization (Können, 1991) have been verified by independent measurements of a partial halo.

REFERENCES CITED

Ambirajan, A.; Look, D.C. 1995. Optimum angles for a polarimeter: part I. OPTICAL ENGINEERING 34 (6): 1651-1658.

Babinet, J. 1840. Sur un nouveau point neuter dans l'atmosphere. COMPTES RENDUS 11: 618-620.

Barrall, M.J.A. 1858. Oeuvres de francois Arago I-V. Paris: Gide.

Berk, A.; Anderson, G.P.; Acharya, P.K.; Bernstein, L.S.; Muratov, L.; Lee, J.; Fox, M.; Adler-Golden, S.M.; Chetwynd, J.H., Jr.; Hoke, M.L.; Lockwood, R.B.; Gardner, J.A.; Cooley, T.W.; Borel, C.C.; Lewis, P.E.; Shettle, E.P. 2006. MODTRAN5: 2006 update. PROCEEDINGS OF THE SPIE VOL 6233. 508-515.

Berk, A.; Bernstein, L.S.; Robertson, D.C. 1989. MODTRAN: a moderate resolution model for LOWTRAN 7. TECH. REP. PL-TR-89-0122 U.S. AIR FORCE PHILLIPS LABORATORY, HANSCOM AIR FORCE BASE, MASS.

Berk, A.; Cooley, T.W.; Anderson, G.P.; Acharya, P.K.; Bernstein, L.S.; Muratov, L,; Lee, J.; Fox, M.J.; Adler-Golden, S.M.; Chetwynd, J.H.; Hoke, M.L.; Lockwood, R.B.; Gardner, J.A.; Lewis, P.E. 2004. MODTRAN5: A reformulated atmospheric band model with auxiliary species and practical multiple scattering options. PROCEEDINGS OF THE SPIE VOL 5571, 78-85.

Bohren, C; Huffman, D. 1983. Absorption and scattering of light by small particles. New York: Wiley.

Bohren, C. 1995. Atmospheric optics. In *Encyclopedia of Applied Physics*, 53-91. New York: VCH Publishers.

Brewster, D. 1847. On the polarisation of the atmosphere. PHIL MAG J SCI 31: 444-454.

Cattrall, C.; Reagan, J.A.; Thome, K.; Dubovik, O. 2005. Variability of aerosol and spectral lidar and backscatter and extinction ratios of key aerosol types derived from selected Aerosol Robotic Network locations. JOURNAL OF GEOPHYSICAL RESEARCH 110: D10S11.

Chepfer, H.; Pelon, J.; Brogniez, G.; Flamant, C.; Trouillet, V.; Flamant, P.H. 1999. Impact of cirrus cloud ice crystal shape and size on multiple scattering effects: application to spaceborne and airborne backscatter lidar measurements during LITE mission and E LITE campaign. GEOPHYSICAL RESEARCH LETTERS 26 (14): 2203-2206.

Chipman, R. 1987. Polarization aberrations. PhD Dissertation. University of Arizona, Tucson.

Chipman, R. 2005. Depolarization index and the average degree of polarization. APPLIED OPTICS 44: 2490-2495.

Collett, E. 1993. Polarized Light: applications and fundamentals. New York: Marcel Dekker.

Conant, J.; Iannarilli, F.; Bacon, F.; Robertson, D.; Bowers, D. 2005. PPACS – a system to provide measured atmospheric aerosol/molecular conditions to EO/IR simulations. Aerodyne Research, Inc. http://www.aerodyne.com/cosr/PPACSWebPages/Conant_PPACS_AtTrPaper_v4.pdf. (accessed November 28, 2006).

Coulson, K. 1988. Polarization and intensity of light in the atmosphere. Hampton: Deepak Publishing.

Coulson, K. 1983. Effects of the El Chichon volcanic cloud in the stratosphere on the polarization of light from the sky. APPLIED OPTICS 22 (7): 1036-1050.

DeVore, J.G.; Thompson, J.H.; Jordano, R.J.; Stair, A.T.; Trowbridge, C.; Joss, P.C.; Rappaport, S.A.; Kristl, J.; McClatchey, R.A. 2001. Effect of Cloud Polarization Properties on Target Discrimination. IEEE AEROSPACE CONFERENCE. BIG SKY, MONTANA, UNITED STATES. MARCH 10-17, 2001: 1985-1994.

Eloranta, E. W.; Grund, C. J. 1991. University of Wisconsin high spectral resolution lidar. OPTICAL ENGINEERING 30(1): 6-12.

Egan, W. G.; Duggin, M.J. 2002. Synthesis of optical polarization signatures of military aircraft. PROCEEDINGS OF THE SPIE VOL 4481: 188-194.

Egan, W. G.; Duggin, M.J. 2001. Optical enhancement of aircraft detector using polarization. PROCEEDINGS OF THE SPIE VOL 4133: 172-178.

Fernald, F.G.; Herman, B. M.; Reagan, J.A. 1972. Determination of aerosol height distribution by lidar. JOURNAL OF APPLIED METEOROLOGY 11: 482-489.

Fetrow, M.P.; Wellems, D.; Sposato, S.H.; Bishop, K.P.; Caudill, T.R.; Davis, M.L.; Simrell, E.R. 2002. Results of a New Polarization Simulation. PROCEEDINGS OF THE SPIE VOL 4481. 149-162.

Fetrow, M. 2006. Air Force Research Laboratory, Albuquerque, NM. Personal Correspondence.

Finger Lakes Instrumentation. 2005. DF-2 Specifications. Online. Available: http://www.fli-cam.com/digital_focusers.htm#Specifications. Accessed 12/7/06.

Gal, J; Horvath, G; Barta, AS; Wehner, RD. 2001. Polarization of the moonlit clear night sky measured by full-sky imaging polarimetry at full Moon: Comparison of the polarization of moonlit and sunlit skies. JOURNAL OF GEOPHYSICAL RESEARCH-ATMOSPHERES 106 (D19): 22647-22653.

Gal, J; Horvath, G; Meyer-Rochow, VB; Wehner, R. 2001. Polarization patterns of the summer sky and its neutral points measured by full-sky imaging polarimetry in Finnish Lapland north of the Arctic Circle. PROCEEDINGS OF THE ROYAL SOCIETY OF LONDON SERIES A-MATHEMATICAL PHYSICAL AND ENGINEERING SCIENCES 457 (2010): 1385-1399.

Hecht, Eugene. 2002. Optics. 4th Ed. San Francisco: Addison-Wesley.

Horvath, G; Pomozi, I; Gal, J. 2003. Neutral points of skylight polarization observed during the total eclipse on 11 August 1999. APPLIED OPTICS 42 (3): 465-475.

Horvath, G; Barta, A; Gal, J; Suhai, B; Haiman, O. 2002. Ground-based full-sky imaging polarimetry of rapidly changing skies and its use for polarimetric cloud detection. APPLIED OPTICS 41 (3): 543-559.

Horvath, G; Gal, J; Pomozi, I; Wehner, R. 1998. Polarization portrait of the Arago point: Video-polarimetric imaging of the neutral points of skylight polarization. NATURWISSENSCHAFTEN 85 (7): 333-339.

Kattawar, G; Plass, G. 1972. Degree and direction of polarization of multiple scattered light. 1: Homogenous Cloud Layers. APPLIED OPTICS 11 (12): 2851-2865.

Kawata, Y. 1978. Circular-polarization of sunlight reflected by planetary atmospheres. ICARUS 33 (1): 217-232.

Klett, J.D. 1981. Stable analytical inversion solution for processing lidar returns. APPLIED OPTICS 20 (2): 211-220.

Können, G.P.; Wessels, H; Tinbergen J. 2003. Halo polarization profiles and sampled ice crystals: observations and interpretation. APPLIED OPTICS 42 (3): 309-317.

Können, G.P.; Muller, S; Tinbergen J. 1994. Halo polarization profiles and the interfacial angles of ice crystals. APPLIED OPTICS 33 (21): 4569-4580.

Können, G.P.; Tinbergen, J. 1991. Polarimetry of a 22° halo. APPLIED OPTICS 30 (24): 3382-3400.

Können, G.P. 1983. Polarization and intensity distributions of refraction halos. JOURNAL OF OPTICAL SOCIETY OF AMERICA 73 (12): 1629-1640.

Kovalev V.A.; Eichinger, W.E. 2004. Elastic lidar. New York: Wiley-Interscience.

Liu, Y. 1996. Measurement of the intensity and polarization of light in the atmosphere. PhD Dissertation. University of Miami.

Liu, Y; Voss, K. 1997. Polarized radiance distribution measurement of skylight 2. Experiment and data. APPLIED OPTICS 36 (33): 8753-8764.

Lu, S.Y.; Chipman R.A. 1996. Interpretation of Mueller matrices based on polar decomposition. JOURNAL OF THE OPTICAL SOCIETY OF AMERICA A 13 (5): 1106-1113.

Lynch, D. 1979. Polarization models of halo phenomena I. The parhelic circle. JOURNAL OF THE OPTICAL SOCIETY OF AMERICA 69 (8): 1100-1103.

Manor, H. 2003. Performance of an optical wireless communication system as a function of wavelength. APPLIED OPTICS 42 (21): 4285-4294

Meadowlark Optics. Sources of error in retarders and waveplates. Internet. Available: http://www.meadowlark.com/applicationNotes/Sources%20of%20Error%20in%20Retarders%20and%20Waveplates.pdf. Accessed: 12/5/06.

Measures, R. 1984. Laser remote sensing: Fundamentals and applications. Florida: Kreiger.

Meadowlark Optics. 2006. Dichroic polymer linear polarizers. Online. Available: http://www.meadowlarkoptics.com/products/PolarizersDichroicPolymer.php. Accessed: 12/12/06.

Mueller, H. 1948. The foundation of optics. JOURNAL OF THE OPTICAL SOCIETY OF AMERICA 38: 661.

Newport. 2006. Precision linear polarizers. Online. Available: http://www.newport.com/store/genproduct.aspx?id=141147&lang=1033&Section=Spec. Accessed 12/12/06.

Newport. 2006. Polarcor linear polarizers. Online. Available: http://www.newport.com/Polarcor-Linear-Polarizers/141148/1033/catalog.aspx. Accessed: 12/12/06.

North, J.A.; Duggin, M.J. 1997. Stokes vector imaging of the polarized sky-dome. APPLIED OPTICS 36 (3): 723-730.

Persons, C. M.; Chenault, D. B.; Jones, M.W.; Spradley, K. D.; Gulley, M. G.; Farlow, C. A. 2002. Automated registration of polarimetric imagery using Fourier transform techniques. PROCEEDINGS OF THE SPIE VOL 4819: 107-117.

Platt. C.M.R.; Scott J.C.; Dilley A.C. 1987. Remote sounding of high clouds Part VI: Optical properties of midlatitude and tropical cirrus. JOURNAL OF ATMOSPHERIC SCIENCE 44: 729-747.

Pomozi, I; Horvath, G; Wehner, R. 2001. How the clear-sky angle of polarization pattern continues underneath clouds: full-sky measurements and implications for animal orientation. JOURNAL OF EXPERIMENTAL BIOLOGY 204 (17): 2933-2942.

Prosch, T; Hennings, D; Raschke. 1983. Video polarimetry – a new imaging technique in atmospheric science. APPLIED OPTICS 22 (9): 1360-1363.

Pust, N.J.; Shaw, J.A. 2006. Dual-field imaging polarimeter using liquid crystal variable retarders. APPLIED OPTICS 45 (22): 5470-5478.

PPS V4.3 command line usage. 2005. Air Force Research Laboratory. Internal Document.

Rajeev, K.; Parameswaran, K. 1998. Iterative method for the inversion of multiwavelength lidar signals to determine aerosol size distribution. APPLIED OPTICS 37 (21): 4690-4700.

Sato, S. 1995. Fisheye lens having a short distance compensating function. Nikon Corporation, assignee. US Patent 5,434,713. 18 Jul. 1995.

Sato, S. 1996. Internal focusing type telephotolens. Nikon Corporation, assignee. US Patent 5,757,555. 25 Nov. 1996.

Schuster, G.L. 2006. Angstrom exponent and bimodal aerosol size distributions. JOURNAL OF GEOPHYSICAL RESEARCH 111 (d7): D07207.

Seldomridge, N. 2005. Dual polarization cloud LIDAR design and characterization. Master's thesis, Montana State University. Online. Available: http://www.montana.edu/etd/available/seldomridge_0805.html.

Seldomridge, N.L.; Shaw, J.A.; Repasky K.S. 2006. Dual-polarization lidar using a liquid crystal variable retarder. Optical Engineering 45(10): 106202.

Shaw, G.E. 1983. Sun photometry. BULLETIN OF THE AMERICAN. METEOROLOGICAL. SOCIETY. 64(1): 4-10.

Shaw, J.A.; Nugent, P.; Pust, N.; Thurairajah, B.; and Mizutani, K. 2005. Radiometric cloud imaging with an uncooled microbolometer thermal infrared camera. OPTICS EXPRESS 13 (15): 5807-5817.

Spinhirne, J. D.; Reagan, J.A; Herman B.M. 1976. Vertical distribution of aerosol extinction cross section and inference of aerosol imaginary index in the troposphere by lidar technique. JOURNAL OF APPLIED METEOROLOGY 19: 426-438.

Stokes, G.G. 1852. On the composition and resolution of streams of polarized light from different sources. TRANSACTIONS OF THE CAMBRIDGE PHILOSOPHY SOCIETY 9: 399-416.

Suhai, B; Horvath, G. 2004. How well does the Rayleigh model describe the E-vector distribution of skylight in clear and cloudy conditions? A full-sky polarimetric study. JOURNAL OF THE OPTICAL SOCIETY OF AMERICA A-OPTICS IMAGE SCIENCE AND VISION 21 (9): 1669-1676.

Suzuki, K. 1998. Lens capable of short distance photographing with vibration reduction function. Nikon Corporation, assignee. US Patent 5,751,485. 12 May 1998.

Thurairajah, B. 2004. Thermal infrared imaging of the atmosphere – The Infrared Cloud Imager. Masters Thesis. Montana State University. Online. Available: http://www.montana.edu/etd/available/thurairajah_04.html.

Thurairajah, B.; Shaw, J.A. 2005. Cloud statistics measured with the infrared cloud imager (ICI). IEEE TRANSACTIONS ON GEOSCIENCE AND REMOTE SENSING 43 (9): 2000-2007.

Tyo, J.S. 2000. Noise equalization in Stokes parameter images obtained by use of variable-retardance polarimeters. OPTICS LETTERS 25 (16): 1198-1200.

Tyo, J.S. 2002. Design of optimal polarimeters: maximum of signal-to-noise ratio and minimization of systematic error. APPLIED OPTICS 41 (4): 619-630.

Watkins, D.S. 1991. Fundamentals of matrix computations. New York: Wiley.

Vermeulen, A.; Devaux, C.; Herman, M. 2000. Retrieval of the scattering and microphysical properties of aerosols from ground-based optical measurements including polarization. I Method. APPLIED OPTICS 39 (33): 6207-6220.

Voss, K.J.; Liu, Y. 1997. Polarized radiance distribution measurements of skylight .1. System description and characterization. APPLIED OPTICS 36 (24): 6083-6094.

Young, S.A. 1995. Analysis of lidar backscatter profiles in optically thin clouds. APPLIED OPTICS 34 (30): 7019-7031.

Xiao, X.; Voelz, D.; Sugiura, H. 2003. Field of view characteristics of a liquid crystal variable retarder. PROCEEDINGS OF THE SPIE VOL. 5158: 142-150.

Xing, Z.F. 1992. On the deterministic and non-deterministic Mueller matrix. JOURNAL OF MODERN OPTICS 39: 461-484.

APPENDICES

APPENDIX A

SELECTION OF MODTRAN VARIABLES

Someone once asked me, “How does MODTRAN work?” In spite of my novice status as a MODTRAN user, I gave a straightforward answer that made MODTRAN seem simple. In reality, MODTRAN is far from a basic program. It is as complex and specific as the various atmospheres that it describes. It is formed from a system of “cards”, rows of descriptor variables that attempt to accurately describe the atmosphere for one line of sight. These variables describe anything from the amount of spectral solar irradiance incidence upon the earth’s upper atmosphere, the amount of aerosols in the boundary layer, the extinction exhibited in a cloud, to the speed of the model used. For a model to be correct, each variable must be carefully chosen with respect to the scenario. Error in selecting important variables could potentially lead to very inaccurate MODTRAN-P models.

MODTRAN is laid out in a series of “cards”. Each card is one or more 80-character line that contains a number of variables. If the reader is interested in the specific syntax of each card, the *MODTRAN 4 User’s Manual* is a good resource. For brevity, syntax specifics will be ignored, while each variable name given by the MODTRAN developers is shown in parenthesis along with the setting I used. This allows future users to understand my models. Brief descriptions of each variable, the chosen value, and the reason for the selection are given. Note, MODTRAN and MODTRAN-P both use the same input card structure—with the exception of the IEMSCT variable which is explained below. Cloud and clear-sky models have slightly different variables.

Card 1 – Main Driver

MODTRAN Band Model (MODTRN = T)

MODTRAN was normally run in the standard mode (T or M). Correlated-k option seemed to cause the MODTRAN-P version to fail. LOWTRAN band models were not recommended, since they are use low resolution and are no longer supported.

Speed of Model (SPEED = M)

Again, correlated-k option did not work for MODTRAN-P. Therefore, speed selection for the regular MODTRAN model did not affect results.

Molecular Composition Model (MODEL = 7)

Standardized models of the earth’s atmosphere can be used instead of radiosonde data. These models describe the molecular composition of the atmosphere. For example, MODEL=2 causes MODTRAN to use a Standard Mid-Latitude Summer profile. Since the radiosonde height profiles of water vapor, temperature, and pressure were necessary for the LIDAR and optical depth processing, these profiles were used to form user-defined molecular models for each variable. Values of other molecules in the atmosphere

(CO_2, CO, N_2, etc.) used the Mid-Latitude Summer default. See Card 2C1 for more details on these default settings.

Slant Path (ITYPE = 3)

All atmospheric paths of observation start at the ground level and look through the entire atmosphere. ITYPE=3 caused the code to look through all layers from the ground level to space.

Mode of Execution (IEMSCT = 4)

MODTRAN can be run in many different modes (i.e. transmittance only, radiance, radiance with scattering, etc.). IEMSCT =4 caused MODTRAN to output both radiance values and the Stokes vectors. This is a new setting for this variable and can only be used with MODTRAN-P.

Multiple Scattering (IMULT=0 or 1)

Degree of polarization in the Earth's atmosphere is highly dependent upon multiple scattering. Because multiple scattering was not properly implemented, both the single-scatter (IMULT = 0) and multiple-scatter (IMULT=1) models were tested for accuracy.

Default Models (M1….M6 = 2, MDEF = 0)

These are the default profiles for the molecular compositions. They are probably irrelevant since the user-defined model default parameters in card 2C1 override these parameters. For safety, they were set to the same default model (Mid-latitude summer) as the default model in card 2C1. MDEF defines the heavy molecules like chlorofluorocarbons. For these molecules, the default profiles were used.

Read Model Atmosphere (IM=1)

IM=1 was used to cause MODTRAN to read a new atmosphere for a new run, since almost all runs require a new atmosphere.

Output Mode (NOPRNT = 0)

The standard output of tape6 was used. This variable has no affect on the values of the polarization, but tape6 was useful for troubleshooting and extracting 550 nm molecular extinctions.

Boundary Temperature (TPTEMP = 0)

This variable is not a concern in the visible. It describes the earth's temperature for looking at targets in the infrared.

Surface Reflectance (SURREF = 0)

No surface reflection was used. Future modeling may use -2 = forest, -1 = fresh snow, etc.

Card 1A – Radiative Transport Driver

Multiple Scattering Algorithm (DIS = T)

The DISTORT multiple scattering option is much more accurate than the older Isaac's algorithm.

Azimuth Dependence in the DISTORT Algorithm (DISAZM = T)

Differences of up to 3% in the degree of polarization were exhibited when this dependence was not added to the model. Since the azimuth dependence is a more accurate descriptor of the multiple scattering, it was assumed that the models that did not use the azimuth dependence were in error. Therefore, in spite of the fact that enabling this variable severely slows MODTRAN, the azimuth dependence was added to all polarization models.

Number of Streams Used by DISTORT (NSTR = 8)

The DISTORT algorithm becomes more accurate with a greater number of streams. Still, increasing the number of streams severely slows MODTRAN. It was necessary to find the least number of streams necessary. The difference in the degree of polarization between 4 and 8 streams was around 2% for most models. This is a significant error. The difference between 8 and 16 streams was only 0.4%. Since this is a small error with respect to the model, 8 streams were selected to reduce the model processing time. **Future validation of MODTRAN-P should consider moving to 16 streams as the instrument-to-model difference becomes less than 2%.**

Read User-Defined Solar Radiance Data (LSUN = F and ISUN=)

MODTRAN was set to use the default solar radiance model.

Carbon Dioxide Mixing Ratio (CO2MX = 370)

This variable has little affect on the molecular model in the visible, but it was set to 370 ppmv to reflect the changes in CO_2 from 330 in the default model to the more accurate 370 ppmv of 2006.

Integrated Water Vapor Scaling Correction (H2OSTR= X.XX)

This correction forces the true integrated water vapor in the column to match the water vapor in the sampled column. When radiosonde data is sampled to the 32-layer MODTRAN profile, the total water vapor may develop a significant sampling error. This variable corrects for that error. The MATLAB sampling functions sond2mod12.m and sond2modaer.m calculated this scaling factor at the time of data sampling. It was then input into MODTRAN.

Ozone Scaling (O3STR = 0)

The default ozone column was used without scaling.

Solar Radiance Filename (LSUNFL =)

This variable was not necessary because LSUN is not used.

Read Binary Version of the Band Model (LBMNAM=T)

This variable causes BMNAME in Card 1A2 to be read. BMNAME the name of the binary band model. See Card 1A2 for more information.

User defined instrument filter (LFLTNM=)

The instrument filter was not used. The degree of polarization is not significantly dependent on very narrow spectral features, so the degree of polarization over a square window that is the same wavelength and bandwidth as each instrument filter was calculated.

Water Vapor Scaling Affect on Aerosols (H2OAER = F)

This variable caused the swelling of the aerosols by the water vapor to be affected by the water vapor scaling factor. This setting was selected because no noticeable affect was seen when the parameter was set to “true”. This is probably because the scaling is a small correction to the water vapor scaling, which is in turn a small correction to the aerosol extinction.

Top of Atmosphere Solar Irradiance Scaling (SOLCON = 0)

The solar irradiance was not scaled.

Note: Card 1A1 was not used.

Card 1A2 – Binary Solar Band Model

Binary Filename (BMNAME=B2001_15.BIN)

This was the same file that the Air Force Research Lab used in their ground models. The 15 cm-1 resolution model is much quicker in the visible bands, where higher resolution is not necessary. Differences between the B98_15.bin file and the B2001_15.bin file were negligible.

Note: Card 1A3 was not used.

Card 2 – Main Aerosol and Cloud Options

Use Aerosol Plus (APLUS =)

This option is used to compress and stretch the aerosol models. It was not used since user-defined aerosol extinction profiles are used in card 2C3.

Aerosol Types (IHAZE= 1, 2, or 6)

The standard models were selected for testing (IHAZE =1 is Rural 23km, IHAZE = 2 is Urban 5km, and IHAZE = 6 is Tropospheric 50 km). Note that the extinction profiles redefine the standard model extinctions (and thus the visibilities). Therefore, this parameter effectively changes the phase function when user-defined extinction profiles are given. **Future work may include providing user-defined wavelength-dependent absorption and asymmetry properties and using Mie scattering phase functions derived from solar radiometer data. (Currently MSU does not have this capability, but will in the near future.) When this happens, IHAZE will equal 7.**

Activate Navy Oceanic Vertical Aerosol Model (CNOVAM =)

NOVAM was not used.

Seasonal Aerosol Model (ISEASN = 0)

Seasonal aerosols were set according to the MODEL variable. For all data for the Spring/Summer 2006, the Mid-Latitude Summer default model caused ISEASN to internally default to spring-summer aerosols.

User-Defined Aerosol Data (ARUSS =)

See IHAZE. This variable was not used, but in future work the variable will need to be set to ‘USS’ along with IHAZE = 7.

Stratospheric Aerosol Model (IVULCN = 0)

Since no major volcanoes have erupted in the last few years, the stratospheric aerosols are assumed to have decayed significantly and a background stratosphere was chosen.

Continental Influence (ICSTL=0)

NOVAM continental influence was not used and has no effect on the model.

Cloud Type (ICLD = 0 for clear skies, ICLD = 1 for cumulus, etc.)

This parameter defines the cloud used. For clear sky models, there were no clouds. For other models, standard clouds were used, while the height and thickness of the cloud were manipulated by later cards.

Army Vertical Structure Algorithm (IVSA = 0)

Not used.

Visibility (VIS=0)

Visibility is a modification to the default aerosol model of the extinction in the boundary layer. With the LIDAR/solar radiometer data, this variable was not useful. It was overridden by card 2C3.

Wind Speeds (WSS=0, WHH=0)

Navy models are not used, so these variables are not necessary.

Rain Rate (RAINRT = 0)

I don't take data when it is raining.

GNDALT (GNDALT=1.524 for Montana State University)

This important variable defined the height of the observer above sea level. MODTRAN uses this as the ending point for the radiative transfer.

Note: Card 2A+ was not used.

Card 2A – Cloud Models

Cloud Thickness (CTHIK= X.XX)

This is the cloud thickness in km. For clouds that the LIDAR can penetrate, a value was determined for this variable. Otherwise, the default thickness was used for thick clouds.

Cloud Altitude (CALT = X.XX)

This is the cloud height in km. The LIDAR is useful for finding this value.

Cloud Extinction (CEXT =X.XX)

The LIDAR gives the cloud extinction in km^{-1}.

Cloud Properties (NCRALT = -9, NCRSPC = -9, CWALN = -9, CCOLWD=-9, CCOLIP = -9, CHUMID = -9, ASYMWD = -9, ASYMIP = -9)

Setting everything to –9 caused the defaults to be used

Note: Card 2B was not used.

Card 2C—User-Defined Atmospheric Data

Number of Layers (ML = XX, nominally 32)

This is the number of layers that was input into the user defined atmosphere. MODTRAN can handle a maximum of 32 layers. Ideally, the sampling of the radiosonde and aerosol data will leave a 32-layer sample. In practice, automated sampling sometimes returned slightly less than 32 layers.

Read User Defined Data for Nitrogen, Carbon Monoxide, etc. (IRD1 = 0)

The default profiles were used for gases where the exact concentrations were not known.

Read User Defined Aerosol Data (IRD2 = 2)

The new version of card 2C3 was selected to input the aerosol data.

Card 2C1—Radiosonde Profile Information

Card 2C1 and 2C3 parameters were read for each of the number of layers defined by ML. The two cards alternate for each level.

Layer Altitude (ZMDL=XX.XX)

ZMDL defines the layer altitude in km. These layers are referenced to sea level.

Layer Pressure and Unit (P = XXX.XX, JCHAR(1) = A)

P is the pressure of the layer. The unit 'A' caused MODTRAN to read the units millibar (mb).

Temperature and Unit (T = XXX.XX, JCHAR(2) = B)

T is the temperature of the layer. The unit 'B' caused MODTRAN to read the units in °C.

Water Vapor (WMOL(1) = XXX.XX, JCHAR(3) = H

Water vapor was read as humidity.

Carbon Dioxide, Ozone (WMOL(2) = 2, WMOL(3) = 2)

Carbon dioxide and ozone were set to the default atmospheric profile values for each. The default atmosphere is the Mid-Latitude Summer. Experimentation into the dependency of the degree of polarization upon the default atmosphere—which determined carbon dioxide and other gases—showed that the difference between the 1976 US Standard Model and the Mid-Latitude Summer model was less than 0.4%. Therefore, I was confident that these gases do not change the models significantly.

Card 2C3 – User-Defined Extinction of Aerosols

Aerosol Profiles (AHAZE(1..4) = XX.XX)

MODTRAN supports four aerosol profiles for each layer. Aerosol 1 is a typical boundary layer aerosol. Aerosol 2 is a typical troposphere aerosol. Aerosol 3 is a typical stratosphere aerosol. Aerosol 4 is a meteor dust aerosol in the upper stratosphere. Using Card 2C3 these standard aerosols types can be used with user-defined extinction profiles. The coefficients are defined at 550 nm in the units of km^{-1}. The LIDAR profile was divided amongst these layers using arbitrarily-defined division altitudes that were similar to the default MODTRAN models. The boundary layer was set from the ground to 3.5 km above sea level. The troposphere was set cover 3.5 to 10 km. The stratosphere was

from 10 to 35 km, while the meteor dust regime of the stratosphere covered from 35 to 80 km.

Rain Rate (RRATZ=0)

Upper level rain was not used.

Note: Cards 2D…2D2 were not used, but will be needed with future solar radiometer data. Cards 2E1 and 2E2 were also not used.

Card 3 – Line of Sight Geometry

Initial Altitude (H1 = 0)

The initial altitude was set to zero. MODTRAN defaulted the initial altitude to the ground altitude during execution.

Zenith angle of the observation path (ANGLE = XX.XX)

For maximum degree of polarization studies, this angle was set initially to 90° and then an iterative process was used to seek the actual maximum degree of polarization for the model. This maximum typically lied at an angle between 82 and 92° from the zenith angle of the sun.

Other Card 3 variables

Only H1 and ANGLE are necessary for a slant to space geometry. Therefore, other variables were set to zero.

Card 3A1 and 3A2 – Solar/Lunar Scattering Geometry

These cards place the sun (or moon) in a proper location for the radiance scattering. This is highly important for polarization studies. MODTRAN has several different ways of inputting the sun position. Only one of these methods proved acceptable for the scattering geometry. This is IPARM = 1.

Aerosol Phase Functions (IPH=2)

The internal Mie generated phase functions were used for the aerosols. **Future work with solar radiometer data will include Mie generated phase functions that reflect derived aerosol size distributions.**

Day of the Year (IDAY = XXX)

The day of the year was determined from the UTC reading of the polarimeter. This is used inside MODTRAN to calculate Earth-Sun distance.

Source (ISOURC=0)

The sun was the source for all models.

Location Parameters (PARM1 = 45.6667, PARM2=111.046)

For IPARM=1, PARM1 and PARM2 define the latitude and longitude. This was set to be the location of Montana State University.

Greenwich time (TIME = XX.XX)

The Greenwich time in decimal hours.

Path Azimuth (PSIPO= XX.XX)

This variable was the path azimuth angle for the observer. For maximum degree of polarization studies, this variable was set to 180° from the location of the sun's azimuth. Variation of the maximum degree of polarization along the azimuth direction was not significant, so it was hard coded to be 180° from the sun.

Other Card 3 variables

All other Card 3 variables were not used.

Note: Card 3B1 and 3B2 were not used. Derivations of the Mie scattering phase matrices will be attained with a solar radiometer with additional wavelengths.

Card 4 – Spectral Range and Resolution

Wavelengths in nanometers (V1= XXX.XX,V2= XXX.XX, XFLAG=N, FLAGS(1) = N)

MODTRAN can handle spectral wavelengths in wavenumbers, micron, or nanometers. Nanometers was selected as the unit of choice. V1 and V2 were selected to straddle the center frequency of the instrument filters with a total bandwidth of 10 nm.

Resolutions (DV =1, FWHM=1)

Since running at a lower resolution did not increase speed, the values of DV and FWHM were set to one wavenumber.

Plot options (YFLAG = R)

This setting caused radiances and Stokes vectors to be plotted in the output file.

Other Card 4 options

All other options were left blank (default).

Note: Cards 4A, 4B1, 4B2, 4B3, 4L1, and 4L2 were not used.

Card 5 – Repeat Options

See MODTRAN documentation for complete details on how to use the same atmosphere with multiple lines-of-sight, multiple wavelengths, etc. These options were used in some cases.

APPENDIX B

OPERATING INSTRUCTIONS FOR POLARIMETER

Warning: The LCVR system should always stay on. **If power is lost to the controller, the calibration of the polarimeter will be lost.** For safety, the LCVR power switch is permanently held by tape in the "on" position. If for some reason the switch is bumped, the LCVR heaters will shut off until a new set point is input from the computer. It is crucial that in the event of an accidental LCVR controller reset that the heater set point be put back into the controller as quickly as possible. If the LCVRs are allowed to cool, the calibration will be lost. (The longer they cool the worse the calibration becomes.) In the event of accidental power loss to the LCVR system, follow the *Meadowlark LCVR Controller Reset* instructions before the LCVRs cool.

System Initialization Steps

1. If the computer is off. Then, turn on the computer and login. After Windows XP initializes, unplug all wires from both the CFW-1 and the DF-2 control boxes (USB, power, and gray wire). Then, for each box, plug the wires back in using this order: USB wire, then power wire, and finally the gray wire. These steps are necessary to get the computer to initialize the Finger Lakes USB interfaces correctly. These steps are only necessary if the computer has been rebooted.
2. Once the computer is on, open MATLAB. If the computer has been rebooted, execute *Set_LCVR_Temperature* at the command prompt. If an error is returned, then follow *Meadowlark LCVR Controller Reset* discussed below.
3. Turn on the DALSA 1M30 Camera.
4. Type Polarization at the command prompt. Select "Yes" to initialize the polarimeter.
5. Set up the instrument. Set the f/#. Tape the joint between the 105 mm Micro and the DF-2—a tight seal is not currently possible to eliminate light leakage.
6. Using the drop down menus, set the lens type, the current f/#, the saving data flag, and the exposure for the current instrument settings. Ensure that the focuses are correct for the calibration. See *MATLAB GUI Operation—Preparations for Data Collection* below for more information.
7. Use the *Take Image Sequence* button to start taking data.
8. For field measurements, use the calibration polarizer that screws onto the near field polarimeter at –22.5° to check the calibration accuracy for possible LCVR calibration jumps.

Meadowlark LCVR Controller Reset

Note: It is crucial that in the event of an accidental LCVR controller reset that the heater set point be reentered into the controller as quickly as possible.

The heater set point is input into the controller via the serial port. The MATLAB routine *Set_LCVR_Temperature* is used to set the controller heater set point. This function is used with no arguments to set the standard set point of tsp:10400. Because

the serial port remains connected during computer power up, the serial buffer of the Meadowlark controller can be corrupted by the motherboard. If this is the case, the polarimeter software and the *Set_LCVR_Temperature* routine will not work correctly. To remedy this problem follow the steps below:

Important: Read and understand all steps before proceeding, as timing is critical. If the LCVRs are allowed to cool the calibration will be lost.

1. Open the MATLAB window and type *Set_LCVR_Temperature*, but do not execute the function.
2. Wait for both heater indicator lights on the LCVRs to turn off. This means the heaters are off and each LCVR temperature is stabilized.
3. Depress the power switch of the Meadowlark LCVR controller until the green power light goes out.
4. Turn the power switch back on. The status light will blink a few times when the system has properly started. If it does not, reset the power switch again.
5. Press *Enter* on the keyboard to execute the *Set_LCVR_Temperature* command.
6. If the set point is successfully input into the controller, an appropriate message will be returned from the routine. If not successful, try the entire process again.

MATLAB GUI Operation – Polarization

Note: Individual commands are shown in **bold**. Menus and scripts are shown in *italics*.

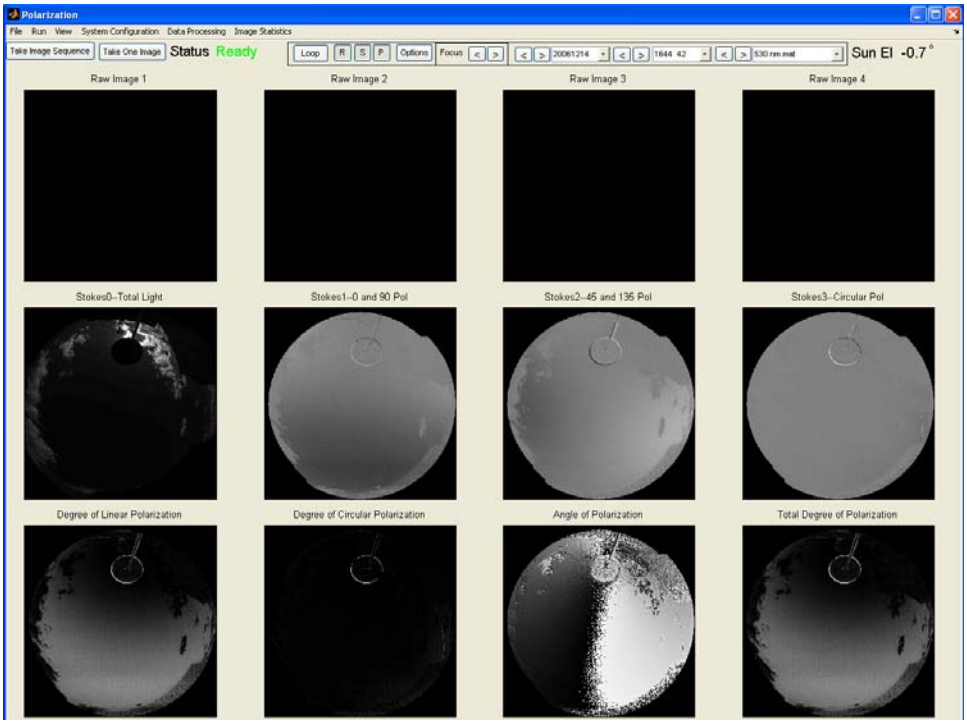

Figure 9.1. Polarization GUI Mainframe

A MATLAB GUI has been designed that operates the polarimeter. The GUI looks much like a standard Windows program, but uses the MATLAB scripted language to execute the commands. Full explanation of the entire code is too exhaustive for this treatment. (The current *Polarization* script and critical data processing routines are over 3500 lines of code.) To open the GUI, type *Polarization* at the MATLAB prompt. If you are just viewing data, polarimeter initialization is not necessary. If data is being collected, select *"Yes"* to initialize the polarimeter. After initialization, the GUI looks should look something like Figure 9.1.

Before any data is taken, the software must be initialized for the current instrument setup. The f/#, the lens, the file save flag, and the exposure times are the critical settings. Also, the software needs to be instructed whether to process the current polarization components after data is collected, or to just save the raw data. By saving only the raw data, the time between successive acquisitions is reduced by about 20 seconds. (The polarization images are later retrieved from post-processing.) Finally, if the imager is to run automatically the loop settings need to be set.

Preparations for Data Collection

To set the f/#, go to the *System Configuration* drop down menu. Then go to *F#* and select the appropriate f/# for the current system (Figure 9.2). Be sure the f/# is the same on the instrument and the code. A wrong setting will corrupt all data processing for the day. The default f/# is f/2.8.

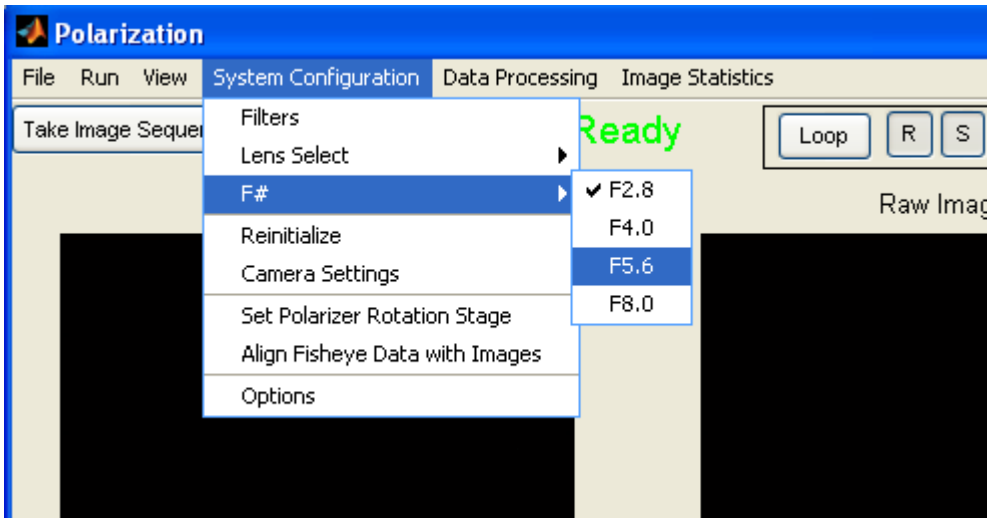

Figure 9.2. Selection of the f/# in the GUI.

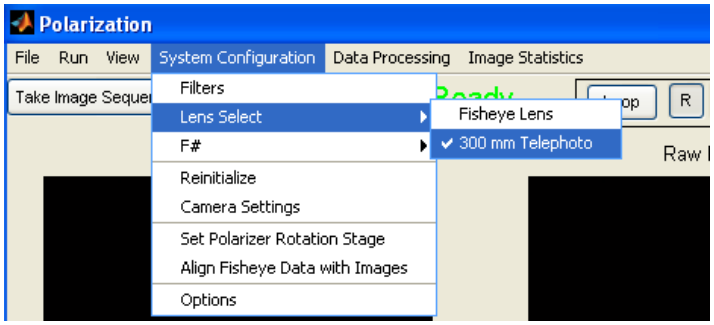

Figure 9.3. Selection of the lens.

To select the appropriate lens, use the *Lens Select* drop down. Select either the **Fisheye** or the **300 mm Telephoto** (Figure 9.3). The check mark will move to the selected lens. In some instances, it may be necessary to operate the polarimeter without a front lens. For example, for field calibration checks, no lens is used. To eliminate the check mark from both lenses, select the checked lens. Now look at the drop down menu, neither lens should be checked. (The default lens is the **300 mm Telephoto**.)

To turn data saving on or off, go to the *File* drop down menu. Select **Save Measured Data**. When this is checked (default value), the data from the polarimeter is saved. Otherwise, the data is not archived, but only held in memory until it is overwritten. For most cases, **Save Measured Data** should be checked. Collecting data without archiving is only recommended for troubleshooting.

Setting the exposures for each filter involves using the Filters GUI embedded in the *Polarization* GUI. Go to the *System Configuration* drop down menu and select *Filters*. The Filter Settings GUI will appear (Figure 9.4).

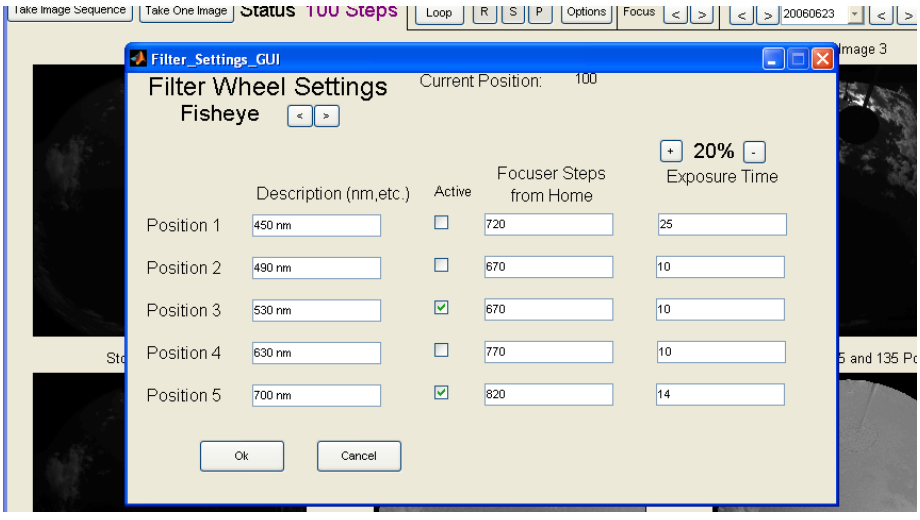

Figure 9.4. Filter Settings GUI.

The Filter Settings GUI controls many of the instruments functions. By using the toggles at the top, the lens for which the settings are being adjusted can be selected. When the buttons are used to toggle different lenses, the new lens settings are updated and available for change. The description boxes describe the filters in the instrument. These should only be changed if the filters are changed. The filter descriptions are the same for all lenses. (These are the only settings displayed that apply to all lenses.) The *Active* column determines which filters are acquired. In the example shown, only the 530 nm and 700 nm filters are active for the fisheye lens. Therefore, if **Take Image Sequence** is selected, first the 530 nm data will be acquired; then, the 700 nm filter will be acquired. If other filters were active, then each filter would be acquired sequentially in order of position in the filter wheel after the **Take Image Sequence** button is selected. The focus positions are unique for each filter and each lens. These position settings are set prior to calibration and should not be adjusted after calibration, because of the focus dependence of the calibration. To help with the initial adjustments, the current focus setting is shown in the GUI. The exposures can be adjusted between 6 and 250 msec. To make adjustments to all wavelengths simple, a ±20% adjustment toggle is at the top of the column. These toggles adjust the exposures of all wavelengths simultaneously.

To disable processing of the polarization parameter online—that is to only save the raw data, go to the *Data Processing* drop down menu. If **Process Online** is checked, then click on it. (Processing the data at the time of acquisition is the default setting.)

After these settings are properly adjusted, data collection can start by pressing **Take Image Sequence**. If it is desired to automatically continue taking data, the **Loop** button can be depressed. This button causes the imager to continue to run the **Take Image Sequence** until the user intervenes. The default delay between acquisitions is 0 seconds. The loop delay time is set in the **Options** GUI, discussed later.

Displaying Data

The primary default display is shown in Figure 9.1. By using the R, S, and P toggles (or their linked settings in the View drop down menu), different views can be achieved. R stands for Raw images, S for Stokes parameters, and P for Polarization parameters. By toggling these different items off, fewer images are displayed on the main GUI and can be viewed with higher resolution. For example, if one the P is toggled, the Polarization parameters of DoLP, DoCP, AoP, and DoP are displayed in a 4 x 4 image inside the mainframe. When all three categories are toggled off, the software reduces the *Polarization* GUI to the toolbar only. This view is useful during data acquisition to simultaneously view the MATLAB command window and status bar of the *Polarization* GUI. Figure 9.5 shows an example of this setup.

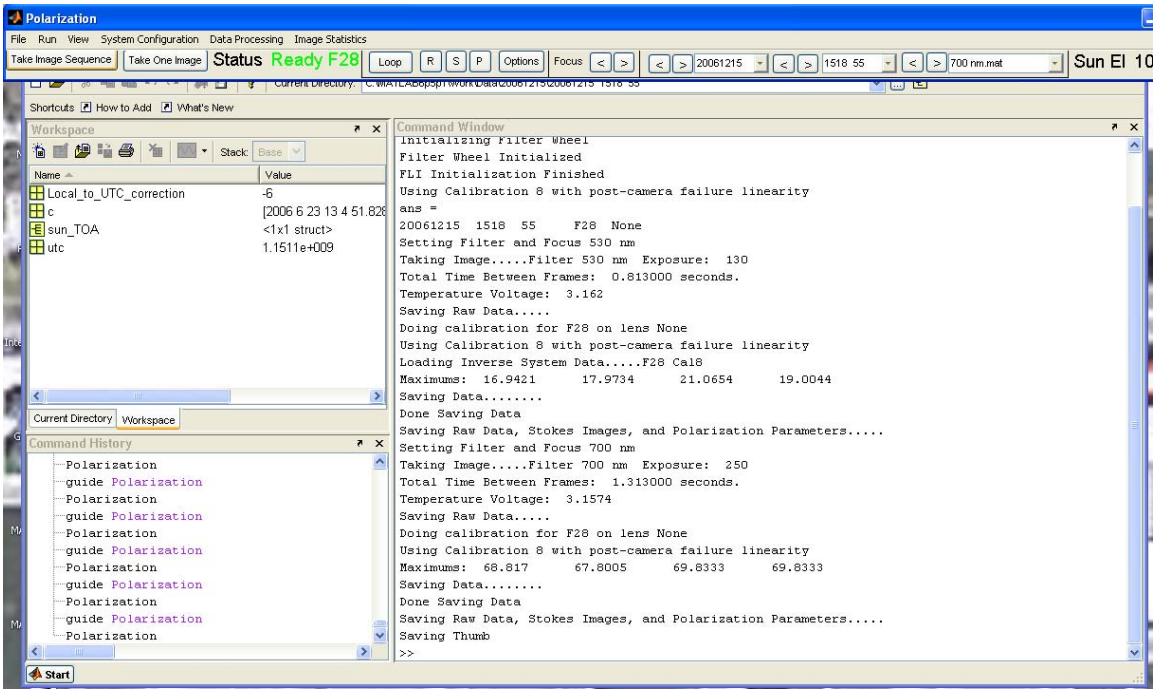

Figure 9.5. Polarization script with only the toolbar view.

Any image in the main frame can be viewed in its own figure by clicking on the image with the mouse. This is helpful, because different parameters are viewed better with different colormaps. After clicking on the image with the mouse, the image (Raw0, DoLP, Stokes2, etc.) shows up in its own enlarged window with a cursor that displays the individual values of each pixel as the mouse is moved over the image.

Many options exist for data viewing. Overexposure, underexposure, and DoLP masks among other things are available. See the **Options** GUI for more information.

Data Storage Format

For the first measurement of each day, a folder is created in the home data directory for the appropriate day. The home data directory is defined in the *Polarization* script—the default is C:\MATLAB6p5p1\work\Data\. For example, data for June 26, 2006 was put in a folder called C:\MATLAB6p5p1\work\Data\20060626\. Within this day folder, each time also has a folder. For example, data taken at 1:04:51 pm MDT was saved in a folder called C:\MATLAB6p5p1\work\Data\20060626\20060626 1304 51\. At the beginning of an image sequence collection, the settings of the data acquisition are all saved within this folder in a file called pol_settings.mat. The pol_settings stores, the lens information, the f/#, the daylight savings correction, exposure settings, UTC time, sun position information, and miscellaneous system information. Finally, as the raw images for each filter are taken, they are stored inside a file that is labeled for the filter. For example, 530 nm.mat stores the data taken at 530 nm. Besides the raw images, the

exact time of the measurement is also stored in this file. This is important for LIDAR comparisons. When the polarimeter data is extracted from the raw data—either in the field or in subsequent data processing—the polarimetric images (Stokes parameters, DoLP, etc.) are appended to the filter file. After a complete image sequence is taken, the time folder has a pol_settings.mat file, and a file labeled for each active filter.

All files are stored using MATLAB .mat files. Since the *double* format used as the standard format in MATLAB is large, a set of algorithms that compressed each polarimetric image to an unsigned 16-bit integer was used. This algorithm kept the necessary precision of all images, but reduces the storage space necessary by a factor of four from the *double* format size. Although this required additional processing, it was crucial. Even with the reduction, the data from about 25 summer days consumed over 1 TB of data storage. (For more information on the reduction see *Convert_Double_to_Uint16* in MATLAB work directory.)

Viewing Previous Data

The *Polarization* GUI was designed to acquire data, browse through past data, or post-process data later. Figure 9.6 shows an example of selecting the time from the drop down menu. When new data is selected, all the available raw data and polarization images are loaded and displayed in the GUI.

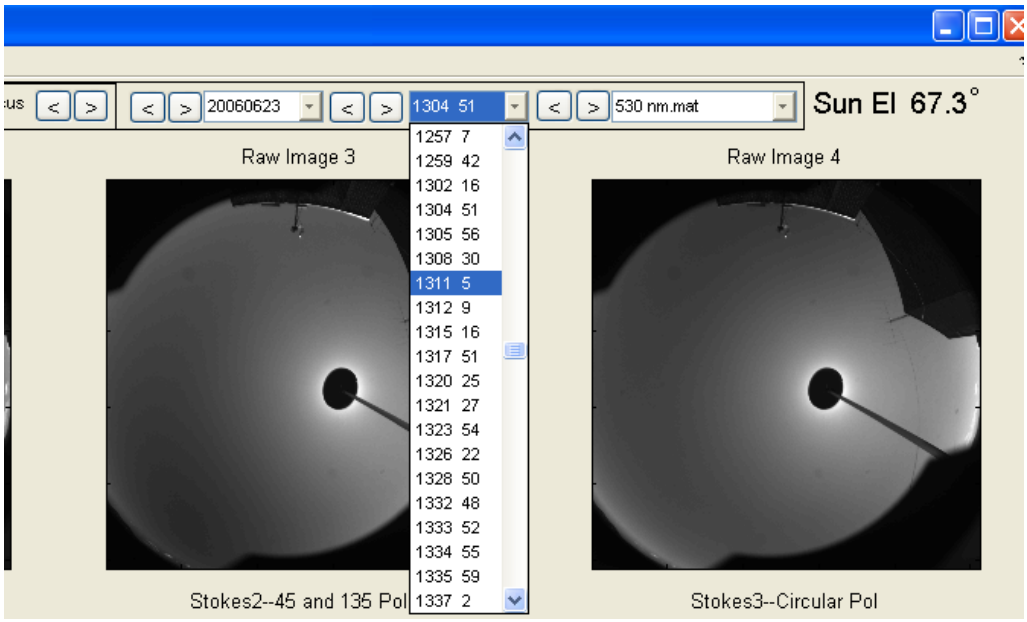

Figure 9.6. Selecting a measurement time.

When a new time is selected, the GUI automatically attempts to load the same filter that was previously viewed. For example, in the case shown, the current data time stamp is 1304 51. If the 1311 5 time is now selected, the GUI will load the 530 nm

filter data for that time—if it is available. If it is not available, the first filter in the new time folder is loaded. Similarly, if an entire new day is selected—shown in the drop down to the left of the time drop down—the GUI attempts to find a time that is closest to the time of the previously selected day. Within that day, it tries to find the same filter. This allows the user to quickly compare data from adjacent days, and times with the same wavelength. For future code, it may be in the best interest of the lab to modify the routine to find the closest solar elevation angle, not the closest time, when switching between days. Only similar solar elevation angles can be compared for properly.

Once a new time directory and data are loaded, the GUI uses the solar elevation data stored in the pol_settings.mat file to update the solar elevation indicator in the upper corner of the GUI (Figure 9.6). See the *Take Image Sequence Procedure* for information on how this information is derived.

It should also be noted that day, time, and filter drop down menus are also updated online as data are acquired. During acquisition, the drop down menu settings reflect the day, time, and filter of the current acquisition.

Options GUI

The GUI options are displayed by either toggling the *Options* toggle or the menu item underneath *System Configuration*. The *Options* GUI is used to set display options for the data (Figure 9.7).

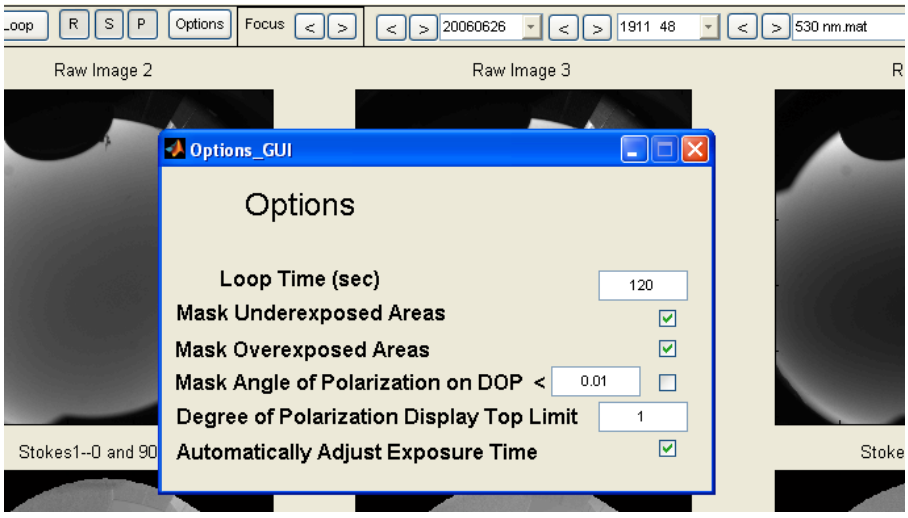

Figure 9.7. Options GUI.

The **Loop Time** sets the delay between successive acquisitions when *Take Image Sequence* is looped. This is not the time between filters, but the time between successive full acquisitions. There is no delay between filters. Successive filter measurements are taken as quickly as possible.

The **Mask Underexposed Areas** checkbox decides whether images displayed in the GUI are masked for exposures that have areas less than 100 DN. Due to the random dark noise of the imager, areas with exposures below this point are considered to have unreliable data. Therefore using this mask covers invalid data during display. Similarly, the **Mask Overexposed Areas** checkbox masks areas above 3900 DN. These areas include both areas of overexposure at 4095 DN and the areas where the linearity of the camera is degrading quickly. Although the linearization of the camera response corrects for this problem, the variability in the correction makes data above 3900 DN less reliable. This problem becomes worst as 4095 DN is approached. To be on the safe side, 3900 DN was selected as the overexposure threshold.

Mask Angle of Polarization on DoP is used to mask areas of the angle of polarization where the degree of polarization is low. For a DoLP = 0, the AoP is necessarily not defined. Since fisheye calibration errors, can corrupt the AoP for low DoLP areas (<0.5%), this mask allows the user to separate areas of the angle of polarization that are valid from areas that reflect only the error imposed by the fisheye calibration matrix. By subjecting low DoLP data to the fisheye calibration data, modeling showed that substantial errors from this source did not occur until the DoLP of the measurement dipped below about 0.5%.

Degree of Polarization Display Top Limit allows the user to rescale the upper limit of the DoLP and DoP in the GUI window. The default range is from 0 to 100% (0 to 1.00 in the data display). For objects of interest with low DoLP, such as halos, the DoLP could not be adequately viewed. This setting remedied the problem.

Automatically Adjust Exposure Time causes the imager to dynamically adjust its own exposure to use the most dynamic range as possible. For the current formulation, the exposure of each filter was individually adjusted by ±10% each time to attain the following conditions: (1) The number of pixels over 3900 DN should be less than 1000. (2) The number of pixels over 3700 DN should be at least 600. (3) The upper exposure limit was 250 msec (This is the maximum exposure that the Dalsa camera can use for a serial triggered, internal programmed integration time.) (4) The lower exposure limit is 6 msec. (Theoretically, the Dalsa 1M30 can go down to 5 msec, but problems encountered with these low exposures limited the camera to 6 msec.) For most skies, these conditions were sufficient. For quickly changing clouds, though, the exposure algorithm sometimes left the user wanting something better. Still, the algorithm was satisfactory.

Data Processing

Two drop down menus—the *Data Processing* and the *Image Statistics* menus—provide the user with various routines for data processing.

Reprocess Current Data is most useful when raw data is viewed that has not been processed. This command retrieves the calibration information for the raw data, processes all the polarimetric images, and appends the processed data to the saved raw data file. **Auto Reprocess Current Data** can be checked to automatically cause the GUI to perform this when unprocessed data is encountered. The **Reprocess Current Day** runs the **Reprocess Current Data** script for all wavelengths and all times in the current day. If only a subset of times is desired to be processed, then the **Reprocess Between Times** is useful. Once this command is selected, the start time needs to be selected from the time select drop down (shown in Figure 9.6). Right click on the beginning time in the menu after selection. Then choose the end time by the same method. If confused look at the MATLAB command prompt, which displays messages while waiting for these directories to be entered.

The **Align Current Filter** starts a process that uses an automatic iterative correlation algorithm that corrects the image for translation shifts between the images. These can arise from polarimeter movement during acquisition of the four raw images. The algorithm can be changed to either maximize the correlation between all four images or minimize the overall Stokes3 component. At the beginning of the process, the GUI prompts the user to select an area of the image to run the correlation. The user should choose an area that has high contrast with little change. Stationary buildings against a clear sky are a good object to consider. The **Align All Filters** item is not currently implemented.

Correct Row Column Crosstalk implements an algorithm that corrects for any leakage of high brightness areas down the row. The CCD readout process causes areas of high brightness to leak into areas of low brightness. This is not a significant problem for sky images. For some target images, a very dark image can be next to a very bright image. The bleeding would reduce the degree of polarization in the dark area if it were not corrected. The coefficients used in the algorithm are derived from lab data. For each pixel in each row, the contribution of the pixel to the subsequent pixel values read out in each row is calculated and subtracted. This algorithm is only needed in special cases.

Get Maximum DoP Current Image finds the maximum degree of polarization in an image after a 9 x 9 median filter removes noise. **Get Maximum DoP over Day** calculates this value for all filters and times in a given day. The variable max_DoLP is appended to the data.

Get DoLP Profile All Wavelengths shows the profile of the DoLP over a user profile. The profile is obtained by user input at the beginning of the process (right click to finish the profile). Then, the DoLP over each wavelength is loaded and retrieved for the same profile. The results are displayed in a new figure, where each line is color coded to the appropriate wavelength. 700 nm is coded in black.

Miscellaneous Commands

Under the *File* drop down menu, the **Open** command can be used to open directories of data that are stored other places. The directory selected should contain all of the day folders. Only day folders will be displayed—that is those that start with "20". Two standard directories are hard coded in the *File* drop down menu. The **Y:\Polarimeter\Data** is the network drive where large archives are stored on another server. The **Home Data Directory** is the directory that is defined in the *Polarization* script. Other hard coded data directories can be added at a later time. Currently, most data has been stored in one of the two directories given.

The **Delete Current Data** command in the *File* drop down menu is used to remove an entire time folder from the current day directory. The image thumb is also deleted from the thumb archive. Then, the file select drop down menu is updated.

Under the *Run* drop down menu, **Take Image** takes one image with the polarimeter at the first active wavelength. This does not take a full polarimetric image, but a single raw image. This command (and its particular button on the toolbar) is used for focusing and troubleshooting. The **Take Image Sequence** button and menu item are used for taking polarimetric data. **Run Configuration Script** is used to run an automatic script. This configuration script can also be run from the MATLAB command line using *Polarization('Run_Config')*. Currently, the capability is not used for anything.

Under the *System Configuration*, **Reinitialize** is useful for resetting the hardware in the event of a glitch. All hardware is restarted as if the *Polarization* script had just been initiated, but the software is not restarted. The **Camera Settings** command is not used. It was used for a previous implementation of the instrument with a different camera. If binning is implemented, this command and GUI will need to be updated. **Set Polarizer Rotation Stage** sets the rotation angle of the Newport motorized rotation state. Since calibration is done with another MATLAB script. This command is rarely used. **Align Fisheye Data with Images** aligns the current calibration with the raw data. This is useful if the imager is bumped and needs to be realigned. For a previous implementation, large aberrations in the center of the fisheye made this step crucial. The current implementation does not have large spatial variations in the calibration over 10s of pixels, so this is not necessary.

The **Focus** buttons (< is shorten, > is lengthen) are used to focus the instrument. Prior to calibration, all focuses should be found for both lenses. Use the **Focus** buttons with the **Take Image** to adjust the appropriate focuses. Then, record them for insertion into the calibration codes and the polarimeter codes.

Take Image Sequence Procedure

Documenting each function within the *Polarization* script is too elaborate for this treatment. Still, the **Take Image Sequence** command (Take_Image_Sequence_Callback

in the code) is a very important portion of the code. Without understand the sequence of taking data, other routines will be confusing. Here is the overview of the steps involved (see the actual code for more information):

1. If the imager is in save mode, steps 2 through 7 are executed.

2. The system clock is used to find the day and time.

3. A day directory (in both the standard data directory and the thumbs directory) is created if it has not been previously, and the time directory is created. This directory becomes the current directory.

4. The *Day Select* and *Time Select* drop down menus are updated for the new acquisition.

5. The current camera and calibration information is retrieved (this data is not currently used, but is saved for possible future usage.)

6. Using winqueryreg, the Local-to-UTC correction is extracted from the Windows XP operating system registry. Having this correction saved with each piece of data is useful during modeling and other data processing that requires UTC, not local time. Without this correction available, day light savings makes the local to UTC correction complicated. (Note: An uncorrected labeling error in the code saves this number as a negative. In reality the Local to UTC correction should be a positive number. All the codes using this number are coded backwards, so the error was left. It is not really an error, just a semantics problem. The variable should be named UTC_to_Local, not Local_to_UTC.)

7. Get the UTC time and use it to calculate the solar zenith and azimuth angles. Using the solar zenith, the solar elevation angle is calculated and displayed in the upper right corner of the GUI.

8. All settings, time variables, hardware variables, sun position variables, F_number and lens variables, exposure and filter variables, and calibration data are saved in the pol_settings file.

9. Steps 9 through 16 are done for each active filter:

10. The filter is set to the appropriate position in the filter wheel.

11. The focus is set for the appropriate filter.

12. The exposure time, and LCVR voltages are retrieved.

13. The Take Image Sequence C++ routine (.dll) is called. This routine initializes the camera serial port, frame grabber board, and memory for the acquisition. Then, the camera settings (such as triggering and exposure) are input into the camera. Then, a dummy image is taken. For each of the raw images, the appropriate LCVR voltage is set for the image, the software waits for the LCVR to stabilize (the LCVR delay in the code), and the image is exposed and downloaded from the camera. (This is an oversimplified explanation. In reality, while the camera is downloading, the next LCVR voltage is set so that less LCVR delay is needed between images.) Four raw images are returned to the MATLAB script.

14. The temperature is checked for adherence to calibration boundaries. If it is low or high, the user is warned and expected to remedy the situation before the imager loses calibration.

15. If in save mode, the raw data is archived and the *Filter Select* drop down menu is updated for the new data.

16. If online processing is enabled, then the data is processed for polarization images. (See *Data Processing Procedure* below for more details.) Overexposure and underexposure masks and warnings are handled by the data processing. If online processing is not enabled, the data is checked for overexposure and underexposure and automatic exposure adjustment is run.

17. After all filters have been taken, a thumb of one of the last raw images (or the Stokes0 image if processed) is written to the thumbs folder for quick data browsing later.

18. If the **Loop** button is depressed, then the imager delays for the *Loop Time Delay* set in the **Options** GUI and the process starts over again. This happens indefinitely until the user disables the **Loop** button.

Data Processing Procedure

All data processing uses the *Reprocess_Filter_in_Curr_Dir.m* and *Process_Raw_Data* scripts to process the polarization data. The routine assumes that the raw images are already in the MATLAB global variable space. Also, it understands that there is a possibility that the appropriate calibration matrices may also be loaded there. The following steps were used to process data:

1. If alignment information is saved with the raw data, the images are aligned. This information would come from the **Align Current Image** routine or other correlation algorithm.

2. If the appropriate calibration information—dark image, linearity correction, near field correction, lens correction, etc.—is not loaded then load it.

3. Mask the top 4 bits of each pixel to zeros, since it is only a 12-bit camera. (The frame grabber can put garbage in the upper 4 bits.)

4. Correct the dark image for the exposure of the image. Longer exposures need more dark image correction. (See *Polarimeter Calibration, Camera Calibration* for more information on this.)

5. Call *Process Raw Data* for steps 6—13.

    6. An overexposure mask was created by finding the number of pixels across all images that were above the threshold. (The overexposure mask is one image.) The underexposure mask was created in the same fashion.

    7. The dark image was subtracted from each image.

    8. Each image was corrected for linearity.

    9. The Stokes images for the near field polarimeter—the polarimeter without the front lens—were extracted using the appropriate calibration.

    10. All Stokes images except Stokes0 were normalized to Stokes0. Now their range of values was between –1 and 1.

    11. The inverse Mueller matrix of each lens was applied to the Stokes parameters retrieved from the near field polarimeter. The resulting Stokes images are the actual measured Stokes images.

    12. From these parameters, the DoLP (called Deg_PoL), DoCP (called Deg_Cir), DoP(called Total_Deg), and the AoP (called Ang_Pol) were calculated.

    13. All images were compressed to unsigned 16-bit integer for data storage using *Convert_Double_to_Uint16*.

14. Finally, the polarization images were appended to the raw data archive file (eg. 530 nm.mat).

System Notes

System Hookup Notes

Connecting the system is straightforward. Each wire is labeled on both ends and connection points are labeled. LCVR1 is the liquid crystal furthest from the camera. Because of space issues, LCVR2 plugs into the LCVR3 port on the Meadowlark

controller. The LCVR commands inside the C++ dll (Take_Image_Sequence_C) that run the image sequence handle this labeling difference.

After a computer reboot the Finger Lakes Instrumentation devices can initialize wrong. To remedy the problem, follow these steps. After Windows XP initializes, unplug all wires from both the CFW-1 and the DF-2 Control boxes (USB, power, and gray wire). Then, for each box, plug the wires back in using this order: USB, then power wire, then gray wire. These steps are necessary to initialize the Finger Lakes USB interfaces correctly.

External Software

External software is minimal since most routines are directly coded in the C++/MATLAB libraries. For the current version of the instrument, Bitflow SDK 4.00 is used to operate the Road Runner (R3-PCI-DIF-L) frame grabber card. After SDK installation, the System Configuration program found under Start->Bitflow->SDK 4.00 must be configured for the DALSA 1M30 camera. Under board operation, the attached camera file should be the Smd1M30PC-1kW1OneShot. When the camera was first bought, it was necessary to use the Camera Editor to modify the Smd1M30PC-1kW1OneShot camera file for a falling pixel clock polarity. Since this time, the camera has worked consistently. The Bitflow R2View is a useful piece of software for viewing camera data while adjusting focus and alignment. For normal operation, all frame grabber control was handled by Take_Image_Sequence_C.dll (see the Take_Image_Sequence_C.dsw workspace under C:\MATLAB6p5p1\work\ BitflowforMatlab\Take_Image_Sequence_C\ for the code.)

Meadowlark software is not necessary, since the Meadowlark LCVR controller is totally controlled by serial commands. For more information on these commands, see the *Meadowlark LCVR Controller Operator's Manual*.

The DALSA 1M30 was not shipped with special operating software. The *DALSA 1M30 Operator's Manual* gives the serial commands necessary to run the camera. For all measurements, the camera is used in STII (Serial Triggered/Internal Integration) model. See the 1M30 manual for specific serial commands.

The FLI C++ SDK was ported to MATLAB by Nathan Pust. The entire port is available online at fli-cam.com under software. All FLI functions were ported individually. (See the workspace FLIForMatlab.dsw in C:\MATLAB6p5p1\ work\FLIforMatlab\ for more information.)

Other Notes

The focuser cannot move beyond 1600 steps without overextending its screws. The polarization code has been hardcoded to enforce this limit.

APPENDIX C

CALIBRATION PROCEDURE

This appendix outlines the general steps needed to calibrate the instrument. Specific understanding of the code is needed to completely understand the calibration process. Several different routines are used to calibrate the instrument. The system matrix extraction and lens calibration routines are complex both mathematically and systematically. To give a better understanding of their operation, the near field and telephoto routines are explained and given in this dissertation. Also, the near field processing routine is given for reference. The fisheye calibration script is similar to the telephoto script. The camera calibration scripts and the processing scripts are not given for brevity.

General Calibration Steps

Note: Items in *italics* refer to the MATLAB script or variable name used for the particular step in the calibration.

1. Hook the imager up. Take sample images with the fisheye lens. Outdoor lighting may be necessary to obtain sufficient exposures. Adjust either the screws that mount the DF-2 to the DALSA 1M30 and/or the final 8-32 bolt slot position that mounts the Thorlabs lens tube to the aluminum frame to adjust the image placement until it is centered. The R2View in the Bitflow SDK is helpful for this adjustment. Using different size spacers on the 8-32 rail will adjust the height of the image. The 8-32 should be used for fine adjustment (<100 pixel), while the DF-2-to-1M30 connection should only be moved for large adjustments. Once the fisheye is aligned, check that the telephoto image also fits into the CCD image fully. If not, split the difference, but weight the fisheye image utilization of the image plane as most important. Also, roughly adjust the focus with the 105 mm Micro lens and 8-32 bolt that fixes the DF-2 to the aluminum frame. Lock down all bolts.

2. Find the focus position of the DF-2 for each lens and each filter. Record these positions and enter them into the *Get_Telephoto_Mueller_Matrix* and *Get_Fisheye_Mueller_Matrix_Compressed* MATLAB scripts. Also, use the fisheye focus position values for the near field calibration scripts, *Get_LCVR2_m01_m02* and *Get_LCVR1and2_m01_m02*

3. Seal instrument. Update the *new_dark_image_filename* variable in *Get_Dark_Image* to reflect the date of the dark image. For example, the dark image taken on October 9, 2006 was labeled: DALSA_1M30_DARK_IMAGE_100906. Get a new dark image. Use *Check_Dark_Image* to check the validity of the new dark image. Then, using difference exposures, find the exposure dependent correction. Update *Get_Nonlinearity_Calibration_w_Variable_Irradiance*, *Get_Telephoto_Mueller_Matrix, Get_Fisheye_Mueller_Matrix_Compressed*, *Get_LCVR2_m01_m02, and Get_LCVR1and2_m01_m02* for the new dark image filename and correction information.

4. Remove the front lens and install the instrument on the lab mount. (This mount provides the –45, 0, +45, and 90° post mounts to calibrate each stripe of the fisheye image later.) Put the luminance standard on the rotating mount close to the aperture of the instrument. (The rotating mount is used to rotate the Sphere Optics luminance standard around the table in the fisheye calibration later.) Change *filename* in *Get_Nonlinearity_Calibration_w_Variable_Irradiance* to reflect the date of the new nonlinearity correction, as was done for the dark image. Turn on the Sphere Optics equipment. To turn on the luminance standard, use LumRadMain (under the Sphere Optics folder on the Start Menu). Then kill the routine in the Windows Task Manager. This will leave the COM ports open for MATLAB use, but keeps the luminance standard on. Then, start MATLAB.) Use the *Get_Nonlinearity_Calibration_w_Variable_Irradiance* routine to take the linearity data. Use the *Process_Nonlinearity_Calibration_w_Variable_Irradiance* function with the appropriate *filename* to save the nonlinearity correction. Update *Get_Telephoto_Mueller_Matrix, Get_Fisheye_Mueller_Matrix_Compressed*, *Get_LCVR2_m01_m02, and Get_LCVR1and2_m01_m02* for the new nonlinearity correction filename.

5. Take lens, image tubes, and both LCVRs off the instrument. Using polarizers. Zero the internal polarizer to be vertical compared to the plane of the aluminum base. This is best accomplished using an optics table and references polarizers.

6. Install the Newport rotation stage with the 4” polarizer between the imager and the luminance standard. Find the zero setting of the 4” polarizer in the Newport stage against the polarimeter polarizer. Record this setting in the angle_of_reference variable in *Get_LCVR_Voltage_Retardance_Curve*, *Get_Telephoto_Mueller_Matrix, Get_Fisheye_Mueller_Matrix_Compressed*, *Get_LCVR2_m01_m02, and Get_LCVR1and2_m01_m02*.

7. Note: This step is not necessary if voltages have previously been selected (see Table 4.1 for current voltages).

   Set the imager to f/4.0. This provides an average of all f/#s. Find the voltage/retardance curves of each LCVR by first placing it on the instrument, then using the rotating polarizer in the 4” Newport stage with *Get_LCVR_Voltage_Retardance_Curve* to obtain the voltage/retardance curve of each LCVR at each wavelength. Using these curves, find the appropriate voltages for each wavelength that correspond to the retardances in Table 3.1. Save these voltages as 5x4 matrices (number of filters by the number of images) in LCVR1_Voltages and LCVR2_Voltages in a file called LCVR_Voltages_450_700_4IMAGE_SYSTEM_[date].mat in the C:\MATLAB6p5p1\work\Polarimeter 4 Stokes Calibration\LCVR Data and Figures directory. Update *Get_Telephoto_Mueller_Matrix, Get_Fisheye_Mueller_Matrix_Compressed*, *Get_LCVR2_m01_m02, and Get_LCVR1and2_m01_m02* for this new file name.

8. Install LCVR2 at an angle 45° to the polarizer. Using *Get_LCVR2_m01_m02*, get the system matrix of LCVR2 at each f/# between 2.8 and 8.0. Set the calibration_name variable to be a new name. This name will be used for all future routines. Set the F_number variable for each new run.

9. Install LCVR1 at an angle 115° to the polarizer. Redo Step 1 to ensure the imager is realigned properly.

10. Remove front lens. Using *Get_LCVR1and2_m01_m02* get the system matrix with both LCVR1 and LCVR2. Set the calibration_name variable to be the new calibration name. Set the *F_number* variable for each new run. (Run for f/2.8, f/4.0, f/5.6, f/8.0)

11. Use *Process_Inverse_System_Matrix_Linear_Only* to obtain a temporary linear calibration. (Set the appropriate calibration name and f/# in the code.) Update *Check_Near_Field_Calibration* for all new calibration data. Then run this script to look for errors in the system matrix. If errors are under 0.5% DoLP for all filter images, the calibration is good. Once the user is satisfied with the calibration, use *Process_Inverse_System_Matrix_w_m03_Model (*with the appropriate calibration number) to process a system matrix that produces all 4 Stokes parameters. To speed the process, use a Linux machine, not a Windows machine. Even with Linux, this process takes about 14 hours. Again use *Check_Near_Field_Calibration* to check the accuracy of the system matrix. (*Check_Near_Field_Calibration* uses –67.5, -22.5, 22.5, and 67.5° polarizer settings to check the near field system matrix. To change the angles uses, adjust the *ref_angles* variable.)

12. Install 300 mm Telephoto lens. Update *calibration_name* in *Get_Telephoto_Mueller_Matrix*. Then, run the script for each of the f/#s.

13. Use *Process_Telephoto_Mueller_Matrix_Data_Symmetrical* to find the inverse telephoto lens data. (First, update the *calibration_name* and *F_number*.)

14. Update *Check_Lens_Calibration* for all variables (focus, calibration, f/#, camera, etc.). Check the telephoto calibration in a similar fashion to the near field calibration.

15. Install the fisheye lens. Due to the large FOV, the fisheye must be calibrated piecewise. To calibrate the fisheye lens, reposition the instrument so the fisheye is as close to the calibration polarizer as possible without restricting the rotation of the luminance standard around the full 180° FOV of the fisheye lens. Set the polarimeter mount angle (-90, -45, 0, or 45). Order does not matter here, as each angle will have covered at some point. (Be careful not to slam the instrument when changing its angle in the mount. If the instrument is slammed, the alignment may move.) Then set the *degree* variable in the *Get_Fisheye_Mueller_Matrix_Compressed* code to match the mount value. Progressively move the Sphere Optics luminance standard around the 180° FOV of the fisheye, so that the entire stripe of the image is calibrated. At each location, run the script. Once the script has begun. It will ask

you to delineate the area of the fisheye that is being calibrated. Use the mouse to select the area of the round luminance standard aperture. Right click when finished. Then, the script will calibrate this selected area of the image. Then, the standard is moved and another position calibrated. This happens about 7 times around the semi-circle of the FOV. Then, the polarimeter is moved to the next mount with a new angle. This happens for each of the four angles (-90, -45, 0, 45). The entire process can take many hours. When all four mount angles have their ~7 images calibrated, calibration stripes have been taken through the fisheye image at –90, -45, 0, and 45.

16. Use *Piece_Together_Fisheye_Mueller_Matrix_Data_Compressed* to make a fisheye polarization image for the whole image. Now, due to the instantaneous rotation of the polarization vector by the fisheye, only the middle sliver of each stripe is valid. The *Fisheye_Lens_Data_Interpolator* is used to select only the section of each slice that does not rotate the angle of polarization. Use *Display_Lens_M* to display the piecewise lens Mueller matrix. Using this data, find the center of the lens data. To find the center, look at the confluence of the M_{32} and M_{23} images. If you use the *pixval* script, remember that its display is labeled [column, row]—as opposed to the usual [row, column]. Insert this point into the interpolator code. Also using this data, figure out the maximum radius that can be interpolated. Insert this into the interpolator code. Run the interpolator code. The area between the four slices is interpolated from the values of each of the slices. The final fisheye Mueller matrix is saved.

17. *Process_Fisheye_Mueller_Matrix_Data_Symmetrical* is used to make the inverse lens Mueller matrix from the interpolated data. Use *Check_Lens_Calibration* to check the fisheye calibration in the same way as the telephoto, but change the lens name. For the fisheye, this routine prompts for the region of the image to be validated, much like the script *Get_Fisheye_Mueller_Matrix_Compressed* prompts for the area to be calibrated. Calibration accuracies of +/-1% should be achievable for the fisheye. Better calibration accuracies should be found for the telephoto.

18. Record all the calibration data names with the active date in the routine *Find_Appropriate_Calibration*. This routine is used to find the right calibration during both data collection and data processing. It is very important.

Note: The Sphere Optics luminance serial connection needs to be connected to COM1 to work correctly.

Note: MATLAB scripts need to be adjusted to the Newport stage COM port number used. If the USB-to-serial converter is used, the COM port number of the hardware can be adjusted in the device manager. Typically, COM3 is used in the codes.

Note: All calibration data and routines are stored in appropriate directories under ~\work\Polarization 4 Stokes Calibration\. The near field data is stored with the voltage/retardance curves under the directory "LCVR Data and Figures"

Explanation of MATLAB Calibration Routines

Near Field Calibration (Get LCVR1and2_m01_m02)

To calibrate the near field polarimeter, the *Get_LCVR1and2_m01_m02* routine is used. For this routine, the polarimeter is mounted to the optics table without a lens. It looks through the 4" polarizer in the Newport rotation stage at the aperture of the Sphere Optics luminance standard.

The goal of the code is to find the system matrix of only the near field polarimeter for each pixel. For each pixel, the system matrix will have four rows and four columns. The last column is modeled using the circular model in *LCVR_Model_Two_LCVR.m* via *Process_Inverse_System_Matrix_w_m03_model.* Without going into details, all elements of the first column are ~.5 due to the ~50% transmittance of the internal polarizer for unpolarized light and the fact that the LCVRs have nearly zero diattenuation. For this instrument, the system matrix was normalized by the transmission. Therefore, all the first column elements of the system matrix are 1, and all fourth column elements are determined by the model. The goal of calibration then is to find the second and third column. Inspection of Equation 10.1 shows how a_{01} and a_{02}—the second and third elements from the first row of the system matrix—can be found. Depending upon the polarizer angle used, a different brightness is measured. For example, on the first line, the calibration polarizer is at 0°, so the Stokes vector is [1 1 0 0]. This vector is multiplied by the first row of the system matrix to find the image brightness ($Image_0$). Using four different polarizer angles, both elements can be found (Equation 10.1).

$$\begin{aligned} \text{Image}_{0} &= 1a_{00} + 1a_{01} + 0a_{02} + 0a_{03} \\ \text{Image}_{-90} &= 1a_{00} - 1a_{01} + 0a_{02} + 0a_{03} \\ \text{Image}_{+45} &= 1a_{00} + 0a_{01} + 1a_{02} + 0a_{03} \\ \text{Image}_{-45} &= 1a_{00} + 0a_{01} - 1a_{02} + 0a_{03} \end{aligned} \tag{10.1}$$

Remember that a_{01} and a_{02} correspond to one set of drive voltages for LCVR1 and LCVR2. A more general form of the entire matrix inversion shows how the entire system matrix can be measured using this method. Notice that the first column which corresponds to Equation 10.1.

$$\begin{matrix} \textit{Voltage}\,1 & \textit{Voltage}\,2 & \textit{Voltage}\,3 & \textit{Voltage}\,4 \end{matrix}$$
$$\begin{bmatrix} \text{Image}_{0} & \text{Image}_{0} & \text{Image}_{0} & \text{Image}_{0} \\ \text{Image}_{-90} & \text{Image}_{-90} & \text{Image}_{-90} & \text{Image}_{-90} \\ \text{Image}_{+45} & \text{Image}_{+45} & \text{Image}_{+45} & \text{Image}_{+45} \\ \text{Image}_{-45} & \text{Image}_{-45} & \text{Image}_{-45} & \text{Image}_{-45} \end{bmatrix} = \begin{bmatrix} a_{00} & a_{01} & a_{02} & a_{03} \\ a_{10} & a_{11} & a_{12} & a_{13} \\ a_{20} & a_{21} & a_{22} & a_{23} \\ a_{30} & a_{31} & a_{32} & a_{33} \end{bmatrix} \begin{bmatrix} 1 & 1 & 1 & 1 \\ 1 & -1 & 0 & 0 \\ 0 & 0 & 1 & -1 \\ 0 & 0 & 0 & 0 \end{bmatrix} \quad (10.2)$$

By multiplying the brightness images on the left by the inverse of the matrix of Stokes vectors on the right, system matrix images of each parameter of the first three columns of the system matrix can found. This is done for each pixel at each filter. The code is then rerun for each f/#.

In the MATLAB code, the variables named m00, m01, and m02 replace a00, a01, and a02 here. In the code, the Raw_Images variable stores all the information on the left hand side of Equation 10.2. The size of Raw_Images is 5x4x4x1024x1024. The first dimension is the number of filters. The second dimension corresponds to the voltage number of the raw image from 1 to 4. The third dimension is the number of the polarizer angle. For example, in Equation 10.2, 0° would be 1, -90° would be 2, 45° would be 3, and -45° would be 4. The last two dimensions are spatial pixel dimensions. The matrix of Stokes vectors is called Stokes_M.

Note: The polarimeter angles used to calibrate could be other angles than 0, 90, -45, and 45. A different polarimeter angle set would change the Stokes parameter matrix on the left of Equation 10.2. The angles chosen were well conditioned, though.

The code works as follows:

1. The user sets the calibration number and the f/# before running the code.

2. Calibration information for the camera dark image, camera linearity, LCVR voltages, focuses, and LCVR2 information is loaded. All variables are initialized. The temperature set point of the LCVRs is checked. The Newport rotation stage is initialized.

3. For each filter, steps 4 through 12 are done.

4. First, the filter wheel and focuser position were set.

5. For each polarizer angle, steps 5-6 are done. The actual polarizer angle order is different than Equation 10.2. It is –90, -45, 0, and 45°. This just reorders the equation, but does not change the results.

6. The calibration polarizer angle is set.

7. Instead of one image, many different images were taken to remove random errors. These images were stored in Raw_Images_Temp. The average of these images was then saved to Raw_Images. At each polarizer angle, all four voltages were taken for the polarimeter angle. This corresponds to one row of Equation 10.2.

8. Dark image and linearity correction was done for each of the 16 images (4 polarizer angles at 4 voltages).

9. The inverse Stokes calibration matrix was calculated.

10. The inverse Stokes calibration matrix was applied to the raw images one column (that is one voltage) at a time. This gives one row of the system matrix at a time. Both m01 and m02 are normalized by m00. This is the average m00. Since Stokes_M is overdetermined, two m00s can be calculated—one by averaging the –90 and 0° polarizer angles, and one by averaging the –45 and 45° polarizer angles. A large difference in these m00's—labeled m00a and m00b in the code—indicates that a large error exists in the raw data. This can come from exposure jitter or other causes. If an error greater than 1.3% was found between the average m00a and m00b, then an error flag was generated.

11. The values of m01 and m02 were stored in LVCR1and2_m01 and LCVR1and2_m02.

12. An averaged system matrix was calculated. It also used the third column model. This average matrix was inverted and applied to the average raw images to recheck the Stokes vectors used to calibrate. If any of the Stokes parameters in any calibration vector was off by more than 1% than an error flag was generated.

13. If no errors were generated, then the next filter was calibrated. If an error was generated, the current filter was redone until no errors were generated. When this occurs, an accurate calibration has been attained.

14. The data from the second and third columns of the system matrix was saved in 'C:\MATLAB6p5p1\work\Polarimeter 4 Stokes Calibration\LCVR Data and Figures' under LCVR1and2_m01_m02_[F_number][calibration_name].

Front Lens Calibration (Get_Telephoto_Mueller_Matrix)

Once the treatment of the near field calibration is understood. Calibration is easily understood for the telephoto lens with *Get_Telephoto_Mueller_Matrix*. The fisheye calibration follows the telephoto calibration, but an area is delineated to be calibrated at the beginning of the routine. The telephoto calibration uses an identical method to the near field calibration. The difference is that the near field has been calibrated, so the instrument returns Stokes vectors instead of raw images. Therefore, a Mueller matrix for the lens is found, not the system matrix (Equation 10.3). Instead of

the columns corresponding to the four different LCVR settings. The columns now correspond to the components of the Stokes parameters.

$$\begin{matrix} Stokes0 & Stokes1 & Stokes2 & Stokes3 \\ \begin{bmatrix} \text{Image}_{0} & \text{Image}_{0} & \text{Image}_{0} & \text{Image}_{0} \\ \text{Image}_{-90} & \text{Image}_{-90} & \text{Image}_{-90} & \text{Image}_{-90} \\ \text{Image}_{+45} & \text{Image}_{+45} & \text{Image}_{+45} & \text{Image}_{+45} \\ \text{Image}_{-45} & \text{Image}_{-45} & \text{Image}_{-45} & \text{Image}_{-45} \end{bmatrix} \end{matrix} = \begin{bmatrix} m_{00} & m_{01} & m_{02} & m_{03} \\ m_{10} & m_{11} & m_{12} & m_{13} \\ m_{20} & m_{21} & m_{22} & m_{23} \\ m_{30} & m_{31} & m_{32} & m_{33} \end{bmatrix} \begin{bmatrix} 1 & 1 & 1 & 1 \\ 1 & -1 & 0 & 0 \\ 0 & 0 & 1 & -1 \\ 0 & 0 & 0 & 0 \end{bmatrix} \quad (10.3)$$

Using a similar method to the near field, the first three columns of the lens Mueller matrix can be extracted. These elements are then normalized by m00 to get rid of transmission. Using similar methods, two different m00s can be found. Any errors in the m00s of greater than .6% trigger the recalibration of the filter. The final column of the lens Mueller matrix is assumed to be a symmetrical reflection of the lower triangle and the matrix was set as follows: m30 = m03, m31 = m13, m32 = m23.

Get_LCVR1and2_m01_m02 MATLAB Code

```
%Nathan Pust
%May 9, 2005

%This script is used to find the system matrix of the two LCVR system
%without the front lens (also called the near-field system).  Using 4
%different angles -90,-45,0,45, the system matrix is measured for a given F
%number and wavelength.

%Focus should be set before these measurements begin to be the focus that
%works with the fisheye lens.  Throughout the entire calibration, the
%focuses should stay the same.  Experimentation has shown that slight focus
%adjustments are not a huge concern, but care should still be taken to
%minimize the change in calibration due to change in focus.

clear

%Sphere Attn: 6000 F2.8
F_number = 'F28'; exp_time = [195 78 52 37 37];

% %Sphere Attn: 4300 F4.0
% F_number = 'F40'; exp_time = [195 78 52 37 37];

% %Sphere Attn:    0 F5.6
% F_number = 'F56'; exp_time = [195 78 52 37 37];

% %Sphere Attn:    0 F8.0
% F_number = 'F80'; exp_time = [250 156 100 70 70];

% %Sphere Attn:    0 F11
% F_number = 'F11'; exp_time = [250 250 200 140 140];

% %Sphere Attn:    0 F16
% F_number = 'F16'; exp_time = [250 250 250 250 250];

LCVR1 = 1;
LCVR2 = 3;  %LCVR2 is plugged into port 3
LCVR_delay = 55;

calibration_name = ['_Cal8'];
clear nonlinearity_correction
load DALSA_1M30_linearity_correction_100906
nonlinearity_correction = DALSA_1M30_linearity_correction;
load('DALSA_1M30_DARK_IMAGE_100906','DALSA_1M30_DARK_IMAGE');
Dark_Img = DALSA_1M30_DARK_IMAGE;

angle_of_reference = 104.25;
no_stage_angles = 4;
stage_ang_increase = 45;
samples = 3;
```

```
focus_points = [720 670 670 770 820];

%Initializations
Raw_Images = single(zeros(5,4,no_stage_angles,1024,1024));
Raw_Images_Av = zeros(5,4,no_stage_angles);
Raw_Images_Temp = single(zeros(4,1024,1024));

if(which(char(['LCVR2_m01_m02_' F_number calibration_name '.mat'])))
   load(char(['LCVR2_m01_m02_' F_number
calibration_name]),'LCVR2_retard_av','LCVR2_rotation_av')
else
   error('No LCVR2_m01_m02 file')
end

%Import LCVR2 Voltages used in system in order [0 150 33.08 180] retardance
load LCVR_Voltages_450_700_4IMAGE_SYSTEM

%Initialization
LCVR1and2_m01 = single(zeros(5,4,1024,1024));
LCVR1and2_m02 = single(zeros(5,4,1024,1024));
LCVR1_retard_av = zeros(5,4);
LCVR1_rotation_av = zeros(5,4);

filter = 1;

%Open LCVR Port
LCVR_port = serial('Com3');
if(strcmp(LCVR_port.status,'open'))
   fclose(LCVR_port);
end
set(LCVR_port,'BaudRate',38400,'DataBits',8,'Parity','none','StopBits',1,...
           'Terminator','CR','FlowControl','None');
fopen(LCVR_port);
fprintf(LCVR_port,'tsp:?')
tsp = fscanf(LCVR_port)
if(~(strcmp(tsp(2:10),'tsp:10400') | strcmp(tsp(1:9),'tsp:10400')))
   error('Temperature did not set in LCVR Controller')
   fclose(LCVR_port);
end
fclose(LCVR_port)

%Open Rotation Stage
rot_port = serial('Com5');
if(strcmp(rot_port.status,'open'))
   fclose(rot_port);
end
set(rot_port,'BaudRate',19200,'DataBits',8,'Parity','none','StopBits',1,...
          'Terminator','CR/LF','FlowControl','Hardware');
fopen(rot_port);
fprintf(rot_port,'1MO');
%Home Rotation Stage
fprintf(rot_port,'1OR');
%Wait for stop moving
```

```
moving = '0';
while(str2num(moving) ~= 1)
   fprintf(rot_port,'1MD?');  %Request moving status
   pause(.050);
   moving = fscanf(rot_port);  %Get Moving Status from Newport Controller
   pause(.050);
end
fprintf(rot_port,'1TB');
fscanf(rot_port);

while(filter < 6)

   filter
   error_flag = 0;
   filter_wheel_dev = FLIOpen('flifil0',514);
   FLISetFilterPos(filter_wheel_dev,filter-1);
   FLIClose(filter_wheel_dev);

   focuser_dev = FLIOpen('flifoc0',770); %770 is FLIDOMAIN_USB | FLIDEVICE_FOCUSER
   FLIHomeFocuser(focuser_dev);
   FLIStepMotor(focuser_dev,focus_points(filter));
   disp('Focuser Initialized')
   FLIClose(focuser_dev);

   %Take Four Stokes Images
   for j=1:no_stage_angles

      %Set Polarizer to -90,-45,0,45
      angle = angle_of_reference + -(j-1)*stage_ang_increase;
      disp(' ')
      disp(['Polarizer angle:  ' num2str(angle)])
      fprintf(rot_port,strcat('1PA',num2str(angle)));
      moving = '0';
      %Wait for stop moving
      while(str2num(moving) ~= 1)
         fprintf(rot_port,'1MD?');  %Request moving status
         pause(.050);
         moving = fscanf(rot_port);  %Get Moving Status from Newport Controller
         pause(.050);

      end

      %Initialize Variables
      Raw_Images_Temp = zeros(4,1024,1024);
      Raw_Images(filter,:,j,:,:) = zeros(4,1024,1024);

      for(sample = 1:samples)

         [Raw_Images_Temp(1,:,:),...
          Raw_Images_Temp(2,:,:),...
          Raw_Images_Temp(3,:,:),...
          Raw_Images_Temp(4,:,:),Temperature]...
            = Take_Image_Sequence_LCVR_C(exp_time(filter),1,1,1,...
```

```
                        LCVR1_Voltages(filter,:),LCVR2_Voltages(filter,:),...
                        LCVR_delay);
    Raw_Images_Temp = double(bitand(Raw_Images_Temp,bin2dec('0000111111111111')));
    Raw_Images(filter,:,j,:,:) = squeeze(Raw_Images(filter,:,j,:,:)) + Raw_Images_Temp;

    format bank
    disp(num2str([mean2(squeeze(Raw_Images_Temp(1,400:600,400:600)))...
            mean2(squeeze(Raw_Images_Temp(2,400:600,400:600)))...
            mean2(squeeze(Raw_Images_Temp(3,400:600,400:600)))...
            mean2(squeeze(Raw_Images_Temp(4,400:600,400:600)))],'   %8.2f'))
    format

  end
  Temperature = strtrim(Temperature);
  Temperature = 6.4692e-005*str2num(Temperature(5:9)) + .4718;
  %disp(char(['Temperature Voltage:  ' num2str(Temperature)]))
  temperatures(filter,j) = Temperature;

  Raw_Images(filter,:,j,:,:) = Raw_Images(filter,:,j,:,:)./samples;

end


%Correct Images for Dark Current and Nonlinearity
for(n=1:4)

  for(j=1:no_stage_angles)

      %Correct for Dark_Img and Exposure
      img = squeeze(Raw_Images(filter,n,j,:,:));
      if(mean2(img(400:600,400:600)) > 3800)
        disp(char(['Warning: Over Exposure  DN: ' mean2(img(400:600,400:600))...
            ' Voltage: ' num2str(n) '  Angle_number: ' num2str(j)]))
      end
      img = img - Dark_Img;
      img = img - (.011*exp_time(filter) - .55);
      img = polyval(nonlinearity_correction,img);
      Raw_Images(filter,n,j,:,:) = img;
      Raw_Images_Av(filter,n,j) = mean2(img(400:600,400:600));
  end
  format bank
  disp(num2str(squeeze(Raw_Images_Av(filter,n,:))','   %8.2f'))
  format
end



%Create Matrix of Stokes Vectors, Invert
for j=1:no_stage_angles

  Stokes_M(j,:) = Stokes_100((j-1)*stage_ang_increase - 90);

end
```

```
Stokes_M_inv = pinv(Stokes_M(:,1:3));

%For every voltage (system setting), find the m00,m01,m02.
for n=1:4

   %Raw_Images(filter,voltage,stage_angle,xpixel,ypixel)

   %Find m00
   m00 = Stokes_M_inv(1,1).*Raw_Images(filter,n,1,:,:) + ...
        Stokes_M_inv(1,2).*Raw_Images(filter,n,2,:,:) + ...
        Stokes_M_inv(1,3).*Raw_Images(filter,n,3,:,:) + ...
        Stokes_M_inv(1,4).*Raw_Images(filter,n,4,:,:);
   %Find m01
   m01 = Stokes_M_inv(2,1).*Raw_Images(filter,n,1,:,:) + ...
        Stokes_M_inv(2,2).*Raw_Images(filter,n,2,:,:) + ...
        Stokes_M_inv(2,3).*Raw_Images(filter,n,3,:,:) + ...
        Stokes_M_inv(2,4).*Raw_Images(filter,n,4,:,:);
   %Find m02
   m02 = Stokes_M_inv(3,1).*Raw_Images(filter,n,1,:,:) + ...
        Stokes_M_inv(3,2).*Raw_Images(filter,n,2,:,:) + ...
        Stokes_M_inv(3,3).*Raw_Images(filter,n,3,:,:) + ...
        Stokes_M_inv(3,4).*Raw_Images(filter,n,4,:,:);

   m01 = squeeze(m01./m00);
   m02 = squeeze(m02./m00);

   m01_mean = mean2(m01(400:600,400:600));
   m02_mean = mean2(m02(400:600,400:600));

   A_mean(filter,n,:) = [1 m01_mean m02_mean 0];

   %Mean Filtering
   %m01 = imfilter(m01,ones(5,5)/25);
   %m02 = imfilter(m02,ones(5,5)/25);
   m00a = squeeze((Raw_Images(filter,n,1,:,:)  + Raw_Images(filter,n,3,:,:))/2);
   m00b = squeeze((Raw_Images(filter,n,2,:,:)  + Raw_Images(filter,n,4,:,:))/2);
   %m00error = (mean2(m00a(400:600,400:600)) - mean2(m00b(400:600,400:600)))...
   %          /mean2(squeeze(m00(1,1,1,400:600,400:600)))

   m00error = (m00a - m00b)./squeeze(m00(1,1,1,:,:));
   imagesc(m00error,[-.01 .01])
   m00error = mean2(m00error(400:600,400:600));
   %Check the m00s if different warn
   if(abs(m00error) > .013)
      disp(['Voltage :' num2str(n) ' is bad at' num2str(abs(m00error))]);
      error_flag = 1;
   end

   LCVR1and2_m01(filter,n,:,:) = single(m01);
   LCVR1and2_m02(filter,n,:,:) = single(m02);

end
```

```
    %For every voltage (system setting), find the averaged m00,m01,m02.  Then, show
    %resulting retardance and rotation angle for LCVR1 from the model.
    retard_guess = [150 35 175 18];
    for n=1:4

        M = Stokes_M_inv*squeeze(Raw_Images_Av(filter,n,:));
        M = M'/M(1);


        angs = lsqnonlin(@LCVR_Model_Two_LCVR,[retard_guess(n) 115],[-20 100],[230 130],...
            [],M(1,2),M(1,3), LCVR2_retard_av(filter,n),LCVR2_rotation_av(filter,n),0);
        LCVR1_retard_av(filter,n) = angs(1);
        LCVR1_rotation_av(filter,n) = angs(2);
        [LCVR2_retard_av(filter,n),LCVR2_rotation_av(filter,n) angs(1) angs(2)];
        %Model m03 from averages
        [m03] = LCVR_Model_Two_LCVR_m03(LCVR1_retard_av(filter,n),LCVR1_rotation_av(filter,n),...
                        LCVR2_retard_av(filter,n),LCVR2_rotation_av(filter,n));
        A_one(filter,n,:) = [M m03];
    end

    disp('Averaged System Matrix')
    squeeze(A_one(filter,:,:))
    disp(['Condition Number is ' num2str(cond(squeeze(A_one(filter,:,:))))])

    disp('LCVR1 Retardance and Rotation Angles')
    format bank
    [LCVR1_retard_av    LCVR1_rotation_av]
    format

    %Calculate A_inv
    A_one_inv(filter,:,:) = pinv(squeeze(A_one(filter,:,:)));

    %Check the Stokes parameters of the raw images, if bad redo the filter
    disp('Stokes Check')
    for j=1:4
        Stokes = squeeze(A_one_inv(filter,:,:))*Raw_Images_Av(filter,:,j)';
        Stokes = (Stokes/Stokes(1))';

        disp(num2str(Stokes,'   %4.4f'))

        if(max(abs(Stokes - Stokes_M(j,:))) > .01) %Check for out of bounds errors (probably a bad image)
            error_flag = 1;
        end
    end

    if(error_flag == 0)  %If no errors
        filter = filter + 1;
    end
end

fclose(rot_port);
```

```
temperatures
disp(char(['Maximum Temp Voltage:  ' num2str(max(max(temperatures)))]))
disp(char(['Minimum Temp Voltage:  ' num2str(min(min(temperatures)))]))

temp_av = mean2(temperatures);

disp(char(['Temperature Voltage Average:  ' num2str(temp_av) ...
        '    Temperature Calculated:  '  num2str(99.37*temp_av - 271.14)]))

%Save Data
cd('C:\MATLAB6p5p1\work\Polarimeter 4 Stokes Calibration\LCVR Data and Figures')
save(char(['LCVR1and2_m01_m02_' F_number calibration_name]),...
   'LCVR1and2_m01','LCVR1and2_m02','exp_time','Raw_Images',...
   'A_mean','A_one','A_one_inv','LCVR1_retard_av','LCVR1_rotation_av','temperatures')
cd ..
cd ..
```

Get_Telephoto_Mueller_Matrix MATLAB Code

```
%Nathan Pust
%May 9, 2005

% This script is used to get the data to calibrate out the effects of the
% Telephoto Lens.  Using 4 different angles of polarization and Stokes vectors
% measured from the near field calibration, the Mueller matrix of the
% Telephoto Lens is calculated.

%Use previously determined focus settings.  Then set the
%appropriate F number in the code.

clear
%Sphere Attn: 5800 F2.8
F_number = 'F28'; exp_time = [210 78 52 35 35];

% %Sphere Attn: 4300 F4.0
% F_number = 'F40'; exp_time = [195 78 52 37 37];
%
% %Sphere Attn:    0 F5.6
% F_number = 'F56'; exp_time = [195 78 52 35 35];
%
% %Sphere Attn:    0 F8.0
% F_number = 'F80'; exp_time = [250 156 100 70 70];

% %Sphere Attn:    0 F11
% F_number = 'F11'; exp_time = [250 250 200 140 140];

% %Sphere Attn:    0 F16
% F_number = 'F16'; exp_time = [250 250 250 250 250];

LCVR1 = 1;
LCVR2 = 3;  %LCVR2 is plugged into port 3
LCVR_delay = 55;

calibration_name = ['_Cal8'];

angle_of_reference = 104.24;
angle_of_reference = angle_of_reference - 90;

focus_points = [720 670 670 770 820];

no_stage_angles = 4;
stage_ang_increase = 45;
samples = 3;  %REMEMBER TO CHANGE BACK TO 3

clear nonlinearity_correction
load DALSA_1M30_linearity_correction_60105
nonlinearity_correction = DALSA_1M30_linearity_correction;
load('DALSA_1M30_DARK_IMAGE','DALSA_1M30_DARK_IMAGE');
Dark_Img = DALSA_1M30_DARK_IMAGE;
```

```
Stokes = zeros(5,4,no_stage_angles,1024,1024,'single');

%Import LCVR Voltages used in system
load LCVR_Voltages_450_700_4IMAGE_SYSTEM
load(char(['Inverse_System_Matrix_4_Image_' F_number calibration_name]),'A_inv')

%Initialization
Lens_M = zeros(5,4,4,1024,1024,'single');


%Open LCVR Port
LCVR_port = serial('Com3');
if(strcmp(LCVR_port.status,'open'))
   fclose(LCVR_port);
end
set(LCVR_port,'BaudRate',38400,'DataBits',8,'Parity','none','StopBits',1,...
          'Terminator','CR','FlowControl','None');
fopen(LCVR_port);
fprintf(LCVR_port,'tsp:?')
tsp = fscanf(LCVR_port)
if(~(strcmp(tsp(2:10),'tsp:10400') | strcmp(tsp(1:9),'tsp:10400')))
   fclose(LCVR_port);
   error('Temperature is not set in LCVR Controller')
end
fclose(LCVR_port)

%Open Rotation Stage
rot_port = serial('Com5');
if(strcmp(rot_port.status,'open'))
   fclose(rot_port);
end
set(rot_port,'BaudRate',19200,'DataBits',8,'Parity','none','StopBits',1,...
          'Terminator','CR/LF','FlowControl','Hardware');
fopen(rot_port);
fprintf(rot_port,'1MO');
%Home Rotation Stage
fprintf(rot_port,'1OR');
%Wait for stop moving
moving = '0';
while(str2num(moving) ~= 1)
   fprintf(rot_port,'1MD?');  %Request moving status
   pause(.050);
   moving = fscanf(rot_port);  %Get Moving Status from Newport Controller
   pause(.050);
end
fprintf(rot_port,'1TB');
fscanf(rot_port);

filter = 1;
while(filter < 6)

   error_flag = 0;
```

```
filter_wheel_dev = FLIOpen('flifil0',514);
FLISetFilterPos(filter_wheel_dev,filter-1);
FLIClose(filter_wheel_dev);

focuser_dev = FLIOpen('flifoc0',770); %770 is FLIDOMAIN_USB | FLIDEVICE_FOCUSER
FLIHomeFocuser(focuser_dev);
FLIStepMotor(focuser_dev,focus_points(filter));
disp('Focuser Initialized')
FLIClose(focuser_dev);

%Take Four Stokes Images
for j=1:no_stage_angles

   %Set Polarizer to -90,-45,0,45
   angle = angle_of_reference + -(j-1)*stage_ang_increase;
   fprintf(rot_port,strcat('1PA',num2str(angle)));
   moving = '0';
   %Wait for stop moving
   while(str2num(moving) ~= 1)
      fprintf(rot_port,'1MD?');  %Request moving status
      pause(.050);
      moving = fscanf(rot_port);  %Get Moving Status from Newport Controller
      pause(.050);

   end

   %Many sample way
   Raw_Images_Temp = zeros(4,1024,1024,'uint16');
   Raw_Images = zeros(4,1024,1024,'uint16');

   for(sample = 1:samples)

      [Raw_Images_Temp(1,:,:),Raw_Images_Temp(2,:,:),...
       Raw_Images_Temp(3,:,:),Raw_Images_Temp(4,:,:),Temperature] = ...
       Take_Image_Sequence_LCVR_C(exp_time(filter),1,1,1,...
                          LCVR1_Voltages(filter,:),LCVR2_Voltages(filter,:),LCVR_delay);

      Raw_Images_Temp = bitand(Raw_Images_Temp,bin2dec('0000111111111111'));
      Raw_Images = Raw_Images + Raw_Images_Temp;

   end
   Raw_Images = Raw_Images./samples;
   Temperature = strtrim(Temperature);
   Temperature = 6.4692e-005*str2num(Temperature(5:9)) + .4718;
   disp(char(['Temperature Voltage:  ' num2str(Temperature)]))
   temperatures(filter,j) = Temperature;


   [Stokes(filter,1,j,:,:),Stokes(filter,2,j,:,:),...
    Stokes(filter,3,j,:,:),Stokes(filter,4,j,:,:)] ...
     = Process_Raw_Data(filter,exp_time(filter),Dark_Img,nonlinearity_correction,...
                   A_inv,[],Raw_Images,'No Normalize');
```

```
   Stokes_Av(filter,:,j) = [mean2(squeeze(Stokes(filter,1,j,510:530,552:570)))...
                        mean2(squeeze(Stokes(filter,2,j,510:530,552:570)))...
                        mean2(squeeze(Stokes(filter,3,j,510:530,552:570)))...
                        mean2(squeeze(Stokes(filter,4,j,510:530,552:570)))];


end


%Create Matrix of Stokes Vectors, Invert
for j=1:no_stage_angles

   Stokes_M(j,:) = Stokes_100((j-1)*stage_ang_increase - 90);

end

Stokes_M_inv = pinv(Stokes_M(:,1:3));


%For every Stokes parameter, find the m00,m01,m02 of the lens.
for n=1:4

   %Raw_Images(filter,voltage,stage_angle,xpixel,ypixel)

   Lens_M(filter,n,1,:,:) = Stokes_M_inv(1,1).*Stokes(filter,n,1,:,:) + ...
                        Stokes_M_inv(1,2).*Stokes(filter,n,2,:,:) + ...
                        Stokes_M_inv(1,3).*Stokes(filter,n,3,:,:) + ...
                        Stokes_M_inv(1,4).*Stokes(filter,n,4,:,:);
   %Find m01
   Lens_M(filter,n,2,:,:) = Stokes_M_inv(2,1).*Stokes(filter,n,1,:,:) + ...
                        Stokes_M_inv(2,2).*Stokes(filter,n,2,:,:) + ...
                        Stokes_M_inv(2,3).*Stokes(filter,n,3,:,:) + ...
                        Stokes_M_inv(2,4).*Stokes(filter,n,4,:,:);
   %Find m02
   Lens_M(filter,n,3,:,:) = Stokes_M_inv(3,1).*Stokes(filter,n,1,:,:) + ...
                        Stokes_M_inv(3,2).*Stokes(filter,n,2,:,:) + ...
                        Stokes_M_inv(3,3).*Stokes(filter,n,3,:,:) + ...
                        Stokes_M_inv(3,4).*Stokes(filter,n,4,:,:);

   Lens_M_mean(filter,n,:) = [mean2(squeeze(Lens_M(filter,n,1,510:530,552:570)))...
                         mean2(squeeze(Lens_M(filter,n,2,510:530,552:570)))...
                         mean2(squeeze(Lens_M(filter,n,3,510:530,552:570))) 0];

end

M = squeeze(Lens_M_mean(filter,:,:)./Lens_M_mean(filter,1,1));

%Symmetrical Matrix Fill
M(1,4) = M(4,1);
M(2,4) = -M(4,2);
M(3,4) = -M(4,3);
M(4,4) = (M(2,2) + M(3,3))/2;
```

```
   Lens_M_mean(filter,:,:) = M;

   disp('Averaged Lens Matrix')
   squeeze(Lens_M_mean(filter,:,:))
   cond(squeeze(Lens_M_mean(filter,:,:)))

   %Calculate Lens_Inv
   Lens_M_mean_inv(filter,:,:) = pinv(squeeze(Lens_M_mean(filter,:,:)));

   %Check for errors in the calibration Stokes vector
   for j=1:4
      Stokes_Check = squeeze(Lens_M_mean_inv(filter,:,:))*(squeeze(Stokes_Av(filter,:,j)))';
      Stokes_Check = (Stokes_Check/Stokes_Check(1))'

      %Check for out of bounds errors (probably a bad image)
      if(max(abs(Stokes_Check - Stokes_M(j,:))) > .006)
         error_flag = 1;
      end
   end

   if(error_flag == 1)
      %Redo the filter
      disp('!!!!!!!!!!!!!!!!!!!!!!!!!!!!!! Error !!!!!!!!!!!!!!!!!!!!!!!!!!!!!!')
      disp('Redo Filter')
   else
      filter = filter + 1
   end

end

fclose(rot_port);
temperatures
disp(char(['Maximum Temp Voltage:  ' num2str(max(max(temperatures)))]))
disp(char(['Minimum Temp Voltage:  ' num2str(min(min(temperatures)))]))

%Save Data
cd('C:\MATLAB6p5p1\work\Polarimeter 4 Stokes Calibration\Telephoto Lens Data')
save(char(['Telephoto_Lens_M_' F_number calibration_name]),...
        'Lens_M','exp_time','Lens_M_mean','Lens_M_mean_inv','temperatures')
cd ..
cd ..
```

Process_Inverse_System_Matrix_w_m03_Model MATLAB Code

```
%Nathan Pust
%
%This script processes the Get_LCVR1and2_m01_m02 data into a polarimeter
%system matrix.  First set the F_number with the calibration name attached
%to the end.


clear;
calibration_dir = ...
   'C:\MATLAB6p5p1\work\Polarimeter 4 Stokes Calibration\LCVR Data and Figures'
%F_numbers = ['F56'; 'F40'; 'F28'; 'F80']
F_numbers = ['F28_Cal8']
sample_rate = 3;
options = optimset('Display','off','MaxIter',30,'TolX',.005,'TolFun',.001);
filters = 1:5;

for p=size(F_numbers,1)

   A_inv = zeros(5,4,4,1024,1024,'single');
   condition = single(zeros(5,1024,1024));
   load(char(['LCVR1and2_m01_m02_' F_numbers(p,:)]),...
         'LCVR1and2_m01','LCVR1and2_m02','filters','Raw_Images')
   load(char(['LCVR2_m01_m02_' F_numbers(p,:)]),...
         'LCVR2_m01', 'LCVR2_m02','filters')

   for filter = filters

      %Find Pseudo_Inverse of System Matrix (A)
      u = waitbar(0,char(['Processing Inverse System Matrix  Filter: ' num2str(filter)]));
      for(i=1:sample_rate:1024)
         tic
         for(j=1:sample_rate:1024)

            %Only do center portion
            if(((i-512)^2 + (j-512)^2) > (40+512)^2)
               continue;
            end

            %Model the m03s in the matrix
            m03 = single(zeros(4,1));
            retard_guess = [150 35 175 18];


            for n=1:4


               %Model LCVR2
               angs = lsqnonlin(@LCVR_Model_One_LCVR,[30 45],[-20 44],[220 46],...
                     options, double(LCVR2_m01(filter,n,i,j)),double(LCVR2_m02(filter,n,i,j)));
               LCVR2_retard(n) = angs(1);
               LCVR2_rotation(n) = angs(2);
```

```
            %Model LCVR1
            angs = lsqnonlin(@LCVR_Model_Two_LCVR,[retard_guess(n) 115],[-20 100],...
                  [230 130],options, double(LCVR1and2_m01(filter,n,i,j)),
                  double(LCVR1and2_m02(filter,n,i,j)), LCVR2_retard(n),LCVR2_rotation(n),0);

            LCVR1_retard(n) = angs(1);
            LCVR1_rotation(n) = angs(2);

            %Make m03 from Models
            m03(n) = LCVR_Model_Two_LCVR_m03(LCVR1_retard(n),LCVR1_rotation(n),...
                                    LCVR2_retard(n),LCVR2_rotation(n));
         end

         Apixel = [1 LCVR1and2_m01(filter,1,i,j) LCVR1and2_m02(filter,1,i,j) m03(1);
                  1 LCVR1and2_m01(filter,2,i,j) LCVR1and2_m02(filter,2,i,j) m03(2);
                  1 LCVR1and2_m01(filter,3,i,j) LCVR1and2_m02(filter,3,i,j) m03(3);
                  1 LCVR1and2_m01(filter,4,i,j) LCVR1and2_m02(filter,4,i,j) m03(4)];

         Apixel_inv = pinv(Apixel);
         A_inv(filter,:,:,i,j) = Apixel_inv;
         condition(filter,i,j) = cond(Apixel);

      end
      toc
      waitbar(i/1024,u)

      F_numbers(p,:)
      [filter i]
      pause(.02)

   end
   close(u)

   %Filter for subsampling
   for n=1:4
      for k=1:4
         A_inv(filter,n,k,:,:) = ...
            imfilter(squeeze(A_inv(filter,n,k,:,:)),ones(sample_rate,sample_rate));
      end
      condition(filter,:,:) = ...
         imfilter(squeeze(condition(filter,:,:)),ones(sample_rate,sample_rate));
   end


   %     h1 = figure;
   %     set(gcf,'Position',[30 38 1216 878])
   %     h2 = figure;
   %     set(gcf,'Position',[30 38 1216 878])
end

clear LCVR2_m01 LCVR2_m02 LCVR1and2_m01 LCVR1and2_m02
load(char(['LCVR1and2_m01_m02_' F_numbers(p,:)]), 'Raw_Images')
```

```
for filter=filters

   for j=1:4
      %Do data check on Calibration data
      %Process Data
      Stokes0 = squeeze(A_inv(filter,1,1,:,:)).*squeeze(Raw_Images(filter,1,j,:,:)) + ...
            squeeze(A_inv(filter,1,2,:,:)).*squeeze(Raw_Images(filter,2,j,:,:)) + ...
            squeeze(A_inv(filter,1,3,:,:)).*squeeze(Raw_Images(filter,3,j,:,:)) + ...
            squeeze(A_inv(filter,1,4,:,:)).*squeeze(Raw_Images(filter,4,j,:,:));

      Stokes1 = squeeze(A_inv(filter,2,1,:,:)).*squeeze(Raw_Images(filter,1,j,:,:)) + ...
            squeeze(A_inv(filter,2,2,:,:)).*squeeze(Raw_Images(filter,2,j,:,:)) + ...
            squeeze(A_inv(filter,2,3,:,:)).*squeeze(Raw_Images(filter,3,j,:,:)) + ...
            squeeze(A_inv(filter,2,4,:,:)).*squeeze(Raw_Images(filter,4,j,:,:));

      Stokes2 = squeeze(A_inv(filter,3,1,:,:)).*squeeze(Raw_Images(filter,1,j,:,:)) + ...
            squeeze(A_inv(filter,3,2,:,:)).*squeeze(Raw_Images(filter,2,j,:,:)) + ...
            squeeze(A_inv(filter,3,3,:,:)).*squeeze(Raw_Images(filter,3,j,:,:)) + ...
            squeeze(A_inv(filter,3,4,:,:)).*squeeze(Raw_Images(filter,4,j,:,:));

      Stokes3 = squeeze(A_inv(filter,4,1,:,:)).*squeeze(Raw_Images(filter,1,j,:,:)) + ...
            squeeze(A_inv(filter,4,2,:,:)).*squeeze(Raw_Images(filter,2,j,:,:)) + ...
            squeeze(A_inv(filter,4,3,:,:)).*squeeze(Raw_Images(filter,3,j,:,:)) + ...
            squeeze(A_inv(filter,4,4,:,:)).*squeeze(Raw_Images(filter,4,j,:,:));

      Stokes1 = Stokes1./Stokes0;
      Stokes2 = Stokes2./Stokes0;
      Stokes3 = Stokes3./Stokes0;

      [mean2(Stokes1(400:600,400:600))...
       mean2(Stokes2(400:600,400:600))...
       mean2(Stokes3(400:600,400:600))]

      %        figure(h1)
      %        subplot(4,4,j)
      %        imagesc(Stokes1)
      %        colorbar
      %        subplot(2,4,j+4)
      %        imagesc(Stokes2)
      %        colorbar
      %
      %        figure(h2)
      %        subplot(2,4,j)
      %        hist(Stokes1)
      %        subplot(2,4,j+4)
      %        hist(Stokes2)
   end

end

% figure
% imagesc(squeeze(condition(filter,:,:)),[0 4])
```

```
    % colorbar

    %Save Data
    cd(calibration_dir);
    save(char(['Inverse_System_Matrix_4_Image_' F_numbers(p,:)]),...
            'A_inv','condition','filters','Apixel','Apixel_inv');
    cd ..
    cd ..

    clear('A_inv','condition','filters','Apixel','Apixel_inv','Raw_Images');

end
```